

## **INFORMATION TO USERS**

**This manuscript has been reproduced from the microfilm master. UMI films the text directly from the original or copy submitted. Thus, some thesis and dissertation copies are in typewriter face, while others may be from any type of computer printer.**

**The quality of this reproduction is dependent upon the quality of the copy submitted. Broken or indistinct print, colored or poor quality illustrations and photographs, print bleedthrough, substandard margins, and improper alignment can adversely affect reproduction.**

**In the unlikely event that the author did not send UMI a complete manuscript and there are missing pages, these will be noted. Also, if unauthorized copyright material had to be removed, a note will indicate the deletion.**

**Oversize materials (e.g., maps, drawings, charts) are reproduced by sectioning the original, beginning at the upper left-hand corner and continuing from left to right in equal sections with small overlaps. Each original is also photographed in one exposure and is included in reduced form at the back of the book.**

**Photographs included in the original manuscript have been reproduced xerographically in this copy. Higher quality 6" x 9" black and white photographic prints are available for any photographs or illustrations appearing in this copy for an additional charge. Contact UMI directly to order.**

# **UMI**

**A Bell & Howell Information Company  
300 North Zeeb Road, Ann Arbor MI 48106-1346 USA  
313/761-4700 800/521-0600**



**UNIVERSITY OF ALBERTA**

**THE NOVEL IMPULSE ATOMIZATION PROCESS**

**BY**

**DING YUAN**



**A thesis submitted to the Faculty of Graduate Studies and Research in partial fulfilment of the requirements for the degree of Doctor of Philosophy.**

**in**

**Materials Engineering**

**DEPARTMENT OF CHEMICAL AND MATERIALS ENGINEERING**

**Edmonton, Alberta**

**Fall, 1997**



**National Library  
of Canada**

**Acquisitions and  
Bibliographic Services**

**395 Wellington Street  
Ottawa ON K1A 0N4  
Canada**

**Bibliothèque nationale  
du Canada**

**Acquisitions et  
services bibliographiques**

**395, rue Wellington  
Ottawa ON K1A 0N4  
Canada**

*Your file Votre référence*

*Our file Notre référence*

The author has granted a non-exclusive licence allowing the National Library of Canada to reproduce, loan, distribute or sell copies of this thesis in microform, paper or electronic formats.

The author retains ownership of the copyright in this thesis. Neither the thesis nor substantial extracts from it may be printed or otherwise reproduced without the author's permission.

L'auteur a accordé une licence non exclusive permettant à la Bibliothèque nationale du Canada de reproduire, prêter, distribuer ou vendre des copies de cette thèse sous la forme de microfiche/film, de reproduction sur papier ou sur format électronique.

L'auteur conserve la propriété du droit d'auteur qui protège cette thèse. Ni la thèse ni des extraits substantiels de celle-ci ne doivent être imprimés ou autrement reproduits sans son autorisation.

0-612-23099-6

**UNIVERSITY OF ALBERTA**

**RELEASE FORM**

**NAME OF AUTHOR: DING YUAN**

**TITLE OF THESIS: THE NOVEL IMPULSE ATOMIZATION PROCESS**

**DEGREE: Doctor of Philosophy**

**YEAR THIS DEGREE GRANTED: 1997**

Permission is hereby granted to the University of Alberta Library to reproduce single copies of this thesis and to lend or sell such copies for private, scholarly or scientific research purposes only.

The author reserves all other publication and other rights in association with the copyright in the thesis, and except as hereinbefore provided neither the thesis nor any substantial portion thereof may be printed or otherwise reproduced in any material form whatever without the author's prior written permission.

A handwritten signature in cursive script that reads "Ding Yuan". The signature is written in black ink and is positioned above a solid horizontal line.

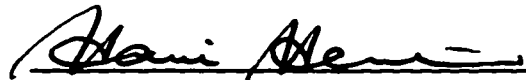
**DING YUAN  
611G-Michener Park  
Edmonton, Alberta  
Canada T6H 5A1**

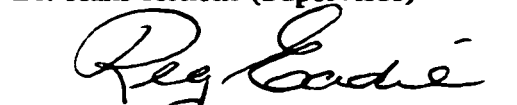
July 21, 1997


UNIVERSITY OF ALBERTA

FACULTY OF GRADUATE STUDIES AND RESEARCH

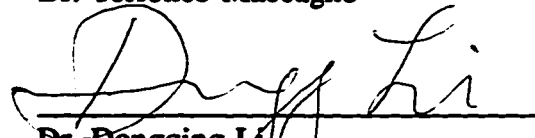
The undersigned certify that they have read, and recommend to the Faculty of Graduate Studies and Research for acceptance, a thesis entitled THE NOVEL IMPULSE ATOMIZATION PROCESS submitted by DING YUAN in partial fulfilment of the requirements for the degree of DOCTOR OF PHILOSOPHY in Materials Engineering.

  
Dr. Hani Henein (Supervisor)

  
Dr. Reginald L. Eadie (Co-supervisor)

  
Dr. Jacob H. Masliyah

  
Dr. Terrence Maccagno

  
Dr. Dongqing Li

  
Dr. Dave Wilkinson (External)

July 17, 1997

## **DEDICATION**

**To my parents, Ji Chun Rong and Yuan Geng Zhou, and my son, Philip Minghao Ma.**

## **ABSTRACT**

**Conventional gas atomization produces droplets and powders that vary widely in size distribution and microstructure, thus making it very costly to produce powders tailor made with a narrow size distribution and microstructure. A novel atomization process, Impulse Atomization Process (IAP), has been developed by the author, that is capable of producing powders with narrow particle size distribution. With IAP, it is feasible to produce powders with engineered shape, size, size distribution, and microstructure by adjusting experimental operating conditions.**

**In this thesis, both the conventional atomization processes and the capillary atomization processes are reviewed. The literature about the effect of cooling parameters on the microstructure is also presented. The experimental apparatus and process of IAP is described. The effect of operating parameters of IAP on the particle size, size distribution, production rate, powder shape, and powder microstructure are presented and discussed. The secondary dendrite arm spacing (SDAS) of two Al-Cu alloy powders produced by IAP was measured, and a Newtonian cooling model accounting for undercooling of the droplets was developed. Both measured and predicted SDAS showed that an increase in droplet superheat and a decrease in droplet size result in a finer powder microstructure. Furthermore, the SDAS of Al-Ni-Fe alloy powder ( $2.3$  to  $4.6 \times 10^{-4}$  m) produced using IAP showed a finer microstructure than would be obtained by either gas or centrifugal atomization for the same sized powders.**



## **ACKNOWLEDGEMENTS**

**The author is very grateful to her supervisor, Dr. H. Henein, and her co-supervisor, Dr. R. L. Eadie, for their directions, patient instructions, and sincere support of her thesis both in experimental work and in writing. She is also in debt to her candidacy and defence committee, Dr. J. Masliyah, Dr. J. Luo, Dr. T. Maccagno, Dr. D. Ivey, Dr. M. Wayman, Dr. A. C. Pierre, Dr. D. Li, and Dr. D. Wilkinson. The support from Dr. Prasad Apté from her work place is also highly appreciated.**

**The author's sincere appreciation also goes to Mr. B. Konzuk, Mr. B. Smith, and Mr. R. Stefaniuk for their contribution in building the experimental apparatus. The author is thankful to Ms. C. Barker for the SEM work. It was also a pleasure for the author to work in the same group with Ms. T. Le, Ms. C. Boyko, Mr. K. Olsen as well as many other students and scholars in the Advanced Materials and Processing Laboratory in University of Alberta.**

**The author is thankful for financial support from the Natural Science and Engineering Research Council of Canada.**

**This thesis might not have been completed without support from the author's family: her parents, Ji Chun Rong and Yuan Geng Zhou, her parents-in-law, Zhang Shu Zhong and Ma Xiang Feng, and her husband, Ma Kunsong. She also feels a debt to her son, Philip Minghao Ma, for not having been able to give him as much care as she would like to because of her thesis work.**

## **TABLE OF CONTENTS**

	<b>Page</b>
<b>CHAPTER 1 INTRODUCTION</b>	<b>1</b>
<b>CHAPTER 2 LITERATURE REVIEW</b>	<b>6</b>
<b>2.1 Overview of Conventional Fluid Atomization</b>	<b>6</b>
<b>2.2 Overview of Capillary Atomization</b>	<b>9</b>
<b>2.2.1 Disintegration Mechanism of Liquid Jets Emanating from a Capillary</b>	<b>10</b>
<b>2.2.2 Theory of Capillary Instability</b>	<b>11</b>
<b>2.2.2.1 Theory Based on Linear Capillary Instability</b>	<b>12</b>
<b>2.2.2.2 Minimum Velocity for Stable Jet Formation</b>	<b>15</b>
<b>2.2.2.3 Deviation from the Linear Capillary Instability</b>	<b>18</b>
<b>2.2.3 Production of Droplets from Continuous Jets</b>	<b>19</b>
<b>2.2.3.1 Production of Metallic Droplets from Continuous Jets</b>	<b>20</b>
<b>2.2.4 Drop on Demand Method</b>	<b>25</b>
<b>2.2.4.1 Production of Droplets by Drop on Demand Method</b>	<b>25</b>
<b>2.2.4.2 Drop on Demand Method Applied to Metals</b>	<b>27</b>
<b>2.2.5 Summary of Atomization Methods</b>	<b>28</b>
<b>2.3 Relationship between Microstructure and Cooling Conditions</b>	<b>29</b>
<b>2.3.1 Relationship between Secondary Dendrite Arm Spacing and Cooling Rate</b>	<b>30</b>
<b>2.3.1.1 Experimental Results</b>	<b>30</b>
<b>2.3.1.2 Empirical Relationship</b>	<b>32</b>
<b>2.3.2 Effect of Superheat and Cooling Rate, Secondary Dendrite Arm Spacing</b>	<b>36</b>
<b>2.3.3 Relationship between Undercooling and Dendrite Arm Spacing</b>	<b>38</b>

2.3.4	Relationship between Cooling Rate and Undercooling	39
2.3.5	Relationship between Particle Size and Secondary Dendrite Arm Spacing	40
2.4	<b>Numerical Models</b>	43
2.4.1	<b>Fundamentals of Heat Transfer of a Droplet</b>	44
2.4.1.1	Newtonian Model	44
2.4.1.2	Droplet Velocity	47
2.4.2	<b>Fundamentals of Nucleation</b>	49
2.4.2.1	Homogeneous Nucleation	49
2.4.2.2	Heterogeneous Nucleation	54
2.4.3	<b>Fundamentals of Growth</b>	55
2.4.3.1	Grain Growth and Dendritic Microstructure	55
2.4.3.2	Kinetics of Growth	57
2.4.3.3	Recalescence	58
2.5	<b>Summary</b>	61
 <b>CHAPTER 3 NUMERICAL MODEL</b>		63
3.1	<b>Assumptions</b>	63
3.2	<b>Model Formulation</b>	66
3.3	<b>Phase Change</b>	68
3.3.1	Stage I: Cooling in the Liquid Range, $T=T_p \sim T_n$ :	69
3.3.2	Stage II: Recalescence, $T=T_n \sim T_r$ :	70
3.3.3	Stage III: Cooling in the Liquid + Solid Range, $T=T_r \sim T_e$ :	73
3.3.4	Stage IV: Eutectic Transformation, $T=T_e$ , $f_s=f_m \sim 1$ :	75
3.3.5	Stage V: Cooling in the Solid Range, $T=T_e \sim T_a$ :	76
3.4	<b>Model Formulation Summary</b>	76
3.5	<b>Thermophysical Properties of Alloy and Gas Atmosphere</b>	78
3.6	<b>Numerical Solution of Droplet Cooling</b>	81

<b>3.7</b>	<b>Nucleation Temperature</b>	<b>83</b>
<b>CHAPTER 4 EXPERIMENTAL</b>		<b>86</b>
<b>4.1</b>	<b>Impulse Atomization Apparatus</b>	<b>86</b>
<b>4.1.1</b>	<b>Furnace</b>	<b>88</b>
<b>4.1.2</b>	<b>Crucible</b>	<b>88</b>
<b>4.1.3</b>	<b>Impulse Applicator</b>	<b>89</b>
<b>4.1.4</b>	<b>Pulsator and Its Controlling System</b>	<b>90</b>
<b>4.1.5</b>	<b>Frame</b>	<b>90</b>
<b>4.1.6</b>	<b>Shell</b>	<b>91</b>
<b>4.1.7</b>	<b>Monitoring System</b>	<b>93</b>
<b>4.2</b>	<b>Impulse Atomization Process</b>	<b>94</b>
<b>4.3</b>	<b>Powder Characterization</b>	<b>96</b>
<b>4.4</b>	<b>Microstructure Characterization</b>	<b>97</b>
<b>4.5</b>	<b>Image Analysis</b>	<b>99</b>
<b>4.6</b>	<b>Summary</b>	<b>100</b>
<b>CHAPTER 5 OPERATING VARIABLES OF IAP - RESULTS AND DISCUSSIONS</b>		<b>101</b>
<b>5.1</b>	<b>Accuracy in Measuring Atomizing Variation</b>	<b>101</b>
<b>5.2</b>	<b>Effect of Frequency</b>	<b>103</b>
<b>5.3</b>	<b>Effect of Relative Amplitude</b>	<b>105</b>
<b>5.4</b>	<b>Effect of Acceleration</b>	<b>108</b>
<b>5.5</b>	<b>Effect of Orifice Size</b>	<b>109</b>
<b>5.6</b>	<b>Effect of Nozzle-Impulse Applicator Distance</b>	<b>112</b>

<b>5.7</b>	<b>Effect of Superheat</b>	<b>112</b>
<b>5.8</b>	<b>Effect of Oxygen Content on Size and Size Distribution and Powder Shape</b>	<b>113</b>
<b>5.9</b>	<b>Effect of Number of Orifices</b>	<b>115</b>
<b>5.10</b>	<b>Effect of Acceleration on Throughput</b>	<b>117</b>
<b>5.11</b>	<b>Effect of Orifice Size on Throughput</b>	<b>119</b>
<b>5.12</b>	<b>Effect of Melt Viscosity on the Process</b>	<b>120</b>
	5.12.1 Background	120
	5.12.2 Experiment	120
<b>5.13</b>	<b>Proposed Atomization Mechanism of IAP</b>	<b>127</b>
	5.13.1 Formation of Discontinuous Streams by IAP	128
	5.13.2 The Number of Drops per Second	129
<b>5.14</b>	<b>Advantage of Impulse Atomization Process</b>	<b>134</b>
	5.14.1 Advantage of IAP over Conventional Fluid Atomization	134
	5.14.2 Advantage of IAP over Capillary Atomization	136
<b>CHAPTER 6 EXPERIMENTAL RESULTS AND DISCUSSION OF MICROSTRUCTURE ANALYSIS OF POWDERS PRODUCED BY IAP</b>		<b>138</b>
<b>6.1</b>	<b>Calibration of Image Analysis</b>	<b>139</b>
<b>6.2</b>	<b>Uniformity of Microstructure of a Al-Cu Alloy Droplet</b>	<b>140</b>
<b>6.3</b>	<b>Reproducibility of Microstructure</b>	<b>144</b>
<b>6.4</b>	<b>Effect of Particle size on Microstructure of Al-Cu Alloys</b>	<b>145</b>
<b>6.5</b>	<b>Effect of Superheat on Microstructure of Al-10wt% Alloys</b>	<b>147</b>
<b>6.6</b>	<b>Microstructural Analysis of Al-Cu Powders</b>	<b>149</b>

6.6.1	Cooling Rate versus SDAS Relationship	149
6.6.2	Cooling Rate from the Model and Estimated according to Structure	150
6.7	Effect of Particle Size on Microstructure of Al-Ni-Fe System	154
6.8	Effect of Atomization Media on Microstructure of Al-Ni-Fe System	155
6.9	Microstructural Analysis of Al-Ni-Fe Powders	156
CHAPTER 7 SUMMARY		159
Future Work		161
FIGURES		163
REFERENCES		238
APPENDIX A	FORTRAN PROGRAM TO CALCULATE THE TEMPERATURE PROFILE OF A Al-17wt%Cu DROPLET	249
APPENDIX B	FORTRAN PROGRAM TO CALCULATE THE TEMPERATURE PROFILE OF A Al-10wt%Cu DROPLET	269
APPENDIX C	ACCELERATION CHARACTERISTICS OF IMPULSE GENERATORS	289
APPENDIX D	FORTRAN PROGRAM TO CALCULATE SECONDARY DENDRITE ARM SPACING	292

## LIST OF TABLES

	<b>Page</b>
Table 2-1 Relationship between the Secondary Dendrite Arm Spacing and Cooling Rate	34
Table 2-2 Average Values of Cooling Rate, Temperature Gradient and Dendrite Spacing [Horwath, 1962]	35
Table 2-3 Relationship between Particle Size and Dendrite Arm Spacing	42
Table 3-1 Physical and Thermal Properties of Al-Cu Alloys	79
Table 3-2 Physical and Thermal Properties of Nitrogen	80
Table 5-1 Estimated Absolute Amplitude of the Impulse Applicator in Air	107
Table 5-2 Effect of Orifice Size on Size and Size Distribution of Powders Produced by IAP	
a). Zn-Pb alloy	111
b). Pb-12wt%Sn alloy	111
Table 5-3 Effect of Number of Orifices per Nozzle Plate on Al-10wt%Cu Alloy	116
Table 5-4 Throughput of Sn-15wt%Pb ( $5 \times 10^{-4}$ m orifice size, 640 K, nitrogen)	118
Table 5-5 Throughput of Zn-Pb Alloy (810-860 K, Nitrogen)	119
Table 5-6 Atomization of Pure Molasses with $3.7 \times 10^{-2}$ m Diameter Plunger	121
Table 5-7 Atomization of Mixtures of Molasses and Water with $3.7 \times 10^{-2}$ m Plunger	123
Table 5-8 Atomization of Mixtures of Water with a $6.5 \times 10^{-3}$ m Plunger	123
Table 5-9 Effect of Nozzle-plunger Distance on the Atomization of Water with a $6.5 \times 10^{-3}$ m Plunger	125

<b>Table 5-10</b>	<b>Effect of Nozzle-plunger Distance on the Atomization of Mixtures of Molasses and Water with a <math>6.5 \times 10^{-3}</math> m Plunger</b>	<b>126</b>
<b>Table 5-11</b>	<b>Effect of Water:molasses Ratio on the Atomization of Mixtures of Molasses and Water with a <math>6.5 \times 10^{-2}</math> m Plunger</b>	<b>126</b>
<b>Table 5-12</b>	<b>Calculation of Number of Droplets from Sieving Results</b>	<b>132</b>
<b>Table 5-13</b>	<b>Number of Droplets per Impulse Produced by IAP</b>	<b>133</b>
<b>Table 6-1</b>	<b>SDAS Measurement of <math>4.6 \times 10^{-4}</math> m Al-17wt%Cu Droplet at Different Portions of the Droplet</b>	<b>143</b>
<b>Table 6-2</b>	<b>SDAS Measurement of <math>5.5 \times 10^{-4}</math> m Al-17wt%Cu Droplet at Different Portions of the Droplet</b>	<b>143</b>
<b>Table 6-3</b>	<b>Effect of Particle Size on SDAS of Al-17wt%Cu Alloys</b>	<b>146</b>
<b>Table 6-4</b>	<b>Effect of Particle Size on SDAS of Al-10wt%Cu Alloys</b>	<b>146</b>
<b>Table 6-5</b>	<b>Effect of Superheat on SDAS of Al-10wt%Cu Alloys</b>	<b>148</b>
<b>Table 6-6</b>	<b>Comparison between Measured and Predicted SDAS as a Function of Particle Diameter for an Al-17wt%Cu Alloy</b>	<b>153</b>
<b>Table 6-7</b>	<b>Comparison between Measured and Predicted SDAS as a Function of Superheat for an Al-10wt%Cu Alloy (Particle Diameter = <math>5.5 \times 10^{-4}</math> m)</b>	<b>153</b>
<b>Table 6-8</b>	<b>Linear Regression Results for <math>\lambda_2 = a_2 D^{b_2}</math> for Al-3.7wt%Ni-1.5wt%Fe from Various Atomization Technique</b>	<b>158</b>



## LIST OF FIGURES

	<b>Page</b>
Figure 2-1. Schematic representation of the disintegration of a liquid sheet by a high velocity gas jet. Stage I: Growth of waves on sheet; stage II: Fragmentation and formation of ligaments; stage III: Breakdown of ligaments into drops. [Dombrowski and Johns, 1963]	163
Figure 2-2. Mechanisms of droplet disintegration. [Schmidt, 1967]	164
Figure 2-3. Disintegration of a liquid jet under the action of vibration.	165
Figure 2-4. Drop-on-demand mode operating sequences: a. rest position; b. early injecting position; c. later injecting position; d. refilling position . [Ashgriz and Yao, 1987]	166
Figure 2-5. Dendrite arm spacing as a function of cooling rate for aluminum & aluminum alloys. [Grant and Perlloux, 1983]	167
Figure 2-6. Effect of cooling rate on primary dendrite arm spacing $\lambda_1$ , secondary dendrite arm spacing $\lambda_2$ and tertiary dendrite arm spacing $\lambda_3$ of Al-5.7wt%Cu alloy. [Taha, 1979]	168
Figure 2-7. (a) Dendrite spacing of 3003 aluminum alloy as function of superheat, M=metal mold, B=brick mold, F=furnace cooled (b) solidification rate as function of superheat for various aluminum alloys cast in the metal and insulating brick mold and furnace cooled. [Mondolfo and Barlock, 1975]	169
Figure 2-8. Relationship between undercooling and dendrite-element size in pure copper ingots. [Jones, 1972]	170
Figure 2-9. Dendrite arm spacing for dendritic specimens and grain size for both dendritic and non-dendritic specimens versus degree of undercooling. Ni-25%Cu-0.2%S alloy. [Skolianos et al, 1982]	171
Figure 2-10. Dimensionless undercooling ( $\Delta T/T_1 \times 10^2$ ) versus cooling rate for aluminium. $\Delta T$ and $T_1$ represent undercooling and equilibrium melting temperature respectively. [Reddy and Sekhar, 1989]	172

Figure 2-11.	Dimensionless undercooling versus cooling rate for Al-5.6%Zn-2.6%Mg-1.5%Cu alloy. [Reddy and Sekhar, 1989]	173
Figure 2-12.	Dimensionless undercooling versus cooling rate for the aluminum copper alloys solidified under an applied pressure of 277.3 MPa; (a) Al-2.2wt%Cu (b) Al-4.4wt%Cu (c) Al-33.2wtCu. [Reddy and Sekhar, 1989]	174
Figure 2-13.	Dendrite arm spacing (secondary) as a function of powder particle diameter for high strength aluminum alloys. [Jones, 1986]	175
Figure 2-14.	Dendrite arm spacing as a function of powder particle diameter for Al-3.7wt%Ni-1.5wt%Fe alloy. [Hildeman et al, 1983]	176
Figure 2-15.	Plot of the drop coefficient against the particle Reynolds number. [Szekely, 1979]	177
Figure 2-16.	Free energy change during nucleation. [Minkoff, 1986]	178
Figure 2-17.	Relationship between nucleation rate and undercooling. [Liu, 1980]	179
Figure 2-18.	The dependence of nucleation temperature $T_n$ on critical energy barrier $\Delta G_c^0$ . For large values of $\Delta G_c^0$ , as for example in homogeneous nucleation ( $\Delta G_c^0$ ), $T_n$ will give a maximum value to undercooling. [Minkoff, 1986]	180
Figure 2-19.	Schematic of dependence of nucleation rate on undercooling. [Liu, 1980]	181
Figure 2-20.	Schematic of a dendrite. [Liu, 1980]	182
Figure 2-21.	Schematic enthalpy versus temperature diagram for cooling and solidification of small alloy droplet for (a) equilibrium freezing and (b) freezing from an undercooled melt. [Lavernia et al, 1988]	183
Figure 2-22.	Enthalpy-temperature diagram showing possible solidification "paths". [Levi and Mehrabian, 1982]	184
Figure 3-1.	Schematic of a: an atomized droplet by IAP; and b: the forces acting on a droplet during free fall.	185
Figure 3-2.	Phase diagram of Al-Cu alloy. [Lyman et al, 1973]	186

Figure 3-3.	Schematic of cooling curve of a Al-Cu droplet in the composition range between 5.65wt%Cu to 33.2wt%Cu.	187
Figure 3-4	Schematic of solidification of a droplet with a radius R and its solidified fraction with a radius r.	188
Figure 3-5.	Droplet streaks for velocity measurement taken by video camera with shutter speed=1/250 s.	189
Figure 3-6.	Velocity profile of a $3.3 \times 10^{-4}$ m Al-17wt%Cu droplet with an initial velocity of 1.13 m/s.	190
Figure 3-7.	Effect of undercooling on SDAS of a $3.3 \times 10^{-4}$ m Al-17wt%Cu droplet.	191
Figure 3-8.	Temperature profile of a $3.3 \times 10^{-4}$ m Al-17wt%Cu droplet with an initial velocity of 1.13 m/s. The amount of superheat was 100 K. The amount of undercooling assumed was 30 K, the time step size was 0.01 s except in stage II where $3 \times 10^{-5}$ s was used.	192
Figure 3-9.	Solid fraction profile of a $3.3 \times 10^{-4}$ m Al-17wt%Cu droplet with an initial velocity of 1.13 m/s. The amount of superheat was 100 K. The amount of undercooling assumed was 30 K, the time step size was 0.01 s except in stage II where $3 \times 10^{-5}$ s was used.	193
Figure 3-10.	Heat transfer coefficient of a $3.3 \times 10^{-4}$ m Al-17wt%Cu droplet with an initial velocity of 1.13 m/s.	194
Figure 3-11.	Cooling curve of a $3.3 \times 10^{-4}$ m Al-17wt%Cu droplet with an initial velocity of 1.13 m/s. The amount of superheat was 100 K. The amount of undercooling assumed was 30 K, the time step size was 0.01 s except in stage II where $3 \times 10^{-5}$ s was used.	195
Figure 3-12.	Cooling curve of a $4.6 \times 10^{-4}$ m Al-17wt%Cu droplet with an initial velocity of 1.13 m/s. The amount of superheat was 100 K. The amount of undercooling assumed was 30 K, the time step size was 0.01 s except in stage II where $3 \times 10^{-5}$ s was used.	196
Figure 4-1	Photograph of the impulse atomization apparatus.	197
Figure 4-2.	A schematic of experimental apparatus.	198

<b>Figure 4-3.</b>	<b>Nozzle pattern used in various atomization experiments.</b>	<b>199</b>
<b>Figure 5-1.</b>	<b>Reproducibility of Impulse Atomization Process.</b>	<b>200</b>
<b>Figure 5-2.</b>	<b>Effect of frequency on geometric mean size and geometric standard deviations.</b>	<b>201</b>
<b>Figure 5-3.</b>	<b>Effect of relative amplitude on geometric mean size and geometric standard deviations.</b>	<b>202</b>
<b>Figure 5-4.</b>	<b>Effect of acceleration on geometric mean size and geometric standard deviations.</b>	<b>203</b>
<b>Figure 5-5.</b>	<b>Effect of nozzle-impulse applicator distance on geometric mean size and geometric standard deviations.</b>	<b>204</b>
<b>Figure 5-6.</b>	<b>Effect of superheat on geometric mean size and geometric standard deviations.</b>	<b>205</b>
<b>Figure 5-7.</b>	<b>Effect of oxygen content on geometric mean size and geometric standard deviations.</b>	<b>206</b>
<b>Figure 5-8.</b>	<b>Effect of oxygen content on powder shape. a). atomized in nitrogen; b). atomized in air.</b>	<b>207</b>
<b>Figure 5-9.</b>	<b>Temperature vs. time for the atomization of Se.</b>	<b>208</b>
<b>Figure 5-10.</b>	<b>Schematic drawing of the formation procedure of discontinuous streams by IAP. (a) formation of a discontinuous stream with application of plunger; (b) break up of the discontinuous stream and retrieve of the plunger; (c) second cycle of (a); (d) oxidized condition without breaking up of the discontinuous stream.</b>	<b>209</b>
<b>Figure 5-11.</b>	<b>SEM photograph of Copper droplets produced by IAP.</b>	<b>210</b>
<b>Figure 6-1.</b>	<b>Standard grid taken under SEM. One grid = <math>6.4 \times 10^{-5}</math> m. a). original picture of the grid; b). skeleton of the grid.</b>	<b>211</b>
<b>Figure 6-2.</b>	<b>SEM micrographs of Al-17wt%Cu droplet. a). surface morphology of the droplet; b). microstructure at the centre part of a <math>4.6 \times 10^{-4}</math> m droplet; c). microstructure at the centre part of the <math>4.6 \times 10^{-4}</math> m droplet.</b>	<b>212</b>

- Figure 6-3. Transferred images of a  $4.6 \times 10^{-4}$  m Al-17wt%Cu droplet. a). original image; b). processed binary image; c). processed skeleton image. 214
- Figure 6-4. SEM micrographs of a  $4.6 \times 10^{-4}$  m Al-17wt%Cu droplet. a). microstructure at the edge of image shown in Fig.6-2b; b) a microstructure of a small cross section of another droplet. 216
- Figure 6-5. SEM micrographs of a  $5.5 \times 10^{-4}$  m Al-10wt%Cu droplet. a). overall microstructure of the droplet; b). microstructure at the centre part of the droplet; c). microstructure at the edge part; d). microstructure at the small section of another droplet. 217
- Figure 6-6. SEM micrographs of a  $4.6 \times 10^{-4}$  m Al-17wt%Cu droplet from two similar runs. 219
- Figure 6-7. SEM micrographs of Al-17wt%Cu droplets in different size ranges. a). mid size =  $6.6 \times 10^{-4}$  m; b). mid size =  $4.6 \times 10^{-4}$  m; c). mid size =  $3.3 \times 10^{-4}$  m; d). mid size =  $2.3 \times 10^{-4}$  m. 220
- Figure 6-8. SEM micrographs of Al-10wt%Cu droplets in different size ranges. a). mid size =  $7.8 \times 10^{-4}$  m; b). mid size =  $5.5 \times 10^{-4}$  m; c). mid size =  $3.9 \times 10^{-4}$  m; d). mid size =  $2.8 \times 10^{-4}$  m; e). mid size =  $2 \times 10^{-4}$  m; f). mid size =  $1.4 \times 10^{-4}$  m. 222
- Figure 6-9. SEM micrographs of a  $5.5 \times 10^{-4}$  m Al-10wt%Cu droplets with different superheat. a). 50 K; b). 100 K; c). 150 K; d). 200 K. 225
- Figure 6-10. Log-normal plot of Al-3.7wt%Ni-1.5wt%Fe produced by IAP in nitrogen. 227
- Figure 6-11. SEM micrograph of an Al-3.7wt%Ni-1.5wt%Fe droplet produced by IAP in nitrogen. a). surface morphology of the powder; b). cross section of a powder; c). micrograph showing the cellular region of the powder. 228
- Figure 6-12. SEM micrographs showing dendrite regions of Al-3.7wt%Ni-1.5wt%Fe droplets in different size ranges produced by IAP in nitrogen. a). mid size =  $5.5 \times 10^{-4}$  m; b). mid size =  $3.9 \times 10^{-4}$  m; c). mid size =  $2.8 \times 10^{-4}$  m. 230
- Figure 6-13. Effect of particle size on the secondary dendrite arm spacing of Al-3.7wt%Ni-1.5wt%Fe droplets produced by IAP in nitrogen. 232

- Figure 6-14.** Log-normal plot of Al-3.7wt%Ni-1.5wt%Fe produced by IAP in helium. 233
- Figure 6-15.** SEM micrographs of Al-3.7wt%Ni-1.5wt%Fe droplets in different size ranges produced by IAP in helium. 234  
a). mid size =  $1.09 \times 10^{-3}$  m; b). mid size =  $7.8 \times 10^{-4}$  m;  
c). mid size =  $5.5 \times 10^{-4}$  m; d). mid size =  $3.9 \times 10^{-4}$  m;  
e). mid size =  $2.8 \times 10^{-4}$  m; f). mid size =  $2 \times 10^{-4}$  m.
- Figure 6-16.** SEM micrograph of Al-3.7wt%Ni-1.5wt%Fe showing very fine lamellar eutectic microstructure. 237
- Figure C-1.** Acceleration vs frequency of impulse generator A used in Pb-Sn alloy runs. 290
- Figure C-2.** Acceleration vs frequency of impulse generator B used in most of runs. 291

## **LIST OF NOMENCLATURE OR ABBREVIATIONS**

<b>a</b>	<b>radius of the disturbed jet; m</b>
<b>a<sub>0</sub></b>	<b>lattice parameter; m</b>
<b>a<sub>1</sub></b>	<b>constant in SDAS vs cooling rate relationship</b>
<b>a<sub>2</sub></b>	<b>constant in SDAS vs particle size relationship</b>
<b>a<sub>3</sub></b>	<b>constant in undercooling vs cooling rate relationship</b>
<b>a<sub>4</sub></b>	<b>constant in undercooling vs particle size relationship</b>
<b>A<sub>i</sub></b>	<b>cross section area of the jet; m<sup>2</sup></b>
<b>A<sub>p</sub></b>	<b>cross section area of the plunger; m<sup>2</sup></b>
<b>A<sub>s</sub></b>	<b>surface area of the droplet; m<sup>2</sup></b>
<b>b<sub>1</sub></b>	<b>constant in SDAS vs cooling rate relationship</b>
<b>b<sub>2</sub></b>	<b>constant in SDAS vs cooling rate relationship</b>
<b>b<sub>3</sub></b>	<b>constant in undercooling vs cooling rate relationship</b>
<b>b<sub>4</sub></b>	<b>constant in undercooling vs particle size relationship</b>
<b>B</b>	<b>kinetic coefficient; m/sK</b>
<b>Bi</b>	<b>Biot number, dimensionless</b>
<b>C</b>	<b>coefficient of contraction, dimensionless</b>
<b>C<sub>A</sub></b>	<b>added mass coefficient, dimensionless</b>
<b>C<sub>D</sub></b>	<b>drag coefficient, dimensionless</b>
<b>C<sub>H</sub></b>	<b>coefficient in history term of droplet velocity governing equation, dimensionless</b>
<b>C<sub>p</sub></b>	<b>specific heat; J/kgK</b>

$C_p^*$	effective specific heat; J/kgK
$C_{pa}$	specific heat of the ambient atmosphere; J/kgK
$C_{pl}$	specific heat of the liquid; J/kgK
$C_{pls}$	specific heat in the liquid-solid range; J/kgK
$C_{pm}$	average specific heat of the droplet in the mushy zone; J/kgK
$C_{ps}$	specific heat of the solid; J/kgK
$d$	jet diameter; m
$d_{50}$	geometric mean particle size; m
$d_i$	mid size of the $i$ th size range; m
$d_m$	effective atomic diameter; m
$D$	droplet or particle diameter; m
$D_0$	pre-exponential term in the diffusion coefficient ( $D$ ) expression; $m^2/s$ .
$D_l$	liquid diffusion coefficient; $m^2/s$
$E$	Energy; J
$E_k$	kinetic energy; J
$E_s$	surface energy from the disturbed condition; $J/m^2$
$E_{s0}$	surface energy from the undisturbed condition; $J/m^2$
$E_t$	total energy, J
$f$	frequency; Hz
$f_m$	optimum frequency; Hz
$f_s$	fraction of solid, dimensionless
$f_{se}$	solid fraction at the end of eutectic transformation, dimensionless
$f_{s(t-s)}$	solid fraction during pro-eutectic transformation, dimensionless



$f_{sp}$	solid fraction at the end of pro-eutectic transformation, dimensionless
$f_{sr}$	solid fraction for a solid with radius $r$ , dimensionless
$h$	heat transfer coefficient; W/mK
$h_m$	heat transfer coefficient at $(i+1/2)$ th step; W/mK
$H$	enthalpy of the system at temperature $T$ ; J
$H_{sm}$	enthalpy of the solid at the melting point; J
$i$	subscript for $i$ th step
$i+1$	subscript for $(i+1)$ th step
IAP	Impulse Atomization Process, abbreviation
$J$	nucleation rate; $s^{-1}$
$k$	wave number; $m^{-1}$
$k_1, k_2, k_3, k_4$	dummy variables in fourth order Runge-Kutta method
$k_a$	thermal conductivity of ambient atmosphere; W/mK
$k_d$	thermal conductivity of the droplet; W/mK
$K$	kinetic growth coefficient; m/sK
$L$	length of the jet; m
$L$	length of the capillary; m
$L_c$	characteristic length; m
$M$	mass of the liquid jet; kg
$M$	subscript for metal
$n$	number of particles
$n_i$	number of particles in $i$ th size range
$Nu_D$	Nusselt number of the droplet, dimensionless

$p_1$	pressure above the capillary; Pa
$p_2$	pressure below the capillary; Pa
$Pr$	Prandtl number, dimensionless
$q_m$	maximum growth rate of a disturbance; m/s
$Q$	volume flow rate; m <sup>3</sup> /s
$Q_D$	diffusion activation energy; J
$r$	radius of the solid; m
$r_c$	critical radius of nucleus; m
$r_j$	jet radius; m
$r_0$	orifice radius; m
$R$	droplet or particle radius; m
$Re_D$	Reynolds number, dimensionless
$S_s$	specific surface area; m <sup>2</sup> /g
<b>SDAS</b>	secondary dendrite arm spacing, abbreviation
<b>Se</b>	subscript for selenium
<b>SEM</b>	scanning electron microscope, abbreviation
$S_p$	specific power input; J/kg
$S_t$	theoretical specific power required to produce droplets; J/kg
$t$	time; s
$T$	temperature; K
$T_a$	ambient temperature; K
$T_c$	cooling rate; K/s
$T_e$	eutectic temperature; K

$T_l$	liquidus temperature; K
$T_m$	melting point; K
$T_n$	nucleation temperature; K
$T_p$	pouring temperature; K
$T_r$	recalescence temperature; K
$u$	relative velocity between the droplet and the fluid; m/s
$u_j$	jet velocity; m/s
$u_t$	fluid velocity in the capillary tube prior to the liquid exiting the capillary hole; m/s
$U$	growth velocity during solidification; m/s
$V$	droplet volume; m <sup>3</sup>
$W$	weight of droplets, kg
$W_0$	weight of a single droplet, kg
$y$	axis of jet direction; m
$z$	height of droplet position; m
$\alpha$	distance amplitude; m
$\alpha_j$	jump distance of the atom; m
$\alpha_s$	thermal diffusivity of ambient atmosphere; m <sup>2</sup> /s
$\beta$	correction factor
$\gamma$	surface tension of the jet; J/m <sup>2</sup>
$\gamma_{ls}$	interfacial energy between liquid and solid; J/m <sup>2</sup>
$\kappa$	Boltzmann's constant; J/K
$\lambda$	wavelength; m

$\lambda_1$	primary dendrite arm spacing; m
$\lambda_2$	secondary dendrite arm spacing (SDAS); m
$\lambda_3$	tertiary dendrite arm spacing; m
$\lambda_c$	critical wavelength; m
$\lambda_m$	optimum wavelength; m
$\mu_a$	dynamic viscosity of the ambient atmosphere; Pa s
$\nu_a$	kinematic viscosity; m <sup>2</sup> s <sup>-1</sup>
$\nu_L$	jump frequency in the bulk liquid, s <sup>-1</sup>
$\nu_{LS}$	frequency with which atoms jump across the liquid-solid interface, s <sup>-1</sup>
$\omega^*$	number of atoms surrounding a critical nucleus
$\Omega$	atomic volume; m <sup>3</sup>
$\psi$	dimensionless enthalpy, dimensionless
$\rho$	density of the liquid jet or droplet; kg/m <sup>3</sup>
$\rho_a$	density of the ambient atmosphere; kg/m <sup>3</sup>
$\sigma_g$	geometric standard deviation
$\theta$	dimensionless temperature, dimensionless
$\tau_{sph}$	spherodization time; s
$\Delta G^0$	free energy change at standard state; J
$\Delta G_v^0$	volume free energy change; J
$\Delta G_c^0$	thermodynamic barrier to form a critical nucleus; J
$\Delta G_a$	activation free energy; J
$\Delta H$	enthalpy change; J

- $\Delta H^0$  enthalpy change at standard state; J
- $\Delta H^*$  effective latent heat of fusion; J
- $\Delta H_f$  latent heat of fusion in the eutectic transformation stage; J
- $\Delta H_{fm}$  latent heat of fusion; J
- $\Delta H_{fp}$  latent heat generated during pro-eutectic transformation; J
- $\Delta H_{fs}$  latent heat generated due to solidification of a solid fraction  $f_s$ ; J
- $\Delta H_t$  total latent heat; J
- $\Delta S^0$  entropy change at standard state; J/K
- $\Delta S_m^0$  entropy change at melting point: J/K
- $\Delta T$  undercooling or supercooling; K
- $\Delta T_{max}$  maximum undercooling or supercooling; K
- $\Delta t$  step size; s
- $\Delta t_{new}$  new step size; s

## **CHAPTER 1: INTRODUCTION**

**Powders and granules are manufactured for applications such as paints, inks, catalysts, explosives, food additives, welding electrodes, and plasma and flame spraying. For each application, different powder characteristics are required such as the mean size, size distribution, shape, composition, and microstructure [Mills, et al., 1984]. Therefore, powders having different characteristics have to be produced. For example, spherical powders are required for metal filter products. On the other hand, irregular shaped powders are used in powder metallurgy for good compressibility and green strength (green strength is the strength of the compacts after compaction and before sintering), and elongated powders for products requiring anisotropic properties. For metals and alloys, a fine powder microstructure is required for high strength applications and a coarse microstructure for good ductility [German, 1994].**

**Therefore, it is very important in general and for powder metallurgy in particular to control the size, size distribution, shape, and microstructure of the powders produced. These powder characteristics are generated by the powder-making technique used. No single powder production process meets all of the requirements of the powder metallurgy industry. Thus, a number of different powder production techniques have been developed. For example, there are mechanical milling, electrodeposition, reduction of metal powder from their oxides, hydro metallurgical processing technologies, and atomization methods**

[Mills et al, 1984].

Atomization technology in powder metallurgy has grown steadily, becoming more sophisticated since World War II. Atomized iron and steel powders occupy about 50% of the market of the ferrous powder industry. Among all the atomization techniques which will be described in the next chapter, the most common one is two fluid atomization. Here, a liquid stream is broken up into fine droplets using a second fluid (e.g. gas, water or oil). These droplets subsequently either solidify into powders or are deposited onto a substrate while still liquid or semi-liquid, e.g., spray deposition. Therefore, any material that can be melted can be atomized into powders and spray deposited.

Capillary atomization<sup>1</sup> is another atomization technique but it has only been developed since the 1970's. One capillary technique produces monodispersed metallic droplets from a vibrated continuous jet of the melt (molten metals, ceramics or slags). One of the main difficulties with this method is that the atomized droplets tend to stick to one another in flight. This likely occurs because of the close proximity, in direction of flight, and high injection speed of the droplets. These subsequently decelerate or accelerate in flight due to turbulence and frictional forces during their free fall trajectory. A number of techniques are used to overcome this problem. For example, droplets are charged using a high voltage charging plate to repel and separate droplets from one another. The use of such additional equipment makes this atomization process more complex, more costly, and in some cases dangerous for adaption to a large-scale industrial

---

<sup>1</sup> also known as one type of single fluid atomization technique .

plant. Furthermore, with this technique, the control over particle size distribution is limited [Chun, 1993].

Another capillary atomization technique is the drop-on-demand method. A flexible diaphragm is vibrated using a high frequency and low amplitude vibration source. The diaphragm transfers the vibrations to the molten metal placed adjacent to an orifice [Kawasaki, 1993]. Such a configuration severely limits the application of this technique to low melting point alloys and their commercialization potential for mass production. Furthermore, only one drop is generated per pulse per orifice. Thus, the ability to atomize melts into powder of desired shape, mean size and size distribution at reasonable melt throughput is still an elusive goal.

Although atomization of melts has been studied intensively, it is still very much an art. A key step in developing a fundamental understanding of atomization is in determining the relationship between the atomizing operating conditions and the resultant powder size distribution and microstructure. It is difficult to study relationships between the atomization operating parameters and resultant sizes, size distribution, and microstructure with the conventional gas atomization technique, since it usually generates powders with a wide size distribution and considerable variation in particle velocity in the spray.

In order to overcome the problems of the existing atomization processes, a new technique, the Impulse Atomization Process (IAP) was developed by the author in the Advanced Materials and Processing Laboratory at the University of Alberta. IAP, which is of the single fluid atomization type, allows one to produce powders with a tailored size



distribution. The size, size distribution, microstructure, and powder shape can be controlled better than with the conventional two fluid atomization processes. The powder characteristics are highly reproducible. It also overcomes many of the drawbacks of capillary techniques such as the continuously vibrated jet and drop-on-demand method.

The first objective of this study is to develop the apparatus and the process of IAP, which overcomes the above mentioned disadvantages of other atomization techniques. The second objective of the thesis is to study the effect of process parameters on powder characteristics. These variables include frequency and amplitude of impulses, orifice diameter, number of holes in the nozzle plate, the distances between the impulse applicator and the crucible bottom, the oxygen content of the atomizing chamber, the superheat of the molten metal, and the viscosity of the melt. The powder characteristics evaluated are size, size distribution, shape, and microstructure. The third objective of this study is to compare powder characteristics produced by IAP with those typically obtained using conventional gas atomization. The fourth objective of this work is to develop a model to understand solidification of droplets produced by IAP.

In the following chapters, the literature that relates to this work will be reviewed. Then a model will be formulated in order to calculate the cooling rate of a droplet produced by IAP. The experimental results showing the effect of operating parameters on the powder characteristics including microstructural analysis will be presented. The results obtained under the above mentioned conditions will be discussed and the microstructural analysis results will be compared with those predicted by the model and the literature. Advantages of IAP will be summarized. Finally, future developments for

**this promising technique will be proposed.**

## **CHAPTER 2: LITERATURE REVIEW**

**This chapter summarizes in four sections previous work related to atomization. The first section will review conventional fluid atomization briefly. A description of the theory of capillary atomization is presented in the second section. This will include the disintegration mechanism, the instability of liquid jets, as well as a review of atomization techniques developed for making monodispersed droplets using a vibrated continuous jet or drop-on-demand methods. In the third and fourth sections of this chapter, the fundamentals of solidification and heat transfer relevant to atomization of molten metals will be presented.**

### **2.1 Overview of Conventional Fluid Atomization**

**Atomization of melts (molten metal, alloys, ceramics and slag) involves the generation of droplets from a melt stream and the solidification of these droplets into powder particles. Various atomization techniques have been developed, such as two fluid atomization, vacuum atomization, centrifugal atomization and ultrasonic atomization [Yule and Dunkley, 1994]. A brief overview of conventional two fluid atomization techniques will be presented in this chapter since it is one of the dominant methods used for producing powders. Two fluid atomization is the process which disintegrates a melt**

stream using another fluid, such as a gas, water, or oil. Atomization occurs by transferring energy from the atomizing fluid (gas, water, or oil) to the melt stream. The efficiency of this energy transfer, and the type of fluid and melt will determine powder characteristics such as shape, size and size distribution. In this section, two fluid atomization using a gas as the atomizing fluid (i.e., gas atomization) will be used as an example to demonstrate the atomization mechanism and process.

See et al. [See et al, 1973] reported that the disintegration mechanism of the melt stream in gas atomization occurs in three stages (see Figure 2-1). Stage I is the primary breakup of the liquid stream; in stage II the droplets are still in a molten state, permitting secondary disintegration and spherodization. Droplets solidify in stage III.

Empirical relationships have been proposed for predicting powder size, size distribution, and shape given the atomizing operating variables [Lubanska, 1970]. Variables affecting powder size include the gas kinetic energy, the gas jet nozzle-melt stream distance, and the melt surface tension, viscosity and superheat. Finer powder is obtained if the kinetic energy of the atomizing media is large and if this kinetic energy is transferred efficiently to the metal stream. This can be achieved using high gas pressures, short jet-to-metal-stream distances, higher gas flow rates and high gas to metal mass flow rate ratio [German, 1994, Huang, 1982].

Melts with a high surface tension yield atomized powder which is more spherical and coarser than lower surface tension metals. It is also easier to obtain fine powders from low viscosity melts and using high superheat. The latter is primarily due to a decrease in melt viscosity and surface tension with increasing temperature. High

superheat also gives molten metal droplets more time to spheroidize before solidifying, therefore, resulting in more spherical powders. Finally, fine powders are more easily attained using small molten metal stream diameters [German, 1994, Huang, 1982].

Gas atomized powders are typically spherical and have smooth surfaces (except with air). The chemical composition is normally well-controlled. However, gas atomization is expensive if gases other than air or nitrogen are used.

The water atomization process is significantly cheaper than gas atomization unless air is used as the gas medium. Particle cooling rates in water atomization are an order of magnitude higher than those achieved in gas atomization. Powders produced by water atomization normally have irregular shapes and have oxidized surfaces. In contrast to gas atomization, there is no evidence of ligament formation as an intermediate step in particle formation in water atomization.

Both water atomization and gas atomization have very low efficiency. The efficiency was defined as the "ratio of the minimum theoretical input power or energy to actual input power or energy to the atomizer [Yule and Dunkley, 1994]. This minimum energy is just that required to create the new surface of the atomized powder. For example, in the production of air atomized zinc powders, a closed nozzle and a gas pressure of  $1 \times 10^6$  Pa air pressure was used yielding an average size of  $2.6 \times 10^{-5}$  m. The production rate of zinc was 0.33 kg/s and the energy efficiency was 0.009% excluding the energy required to heat the melt [Yule and Dunkley, 1994]. Similarly, in the production of water atomized iron powder an efficiency number of 0.036% was achieved when 7 l/kg at  $1 \times 10^7$  Pa water pressure was used for a production rate of 5 kg/s. These processes also

produce powders with wide size distributions. The typical size distribution is normally quite large with a standard deviation of 1.8-2.4 for gas atomization [Dunkley and Palmer, 1986]. This standard deviation represents  $d_{84}/d_{50}$  from a log-normal analysis of a size distribution [Boyko and Henein, 1993].

Satellite formation are common in both processes. Due to the complexities of the processes, it is hard to control process parameters in order to obtain reproducible and desired size and size distribution of powders [German, 1994, Huang, 1982].

## **2.2 Overview of Capillary Atomization**

Other atomization processes such as capillary atomization have been developed and will now be reviewed. In capillary atomization a liquid column is formed from a capillary or an orifice and subsequently breaks up either by surface tension or by applied periodical forces. Capillary atomization, also termed single fluid atomization, produces powder with controlled characteristics of size and distribution. One variation of the technique produces monodispersed droplets from vibrated continuous jets. This process is based on Rayleigh's theory of instability of liquid jets [Aldinger et al, 1977]. Another variation is the drop-on-demand method.

In the following sections, the disintegration mechanisms of liquid jets emanating from a capillary and Rayleigh's theory of instability of liquid jets will be reviewed. Then the characteristics of continuous jet and drop-on-demand methods will be illustrated.

### **2.2.1 Disintegration Mechanisms of Liquid Jets Emanating from a Capillary**

As it is important to understand the disintegration mechanism of an atomization process, this section will briefly review the disintegration mechanisms of liquid jets emanating from a capillary.

According to Schmidt [Schmidt, 1967], a fluid flowing out of a capillary tube will disintegrate or atomize by one or by some combination of four mechanisms (see Figure 2-2). They are drip-off, drop disintegration, wave disintegration, and atomization [Schmidt, 1967].

A fluid at rest in a capillary placed at the bottom of a crucible is subjected to gravity, surface tension (fluid-gas), and capillary forces (fluid-capillary walls). Under high capillary forces the fluid will wet the walls of the capillary and flow to the tip of the tube. The fluid will continue to accumulate at the tip of the capillary until the gravity force on the fluid segment outside of the capillary overcomes the surface tension on that fluid segment. Drip-off of fluid will then occur. When a low pressure is applied to the fluid in the capillary, the same disintegration mechanism will still be operative for small exiting velocities of fluid and is often termed the drop-on-demand method.

Under a higher applied pressure or a larger exiting fluid velocity, a continuous jet will be formed at the tip of the capillary. This jet will eventually break up into droplets with a broad size distribution because the jet is dynamically unstable under the action of surface tension (see Figure 2-2b). The resultant droplet sizes will be about the same order of magnitude as the original stream diameter. This phenomenon is termed drop

disintegration. In wave disintegration, a periodic disturbance of known frequency is imposed on the continuous jet. The stream will again break up by Rayleigh instability into droplets having a size distribution which is related to the imposed frequency [Rayleigh, 1878]. Again the droplet sizes will be of the same order of magnitude as the stream diameter (see Figure 2-2c). Monodispersed droplets will be formed if the disturbance imposed in wave disintegration is at the optimum frequency given by Rayleigh theory (Section 2.2.2.1). The vibrated continuous jet method is characterized by this mode of operation. The minimum velocity to be attained by the continuous jet can be calculated and will be presented in Section 2.2.2.2.

The atomization mechanism shown in Figure 2-2d will take place under much higher jet velocities. The resultant droplet size distribution is wide, with the droplets having a size smaller than the diameter of the original stream diameter.

### **2.2.2 Theory of Capillary Instability**

In this section, a theory of linear capillary instability will be presented. Then the minimum velocity required to form stable jets will be discussed. Subsequently, literature dealing with deviations from linear capillary instability will be summarized.



### 2.2.2.1 Theory Based on Linear Capillary Instability

Linear capillary instability theory dates back to the nineteenth century. The disintegration of liquid jets was first observed experimentally by Savart [Dabora, 1967]. He found that the length of the stable portion of a disintegrating liquid jet is proportional to the diameter of the orifice. His results were further explained and interpreted by Plateau [Rayleigh, 1945]. The first theoretical explanation was carried out by Rayleigh [Rayleigh, 1878] and will now be summarized.

Let us consider a capillary or an orifice with radius  $r_o$ , as shown in Figure 2-3. There is a cylindrical jet coming out of this capillary with radius  $r_j$ . Rayleigh [Rayleigh, 1878] considered that the cylinder is subjected to an extremely small amount of sinusoidal natural disturbance with amplitude  $\alpha$  with a wavelength  $\lambda$  along its axis direction  $y$ . Its wave number is expressed as  $k=2\pi/\lambda$ <sup>1</sup>. With time,  $t$ , the radius,  $a$ , of the disturbed surface of the cylinder will vary along the  $y$ -axis, according to:

$$a=r_j+\alpha\cos ky \quad (1)$$

After calculating the surface energy,  $E_s$ , from the disturbed condition, and the surface energy,  $E_{s0}$ , from the undisturbed condition, an energy balance before and after the disturbance is applied to the jet. Rayleigh obtained the following equation:

---

<sup>1</sup> Symbols are also defined in the Nomenclature Section.

$$E_s - E_{s0} = \frac{\pi \alpha^2}{2r_j} (k^2 r_j^2 - 1) \gamma \quad (2)$$

where  $\gamma$  is the surface tension of the jet (fluid-gas). From Equation (2), it is obvious that if  $kr_j > 1$ , the surface energy is greater after displacement than before. Therefore, if  $\lambda < 2\pi r_j$ , the displacement to the system is stable. That is, only when the wavelength of the displacement is larger than the circumference of the jet, will the disintegration of the liquid jet take place. This is the lower limit of the operating wavelength for linear capillary instability.

Rayleigh [Rayleigh 1878] showed that the maximum growth rate,  $q_m$ , of a disturbance is given by:

$$q_m = 0.97 \left( \frac{\gamma}{\rho d^3} \right)^{0.5} \quad (3)$$

where  $d$  is the diameter of the jet and  $\rho$  is the density of the liquid. This maximum growth rate occurs when the wavelength of the disturbance  $\lambda_m$  is given by:

$$\lambda_m = \sqrt{2} \pi \times 2r_j \quad (4)$$

This is obtained by taking the derivative of Equation (2) with respect to  $r_j$  to find the most favourable energy condition. Rayleigh [Rayleigh, 1878] showed that  $\lambda_m = 4.508 \times 2r_j$  using Lagrange's interpolation approximation. The cylindrical jet breaks up most rapidly with this disturbing wavelength. In other words, at this condition, the jet will break into ligaments of equal length  $\lambda_m$ . When these ligaments spheroidize they will become droplets of equal volume. This is the theoretical optimum operating wavelength for linear capillary instability to hold monodispersed droplets. The corresponding value obtained

by Plateau [Rayleigh, 1935] from experiments by Savart [Dabora, 1967] was  $4.38 \times 2r_j$ .

Considering the relationships between wavelength, frequency and velocity of the jet, we have:

$$f_m = \frac{u_j}{\sqrt{2\pi} \times 2r_j} \quad (5)$$

where  $f_m$  is the optimum operating frequency to produce uniform droplets and  $u_j$  is the jet velocity. In the condition of a ligament of liquid jet with radius of  $r_j$  and length of  $\lambda$ , its volume is:

$$V = \pi r_j^2 \lambda \quad (6)$$

It will spherodize into a droplet with a radius  $R$  with the volume:

$$V = \frac{4}{3} \pi R^3 \quad (7)$$

Accordingly, by volume conservation we have (equating Equation (6) to (7)):

$$R = \left( \frac{3}{4} r_j^2 \lambda \right)^{\frac{1}{3}} \quad (8)$$

Substituting Equation (4) into Equation (8) yields the relationship between the droplet radius and jet radius for optimum jet break-up as given by:

$$R = 1.89 r_j \quad (9)$$

That is to say, drops resulting from a liquid jet will break up at the wavelength of maximum instability and will have a monodispersed diameter which is 1.89 times that of the jet diameter.

### 2.2.2.2 Minimum Velocity for Stable Jet Formation

In this section, the minimum velocity to form a continuous jet will be calculated [Schneider, 1964]. The main driving force for a stable jet to exit the orifice is the pressure difference between the top and the bottom of the capillary tube. This driving force will result in the jet having kinetic energy (i.e. due to the average jet velocity  $u_j$ ) and surface energy (i. e. due to surface tension) upon the jet exiting the orifice. The total energy ( $E_t$ ) due to the work done by the driving force should be equal to the kinetic energy ( $E_k$ ) and the surface energy ( $E_s$ ) of the jet on exiting the orifice. The driving force of the jet may be represented by the kinetic energy of the jet just prior to exiting the orifice. Therefore,

$$E_t = E_k + E_s \quad (10)$$

and

$$\frac{dE_t}{dt} = \frac{dE_k}{dt} + \frac{dE_s}{dt} \quad (11)$$

In general, the rate of change of kinetic energy is given by:

$$\frac{dE}{dt} = \frac{d}{dt} \left( \frac{1}{2} M_j u_j^2 \right) \quad (12)$$

where  $E$  is energy,  $t$  is time, and  $M_j$  and  $u_j$  are the mass and velocity of the liquid jet, respectively.

If the velocity under the fully developed laminar flow conditions in the capillary tube,  $u_j$ , is assumed to be constant for a small jet of finite length  $L_j$  and cross-sectional

area  $A_j$ , Equation (12) becomes:

$$\frac{dE}{dt} = \frac{1}{2} \rho u_c^3 dA_j \quad (13)$$

where  $A_j$  is the cross section of the jet and  $\rho_j$  is the density of the fluid jet. Therefore, the total kinetic energy of the jet per unit time  $dE/dt$  is of the form:

$$\frac{dE_k}{dt} = \frac{1}{2} \int \rho_j u_c^3 dA_j = \rho_j \pi r_0^2 u_c^3 \quad (14)$$

The rate of increase in potential energy  $dE_p/dt$  is given by the rate of increase of area multiplied by the surface tension,  $\gamma$ ,

$$\frac{dE_p}{dt} = 2\pi r_j \gamma u_j \quad (15)$$

where  $u_j$  is the average exit velocity of the jet with radius  $r_j$  out of the capillary, which is assumed to be uniform and constant throughout the jet.

The rate of kinetic energy transfer in the jet is:

$$\frac{dE_k}{dt} = \frac{1}{2} \rho \pi r_j^2 u_j^3 \quad (16)$$

Substituting Equations (14), (15) and (16) into Equation (11) yields:

$$\rho \pi r_0^2 u_c^3 = 2\pi r_j u_j \gamma + \frac{1}{2} \rho \pi r_j^2 u_j^3 \quad (17)$$

Applying continuity to the jet and capillary yields, for incompressible fluids:

$$u_c r_0^2 = u_j r_j^2 \quad (18)$$

Substituting from the continuity Equation (18) into Equation (17) and solving for

$u_t^2$  it is found that:

$$u_t^2 = \frac{2\gamma}{r_j \rho} + \frac{1}{2} u_j^2 \quad (19)$$

If the coefficient of contraction,  $C$ , is defined as  $r_j^2/r_o^2$ , it is noted from Equation (18) that:

$$u_t = C u_j \quad (20)$$

and hence Equation (19) becomes:

$$u_t^2 = \frac{2\gamma}{r_j \rho} + \frac{1}{2 C^2} u_t^2 \quad (21)$$

Solving for  $C$  yields:

$$C = \sqrt{\frac{1}{2 - \frac{4\gamma}{r_j \rho u_t^2}}} \quad (22)$$

Since  $C$  must be less than or equal to one in order to form a stable jet, Equation (22) predicts the minimum velocity required to form a stable jet as:

$$u_t^2 \geq \frac{4\gamma}{r_j \rho} \quad (23)$$

This equation together with Equation (5) defines the operating limits (minimum velocity and optimum wavelength) to produce monodispersed droplets.

### 2.2.2.3 Deviation from the Linear Capillary Instability

The linear theories predict that a jet subjected to surface tension and inertia should break up into uniform-sized droplets, forming one drop per disturbance wavelength. Also, the linear theory suggests that the form of the disturbed jet surface should be an expanding sinusoidal curve. However, these ideal conditions are hard to achieve in practice. Satellite drops, which are small droplets formed during the disintegration of the liquid jets, are experimentally observed. The formation of satellite droplets is believed to occur due to non-linear capillary instability [Schummer and Tebel, 1982].

The theory of non-linear capillary instability has been studied by numerous researchers [Yuen, 1968, Goedde and Yuen, 1970]. The most important result related to this area is reported by Schneider and Hendricks [Schneider and Hendricks, 1964]. Based on Rayleigh's theoretical results for an optimum wavelength of  $\lambda_m = 9r_j$ , Schneider and Hendricks found experimentally that uniform droplets can still be formed in the range of:

$$7r_j \leq \lambda \leq 14r_j \quad (24)$$

This observation is so important that it has been cited by many other authors since 1964. Equation (24) gives the minimum and maximum wavelength limits. Hence, the interval containing maximum and minimum operating frequencies for a given jet diameter with a given jet velocity is:

$$\frac{u_j}{14r_j} \leq f \leq \frac{u_j}{7r_j} \quad (25)$$

where  $f$  is an externally applied frequency to the jet. From Equation (8) we can see that

droplet size is proportional to  $\lambda^{1/3}$ . Substituting the minimum and maximum wavelength into Equation (8), we obtain the minimum droplet size of  $R=1.74r_j$  and the maximum droplet size of  $R=2.19r_j$  by varying the frequencies in the range mentioned above, or  $2.24\pi r_j \leq \lambda \leq 4.46\pi r_j$  instead of Equation (4).

However, droplets cannot be made arbitrarily small by making the wavelength of the disturbance smaller and smaller because the cylinder of liquid is stable with regard to displacement from equilibrium for disturbances whose wavelength is less than  $2\pi r_j$  as shown by Rayleigh's theory [Rayleigh, 1878]. Increasing the wavelength to the above range will cause the formation of satellite droplets or secondary atomization [Dabora, 1967]. Wedding [Wedding, 1975] argued that the relationship proposed by Schneider and Hendricks is not applicable for all generator aperture diameters. They found that a monodisperse aerosol could be generated in the range of  $2\pi r_j \leq \lambda \leq 15.56r_j$ , depending on the orifice diameters.

The growth rate of the surface disturbance measured by some investigators only agreed qualitatively with Rayleigh's results [Crane et al., 1964]. All the non-linear instability theories involved complicated mathematical derivations and the details will not be presented here [Crane et al., 1964, Chaudhary and Redekopp, 1980 a, b, c].

### **2.2.3 Production of Droplets from Continuous Jets**

Numerous experiments were conducted in the 1960's and 1970's based on the classical theory developed by Rayleigh [Rayleigh, 1878]. However, most of the work was



done in the field of non-metallic materials, especially for liquid droplets at room temperature. The theory has been widely used in the following fields: ink-jet printing [Lavanoni, 1977, Keur and Stone, 1976; Curry and Portig, 1977; Heinzl, 1985]; pesticide sprays [Bous et al, 1974; Yates and Akesson, 1979, Roth and Porterfield, 1970]; aerosol generator [Wedding, 1975; Berglund and Liu, 1973; Burgoyne and Cohen, 1952; Strom, 1969]; nuclear technology [Schummer and Tebel, 1982]; combustion [Dabora, 1967; Araki and Masuda, 1979]; and in the field of studying the collision, coalescence and rebound of small water droplets [Mason et al, 1963; Mason and Brownscombe, 1964], etc. Of the papers reviewed, only a few deal with metallic systems [Aldinger et al, 1976; Biennu, 1984; Brandau, 1993; Chun, 1992 and 1993].

This section reviews the theory and previous work that has been done to produce monodispersed droplets and its application to metallic system.

### **2.2.3.1 Production of Metallic Droplets from Continuous Jets**

The production of metallic droplets based on the aforementioned theory is more complicated than for room temperature liquids, due to the high temperature of operation. Reactions between the molten metal and other objects, such as crucibles and nozzles, which are in contact with the molten metal have to be avoided. The atmosphere must be controlled in order to prevent the metal from oxidizing at high temperatures. Therefore, work in this field has been rather limited. In this section, the characteristics, advantages and disadvantages of previous work in this field will be outlined.

**Aldinger, et al. [Aldinger et al, 1976] produced lead, aluminum, copper, mild steel, astroloy, and beryllium droplets. The crucible material was not mentioned in their paper. After induction melting, the liquid metal passed through a single orifice at the bottom of a crucible and a continuous jet was formed by applying an over pressure in the crucible. Vibrations were applied to the crucible. Uniform-sized (actually a narrow size range) droplets were obtained, resulting in over 90% of the powders generated being in the  $1.5$  to  $2 \times 10^{-3}$  m size range. They concluded that there was no problem to produce uniformly sized particles with a diameter of several millimetres, while the production of fine powder particles of uniform size was rather difficult.**

**Biennu [Biennu, 1984] produced tin, calcium, magnesium and aluminum granules. His method essentially consisted of the formation of a continuous jet of molten metal, the disintegration of this jet into individual drops by vibration, and the solidification of the drops by cooling to form granules. The vibration was supplied through a rod attached at right angles to the tip of an orifice of a U-shaped tube. The rate of injection of the molten metal through the vibrating orifice was regulated by adjusting the pressure difference above and below the melt.**

**Droplets of molten metal formed at the end of the vibrating orifice were dispersed within a cooling tower by means of an annular electrode surrounding the jet. This electrode was electrically charged by a 5000 V electrical power source in order to prevent the disintegrated droplets from colliding and coarsening. The temperature difference between the molten metal at the formation point of the jet and the atmosphere into which the vibrating orifice opens was at least 200 K.**

The particles made by this method were uniform and spherical. However, both the apparatus and the process are relatively complicated. Examples of tin, calcium, magnesium, and aluminum powder of  $0.5$  to  $2 \times 10^{-3}$  m diameter were presented. The design and vibration of the orifice dramatically limits the range of orifice materials that can be used, and makes it difficult to place multiple orifices in the atomizing unit. Furthermore, because a pressure difference is required, precise timing and control of both the pressure difference and vibration is needed. Finally, the pressurization of the melt further complicates continuous operation of the process.

Bradau et al. [Bradau et al, 1993] produced, from a melt, spherical particles with a narrow particle size range. The droplets were generated by means of vibrating nozzles. The liquid phase, the nozzle and the drop distance for the droplets were maintained at a constant temperature of 1 to 10 K above the melting temperature of the melt until the spherical shape of the falling droplet had stabilized. The formation of tear-drop shapes and droplet coalescence were thus avoided. The droplets had to be immediately chilled by a gas or liquid with temperature at least 100 K below the melt temperature. It would be difficult to control the melt temperature this accurately in mass production. Furthermore, a very complicated shape of nozzle (tube) was used and since it was vibrated, its application to ceramic materials is unlikely to be feasible. It is also difficult to incorporate a multiple hole assembly. Gas over-pressure was needed for the melt to pass through the feed line. Finally, due to sealing difficulties, the atmosphere in the cooling part of the chamber could not be controlled as desired.

Chun and Passow [Chun and Passow, 1992 and 1993] developed a process using

the same basic ideas to produce uniform droplets from a continuous jet except that they vibrated the melt as opposed to the nozzle. Tin alloy droplets within 5% of the nominal diameter were generated on a laboratory prototype.

To generate a spray, a continuous liquid jet was forced through an orifice by applying an over pressure. The jet was then disintegrated into droplets by applying a high frequency ( $15 \times 10^3$  Hz) vibration in the melt close to the orifice. By varying the frequency of vibration, the droplet size was varied by as much as 20%. Different sized orifices further extended the possible range of droplet size. An early problem was that the droplets tended to stick together in their travelling direction, which is typical of this technique. To repel the particles from one another, they charged the droplets using a high voltage of 400 to 850 V, as did Bienvenu [Bienvenu, 1993]. The charged droplets scattered as they fell down. The spray formed a hollow cone with high spray density regions at two points across from one another on its rim.

Using this apparatus, droplet deposition experiments were performed to determine the effect of droplet impact and mass flux on spray deposit characteristics. Since a pressure differential is needed to form a continuous jet, continuous operation at high temperatures is a problem. This typically results in poor atmosphere control at these temperatures. Precisely matching jet formation and jet vibration may also be a problem (i.e., a premature jet may be formed).

In summary, metallic droplets have been produced using continuous jets. However, an over pressure is required to form continuous jets, which adds to the complexity of the equipment. Since droplets were formed by applying high frequency

vibration to the continuous jets, the disintegrated droplets tended to stick to each other in flight. For example, according to Raleigh's theory, the minimum velocity to form a stable molten tin jet with  $8.7 \times 10^{-5}$  m diameter is 2.6 m/s. An example shown by Chun et al (1992) was an initial droplet velocity of 7.5 m/s and an impact velocity on the substrate of about 6 m/s for a solder jet diameter of  $8.7 \times 10^{-5}$  m. Clearly, the droplets decelerate in their downward trajectory. Furthermore, when operated at the optimum frequency, the distance between the individual droplets is between 0 and  $1.38d$ , where  $d$  is the diameter of the droplets. With such a high velocity any uneven acceleration or deceleration due, say, to turbulence between the droplets or deceleration to the droplet terminal velocity will further reduce the distance between the droplets, resulting in coalescence. In practice, the experimental conditions are often far from ideal, which makes the coalescence even worse. Therefore the droplets are charged with high voltage devices to avoid this problem. This not only adds complexity to the apparatus, but also makes net shape control of the mass flux of the spray very complex. The other solution to the problem of droplet coalescence is to use precise temperature control of the melt. This requirement makes it impractical to apply to mass production. Furthermore, while this approach may work for pure metals, difficulties will be encountered when atomizing alloys. These commonly have a large solidification temperature range (from liquidus to solidus). Finally, all these methods require specific nozzle construction and design, making the scale-up of the continuous jet method very difficult.

## **2.2.4 Drop-on-Demand Method**

### **2.2.4.1 Production of Droplets by Drop-on-Demand Method**

The drop-on-demand method found its first applications in the ink-jet printing industry [Heinzi and Hertz, 1985]. Ashgriz and Yao [Ashgriz and Yao, 1983] applied the drop-on-demand technique to combustion. As shown in Figure 2-4, the basic apparatus of the drop-on-demand method consists of a vibration source, such as a piezoelectric crystal transducer, a liquid in its container supplied by its reservoir, and a nozzle (or nozzles). The steps of the drop-on-demand operation are described as follows.

When the liquid in the container is not pressurized, it is in its rest position (Figure 2-4a). The amount of liquid in the orifices of the nozzle plate of the geometry is affected by the surface tension of the liquid (liquid-gas), the contact angle between the liquid and the nozzle material, and the geometry of the orifices in the nozzle. In the case of ink-jet printing, the ink pressure in the container in the rest position is maintained slightly below atmospheric pressure. This forms a stable concave meniscus within the nozzle, regardless of whether the plate surrounding the nozzle is wettable or not, thereby, preventing leakage of ink. When a voltage pulse is applied to the piezoelectric plate, a pressure pulse is generated in the container (Figure 2-4 b to c). As a result, one droplet per orifice is ejected. When the pulse ends, the plate returns to its original position (Figure 2-4d) and the orifices in the nozzle are refilled with liquid by the capillarity force, and the liquid resumes its rest position as in Figure 2-4a. The design parameters, such as the orifice

length and shape, pulse pressure, and pulse duration were developed by [Beasley, 1977] for a single orifice system.

In practice, when the meniscus retreats back into the container after the droplet is ejected, gas bubbles might be sucked into the liquid container and influence the formation of the next drop. Therefore, thick nozzle plates are used which efficiently eliminate the formation of gas bubbles in the container. However, the thicker the plate, the more the viscous force will attenuate the pressure pulse. This problem can be overcome by tapering the orifice diameter with the larger diameter on the liquid container side as shown in Figure 2-4.

In this operation the droplet generation frequency could be varied as desired. However, the generated droplets usually show a wide spectrum of sizes. Since the orifices at different positions on the plate experience different magnitudes of pressure pulses. In practice, if there is a liquid film on the top of the orifice plate, the droplet will have to tear away from the liquid film and will have a different size from that generated from a hole on a dry plate. This liquid film usually exists due to the minor leakage of liquid from the slight pressure difference across the orifice plate. Additionally, any imperfections of the orifice hole will disturb the pressure wave in the hole and cause the generation of satellite droplets.

#### **2.2.4.2 Drop-on-Demand Method Applied to Metals**

**Kawasaki et al. [Kawasaki et al, 1993] applied the drop-on-demand method to metallic systems. Their experimental apparatus consisted of a piezoelectric transducer controlled by a function generator, a molten metal container with its metal diaphragm in contact with the transducer. The nozzle plate had a single orifice drilled in its centre. The metal diaphragm was made of a stainless steel plate of  $1 \times 10^{-4}$  m in thickness and  $1.5 \times 10^{-2}$  m in diameter. The orifice size was less than  $4 \times 10^{-4}$  m in diameter.**

**In their experiments, a bismuth based eutectic alloy, woodmetal, was tested as the atomized fluid. The tundish container was heated to 420 K which was about 70 K above the melting point of the alloy. The tundish was connected to a reservoir by a pipe. After the metal was melted, rectangular waves were generated by a function generator used for controlling the form of the output wave of a power amplifier. The output power of the amplifier was applied to the piezoelectric transducer to drive the metal diaphragm in a clapping action. Molten metal was injected downward to the atomizing chamber. A droplet of liquid metal was formed at the orifice and was solidified during flight in the atmosphere. The pulse frequency was varied over the range 0.1 Hz to 100 Hz. The displacement of the metal diaphragm was varied up to  $1.5 \times 10^{-5}$  m. The pulse width ratio of power-on and power-off was 1 to 1.**

**The results showed that when the injection rate was high, each pressure pulse yielded one liquid droplet having a size almost equal to the orifice diameter, about  $4 \times 10^{-4}$  m. A similar result was confirmed in the case of an orifice diameter of about  $1 \times$**



$10^{-4}$  m. The standard deviation of the mean diameter of the particles was 15%. In the low speed range, molten metal was forced out from the orifice without disintegration until its weight balanced with the surface tension at the operating temperature. This particle was about six times as large as the pulsated orifice-injected particles. This low speed range of droplet formation corresponded to the dripping mechanism (Figure 2-2a). Tear-shaped particles with a surface oxide film were observed when the process was performed in air, while spherical particles resulted when the melt was injected into an inert gas atmosphere.

In summary, the drop-on-demand method produces one droplet per pulse. It requires a flexible diaphragm that is in contact with molten metal. As a result, its application is very limited since diaphragm materials that are flexible and inert with molten metals and alloys are quite limited. This process is still in its early developmental stage for metallic droplet production.

#### **2.2.5 Summary of Atomization Methods**

In this section, the principles of both conventional fluid and capillary atomization were reviewed. Powders produced by two fluid atomization normally have a wide size distribution. Powders produced by capillary atomization generally have a narrower size distribution. However, with continuous jet capillary atomization, an over pressure is required to form a continuous jet. This requires good sealing of the tundish, which is difficult to achieve in practice, especially for continuous higher temperature operation.

Specific designs for the nozzle are required, which makes the process difficult to scale up. Because of the high droplet velocity, longer flight distances are required for droplet solidification. The process normally requires a high frequency and a low amplitude vibration source. Because the droplets tend to stick to one another, a high voltage device is required to charge particles. The drop-on-demand method is in its early stage of development for metallic droplet applications. The requirement for a flexible diaphragm severely limits its high temperature applications.

Since atomization involves solidification of droplets, the solidification theory will be briefly introduced in the next three sections. The relationship between the microstructure and cooling conditions will be reviewed. The numerical models which deal with the solidification of a droplet will also be introduced.

### **2.3 Relationship between Microstructure and Cooling Conditions**

Solidification is a phase transformation from liquid to solid. The microstructure of the solid depends on the cooling conditions of a given alloy. Therefore, it is important to study the relationship between the microstructure and cooling conditions.

Rapid Solidification Processing enables us to obtain a high velocity of the solidification front during the transformation from liquid to solid. This high velocity of the solidification front results from a large amount of undercooling which can in turn result in large departures from equilibrium composition and produce size-refined and even segregation-free microstructure. This in turn can yield better material properties. For

example, using a 55% Al-Zn coating on sheet steel, Cleary [Cleary, 1985] showed that the rapid cooling which results in a smaller dendrite arm spacing improves the corrosion resistance of the coating.

A general way to achieve large undercoolings is by the rapid formation of a small dimension (typically  $< 1 \times 10^{-4} \text{ m}$ ) of liquid material to minimize the presence of heterogeneous nuclei. Good contact with an effective heat sink must also be established. Atomization processing is one of the most effective ways to achieve this objective.

In Section 2.3, the primary parameters, such as cooling rate, superheat, undercooling, and particle size, that affect the microstructure (in terms of Secondary Dendrite Arm Spacing) during solidification will be reviewed. The theory of dendritic growth will be presented in Section 2.4.3.

### **2.3.1 Relationship between Secondary Dendrite Arm Spacing and Cooling Rate**

#### **2.3.1.1 Experimental Results**

Much experimental results have been reported for the relationship between Secondary Dendrite Arm Spacing and cooling rate and between grain size and cooling rate. The primary dendrite arm spacing provides a poor correlation because of the relatively large primary dendrite spacing. This is further complicated by cooling conditions within the primary dendrite arms. In the case of tertiary dendrite arm spacing, these are sometimes too small to be measured, or are not developed during grain growth.

Therefore, only Secondary Dendrite Arm Spacing results are typically presented [Flemings, 1974].

Figure 2-5 shows the effect of cooling rate on Secondary Dendrite Arm Spacing for aluminum, and the degree of structural control which is attainable through various rapid solidification techniques. According to Equation (26), a plot of Secondary Dendrite Arm Spacing and the cooling rate on log-log scale follows a straight line (Figure 2-5) [Grant and Perlloux, 1983]. Coefficients  $a_1$  and  $b_1$ , as will be presented in Section 2.3.1.2, are empirical with as yet no fundamental dependence on alloy properties. However, some trends are evident. For example, the curve pertaining to copper is steeper but less well-defined. For highly alloyed materials, the curve can be expected to flatten out because of the lower thermal conductivity of the liquid metal [Grant and Perlloux, 1983].

Table 2-1 shows the relationship between the Secondary Dendrite Arm Spacing and cooling rate for a few alloy systems. It can be seen that for most alloys,  $b_1$  is in the range of 0.2-0.4, while  $a_1$  is around 40 in most cases.

The effect of cooling rate on the Secondary Dendrite Arm Spacing of Al-5.7%wtCu alloy is shown in Figure 2-6 by Taha [Taha, 1979]. Horwath and Mondolfo [Horwath and Mondolfo, 1962] investigated the relationship between the Secondary Dendrite Arm Spacing and the cooling rate for a wide range of aluminum-copper alloys under casting conditions. The various cooling rates and corresponding temperature gradients were obtained under different conditions. For example, the slowest and moderate cooling rates were obtained by holding the crucible which contained the melt within either a sand bath or a metallic beaker inside a furnace whose heat input was

reduced as desired. The fastest cooling rates were obtained by pouring the alloy into a metallic mould. The cooling rate was calculated by measuring the pouring temperature and the time to reach complete freezing. Note that this will underestimate the cooling rate as the calculated values will include cooling through the superheated liquid.

The cast samples were sectioned vertically. The dendrite arm spacing was measured on dendrites whose primary stalks were perfectly parallel to the plane of polish. The distance from centre to centre of each arm was considered to be the primary spacing. All side arms with observable or reasonably assumable connection to the primary stalk were also measured. Approximately 60 individual measurements were taken on each sample and averaged. Variation of spacing between dendrites in the same specimen was always less than 10 per cent. The results for Al-10wt%Cu, Al-15wt%Cu, and Al-20wt%Cu are listed in Table 2-2.

#### **2.3.1.2 Empirical Relationship**

A commonly accepted empirical relationship between the Secondary Dendrite Arm Spacing (SDAS),  $\lambda_2$  ( $10^{-6}$  m), and the average cooling rate,  $T_c$  (K/s), which is the average slope of the time-temperature curve, is given by Equation (26). This slope is taken over the interval when solid first appears, the liquidus, to when liquid last disappears, the solidus [Mills et al, 1995]. The relationship between SDAS and the cooling rate is given by:

$$\lambda_2 = a_1 (T_c)^{-b_1} \quad (26)$$

where  $a_1$  and  $b_1$  are alloy specific constants for a given system [Khedkar and Nash, 1986]. Under steady-state conditions, the cooling rate can also be calculated from the product of the temperature gradient at the tip of the solidification front and the growth rate of the front [Minkoff, 1986].

It is obvious from Equation (26) that a finer microstructure will result from a higher cooling rate. The experimental results which support the above formula are shown in the last section.

For a given alloy, changes in processing conditions will affect the values of SDAS. These conditions, to be discussed in the following section, include melt superheat, undercooling and cooling rate.

**Table 2-1 Relationship between the Secondary Dendrite Arm Spacing and Cooling Rate for a Few Alloys**

Alloy	a	b	Ref
Maraging 300	40	0.3	Frommeyer and Vogt, 1987
Inconel 718	34	0.34	Frommeyer and Vogt, 1987
Al-4.5wt%Cu	40	0.39	Frommeyer and Vogt, 1987
Eutectic Fe-C, Ni-hard	40	0.4	Frommeyer, 1985
55%Al-Zn	0.33-0.5	0.21-0.22	Cleary, 1985

**Table 2-2 Average Values of Cooling Rate, Temperature Gradient and Dendrite Spacing [Horwath and Mondolfo, 1962]**

Copper (wt%)	Cooling rate (K/s)	SDAS ( $10^{-6}$ m)
10	54	131.0
	124	-----
	474	59.6
	1086	52.0
	102000	15.6
15	45	103.0
	138	76.4
	342	54.0
	1116	41.6
	102000	14.0
20	40	93.2
	106	64.0
	461	44.0
	1242	32.8
	104400	10.9



### **2.3.2 Effect of Superheat and Cooling Rate on the Secondary Dendrite Arm Spacing**

The work of Marcantonio and Mondolfo [Marcantonio and Mondolfo, 1974], and Mondolfo and Barlock [Mondolfo and Barlock, 1975] showed that when aluminum alloys were superheated after fluxing, the size of the constituents and the interdendritic spacing were smaller than in castings not superheated. This was attributed to "denucleation", that is removal of nucleants, which forced freezing at higher undercooling and therefore at a faster rate.

In their experiments, the total solidification time, which is defined as the time from pouring to the completion of solidification, was directly proportional to the superheat. It was not shown where the temperature measurements were taken in the samples. The metallographic samples were taken from a surface parallel to the surface of a  $7 \times 10^{-2}$  kg sample and  $5.5 \times 10^{-3}$  m inside the sample.

The results of the effect of superheat on the interdendritic spacing of 3003 alloy showed that increasing the superheat reduces the interdendritic spacing under three different cooling conditions: metal mould, brick mould, and furnace cooled respectively as shown in Figure 2-7a [Mondolfo and Barlock, 1975]. The effect is more obvious under fast cooling conditions, as in a metal mould. The results were further confirmed by plotting the superheat versus solidification rate as shown in Figure 2-7b [Mondolfo and Barlock, 1975]. The cooling rate will increase with increasing solidification rate; therefore, as the superheat increases, the cooling rate will also increase.

All the data reported are consistent with the hypothesis that superheating produces

a reduction of size and/or number of nucleants but not their complete elimination, since at low cooling rates the number and/or size of the nucleants still appears sufficient to provide all the nucleation needed. At the higher solidification rates the number and/or size of the nucleants is too small. The heat removal is faster than the latent heat evolution until some growth of the nuclei has taken place. The higher the superheat or the longer the holding time at the pouring temperature, the more likely that the molten metal tends to reduce the quantity of nucleants. Hence the chance of heterogeneous nucleation becomes smaller, which corresponds to a higher undercooling. However, since the number, size and possibly the nature of nucleants varies from sample to sample, there is a substantial amount of scatter in the relationship between undercooling and superheating. It was not indicated what these nucleants are.

Jackson, et al. [Jackson et al, 1966] cast the ammonium chloride-water system at various saturated temperatures and superheat. It was found that at a small superheat, i.e., for pouring temperatures close to the saturation temperature of a given solution, a "big-bang nucleation" phenomenon was observed. In this case, the crystals appeared throughout the liquid during pouring. The crystals swirled as the casting was poured, producing a snow-storm effect. There was no columnar region in these castings. This "big-bang" nucleation is eliminated by increasing the superheat before pouring.

At the superheat region away from "big-bang", i.e., in the large amount of superheat region ( $\geq 25$  K), faster cooling was achieved with higher superheat. The crystal flakes also seem smaller with higher superheat. This result is in agreement with the work of Marcantonio and Mondolfo in the large superheat range mentioned above.

### **2.3.3 Relationship between Undercooling and Dendrite Arm Spacing**

Since the growth velocity depends approximately on the square of undercooling [Liu, 1980]], it follows that extremely fine dendrites can be produced in highly undercooled droplets. This is, of course, just as valid for pure metals as it is for solid-solution alloys, but the morphology of fast-growing dendrites can be observed far more easily in the latter case [Jones, 1972]. As shown in Figure 2-8 for pure copper, the dendrite element size reduces as the undercooling increases [Jones, 1972].

Skolianos, et al. [Skolianos et al, 1982] plotted the dendrite arm spacing for dendritic specimen and grain size for both dendritic and nondendritic specimens versus degree of undercooling for Ni-25%Cu-0.2%S alloy in Figure 2-9. It can be seen that the dendritic size decreases with increasing undercooling and there is a critical value of undercooling of about 160 K for this alloy, below which coarsening has an effect on nondendritic grains but no effect on the grain size of dendritic specimens. In their experiments, temperatures were directly measured in a cylindrical ingot.

Turnbull and Cech [Turnbull and Cech, 1950] measured undercooling of metallic droplets by observing them on a hot stage microscope. Metallic particles placed on the hot stage, and heated above their melting point, became spherical droplets. Upon cooling, the change of surface of the droplet appearance (a disruption of the smooth surface to one apparently having many sharp ridges and protrusions) indicated the beginning of solidification. Another indication of the beginning of the solidification was a sudden brightening or "blick" occasioned due to recalescence. Thus the amount of undercooling

was calculated by the difference between the melting point and the recorded beginning of the solidification temperature.

Another technique to measure undercooling was illustrated by Perepezko, et al. [Perepezko et al., 1979]. In this technique, droplet dispersions of metals and alloys were produced by emulsifying a mixture of liquid metal sample and organic carrier fluid with a high-speed shearing device. After preparation, the emulsion was transferred to a sample tube of a Differential Thermal Analysis (DTA) apparatus. The DTA thermograms indicate the nucleation temperature, from which undercooling can be calculated. The difficulty of this technique is the requirement of a carefully selected carrier fluid with tolerance to oxidizing atmosphere at temperatures above the melting point of the metal under study, and an appropriate surfactant agent.

#### **2.3.4 Relationship between Cooling Rate and Undercooling**

Reddy and Sekhar [Reddy and Sekhar, 1989] reported the nucleation temperature at various cooling rates as shown in Figure 2-10 for dimensionless undercooling versus cooling rate. The ingot size was 0.06 m diameter and 0.12 m long. The experiments were performed under pressure to achieve fairly high cooling rates. The cooling curve of the casting was recorded by a specially designed thermocouple assembly with a very small lag time of  $0.5 \times 10^{-3}$  s. The nucleation temperature, hence undercooling, was determined from the cooling curve. In the range of measurements, the undercooling is seen to increase with increasing cooling rate. The line in Figure 2-10 is a linear-least-

squares fit for all points up to cooling rates of 2000 K/s. Below 1000 K/s the line is slightly non-linear to indicate that it should approach the origin [Reddy and Sekhar, 1989]. Caretti and Berfonello showed that for small amount of undercooling, the cooling rate is directly proportional to the square of undercooling [Caretti and Berfonello, 1983].

Figures 2-11 and 2-12 show the dimensionless undercooling at different cooling rates for various aluminum alloys of Al-5.6wt%Zn-2.6wt%Mg-1.5%Cu, Al-2.2wt%Cu, Al-4.4wt%Cu and Al-33.3wt%Cu respectively. All of the above results show that undercooling increases with increasing cooling rate.

Cooling rate of the cast metal can be measured directly by embedding a rapid-response thermocouple in the metal [Duflos, 1987]. However, direct measurement of cooling rate of atomized powder is difficult. It is often determined using a heat transfer model [Acrivos, 1976] or by microstructure measurement together with a known relationship to cooling rate [Frommeyer, 1985].

### **2.3.5 Relationship between Particle Size and Secondary Dendrite Arm Spacing**

There is also a power law relationship between the Secondary Dendrite Arm Spacing and the atomized particle size:

$$\lambda_2 = a_2 D^{b_2} \quad (27)$$

where  $\lambda_2$  refers to the Secondary Dendrite Arm Spacing,  $D$  refers to the atomized particle size, and  $a_2$  and  $b_2$  are constants. The rationale for this relationship is that the temperature gradients in a droplet are negligible, therefore all points in a droplet will experience the

same cooling rate. The coefficients  $a_2$  and  $b_2$  in Equation (27) have different magnitudes of the values of  $a_1$  and  $b_1$  in Equation (26) for the same alloy. From Equation (27), we can see that when the atomized particle size increases, the dendrite arm spacing increases exponentially in a power law relationship since  $b_2$  is positive.

Figure 2-13 shows the Secondary Dendrite Arm Spacing as a function of powder particle diameter for high strength aluminum alloys. The powders were produced by argon atomization. The data are well correlated over the range  $0.4 < \lambda < 6 \times 10^{-6}$  m and  $0.7 < D < 300 \times 10^{-6}$  m. Using Equation (27) the regression coefficients are  $a_2 = 0.13$  and  $b_2 = 0.67$  [Jones, 1986].

Table 2-3 summarizes some experimental results from the literature. From this table it can be seen that  $a_2 = 0.01-0.13$  and  $b_2 = 0.5-1.3$  for most of the alloys. Figure 2-14 shows the relationship between Secondary Dendrite Arm Spacing and particle size of Al-3.7wt%Ni-1.5wt%Fe alloy atomized both by gas atomization and centrifugal atomization. Values of  $a_2$  of 0.016 and  $b_2$  of 1.036 were obtained after regression for gas and centrifugal atomization.

**Table 2-3 Relationship between Particle Size and Dendrite Arm Spacing for Various Alloys**

Alloys	$a_2$	$b_2$	References
Ti-6Al-4V Rotating electrode process		0.9	Broderick et al, 1985
IN 792 Rapid Solidification Rate	0.116	0.574	Cosandey et al, 1982
IN 792 Argon Atomized	0.13	0.605	Consandey et al, 1982
Eutectic Fe-C, Ni hard Atomized & quenched in liquid N <sub>2</sub> and He		1.333	Frommeyer, 1985
Al-3.7wt%Ni-1.5wt%Fe Air & Centrifugally atomized*	0.016	1.036	Hildeman et al, 1983

\*: regression data by digitizing Figure 2-15.

## **2.4 Numerical Models**

**Rapid solidification processing has received an enormous amount of attention in recent years and continues to be the subject of intensive research. Atomization is perhaps the process with the highest potential for large-scale exploitation of the microstructural benefits achieved by rapid solidification.**

**In order to understand various atomization processes, and thus improve the control of these atomization processes, many researchers have developed mathematical models in this area. One of the most interesting and important aspects of this topic in helping us understand both the fundamentals of rapid solidification and the atomization process is the thermal history of droplets during atomization.**

**After being atomized, a molten metal droplet will undergo cooling in the liquid state, nucleation of a crystallite (due to which, recalescence may be involved), growth of the crystallite until the droplet is fully solidified, and further cooling in the solid state. In the meantime, the droplet is accelerating or decelerating towards its terminal velocity.**

**It is important to understand the basic concepts of solidification and transport phenomena such as thermodynamics, nucleation theory, microstructure development, heat transfer, and fluid flow during atomization. This understanding will permit the development of models which can predict the interrelationship between rapid solidification processing and the resulting structure. These models, once developed, can in turn be used to determine the desired atomization conditions required to yield a given microstructure.**



### **2.4.1 Fundamentals of Heat Transfer of a Droplet**

Levi and Mehrabian [Levi and Mehrabian, 1982] carried out the most comprehensive study of the heat flow model for rapidly solidified undercooled droplets. The solidification of undercooled spherical droplets of pure material (with a single melting point) was analyzed using both Newtonian and non-Newtonian cooling models. Relationships were established between atomization parameters, the growth kinetics, the interface velocity and undercooling, and other solidification variables. Simulation of the solidification in an undercooled droplet when a single nucleation event occurred at its surface was presented. The effect of multiple nucleation events, undercooling, and heat transfer coefficient on the thermal history of the droplets was also discussed in detail. The model addressed the solidification process in accounting for cases where the temperature distribution within the droplets (non-Newtonian model) is important in the case of a large Biot number. The solidification of an alloy with a range of melting temperatures was not addressed in their paper, but will be dealt with in this thesis.

#### **2.4.1.1 Newtonian Model**

Due to the relatively high thermal conductivity of small droplets and their small dimensions, the temperature gradient within the droplets can often be neglected. Therefore, this case can be treated by the lumped capacitance method. The essence of the lumped capacitance method is the assumption that the temperature of the solid is

spatially uniform at any instant during the transient process. It is also called a Newtonian model. Now we introduce the Biot number (Bi). It is the ratio of the internal thermal resistance of a solid to the boundary layer thermal resistance and is defined as:  $Bi = hL_c/k_d$ , where  $L_c$  is the characteristic length equal to the droplet diameter  $D$  in atomization,  $h$  the heat transfer coefficient between the droplet and the gas atmosphere, and  $k_d$  the thermal conductivity of the droplet.

When  $Bi < 0.1$ , the error associated with using the lumped capacitance method is small [Incropera and Dewitt, 1981]. When  $Bi \ll 1$ , the resistance to conduction within the solid is much less than the resistance to convection across the droplet surface boundary layer. This condition is usually well-satisfied for metal droplets which are less than  $1 \times 10^{-3}$  m in diameter.

Neglecting temperature gradients within the solid, we can now consider the transient temperature response by formulating an overall heat balance on the droplet. This balance equates the rate of heat loss at the surface of the droplet to the rate of change of heat within the droplet. Therefore:

$$\rho V c_p \frac{dT}{dt} = -hA_s (T - T_a) \quad (28)$$

where  $\rho$  is the density of the droplet,  $V$  is the volume of the droplet and  $c_p$  is the specific heat of the droplet,  $A_s$  is the surface area of the droplet,  $T_a$  is the ambient temperature, and  $h$  is the convection heat transfer coefficient, which can be obtained from:

$$h = Nu_D \frac{k_a}{D} \quad (29)$$

where  $Nu_D$  is Nusselt number defined as the ratio of convection heat flux to conduction heat flux that would occur through a droplet of diameter  $D$ ,  $k_a$  is the thermal conductivity of the ambient atmosphere.

Heat transfer correlations for  $Nu_D$  have been proposed for spheres and for the case of convective heat transfer from freely falling liquid drops. Ranz and Marshall proposed [Ranz and Marshall, 1952]:

$$Nu_D = 2 + 0.6 Re_D^{1/2} Pr^{1/3} \quad (30)$$

where  $0 \leq Re_D \leq 200$  and  $0.69 \leq Pr \leq 0.73$ .

$Re_D$  is the Reynolds number calculated using Equation (31) [Incropera and Dewitt, 1981]:

$$Re_D = \frac{\rho_a u D}{\mu_a} \quad (31)$$

where  $\rho_a$  and  $\mu_a$  are the density and viscosity of the ambient atmosphere respectively,  $u$  is the relative velocity between the droplet and the fluid, and  $D$  is the droplet diameter.  $Pr$ , the Prandtl number, is the ratio of momentum to thermal diffusivity [Incropera and Dewitt, 1990]:

$$Pr = \frac{\nu_a}{\alpha_a} = \frac{c_{pa} \mu_a}{k_a} \quad (32)$$

where  $\nu_a$  is the kinematic viscosity (for momentum transfer) and  $\alpha_a$  is the thermal diffusivity of the ambient atmosphere. Thermal diffusivity ( $\alpha_a = k_a / (\rho_a c_p)$ ) measures the

ability of a material to conduct thermal energy relative to its ability to reach a new equilibrium condition. Under the experimental conditions tested in this study for Impulse Atomization,  $Re_d$  ranged from 20 to 100 and  $Pr$  for nitrogen is approximately 0.71. Thus, these operating conditions are well within the range of applicability of Equation (30).

Radiation can easily be taken into account with a modification of Equation (28), however it is often found to be negligible in atomization research [Gutierrez-Miravete et al, 1989].

Substituting Equations (29) to (32) in Equation (28) and solving it simultaneously with Equation (33), which will be presented in Section 2.4.1.2, the cooling curve of a droplet can be obtained after taking solidification into account, as will be presented in Sections 2.4.2 and 2.4.3.

#### 2.4.1.2 The Droplet Velocity

As Guthrie, et al. [Guthrie et al, 1975] proposed, when a solid particle is accelerated or decelerated during its motion in a fluid, the statement of Newton's second law (mass times acceleration equals the sum of the forces acting on a particle) takes the following form:

$$\frac{1}{6} \pi D^3 \rho \frac{du}{dt} = \frac{1}{6} \pi D^3 (\rho - \rho_a) g - 2 C_D \pi D^2 \rho_a u |u| - C_A \frac{1}{6} \pi D^3 \rho_a \frac{du}{dt} - 4 C_H D^2 (\pi \rho_a \mu)^{1/2} \int_0^t \frac{du}{dt} \frac{dt}{\sqrt{t-\tau}} \quad (33)$$

The term on the left-hand side is mass times acceleration. The first two terms on the right-hand side represent the buoyancy force and the drag force which are always opposite to the direction of motion, hence, the absolute value sign on one of the velocities.  $C_D$  is the dimensionless drag coefficient. It has been found experimentally that the drag coefficient is a function of both Reynolds number (Equation (31)) and also the shape of the particle.

The third term on the right hand side of Equation (33) corresponds to the "added mass", which allows for the fact that not only the droplet has to be accelerated but also a portion of the fluid which adheres to the particle. The value of the added mass coefficient  $C_A$  was taken as 0.5; alternatively, it has been assumed to depend on the particle velocity and on the acceleration. This term can be neglected in a low density fluid such as a gas. The last term on the right-hand side is designated the "history term" which is an attempt to allow for the dependence of the instantaneous drag on the state of development of the fluid motion around the droplet. In the classical literature,  $C_H$  is assigned a value of 6.0 while in more recent work  $C_H$  was allowed to vary with the velocity and the acceleration. This term can also be neglected for low viscosity and low density fluids such as a gas. When  $(du/dt)$  in Equation (33) equals zero, the problem will reduce to the evaluation of the steady-state, or terminal velocity.

Figure 2-15 shows a plot of an experimentally determined relationship between the drag coefficient,  $C_D$ , and the Reynolds number,  $Re_D$ . This plot may be divided into four distinct regions as follows:

- (i)  $10^{-3} < Re_D < 2$ . Creeping flow or Stokes' law region. In this region the drag

force is linearly proportional to the inverse of the particle Reynolds number and may be written as:  $C_D=24/Re_D$ .

(ii)  $2 \leq Re_D \leq 500$ . Intermediate region. In this region the experimental data may be represented by the following approximate relationship:  $C_D = 18.5/Re_D^{0.6}$ .

(iii)  $500 \leq Re_D \leq 2 \times 10^5$ . Newton's law region. In this region the drag coefficient is approximately constant and is independent of the Reynolds number:  $C_D \approx 0.44$ .

(iv)  $Re_D > 2 \times 10^5$ . In this region the drag coefficient drops to a rather low value of 0.09 from which it rises slowly for higher values of the Reynolds number.

When a droplet is accelerating towards its terminal velocity, such as in atomization, the velocity of the droplet trajectory can be calculated numerically using Equation (33). The added mass and history terms may be neglected due to the small density of the gas. This solution coupled with the solidification of the droplet will be presented in Chapter 3.

## **2.4.2 Fundamentals of Nucleation**

### **2.4.2.1 Homogeneous Nucleation**

When a solid forms within its own melt without the aid of heterogeneous nuclei, it is said to nucleate homogeneously. This manner of nucleation requires a large driving force (from undercooling) because the surface energy of the nucleus makes a relatively large contribution to its total free energy [Flemings, 1974]. In homogeneous nucleation,

all the potential foreign nucleants should be completely eliminated. As this is impossible in most production processes, most solidification processes we deal with involve heterogeneous nucleation. Even so, it is important to understand the fundamentals of homogeneous nucleation.

The free energy change of a system due to solidification is expressed by:

$$\Delta G^0 = \Delta H^0 - T\Delta S^0 \quad (34)$$

At the melting point, the system is in equilibrium. Therefore,  $\Delta G^0=0$ , i.e.,

$$\Delta S_m^0 = \frac{\Delta H_{fm}}{T_m} \quad (35)$$

where  $\Delta H_{fm}$  is the latent heat of fusion and  $T_m$  is the melting point. The free energy change due to solidification at any temperature other than  $T_m$  is obtained by substituting Equation (35) into (34):

$$\Delta G^0 = \frac{\Delta H_{fm} (T_m - T)}{T_m} \quad (36)$$

or

$$\Delta G^0 = \frac{\Delta H_{fm} \Delta T}{T_m} \quad (37)$$

The total free energy of the liquid system that contains some solid crystals consists of two parts: one is the free energy difference between the volume of liquid and solid, which is the driving force for solidification, and the other is the surface energy due to the existence of the liquid-solid interface. The surface energy increases the total free energy

of the system. Suppose that the solid crystal takes a spherical shape and has a radius  $r$ , then the total free energy change of the system is given by:

$$\Delta G^0 = -\frac{4}{3}\pi r^3 \Delta G^0_v + 4\pi r^2 \gamma_{ls} \quad (38)$$

where  $\Delta G^0_v$  is the free energy difference between the volume of liquid and solid per unit volume.  $\Delta G^0_v$  decreases with increasing radius and makes the system more stable.  $\gamma_{ls}$  is the interfacial energy between liquid and solid, which increases with increasing radius, and makes the system less stable. Therefore, there exists a critical radius  $r_c$ , which corresponds to the maximum energy barrier of the system, as shown in Figure 2-16 [Minkoff, 1986]. The particle radius  $r_c$  is termed the critical nucleus. Particles larger than this are stable and grow; particles smaller than  $r_c$  form spontaneously in the liquid metal both above and below the equilibrium melting point. They do so because in this way they increase the entropy of the system; However, they are not stable. This value of  $r_c$  can be obtained from the first derivative of Equation (38):

$$r_c = \frac{2\gamma_{ls}}{\Delta G^0_v} \quad (39)$$

The radius  $r_c$  of a spherical particle which is just stable at an undercooling  $\Delta T$  is given by substituting Equation (37) into Equation (39):

$$r_c = -\frac{2\gamma_{ls}T_m}{\Delta H_{fm}\Delta T} \quad (40)$$

Substituting Equation (40) back into Equation (38) yields:



$$\Delta G_c^0 = \frac{16\pi}{3} \frac{\gamma_{ls}^3 T_m^2}{[(\Delta H_{fm})^2 \Delta T^2]} \quad (41)$$

The nucleation rate (the number of nuclei per unit time and volume) is governed by two terms. One is the energy fluctuation factor  $\exp(-\Delta G_c^0/\kappa T)$ , which is a strong function of undercooling and shows the probability of forming the short range ordering cluster with critical nucleus in the liquid. The greater the number of these critical nuclei, the greater the probability that within a given time one will grow and initiate solidification. The other factor is the diffusion factor,  $\exp(-Q_D/\kappa T)$ , where  $Q_D$  is the diffusion activation energy. The diffusion factor can be alternatively expressed as  $\omega^* v_{LS}$ , where  $\omega^*$  is the number of atoms surrounding a critical nucleus and  $v_{LS}$  is the frequency with which atoms jump across the liquid-solid interface. Therefore the nucleation rate can be expressed as:

$$J = \omega^* v_{LS} \exp(-\Delta G_c^0/\kappa T) \quad (42)$$

For a spherical nucleus,  $\omega^*$  is approximately given by:

$$\omega^* = \frac{4\pi r_c^2}{a_0^2} \quad (43)$$

The jump frequency of atoms in the bulk liquid is  $v_l = 6D_l/\alpha_j^2$ , where  $\alpha_j$  is the jump distance and  $D_l$  is the liquid diffusion coefficient. The frequency with which each atom strikes the liquid-solid interface is usually taken to be one-sixth its jump frequency in the bulk liquid because it reaches the interface by jumping in only one of six possible directions. Taking  $\alpha_j = a_0$ , we arrive at the expression for  $v_{LS}$ :

$$v_{LS} = \frac{D_L}{a_0^2} \quad (44)$$

Substituting Equations (41), (43) and (44) into Equation (42), we finally arrive at the classical expression for homogeneous nucleation in bulk liquid:

$$J = \frac{4\pi n r_c^2 D_1}{a_0^4} \exp\left[-\frac{16\pi\gamma_{ls}^3 T_B^2 \Omega^2}{3\Delta H_{fs} \Delta T^2 \kappa T}\right] \quad (45)$$

Hirth [Hirth, 1978] used a relationship for the homogeneous nucleation under nonequilibrium conditions in a similar form as follows:

$$J = 10^{-2} 4\pi (r_c/a_0)^2 (a_0/\Omega) D_1 \exp\left(-\frac{16\pi\gamma_{ls}^3 \Omega^2 T_B^2}{3\kappa T_B \Delta H_{fs}^2 \Delta T^2}\right) \quad (46)$$

where  $10^{-2}$  is the so-called nonequilibrium factor,  $r_c$  is the critical nucleus radius,  $a_0$  is the atomic diameter,  $D_1$  is the liquid diffusivity,  $\gamma_{ls}$  is the solid-liquid interfacial energy,  $\Omega$  is the atomic volume and  $\kappa$  is Boltzmann's constant. Equation (46) is for the rate of steady-state nucleation.

The thermodynamic barrier to formation of a critical nucleus  $\Delta G_c^0$  decreases rapidly with increasing undercooling. The nucleation rate is so sensitive to the term within the exponential that changes of several orders of magnitude in values of the pre-exponential term do not appreciably affect the calculated undercooling for sensible nucleation. Figure 2-17 shows schematically the dependence of nucleation rate on undercooling [Liu, 1980].

Figure 2-18 shows the dependence of nucleation rate on the critical nucleus value  $r_c$  and corresponding critical free energy barrier  $\Delta G_c$ . It shows the dependence of nucleation temperature  $T_n$  on  $\Delta G_c$ . For large values of  $\Delta G_c$ , as for example in homogeneous nucleation,  $T_n$  will give a maximum value to  $T_m - T_n$ .

#### **2.4.2.2 Heterogeneous Nucleation**

In liquid metal systems of significant volume, the liquid-solid transformation is generally nucleated heterogeneously. A new solid phase may start by nucleating at the surface of a mould, or it may appear on solid surfaces within the melt. Even impurities in the melt may act as nucleating agents [Minkoff, 1986].

Heterogeneous nucleation greatly reduces the volume of cluster needed to reach the critical radius of homogeneous nucleation. Therefore, in contrast to homogeneous nucleation, solidification may proceed with less undercooling.

Figure 2-19 shows the relationship between the nucleation rate and undercooling under heterogeneous and homogeneous nucleation conditions. The actual amount of undercooling under heterogenous conditions depends on the solidification material and its size (which determines the chance of containing an impurity nucleant), the amount of impurities, the type of impurities and the shape of the impurities.

Although techniques have been developed to measure the undercooling or the nucleation temperature of a droplet as described in Section 2.3.3, it is limited and difficult to practice in reality. For example, in the hot stage microscope method, it was found that

the amount of undercooling varied from particle to particle due to metal purity, despite efforts to use fairly pure metal. Hence, only the maximum undercooling was reported [Turnbull, 1950]. With the emulsion technique, it was difficult to find the right organic carrier fluid and an appropriate surfactant which would not react with the metal, would be stable above the metal's melting point, and would make an ideal suspension with the molten metal [Perepezko et al, 1979].

The actual undercooling of an alloy is mainly dependent on its purity. Hence, the larger the dimension of the alloy, the greater the chance for it to have heterogeneous nucleants, and the less the undercooling. Hence, in general, the undercooling of an ingot is often low, e.g., a few degrees, while the undercooling of small droplets is often high, a few tens of degrees.

### **2.4.3 Fundamentals of Growth**

#### **2.4.3.1 Grain Growth and Dendritic Microstructure**

After nucleation, transfer of atoms from the liquid to a nucleus depends on the structure of the solid-liquid interface. In turn, the structure of the solid-liquid interface depends on the chemical properties of the alloy and the thermodynamic environment of the growing crystal [Liu, 1980].

For pure metals, the solidification front is stable at the melting temperature  $T_m$ . The growing velocity of the solid crystal interface depends on the temperature of the

**interface. The undercooling in the solid-liquid interface provides the driving force for the solid crystal to grow. The higher the undercooling, the faster the crystal grows.**

**The morphology of the crystal is determined by the thermodynamic conditions in the solidification front. If the temperature gradient in the solidification front is positive, the interface is isothermal and grows steadily with a flat solidification front. If the temperature gradient in the solidification front is negative, a protrusion on the interface will meet a liquid at even lower temperature and grow even faster. Therefore, the solidification interface is not stable and will grow into branches called dendrites, as shown in Figure 2-20. This dendritic structure is common in metals.**

**Dendritic growth is more favourable in alloys. Under a negative temperature gradient, a dendritic structure will be formed as described above. Even under a positive temperature gradient, a dendritic structure will still be formed if the alloy is subject to constitutional undercooling conditions. Dendrites in alloys form with a solute content significantly different from the average solute content of the alloy. Consequently, the solute concentration in the dendrite is different from that in the interdendritic region. This solute segregation pattern is characterized by the primary- and secondary-dendrite spacings and controls the mechanical properties of solidified alloys [Trivedi, 1989].**

**Dendrite Arm Spacings were defined by Taha [Taha, 1979] as follows: Primary Dendrite Arm Spacing is the number of dendrite centres in the cross-section which intersects a line of fixed length drawn along the direction of closest primary dendrite packing. Secondary Spacing is the number of secondary arms in the longitudinal section which intersects a line of fixed length lying perpendicular to the secondary arms and**

parallel to the primary arms. It was already shown in Section 2.3.1 how the Secondary Dendrite Arm Spacing is related to the local cooling rate of the alloy during solidification.

#### 2.4.3.2 Kinetics of Growth

The classical treatment of continuous growth leads to an expression for the velocity  $U$  of the form:

$$U = \frac{D_l}{d_m} \left[ 1 - \exp\left(-\frac{\Delta H_m \Delta T}{\kappa T T_m}\right) \right] \quad (47)$$

where  $D_l$  is the self diffusivity in liquid,  $d_m$  is the effective atomic diameter (taken as the atomic jump distance),  $\Delta H_m$  is latent heat of fusion per molecule,  $\Delta T$  is undercooling,  $\kappa$  is Boltzmann's constant,  $T$  is temperature, and  $T_m$  is the melting temperature. Determination of the variations in liquid diffusivity with undercooling is difficult, although extrapolation and interpolation of viscosity data for liquids and metallic glasses have been attempted [Clyne, 1984]. The above expression reduces to the Wilson-Frenkel [Clyne, 1984] form at low  $\Delta T$  as follows:

$$U = \frac{D_l \Delta H_m \Delta T}{d_m \kappa T_m^2} \quad (48)$$

The introduction of a correction factor,  $\beta$ , has been suggested [Cahn et al, 1964] to account for the fact that the jump distance across the crystal-melt interface may be somewhat smaller than that for diffusion in the bulk liquid. It is thus common to see reference to a kinetic coefficient  $B$  (representing the proportionality constant between

crystal growth velocity and undercooling), given by the expression:

$$B = \frac{\beta D_1 \Delta H_{fm}}{d_m \kappa T_m^2} \quad (49)$$

The basis for expecting  $\beta > 1$  is somewhat obscure and its value has been taken as unity by some authors [Clyne, 1984; Levi and Mehrabian, 1982]. The value of the kinetic coefficient B may thus be estimated from thermophysical data and, although errors will clearly arise from the unknown property variations (particularly  $D_1$  at high  $\Delta T$ ), these estimates are at least not prone to the gross uncertainty of the nucleation calculations (which stem primarily from the  $\gamma_n^3$  term and from the effects of nucleants).

#### 2.4.3.3 Recalescence

Recalescence is the rapid heating of an undercooled molten sample resulting from the nucleation of the solid phase and the subsequent rapid release of the latent heat of fusion.

The recalescence temperature  $T_r$  was calculated according to Lavernia, et al. [Lavernia et al, 1987]:

$$\Delta H_{fm} V \frac{df_s}{dt} = h (T_r - T_m) A_s \quad (50)$$

where  $\Delta H_{fm}$  is the amount of latent heat still within a partially solidified droplet at the end of recalescence, V is the droplet volume,  $f_s$  is the fraction of solid, h is heat transfer coefficient, and  $A_s$  the surface area of the droplet.

The rate of growth of a solid phase for the small amount of undercooling considered here can be estimated from [Coriell and Turnbull, 1982]:

$$\frac{df_s}{dt} = \frac{3K(T_l - T_r)}{r_d} \quad (51)$$

where  $T_l$  is the liquidus temperature,  $T_r$  recalescence temperature, and  $K$  the kinetic growth coefficient, which is the same as  $B$  explained in Section 2.4.3.2. Therefore, using suitable values for  $K$ , one can readily estimate  $T_r$ .

Coriell and Turnbull [Coriell and Turnbull, 1982] assumed that the recalescence was essentially complete within a time interval which was smaller than the time step used in their thermal calculation. Since the recalescence was driven by undercooling, as the droplet heats up, the rate of heat release decreases and recalescence terminates when the rate of heat release becomes comparable to the rate of heat extraction from the outer surface of the droplet. Therefore, at the end of recalescence, the rate of releasing latent heat and the rate of heat extraction through the outer surface became equal.

For the cooling of mushy droplets where both solids and liquids coexist, the relationships between  $H$  and  $T$  are shown in Figure 2-21 both with and without undercooling [Lavernia et al, 1987]. For the case without undercooling, the  $H$  vs.  $T$  relationship in the mushy zone is linear. With undercooling, the freezing does not start at the liquidus temperature of an alloy on cooling. The enthalpy curve continues to decrease along the extrapolation of the liquid enthalpy curve until the nucleation temperature  $T_n$  is reached. At this point, recalescence starts and the temperature of the droplet rises. At the end of recalescence the droplet temperature is  $T_r$  and the effective



latent heat content is  $\Delta H^*$ . Then the droplet will continue to solidify as if it has experienced an undercooling step, except that the overall solidification time will be correspondingly shortened. The estimation of the nucleation temperature  $T_n$  and the kinetic growth coefficient  $K$  could be difficult. It is not clear how they estimated  $T_n$  and  $K$ . Clyne [Clyne, 1984] presented the formulation for the calculation of  $K$ .

For larger amount of undercooling, a model was suggested by Levi and Mehrabian [Levi and Mehrabian, 1982]:

$$(H-H_{sm}) = [\Delta H_{fm} + C_{pl}(T-T_m)](1-f_s) + C_{ps}(T-T_m)f_s \quad (52)$$

where  $H$  is the enthalpy of the system at temperature  $T$  and fraction solid  $f_s$ ,  $H_{sm}$  is the enthalpy of the solid at the melting temperature,  $C_{pl}$  and  $C_{ps}$  are the specific heat of solid and liquid respectively,  $T_m$  is the melting point, and  $\Delta H_{fm}$  is the latent heat of fusion.

Equation (52) can be rewritten in terms of dimensionless enthalpy  $\psi$  and temperature  $\theta$  as:

$$\psi = (1+\theta)(1-g) + \frac{C_{ps}}{C_{pl}}g\theta \quad (53)$$

where  $\psi = (H-H_{sm})/\Delta H_{fm}$ , and  $\theta = c_{pl}(T-T_m)/\Delta H_{fm}$ .

Figure 2-22 [Levi and Mehrabian, 1982] is the enthalpy-temperature diagram showing the possible solidification "paths". The system can conceivably follow any "path" of decreasing enthalpy in the supercooled region ( $\psi > 1$ ), starting the nucleation temperature ( $\theta_n < 0$ ) on the liquid line and ending at some point on the solid line. A vertical path represents isothermal solidification, of which a limiting case is the non-

undercooling situation of a pure metal. A horizontal path represents isenthalpic (or adiabatic) solidification. In a path such as the curve 3, two distinct solidification regimes can be identified. The first one is the recalescence or "rapid-solidification" stage. A supercooled droplet absorbs most of the liberated heat of fusion and the heat loss to the surroundings is more or less irrelevant. The second regime is one of a "slower growth". It develops after droplet undercooling has been largely relieved, thereby limiting the progress of solidification to conditions imposed by the external heat flow. This regime usually involves temperatures close to the melting point of a metal and is roughly isothermal.

The thermal history reflects the competition between the external rate of heat extraction and the recalescence rate (release of latent heat). The recalescence rate is proportional to the solidification rate (change in fraction solid with time,  $df/dt$ ). The latter is in turn a product of the solid-liquid interface velocity and its area.

## **2.5 Summary**

In this chapter, conventional fluid atomization and other capillary atomization theory and techniques were reviewed. The conventional fluid atomization process produces powder with a wide size distribution with satellite formation and low efficiency. The method of producing droplets from the vibrated continuous jet requires the application of overpressure, a charging device, and is impractical for high melting point systems. The drop-on-demand method is also limited to low melting point systems and

**seems inefficient in producing one droplet per impulse per orifice. Therefore, the Impulse Atomization Process was developed to overcome these drawbacks.**

**The solidification theory for the solidification of an undercooled droplet was also reviewed in this chapter. As heat is extracted from a falling droplet, it undercools. After the beginning of the nucleation, grain growth starts with recalescence and continues after reaching its recalescence temperature until the completion of solidification. The SDAS is the only experimental measure of the cooling rate of an atomized droplet because of the difficulty of temperature measurement on a fast-moving small droplet. Measurement of nucleation temperature or undercooling is also very difficult. Estimates are made based on some literature information.**

## **CHAPTER 3:            NUMERICAL MODEL**

**In this chapter, a numerical model will be developed to calculate the cooling curve of a free-falling molten metal droplet. As shown in Figure 3-1a, an alloy was melted in a crucible. A molten metal droplet emanates from the crucible with an initial velocity  $u_0$  and an initial (pouring) temperature  $T_p$ . While the model is valid for any material, it was only applied to Al-Cu alloys. The predicted droplet cooling curve will subsequently be used to estimate the droplet cooling rate during solidification and its undercooling temperature.**

### **3.1 Assumptions**

**Consider a drop of molten metal atomized and spherodized immediately upon exiting the atomizing nozzle. As it falls under gravity to the bottom of the atomization tower, this spherical droplet will lose heat to the static gas surroundings, as shown in Figure 3-1b. The assumptions for the model describing the thermal history of the droplet are:**

- (1)    The static gas environment in the atomizer is at a constant temperature,  $T_a$ .**
- (2)    The droplet spherodizes immediately upon leaving the orifice.**

- (3) **The initial temperature of the droplet is taken as the molten metal temperature in the crucible as shown in Figure 3-1a.**
- (4) **No droplet oscillations, distortions or collisions occur. The trajectory of individual droplets is unaffected by surrounding droplets in the stream.**
- (5) **The densities of liquid and solid are the same and constant.**
- (6) **Radiation is negligible.**
- (7) **Newtonian model cooling occurs, i.e., assume the temperature distribution within the droplet is negligible.**
- (8) **The droplet solidifies with an assumed amount of undercooling.**
- (9) **Solidification begins heterogeneously from a single nucleus in the droplet.**
- (10) **Both solid and liquid solutions behave ideally, i.e., thermophysical properties can be calculated using a weighted average.**
- (11) **No further phase transformations occur after solidification is complete.**
- (12) **No solute segregation occurs in the droplet during solidification.**

In the following text, assumptions (1), (2), and (7) will be justified prior to the detailed description of the model. It was observed that throughout the duration of an experiment the temperature in the lower part of the chamber is unchanged. Since atomization takes place in a relatively static environment, assumption (1) is reasonable.

According to Nichiporenko [Nichiporenko, 1976], the time taken for a ligament to spheroidize in atomization is:

$$\tau_{sph} = \frac{3\pi^2\mu}{4V\gamma} (R^4 - r_j^4) \quad (54)$$

where  $\tau_{sph}$  is the time needed for the droplet to spherodize (in seconds),  $\mu$  is the viscosity of the molten metal (in N·s·m<sup>-2</sup>),  $V$  is the volume of the droplet (in m<sup>3</sup>),  $\gamma$  is the surface tension (liquid-gas) of the molten metal (in Nm<sup>-1</sup>),  $R$  is the radius of the droplet after the spherodization and  $r_j$  is the radius of the cylindrical jet (assume the length to diameter ratio is  $2^{1/2}\pi$  according to Rayleigh's theory) before spherodization.

For a  $5 \times 10^{-4}$  m aluminum droplet at 970 K, the surface tension under Ar is 0.875 N/m [Weast, 1968] and the viscosity  $1.1 \times 10^{-6}$  Pa s [Szekely, 1979]; the spherodization time is  $5 \times 10^{-7}$  seconds according to Equation (54). This is less than the step size (larger than 0.00001 sec) which was used in this model.

One should keep in mind that assumption (2) is not valid when the solidification time is shorter than  $\tau_{sph}$  or when the formation of oxides on the surface of the droplet prevents spherodization. However, it is a very reasonable assumption under most experimental conditions, i.e., atomization in an inert gas atmosphere.

The Biot number is obtained from  $Bi = hL_c/k = hD/k_d$ . For an Al droplet with velocity of 1 m/s and a diameter of  $5 \times 10^{-6}$  m, the Biot number is calculated to be  $2 \times 10^{-3}$ , which indicates that assumption (7) is reasonable.

The mathematical model of the cooling curve of a droplet will now be developed.

### 3.2 Model Formulation

The governing equation for the thermal history of the droplet undergoing no phase change is given by a heat balance shown in Equation (28). Substituting droplet diameter  $D$  and rearranging Equation (28) yields:

$$\frac{dT}{dt} = -\frac{6h}{D\rho C_p(T)} (T - T_a) \quad (55)$$

where  $T$  is the droplet temperature at any time  $t$ ,  $T_a$  is the ambient temperature in the atmosphere, and  $\rho$  and  $C_p$  are the density and specific heat of the droplet respectively.  $h$  is the convection heat transfer coefficient which can be calculated using Equations (29) and (30). Subsequently, the Reynolds and Prandtl numbers can be obtained from Equations (31) and (32) respectively. It is evident that the thermal history of a droplet will be a function of its free-fall velocity which now must be formulated.

Figure 3-1b shows that a free-falling droplet is subject to gravity, buoyancy, and drag forces. A model to determine the free-falling droplet velocity from Newton's second law was proposed by Guthrie, et al. [Guthrie et al, 1975] as follows:

$$V\rho \frac{du}{dt} = V(\rho - \rho_a) g - \frac{C_d A}{2} \rho_a u^2 \quad (56)$$

The effects of the "added force" and the "history term" based on Equation (33) are not taken into account. The term on the left-hand side is the mass of the droplet times the acceleration. The first term on the right-hand side is the gravity force minus the buoyancy force; the second term is the drag force which is opposite to the direction of

motion. Here  $V$  is the volume of the droplet,  $\rho$  is the density of the droplet,  $\rho_a$  is the density of ambient gas,  $g$  is the gravitational acceleration,  $u$  is the relative velocity between the droplet and the ambient gas (here we take  $u_a = 0$ , therefore  $u$  is taken as the droplet velocity),  $A$  is the cross-sectional area of the droplet,  $C_d$  is the drag coefficient which is a function of Reynolds's number, (Figure 2-16) [Szekely, 1979]. For the spherical shape and the Reynolds number range which are dealt with in this particular problem,  $C_d = 18.5/Re_D^{0.5}$  for  $2 \leq Re_D \leq 500$  [Szekely, 1979]. The Reynolds number was 20 to 100 for a  $3.3 \times 10^{-4}$  m Al-17wt%Cu droplet in the model.

Rearranging Equation (56) and substituting the droplet diameter  $D$  for  $V$  yields:

$$\frac{du}{dt} = \frac{\rho - \rho_a}{\rho_a} g - \frac{3}{4} \frac{\rho_a}{\rho} \frac{C_d}{D} u^2 \quad (57)$$

The velocity  $u$  can be expressed as:

$$\frac{dz}{dt} = u \quad (58)$$

where  $z$  is the height of the droplet position.

The numerical solution of Equations (55) and (29) to (32), including the modelling of the liquid-solid transformation, will be discussed in detail in sections 3.2 and 3.3. The solution of Equations (57) and (58) was solved numerically to define the complete droplet trajectory, i.e., velocity and free-fall height as a function of time. The thermal profile,  $T=T(z)$ , and cooling curve,  $T=T(t)$ , can then be obtained.

Euler's method was chosen to solve Equations (57) and (58), together with Equation (31) and the relationship between  $C_d$  and  $Re_d$  [Chapra and Canale, 1985] and



can be expressed as follows:

$$u_{i+1} = u_i + \left( \frac{\rho - \rho_s}{\rho} g - \frac{3}{4} \frac{\rho_s}{\rho} \frac{C_d}{d} u_i^2 \right) \Delta t \quad (59)$$

$$z_{i+1} = z_i + u_i \Delta t \quad (60)$$

$$C_d = 1.85 / Re_{Di}^{0.5} \quad (61)$$

and

$$Re_{Di} = \frac{\rho u_i D}{\mu} \quad (62)$$

The numerical solution together with phase change will be further discussed in Section 3.6. The issues of convergence and stability will also be addressed in that section.

### 3.3 Phase Change

Figure 3-2 is the phase diagram of the Al-Cu binary system. For the alloys 10wt% Cu (alloy 1) and 17wt%Cu (alloy 2), two phase transformations take place under equilibrium conditions. After the molten metal has cooled from the pouring temperature  $T_p$  to the liquidus temperature  $T_l$ , solidification begins and an aluminum-rich solid solution with up to 5.65% Cu in solution is formed as the temperature is cooled further. When

the droplet temperature reaches the eutectic temperature of 821 K, the eutectic phase transformation will take place in the remaining liquid with a composition of Al-33.2% Cu.

In practice, under non-equilibrium conditions, solidification undergoes five stages as shown in Figure 3-3:

- (1) Cooling of the liquid phase from the pouring temperature  $T_p$  to the nucleation temperature  $T_n$ .
- (2) Recalescence due to the latent heat releasing faster than removal of heat at the droplet surface.
- (3) Formation of the pro-eutectic phase.
- (4) Eutectic phase transformation.
- (5) Cooling stage in the solid particle after completion of solidification.

### 3.3.1 Stage I: Cooling in the Liquid Range, $T=T_p-T_n$ :

In this stage of cooling, the rate of heat dissipation from the droplet to its immediate vicinity is controlled simply by convection. Thus, the governing equation is Equation (57), where  $C_p$  is that of the liquid metal  $C_{pl}$ . The equation holds from the pouring temperature  $T_p$  until solidification starts at the given nucleation temperature  $T_n$ , which corresponds to a certain amount of undercooling  $\Delta T=T_l-T_n$ , where  $T_l$  is the liquidus temperature. Therefore the governing differential equation for cooling in stage I is:

$$\frac{dT}{dt} = -\frac{6h}{D\rho C_{pl}(T)} (T - T_a) \quad (63)$$

Around  $T_a$ , a partial step size (time) was used so that the temperature at that partial step size was exactly  $T_a$ . Similar stepping techniques were used for all of the other stages. The justification for choosing  $T_a$  will be discussed in Section 3.5.

### 3.3.2 Stage II: Recalescence, $T = T_a - T_c$ :

In this stage, since solidification starts at a nucleation temperature  $T_n$  with a certain amount of undercooling  $\Delta T$ , the rate of latent heat generation is very large. This amount of latent heat cannot be released quickly enough to the environment, through the surface of the droplet, by convection. As a result, the temperature of the droplet increases. Therefore, three kinds of heat are competing with each other in the recalescence stage. The first is the release of the latent heat generated due to the nucleation and growth of a solid phase from a molten metal. The release rate of latent heat is expressed as  $dq_1/dt$ . The second is the rate of heat used to heat up the droplet,  $dq_2/dt$ . The third one is the convection of heat to the environment through the surface of the droplet. This convection rate is  $dq_3/dt$ . The change of liquid-solid interfacial energy ( $2\pi r \gamma_{ls} dr/dt$ ) is neglected since it is much smaller than  $dq_1/dt$ . From the conservation of energy, we have for this stage:

$$\frac{dq_1}{dt} = \frac{dq_2}{dt} + \frac{dq_3}{dt} \quad (64)$$

The three terms in Equation (64) can be formulated according to the

aforementioned three physical processes as follows:

$$\frac{dq_1}{dt} = \rho V \frac{d\Delta H_{fs}}{dt} \quad (65)$$

or for a given  $T_s$ , according to equilibrium conditions, a certain solids fraction must be present. This is directly associated with a quantity of latent heat that must be released by the droplet for that assumed  $T_s$  and alloy composition:

$$\frac{dq_1}{dt} = \rho V \Delta H_{fs} \frac{df_s}{dt} \quad (66)$$

where  $\rho$  is the density of the droplet,  $V$  is the volume of droplet,  $\Delta H_{fs}$  is the amount of latent heat generated due to solidification of a solid fraction  $f_s$ , and  $\Delta H_n$  is the total amount of latent heat per unit mass of droplet. And Equation (67) can be expressed as [Holliday and Resnick, 1988],

$$\frac{dq_2}{dt} = \rho V C_{pm}(T) \frac{dT}{dt} \quad (67)$$

where  $C_{pm}$  is a function of temperature and is the average specific heat of the droplet which can be calculated from:

$$C_{pm}(T) = C_{ps}(T) f_s + C_{pl}(T) (1 - f_s) \quad (68)$$

where  $C_{ps}$  and  $C_{pl}$  are the specific heat of solid and liquid respectively. And,

$$\frac{dq_3}{dt} = hA_s (T - T_a) \quad (69)$$

where  $h$  is the heat transfer coefficient,  $A_s$  is the surface area of the droplet, and  $T_a$  is the ambient temperature.

If we assume a single internal nucleation event, then:

$$f_s = \frac{r^3}{R^3} \quad (70)$$

where  $r$  is the radius of the solidified fraction and  $R$  is the radius of the droplet including both solids and liquids, as shown in Figure 3-4.

Substituting Equation (70) into Equation (66) and expressing droplet volume  $V$  by droplet radius  $R$ , the re-arrangement of the equation yields:

$$\frac{dq_1}{dt} = 4\pi r^2 \rho \Delta H_{fs} \frac{dr}{dt} \quad (71)$$

where  $dr/dt$  can be taken as the growth velocity of the solid phase.

For small undercooling (e.g. less than 50 K), the growth velocity,  $dr/dt$ , can be calculated from Equations (48) and (49) so that:

$$\frac{dq_1}{dt} = 4\pi r^2 \rho \Delta H_{fs} B \Delta T \quad (72)$$

where  $\Delta T = T_i - T$  and

$$B = \frac{\beta D_L \Delta H_{fm}}{d_m \kappa T_m^2} \quad (73)$$

For larger undercooling (e.g. large than 50 K), substitute Equation (48) into Equation (72). Substitute Equations (71), (67), and (69) into Equation (64), express  $V$  and  $A_s$  by  $R$ , and rearrange to yield:

$$\frac{dT}{dt} = \frac{3r^2 B \Delta H_{ft} (T_l - T)}{R^3 C_{pm}} - \frac{3h(T - T_a)}{Rp C_{pm}} \quad (74)$$

Recalescence continues until the rate of heat accumulation in the droplet is equal to zero. Thus, the end of stage II occurs when:

$$\frac{dq_2}{dt} = 0 \quad (75)$$

or

$$\frac{dT}{dt} = 0 \quad (76)$$

at  $T=T_r$  (recalescence temperature, which is lower than liquidus  $T_l$ ). At that point, the droplet temperature does not increase any further.

### 3.3.3 Stage III: Cooling in the Liquid + Solid Range, $T=T_r \sim T_e$ :

As solidification continues, the liquid fraction decreases while the solid fraction increases. Their proportions are given by the phase diagram. Using the lever rule, the amount of equilibrium pro-eutectic phase can be calculated from the Al-Cu phase diagram as  $f_{sp}$ , which corresponds to the amount of latent heat,  $\Delta H_{sp}$ , at a specified temperature for a given alloy composition. This pro-eutectic phase transformation takes place preferentially until the semi-solid droplet temperature reaches the eutectic temperature and the composition of the liquid reaches the eutectic composition. The solidification model

for this stage is formulated as follows.

At the final moment of recalescence, the solid fraction can be calculated from Equation (70) as  $f_{sp}$ . Then the solid fraction which will solidify in stage III,  $f_{s(1-s)}$ , is given by:

$$f_{s(1-s)} = f_{sp} - f_{sz} \quad (77)$$

where  $f_{sp}$  is the total solid fraction before eutectic transformation. The corresponding amount of latent heat of solidification which will be released in stage III is then:

$$\Delta H_{f(1-s)} = f_{s(1-s)} \cdot \Delta H_{ft} \quad (78)$$

Now an effective heat capacity,  $C_p^*$ , is introduced in this stage:

$$C_p^* = \frac{\Delta H_{f(1-s)}}{T_r - T_e} \quad (79)$$

where  $(T_r - T_e)$  is the temperature change during stage III.

If the average specific heat in the liquid-solid range is expressed by  $C_{pl}(T)$  considering the liquid-solid proportion change but neglecting the composition change, then replacing  $C_p$  in Equation (55) by  $C_p^* + C_{pl}(T)$ , the governing equation in stage III is obtained:

$$\frac{dT}{dt} = - \frac{6h}{D\rho (C_p^* + C_{pl}(T))} (T - T_e) \quad (80)$$

The solid fraction is assumed to be linearly proportional to the temperature change:

$$f_s = f_{sz} + f_s(1-s) \frac{T_r - T}{T_r - T_e} \quad (81)$$

Thus Equations (80) and (81) apply until the droplet temperature reaches the eutectic temperature  $T_e$ .

### 3.3.4 Stage IV: Eutectic Transformation, $T=T_e$ , $f_s=f_{sz}-1$ :

In stage IV, a eutectic phase forms at a constant temperature. Since the latent heat is released at a constant temperature, the effective heat capacity method used in stage III is not applicable to the eutectic transformation. The governing equation for stage IV can be written in a similar way to Equation (28):

$$\rho V \frac{d\Delta H_f}{dt} = -hA_s (T_e - T_a) \quad (82)$$

where  $\Delta H_f$  is the latent heat of fusion. In this stage,  $\Delta H_{fp} < \Delta H_f < \Delta H_{ft}$ , where  $\Delta H_{ft}$  is the total amount of latent heat and  $\Delta H_{fp}$  is as defined in Section 3.2.3, and:

$$f_s = f_{sp} + (1 - f_{sp}) \frac{\Delta H_f - \Delta H_{fp}}{\Delta H_{ft} - \Delta H_{fp}} \quad (83)$$

Equations (82) and (83) describe the eutectic solidification which occurs until  $f_s=1.0$ .



### 3.3.5 Stage V: Cooling in the Solid Range, $T_s \leq T \leq T_a$ :

Once solidification is completed, the cooling of the particle in the solid range is governed by a small modification of Equation (55). Thus,

$$\frac{dT}{dt} = -\frac{6h}{D\rho C_{ps}} (T - T_a) \quad (84)$$

where  $C_{ps}$  is the specific heat of solid.

### 3.4 Model Formulation Summary

In summary, this model calculates the thermal profile of a molten metal droplet in the atomizer, formed at a pouring temperature  $T_p$  and an initial velocity  $u_0$ . As the droplet cools and solidifies, its velocity and trajectory are given by Equations (57) and (58). The droplet velocity affects the Reynolds number, which in turn affects the heat transfer coefficient,  $h$ . Thus, the droplet velocity and trajectory must be determined prior to solving for the droplet cooling curve. This was achieved using the following procedure.

Although the initial velocity of the droplet was not measured directly, the droplet velocity at the position about 0.33 m below the bottom of the crucible was measured using a high-speed shutter camera. Figure 3-5 shows the streak of a droplet movement taken in this manner. The lengths of the streaks were measured at different frames in the

videotape and averaged. The droplet velocity was obtained by the length of the streak divided by the shutter speed. Thus, the average droplet velocity corresponding to Figure 3-5 is 2.17 m/s. The accuracy of velocity measurement on the screen was estimated as 0.05 m/s, which will result in about 2 K/s difference in cooling rate calculation. The main velocity measurement error from the determination of which streak is for which particle size. The initial velocity of the droplet can be back calculated accordingly.

From this velocity information, the initial velocity of the droplet was back calculated using Equations (59) to (62). Figure 3-6 shows the velocity profile of a  $3.3 \times 10^{-4}$  m Al-17wt%Cu droplet profile. The velocity measured at the camera position was 2.17 m/s, corresponding to an initial velocity of 1.13 m/s. The droplet almost reached its terminal velocity at the bottom of the atomization tower. Should more research fund have been available, more video cameras could have been placed at various positions of the atomizer to verify the velocity profile.

A droplet emanating from the atomization nozzle cools in the liquid range from the pouring temperature,  $T_p$ , until it reaches the nucleation temperature,  $T_n$ , which corresponds to a certain amount of undercooling, during the first stage. The thermal history of the droplet is given by Equation (55). After nucleation, recalescence takes place until the droplet reaches the recalescence temperature,  $T_r$ , where recalescence ceases, since the rate of heat convected to the environment is equal to the rate of latent heat released during Stage II. The equation governing heat flow during stage II is given by Equation (64). Pro-eutectic solidification and cooling, stage III, occurs next, in the temperature range between  $T_r$  and the eutectic temperature,  $T_e$  (Equations (55) & (80)).

The solidification during eutectic transformation then follows at a constant temperature,  $T_e$  (Equation (82)), until the entire droplet is solid. The last stage of the solidification is simply the cooling of the powder until it reaches the ambient temperature,  $T_a$ , or the bottom of the atomizing chamber (Equation (84)). These ordinary differential equations must be solved numerically. The thermophysical properties of the alloy and the gas atmosphere must be known as well as the phase diagram of the alloy of interest. In the next section, the solution of this model will be applied to the Al-Cu alloy system.

### **3.5 Thermophysical Properties of Alloy and Gas Atmosphere**

The droplet velocity and cooling model will now be applied to calculating the cooling curves of Al-10wtCu and Al-17wtCu droplets. Since not all the thermophysical property data of these alloys are available, the properties of pure aluminum and copper will be used by calculating the weighted average of the properties of these elements (assumption number 10). These properties are listed in Table 3.1

The atomization experiments with Al-Cu alloys were performed in nitrogen atmosphere. Thus thermophysical properties of nitrogen are listed in Table 3-2:

**Table 3-1 Thermophysical Properties of Al-Cu Alloys**

Properties	Aluminum	Copper	Al-10wt%Cu	Al-17wt%Cu	Ref *
Density (kg/m <sup>3</sup> )	2702	8920	3320	3760	1
Molecular Weight (×10 <sup>-3</sup> kg)	26.98	63.55			1
Latent Heat of Fusion (J/mol)	273079	291304	274902	276177	1
Thermal Conductivity at 300 K (W/mK)	237	401	253	265	1
Specific Heat of Liquid C <sub>pl</sub> (J/kg/K)	1084.51	493.35	1025.4	984.0	2
Specific Heat of Solid C <sub>ps</sub> (J/kg/K)	765.35+0.4586T	355.87+0.09867T	724.4+0.4226T	695.7+0.3974T	2
Liquidus T <sub>l</sub> (K)			908	884	3
Eutectic Temperature T <sub>e</sub> (K)			821	821	3
Solid Fraction of Pro-eutectic f <sub>sp</sub>			0.8421	0.588	3
Latent Heat of Fusion for Pro-eutectic ΔH <sub>fp</sub> (J/kg)			319000	215000	1
ΔT <sub>max</sub> (50 ×10 <sup>-6</sup> m)(K)**	130	236	141	148	4
β	1	1	1	1	5
Activation Free Energy ΔG <sub>a</sub> (J/mol)	4.15×10 <sup>-20</sup>	6.6×10 <sup>-20</sup>			5
Diffusion Coefficient D <sub>0</sub> (m <sup>2</sup> /s)***	2.0×10 <sup>-7</sup>	0.8×10 <sup>-7</sup>			5

\* 1-Weast et al, 1988; 2-Wicks and Block, 1963; 3-Lyman et al. 1973; 4-Turnbull, 1950; 5-Clyne, 1984.

\*\* Maximum undercooling for 50 ×10<sup>-6</sup> m droplets

\*\*\* D<sub>0</sub> is used to calculate D<sub>i</sub>=D<sub>0</sub>exp(-ΔG<sub>a</sub>/κT)

**Table 3-2 Thermophysical Properties of Nitrogen at Atmospheric Pressure**

<b>Properties</b>	<b>Values</b>	<b>Reference</b>
<b>Density (kg/m<sup>3</sup>)</b>	<b>1.2506</b>	<b>Weast, 1988</b>
<b>Viscosity (Pa s)</b>	<b>1.781×10<sup>-5</sup></b>	<b>Weast, 1988</b>
<b>Thermal Conductivity (W/mK)</b>	<b>0.0261</b>	<b>Weast, 1988</b>
<b>Temperature (T<sub>0</sub>) (K)</b>	<b>293</b>	

### 3.6 Numerical Solution of Droplet Cooling

The solution of the thermal profile and the cooling curves of different sizes of droplets atomized at different temperatures can be readily calculated numerically. A fourth-order Runge-Kutta method was chosen to solve each of the ordinary differential equations formulated in Section 3.2. It is a widely used method with the truncation error proportional to the fourth power of the step size. The discretization and solution of the ODE's will be discussed using Equation (55) as an example. Using the fourth-order Runge-Kutta method, Equation (55) is expressed as follows [Chapra and Canale, 1985]:

$$T_{i+1} = T_i + \left[ \frac{1}{6} (k_1 + 2k_2 + 2k_3 + k_4) \right] \Delta t \quad (85)$$

where  $T_{i+1}$  is the temperature at the (i+1)th step,  $T_i$  the temperature at the ith step,  $\Delta t$  the time step size, and

$$k_1 = -\frac{6h_{i+1}}{D\rho C_{p1}(T_i)} (T_i - T_a) \quad (86)$$

$$k_2 = -\frac{6h_a}{D\rho C_{p1}(T_i + \frac{1}{2}k_1\Delta t)} (T_i + \frac{1}{2}k_1\Delta t - T_a) \quad (87)$$

$$k_3 = -\frac{6h_a}{D\rho C_{p1}(T_i + \frac{1}{2}k_2\Delta t)} (T_i + \frac{1}{2}k_2\Delta t - T_a) \quad (88)$$

$$k_4 = -\frac{6h_{i+1}}{D\rho C_{p1}(T_i + k_3\Delta t)} (T_i + k_3\Delta t - T_a) \quad (89)$$

where  $h_i$ ,  $h_{i+1}$ , and  $h_m$  are the heat transfer coefficients at the  $i$ th step,  $(i+1)$ th step, and  $(i+1/2)$ th step respectively. A partial step size was used for the transition from one stage to the next stage to reduce the amount of error that would occur during the calculation. Similarly, Equation (74) was discretized for the recalescence range, Equation (80) for the cooling in the liquid + solid range, Equation (82) for the eutectic transformation, and Equation (84) for the cooling in solid range using the fourth-order Runge-Kutta method.

The numerical model was written in FORTRAN 77 as shown in Appendix A and compiled using Microsoft Fortran compiler V5. The program was executed on a 33 MHz PC running DOS v6.2. The solution conditions required to obtain a convergent and stable solution were determined. Accuracy increases with decreasing step size from 0.01 s to 0.00005 s for the four stages of cooling other than the recalescence stage. Due to the very short period of time it takes to complete recalescence, stage II, a much smaller step size is used in this stage than for the other stages. This new step size,  $\Delta t_{\text{new}} = \Delta t/f$ , for the recalescence range is obtained by using the step size,  $\Delta t$ , divided by a step size factor,  $f$ , which is larger than 1. If the new step size is too large (e.g.,  $\Delta t_{\text{new}} = 1 \times 10^{-4}$  s), the system will be unstable. For example, for a  $3.3 \times 10^{-4}$  m Ai-17wt%Cu droplet with 30 K undercooling, 100 K superheat, and 1.13 m/sec initial velocity, the system will become unstable if the new step size in the recalescence range is larger than  $1 \times 10^{-4}$  s. The accuracy increases with decreasing step size until the round off error becomes significant. This occurs when the new step size is  $\Delta t_{\text{new}} < 1 \times 10^{-5}$  sec for this example. It now remains

to show how the nucleation or undercooling temperature was determined.

### 3.7 Nucleation Temperature

According to Figures 2-10 to 2-12, the relationship between undercooling,  $\Delta T$ , and the cooling rate,  $T_c$ , can be approximated by:

$$\ln \Delta T = a_3 + b_3 \ln T_c \quad (90)$$

Substituting Equation (26) into Equation (90) yields:

$$\ln \Delta T = a_3 + \frac{b_3}{b_1} \ln a_1 - \frac{b_3}{b_1} \ln \lambda_2 \quad (91)$$

We next obtain Equation (92) by substituting Equation (27) into Equation (91):

$$\ln \Delta T = a_3 + \frac{b_3}{b_1} \ln a_1 - \frac{b_3}{b_1} \ln (a_2 D^{b_2}) \quad (92)$$

which can be re-written as:

$$\ln \Delta T = a_4 + b_4 \ln D \quad (93)$$

where  $a_4$  and  $b_4$  are constants.

According to Turnbull [Turnbull, 1950], the maximum amount of undercooling,  $\Delta T_{\max}$ , was measured for  $5 \times 10^{-5}$  m diameter pure aluminum and copper metals, while the amount of undercooling for  $1 \times 10^{-6}$  m<sup>3</sup> droplets was taken as  $0.05 \Delta T_{\max}$ . Substituting the values of  $D = 5 \times 10^{-5}$  m and  $1/6 \pi D^3 = 1 \times 10^{-6}$  m<sup>3</sup>, and  $\Delta T_{\max}$  values from Table 3-1,  $a_4$  and  $b_4$  were obtained as -0.385 and 0.543 respectively for Al-17wt%Cu, and -1.428 and -0.644



respectively for Al-10wt%Cu alloy.  $\Delta T(D)$  can then be calculated for each alloy and each particle size. Considering the impurities in the alloy, the  $\Delta T(D)$  values used in the model were one third of those calculated according to Equation (93).

As will be shown in Chapter 6 and Chapter 2, SDAS is affected by cooling rate. Figure 3-7 shows the effect of undercooling on the SDAS of a  $3.3 \times 10^{-4}$  m Al-17wt%Cu droplet with 100 K superheat, as a result of the effect of undercooling on the cooling rate. As shown in Figure 3-7, the SDAS decreases with increasing undercooling. The result is reasonable since larger undercooling can result in a higher cooling rate, hence smaller SDAS. Therefore, the model is affected by undercooling and the results have the right trend. However, the model is not extremely sensitive to the undercooling; a small change in undercooling does not change the modelling results significantly.

In this model, Equation (48) was used to calculate the growth rate, which is valid for small undercooling only. The model can be improved by using Equation (47) for larger undercooling and by the future work proposed in Chapter 7. More representative modelling results could be obtained when accurate thermodynamic data are available.

Figure 3-8 shows the temperature profile of an Al-17wt%Cu droplet of  $3.3 \times 10^{-4}$  m in diameter calculated by a FORTRAN PROGRAM THERMAL (Appendix A). The amount of undercooling was assumed to be 53 K according to Equation (93). The step size of stages I and III-V was 0.01 s, while the step size used in stage II was  $2 \times 10^{-5}$  s. Figure 3-9 shows the change of solid fraction at different positions of the tower under the same conditions as in Figure 3-8. This information is useful for the application of spray deposition of IAP. It clearly shows at what positions of the tower the droplet begins to

solidify, finishes solidification, and reaches the desired fraction of solid.

Figure 3-10 shows the change of the heat transfer coefficient with time as the droplet travels down to the bottom of the atomization tower. It indicates that under IAP conditions the heat transfer coefficient is smaller than that of gas atomization [Stone and Tsakiroopoulos, 1992].

Figure 3-11 shows the cooling curve of a  $3.3 \times 10^{-4}$  m droplet with 100 K superheat. The amount of undercooling assumed is 53 K. The back calculated initial velocity is 1.13 m/s, and the step size used in the numerical calculation is 0.01 s for all of the stages except stage II, where  $2 \times 10^{-5}$  s is used. The droplet solidification corresponds to an average cooling rate of 499 K/s.

The cooling curve of another droplet of a different size ( $4.6 \times 10^{-4}$  m in diameter) atomized under the same conditions is shown in Figure 3-12. The step size used in this calculation was the same as that in Figure 3-11; the undercooling used was 44 K according to Equation (93). The corresponding average cooling rate obtained was 304 K/s.

Similar results for other particle sizes and Al-10wt%Cu alloy were also obtained using a FORTRAN program as shown in Appendix B. Those results will be presented in Chapter 6.

## **CHAPTER 4:           EXPERIMENTAL**

**In this chapter, the experimental apparatus for the Impulse Atomization Process will be described. This device was designed and manufactured at the University of Alberta. The experimental procedure developed for atomization using this apparatus will then be described, and finally, the methods used for powder characterization, microstructural explanation, and image analysis will be presented.**

### **4.1     Impulse Atomization Apparatus**

**In this section, the layout of the Impulse Atomization apparatus will be briefly explained to provide an overall idea of how the system works; the apparatus design will then be further described in more detail.**

**Figure 4-1 is a photograph of the Impulse Atomization apparatus and Figure 4-2 is a schematic drawing of the apparatus. There are five principle components to this apparatus: (1) the melting part, in which different kinds of metals and alloys are melted; (2) the vibration system, by which the Impulse Atomization Process is carried out; (3) the adjusting system, which allows the precise control of conditions under which atomization occurs; (4) the environmental chamber, in which the atomization takes place under the desired atmosphere; and (5) the monitoring system, which allows one to**

observe and record the atomization process.

In the melting system, a furnace melts the charge placed inside a crucible. This furnace can be either a resistance or induction furnace. The crucible is made of an appropriate ceramic material. In these experiments high density, high purity alumina was used. A thermocouple is placed inside the crucible to monitor the melt temperature.

Once the material inside the crucible is melted, it can be pushed by the vibration system through the holes in the nozzle plate using the impulse applicator. A discontinuous force is repeatedly applied to the fluid in the direction of the openings. The force is sufficient to impel the fluid through the openings as discrete elongated fluid segments. The impulse applicator is connected to the plunger by a piece of threaded aluminum rod. The frequency of the pulsator is controlled by a function generator and the amplitude of vibration varied using the voltage of the amplifier.

A frame was designed and constructed to hold the furnace, crucible, and pulsator as well as to precisely control the relative position between the impulse applicator and the nozzle plate. The stainless steel atomizing chamber can be evacuated and back filled with the desired gas, such as an inert gas. An oxygen analyzer determines the oxygen content in the chamber.

Movement of droplets produced by Impulse Atomization Process is viewed and recorded through viewing ports on the tower using a high-speed shutter video camera. Powders are collected at the bottom of the tower.

#### **4.1.1 Furnace**

Either a resistance or induction furnace was used to melt the charge in the crucible. A heating element for the resistance furnace was wound into a cylindrical shape and held in place with castable cement. A K type thermocouple was cemented to the inner wall of the cylindrical heating element. This furnace was controlled by a temperature controller up to 1070 K.

For melting and atomizing higher melting point alloys, an induction furnace was used. Since the alumina crucible is a poor heat conductor, a graphite susceptor was placed between the crucible and the induction coil to ensure more efficient and uniform heating. In order to avoid direct contact between the induction coil and the graphite susceptor, alumina powder was cast into a cylindrical shape and this alumina collar was wrapped around the graphite susceptor. The castable alumina powder contained 90-95% of alumina. A Locon blanket from Fiberfrax Ceramic Fibre Products was placed around the induction coil to provide further insulation to the furnace. A piece of fire brick was used underneath the induction furnace-crucible assembly, in order to insulate the frame of the tower from the assembly.

#### **4.1.2 Crucible**

Since the crucible used for the resistance furnace is different from that for the induction furnace, two kinds of procedures were used for fabricating the crucibles.

The crucible for the resistance furnace was made of either an alumina tube ( $44 \times 10^{-3}$  m ID,  $50 \times 10^{-3}$  m OD, and  $100 \times 10^{-3}$  m long) or an alumina crucible ( $54 \times 10^{-3}$  m ID,  $60 \times 10^{-3}$  m OD, and  $105 \times 10^{-3}$  m long) with a  $41 \times 10^{-3}$  m diameter hole cut in the bottom and an alumina disc with holes. These two pieces were cemented together using an adhesive. The alumina disc with holes is called the nozzle or nozzle plate. This crucible-nozzle combination is good for the resistance furnace up to  $500^{\circ}$  C.

Holes of various patterns were drilled in the alumina nozzle plate. A number of hole patterns can be machined in the nozzle plate, as shown in Figure 4-3 a, b, c and d. The holes were examined before use. Since the holes were often not perfectly round, the average hole sizes were calculated based on two measurements taken in perpendicular directions at the exit end of the orifice.

#### **4.1.3 Impulse Applicator**

The impulse applicator consisted of an alumina tube cemented to an alumina disc. The impulse applicator was dried and cured using a procedure similar to that used for the crucible. The impulse applicator was then connected to the pulsator. Convective cooling, as required, was supplied by a fan directed towards the ceramic tube and alumina rod connection point.

#### **4.1.4 Pulsator and Its Controlling System**

There are a number of mechanisms available to provide the impulse force and frequency desired for IAP. These devices range from mechanical to electromagnetic in design. The work described in this thesis is based on the use of an electromagnetic device with a frequency range from 10 Hz to  $20 \times 10^3$  Hz. The two pulsators, also called impulse generators (A and B), were supplied by the same manufacturer but had slightly different characteristics.

The pulsator was driven by an amplifier which was connected to a function generator. The amplifier was linked with a regulated power supply. The function generator can generate different kinds of wave patterns, such as sine and square waves. Sine waves were used for the present work. The frequency of the pulsator was controlled by the function generator with an accuracy of  $\pm 1$  Hz. The absolute amplitude of the pulsator was not measured, however the relative amplitude was recorded as a percentage of the maximum amplitude supplied by the pulsator together with the power supply and amplifier at a specific frequency. This relative amplitude was controlled with the aid of a volt potential meter.

#### **4.1.5 Frame**

A frame was designed to hold and align the pulsation system. This frame consists of three threaded rods connected to three steel plates at different levels. The threaded

rods were screwed into the bottom plate. The rods then went through the holes in the middle and top plates. The middle and top plates can be moved up and down and levelled as desired.

The top plate holds the pulsator and a heat exchanger. A hole in the top plate allows the pulsator to be clamped to the plate using an adjustable circular clamping band. The top plate can be moved up and down along the threaded rods to allow precise adjustment of the relative position between the pushing unit and the crucible both in the horizontal and vertical directions.

The middle plate holds and clamps the crucible very tightly. A refractory collar between the crucible and the circular clamp both limits heat conduction and increases the friction between the crucible and the clamp. The crucible can be positioned in the horizontal plane as desired.

The third plate holds the furnace as mentioned above. Both induction coils and some of the cooling tubes also run through this plate. Additional cooling systems were installed so that the apparatus could be operated at temperatures up to 1900 K.

#### **4.1.6 Shell**

The shell of the atomization chamber is mainly made of  $3 \times 10^{-3}$  m thick stainless steel. It consists of four parts: a crane-operated removable cap; a centre section with all the wire connectors and gas and water inlets and outlets; a middle section with viewing and monitoring equipment; and a bottom section for collecting powder.



The cap of the atomizing chamber was designed to be easily removed and reattached to permit access to the top section of the atomizer. It allows the adjustment of the pulsation system at the upper part of the tower and is crane-operated. A window of 0.21 m in diameter is open in the cap, can be sealed, and allows quick access, when needed, to the top part of the tower during or between atomization trials. For example, it can be used for adding more raw material during a run. A safety valve was installed on the cap to release the pressure of the tower if the overpressure was above  $70 \times 10^3$  Pa. A three-way valve was also installed on the cap; it directs the connection of the tower to either to the gas supply or the vacuum pump, or it can simply be used to shut the connection to both vacuum and gas lines.

Connections of thermocouple, pulsator, electrical light source, cooling water inlets and outlets, cooling gas inlet for the pulsator, and the induction cables enter the tower through the centre section. Four small windows are located in the top part of this section for viewing and monitoring the atomization process, with a camera holder installed right above one of the windows. The glass windows are  $9 \times 10^{-2}$  m in diameter.

The bottom section of the atomizing chamber consists of a cylindrical-shaped shell and a stainless cone which was designed to guide the droplets toward the powder collector at the bottom of the tower. The powder collector is removable. It can also contain various kinds of fluids for quenching the powder. A two-way valve was installed on this powder collector to either shut off or connect to a T connector which is connected to either a gas outlet or the oxygen analyzer.

#### **4.1.7 Monitoring System**

Four small viewing ports are positioned in the middle section of the atomization chamber as mentioned in the last section. These ports are used for directing light into the tower, viewing the droplet spray and photographing the spray. Specifically, the droplet movement is monitored by a SONY high-speed shutter CCD colour video camera, model number DXC-151. It uses 12 V, 1 A DC which is converted by a camera adaptor (SONY, CMA-D1) to the regular electrical source of 120 V ac, 60 Hz. The camera has 768 x 493 picture elements, ensuring a high resolution image. A clear picture can be obtained even when shooting a rapidly moving object or shooting in low light. Its electronic shutter has nine speed settings: 1/125, 1/250, 1/500, 1/1000, 1/2000, 1/4000, and 1/10000 second, which enable us to measure the droplet velocity. The video camera is fixed to the camera holder and operates at a filming rate of 30 frames/second.

The droplet movements are recorded on Super VHS SONY VCR. This VCR can play the videotape frame by frame to allow the off-line measurement of the droplet speed. An Amdek monitor (Video-300A) is used to view droplet movement.

Thermocouples are used to measure the temperature of the melt in the crucible, the temperature inside the tower in the vicinity of the pulsator, or the temperature at other places such as the powder collector, if needed.

When the atomization chamber is under positive pressure, the valve directing the gas into the oxygen analyzer is open and oxygen content in the atomization tower can be measured. The oxygen analyzer (Centorr Model 2A) uses 120 V voltage and 1400 W

power. The maximum pressure allowed for the analyzer is  $5 \times 10^5$  Pa which is well beyond our working range.

## **4.2 Impulse Atomization Process**

First of all, the distance from the plunger to the nozzle plate was adjusted to the desired value with the adjusting system described in Section 4.1.5. After a thermocouple was placed in the crucible at a fixed position, solid metal was put in the crucible. A piece of stainless steel foil was used to cover the crucible. An insulating cover was then placed on the stainless steel cover. These covers insulate the junction of the impulse applicator and aluminum connector and also help keep the temperature of the crucible more uniform. The third use of these covers is to keep metal or alloy inside the crucible when splashing occurs under very high amplitude conditions. The atomizer was then closed, sealed, evacuated, and backfilled with inert atmosphere if desired. The oxygen level in the atomizing chamber was monitored by an oxygen analyzer (Model 2A).

After turning on all the cooling systems, the metal or alloy was then melted by the induction or resistance furnace. The furnace was heated at a rate of 0.33 K/s until the metal was melted to the desired atomization temperature. Normally the furnace was kept at the atomization temperature for about 1200 seconds before atomization.

The amplitude of the function generator and the potentiometer of the amplifier were adjusted to the desired degree of relative amplitude. The time for the start of the experiment was recorded. The photographic recording system was turned on and the

shutter speed of the video camera was adjusted as desired.

When the shutter speed of the video camera was very high (e.g., 1 picture per 1/10000 s), a spherical droplet appeared as a spherical dot on the monitor. However, when a low shutter speed (e.g., 1 picture per 1/500 s) was used, a streak was visible on the monitor. The lower the shutter speed, the longer the streak. The length of the streak is a function of the shutter speed and droplet velocity. Therefore, subsequent to the experiments, the droplet velocity can be calculated based on measurements of the streaks on the videotape.

Droplet velocity = streak length (in m)\*shutter speed (in s<sup>-1</sup>).

Using a standard grid pattern, it was found that the image at the edges of the monitor was distorted. The pictures at the centre of the monitor up to within  $25 \times 10^{-3}$  m of the edge of the monitor had minimum distortion. Streak measurements were performed in this area. Furthermore, it was also observed that in this region of minimum distortion, the streak intensity varied. Since the atomized metal droplets often formed a cone of droplets, the droplets would frequently have different depths of field at the filming height thereby reflecting light differently. By choosing the streaks having similar intensity, it was likely that they would be from droplets at a similar position within the spray stream. At different depths of field, different magnifications were shown in the videotaped pictures. By choosing the streaks from a similar position in the spray stream, the error from different magnifications was minimized. Given a fixed position for the video camera and the same zoom lens, the magnification was fixed and could be checked by videotaping a ruler.

Following atomization, the powders collected at the bottom of the atomizing chamber were prepared for characterization.

### **4.3 Powder Characterization**

A number of measurements were made to characterize the atomized powder. These included weight, bulk density, flowability, size distribution, and shape.

Powders collected at the bottom of the atomizer were weighed. The atomization throughput was calculated by dividing the measured weight by the production time. The apparent density and flowability were measured according to Metal Powder Industries Federation Standards Test #04 [MPIF Standard 04] or #28 [MPIF Standard 28] and #03 [MPIF Standard 03] respectively. The apparent density measurement for free-flowing powders was carried out using a Hall meter [MPIF Standard 04]. However, because some of powders made by IAP are very big and/or have an irregular shape, the apparent density had to be measured using the Carney apparatus for non-free-flowing metal powders [MPIF Standard 28]. Flowability was measured only for those samples that could freely flow through the Hall flow meter.

Sieve analysis was also done according to MPIF Standard 05 [MPIF Standard 05]. Since, in some cases, the total amount of sample was less than 0.1 kg, analysis was performed using the whole lot rather than 0.1 kg. The sieve analysis results were reported using Log-normal plots [Boyko and Henein, 1993] to determine the geometric mean size and the geometric standard deviation of a powder size distribution. Powder shape was

examined using a Hitachi S-2700 Scanning Electron Microscope (SEM) .

#### **4.4 Microstructure Characterization**

To understand the characteristics of this new atomization technique, the microstructure of the IAP powder was examined and compared with that obtained in other atomization processes. Most of the powders examined had low melting points, therefore cold mounting was used to limit the possibility of recrystallization during the preparation of samples. Sealtronic epoxy resin was mixed with hardener at a ratio of 2:1 by volume or 2.2:1 by weight and stirred slowly (to eliminate the generation of bubbles) for about 1800 s. The epoxy mixture was allowed to set for about 30 minutes to eliminate any of the bubbles generated during the mixing process. Powders of different sieving ranges were placed in separate moulds and then the epoxy mixture was poured into each mould. The samples were cured for 24 hours. No appreciable increased temperature was measured during the curing process. After curing, the samples were taken out of the moulds (this was not necessary if a piece of plastic tube was used) and ground with successively finer silica-sand paper from 240 to 600 grit. After grinding, a rough polishing was performed using 6  $\mu\text{m}$  diamond paste on an automatic polishing wheel at low speed for aluminum-copper alloys. For the lead-tin alloy, rough polishing was done manually on a small polishing wheel with  $6 \times 10^{-6}$  m diamond paste.

Final polishing was done using  $3 \times 10^{-7}$  m alumina paste on the automatic polishing wheel at high speed for aluminum-copper powders. Intermediate polishing was

performed on a small polishing wheel manually with  $3 \times 10^{-7}$  m alumina paste for lead-tin alloy powders. Final polishing for lead-tin alloy powder was done by using colloidal silica (pH=9.8). After polishing, the surface of the specimen was immediately given a water wash.

For lead-tin alloy powder, the following etchant was prepared:  $80 \times 10^{-6}$  m<sup>3</sup> glycerol mixed thoroughly with  $10 \times 10^{-6}$  m<sup>3</sup> nitric acid and  $10 \times 10^{-6}$  m<sup>3</sup> acetic acid. The mixture was then heated to 311-315 K and the samples etched for about 300 s. For aluminum-copper alloy powder, diluted Keller's reagent [Lyman, 1973] was used that is, dilute Keller's reagent 1:1 with water. The Keller's reagent is a mixture of  $2 \times 10^{-6}$  m<sup>3</sup> HF (48%),  $3 \times 10^{-6}$  m<sup>3</sup> HCl (concentrated),  $5 \times 10^{-6}$  m<sup>3</sup> HNO<sub>3</sub> (concentrated), and  $190 \times 10^{-6}$  m<sup>3</sup> water. The sample was immersed in the reagent for about 10 s.

After etching, samples were examined under an optical microscope. For the samples that were intended to be examined in the SEM, over etching was necessary. Samples were then carbon-coated and examined in the SEM. For large powders, the microstructure in different areas such as in the centre part of the powder, at the edge of the powder, and in the small section (those powders not ground to the centre section yet) were examined. Both pictures and digitized images were taken for the areas of interest. The digitized images were converted into TIFF files which were then used for image analysis.

Dendrite arm spacings were measured either manually or using an image analyzer. The procedure of image analysis will be described in the next section.

#### **4.5 Image Analysis**

**Image analysis of a microstructure was performed with a software package named Optimas v3.01 [BioScan, 1991], an image analysis toolbox. It can be used for both image processing and image measurement. In order to measure the Secondary Dendrite Arm Spacing, the digitized image obtained from the SEM was processed so that the eutectic regions appeared black and the dendrites white. Then the white dendrites were shrunk into a skeleton of the dendritic structure by the SkeletonizeFilter function in Optimas. This function reduces background objects (white dendrites) in an image to a series of line segments by eroding the binary image to single pixel wide line segments. A line was drawn across a number of Secondary Dendrite Arms. The luminance of the points of intersection between the line drawn and the Secondary Dendrite Arm skeleton was high, while in the other parts low. A FORTRAN program, as shown in Appendix D, was written to distinguish the points of intersection based on luminance measurements made on the imaging system, to calculate the coordinates of the points of intersection, and to calculate the Secondary Dendrite Arm Spacings based on the coordinates of the points of intersections.**

**These measured Dendrite Arm Spacings were compared with those reported in the literature from other powder-making techniques, such as gas and centrifugal atomization. In addition, the measured Secondary Dendrite Arm Spacings were compared with those predicted from cooling rate calculations from a specific alloy. The predictions were obtained using the model described in Chapter 3.**



#### **4.6 Summary**

**The apparatus and the powder characterization described above were used to study the effect of operating parameters such as applied frequency and relative amplitude (or acceleration of the impulse applicator), nozzle-impulse applicator distance, orifice size of the nozzle, viscosity of the melt, melt superheat, and oxygen content, on the following powder and process characteristics: size, size distribution, alloy throughput, droplet velocity, microstructure, powder flow rate, apparent density, and powder shape. These studies will be described in the next chapter.**

## **CHAPTER 5: OPERATING VARIABLES OF IAP - RESULTS AND DISCUSSION**

Operating parameters, such as frequency, relative amplitude, orifice size, nozzle-impulse applicator distance, superheat, oxygen content, number of orifices, and crucible bottom to pulsator distance will profoundly influence the quality of powders. However, the effect of these parameters is more empirical knowledge than theoretical understanding. In this chapter, the effects of several operating variables on powder size and size distribution, powder shape, and throughput of droplets produced by IAP will be presented and discussed. Furthermore, the effect of viscosity for highly viscous melts will also be presented and discussed. These results will clearly illustrate the flexibility of the IAP to generate droplets of desired characteristics. The disintegration mechanism of liquid jets from a capillary will be presented. The disintegration mechanism of IAP will also be proposed and compared with those for continuous jet and drop-on-demand methods. Finally the advantages of IAP will be summarized.

### **5.1 Accuracy in Measuring Atomizing Variation**

In this thesis, all geometric mean particle sizes and standard deviations were calculated using a log-normal spreadsheet procedure developed by Boyko and Henein [Boyko and Henein, 1993]. In this procedure, the cumulative particle size distribution of

the screen analysis was calculated using a spreadsheet package. Then the log-normal probability distribution function was calculated based on a series approximation of 16 terms. The geometric mean particle size,  $d_{50}$ , was calculated after the rendition of the distribution to a "Gaussian" distribution. The geometric standard deviation,  $\sigma_g$ , was calculated from the ratio of  $d_{84}$  to  $d_{50}$ .

Figure 5-1 shows two typical log-normal plots of Zn-0.05wt%Pb alloy atomized by IAP. The nozzles used for both experiments were composed of a linear array of seven holes as shown in Figure 4-3b with a nominal hole size of  $5 \times 10^{-4}$  m. The frequency used was 200 Hz, while the relative amplitude used was 29% of the maximum supplied by the impulse generator A. The separation distance between the nozzle (bottom of the crucible) and the impulse applicator was about  $1.3 \times 10^{-3}$  m. Droplets were atomized at 810 K and 820 K into a nitrogen atmosphere which contained 200 ppm oxygen and 160 ppm oxygen in Figure 5-1a and 5-1b, respectively. The results, presented in Figure 5-1a and 5-1b, show geometric mean sizes of  $6.79 \times 10^{-4}$  m and  $6.60 \times 10^{-4}$  m. They are within  $2 \times 10^{-5}$  m. The geometric standard deviations of powders from these two runs were 1.44 and 1.46, a difference of 0.02. The results indicate good reproducibility. Droplets were spherical in both experiments.

Similarly, two experiments for Zn-0.05wt%Pb were performed using a smaller nominal hole size of  $1.5 \times 10^{-4}$  m (1 hole in the centre as shown in Figure 4-3a). The alloy was atomized at 790 K using a frequency of 100 Hz and a relative amplitude of 57% maximum. The droplets were atomized into nitrogen containing 200 ppm oxygen in one run and 250 ppm oxygen in the other run. The nozzle to impulse applicator

distance was  $1.7 \times 10^{-3}$  m in both runs. The corresponding geometric mean size was  $3.53 \times 10^{-4}$  m for the first run and  $3.69 \times 10^{-4}$  m for the second, while the geometric standard deviation was 1.22 and 1.25 respectively. The change of geometric mean size was within  $2 \times 10^{-5}$  m and the change of geometric standard deviation was 0.03, which agreed with the results obtained using a larger nozzle size. Therefore, the Impulse Atomization technique yields good reproducibility of particle size and size distribution within 5%.

The results presented in this section show a good reproducibility of the Impulse Atomization Process. The experimental parameters can normally be controlled quite precisely. The accuracy of frequency control is  $\pm 0.1$  Hz and the accuracy of relative amplitude control is 2% maximum. The oxygen content reading panel is a log scale with a reading accuracy within 5%. The theoretical value of accuracy for nozzle-impulse applicator distance is  $7 \times 10^{-6}$  m as described in Chapter 4. The temperature reading is  $\pm 0.1$  K while the control of the temperature in the induction furnace is normally within 10 K. The orifice size of the nozzle can be manufactured within the accuracy of  $\pm 2 \times 10^{-5}$  m in most cases in this work and it can normally be measured accurately within  $5 \times 10^{-6}$  m.

## **5.2 Effect of Frequency**

With a nozzle having a nominal hole size of  $5 \times 10^{-4}$  m in a square pattern of 37 holes as shown in Figure 4-3c, Pb-12wt%Sn alloy was atomized at 670 K in air. It is seen in Figure 5-2 that the geometric mean size decreases from 1123 to  $899 \times 10^{-6}$  m with

increasing frequency from 120 Hz to 240 Hz, while the geometric standard deviation increases from 1.34 to 1.49. The experiments were performed at approximately the same acceleration conditions as will be shown in Section 5.4.

Only a small range of frequencies were studied (120-240 Hz). Appendix C shows the resultant acceleration of the impulse generator for each applied frequency. Since the acceleration of impulse generator B is nearly unchanged in the range of frequencies from 120 Hz to 240 Hz, it was chosen to study the effect of frequency on size and size distribution of the droplets produced by this vibrator.

The wavelength,  $\lambda$ , is obtained from:

$$\lambda = \frac{u}{f} \quad (94)$$

where  $u$  is the velocity of the discontinuous stream and  $f$  is the frequency of the vibrator applied to the discontinuous stream.

Using high-speed video photography (Chapter 4) and a mathematical model (Chapter 3), it was determined that the initial velocity of the droplets was of the order of 1 m/s.

It was assumed that the stream diameter is equal to the orifice diameter of the nozzle. The minimum velocity to form a  $5 \times 10^{-4}$  m continuous jet is 1.6 m/s according to Equation (23). The actual jet velocity in these experiments were not measured but was estimated about 1 m/s. According to Rayleigh's theory (Equation (4)), the optimum wavelength for a discontinuous stream diameter of  $5 \times 10^{-4}$  m is therefore  $2.22 \times 10^{-3}$  m. This corresponds to an optimum frequency of about 730 Hz for generating monodispersed

droplets. Clearly, the neither velocity nor the frequencies used in these experiments were optimized. As a result, the droplets formed were not monodispersed but had a distribution as seen in Figure 5-1.

In addition, a discontinuous stream with an exit velocity of 1 m/s at an applied frequency of 120-240 Hz, yielded a wavelength of 8.3 to  $4.2 \times 10^{-3}$  m. This range was clearly larger than the critical wavelength of  $1.5 \times 10^{-3}$  m ( $\lambda_c = \pi d$ ). Recall that for  $\lambda < \lambda_c$ , the segments of fluid will spherodize into a single droplet. Thus, we would expect that each segment will break-up into multiple droplets. This will be shown again in Section 5.13.

### 5.3 Effect of Relative Amplitude

Although the absolute amplitude applied by the pulsator was not measured, the relative amplitude of the impulse applicator was controlled and recorded as the percentage of the maximum amplitude achievable by the pulsator at a given frequency. To study the effect of relative amplitude on the geometric mean size and geometric standard deviation, Sn-15wt%Pb alloy was atomized at 640 K in a nitrogen atmosphere with 100 ppm oxygen content. For these experiments the atomizing nozzle was comprised of a single hole in the centre of the nozzle plate with nominal diameter of  $5 \times 10^{-4}$  m as shown in Figure 4-3a. A frequency of 100 Hz was used in these experiments. It is evident from Figure 5-3 that the geometric mean size decreases significantly from  $7.5 \times 10^{-6}$  m to  $4.7 \times 10^{-6}$  m when the relative amplitude increases from 10% to 29%, while the geometric standard

deviation increases from 1.39 to 1.67.

Although the amplitude of the plunger immersed in the molten metal was not measured, the amplitude of the impulse applicator in air was estimated as shown in Table 5.1. This was done by placing a ruler marked with reference points next to the plunger. The amplitude was then estimated by reading how much the marker was moved during the operation. The amplitude of the plunger in the molten melt is expected to be smaller than the values shown in Table 5.1.

The results also showed that smaller droplets were obtained with higher relative amplitudes. This result is reasonable because the higher the relative amplitude, the higher the absolute amplitude, and hence the higher the acceleration of the plunger, that is, the higher the force applied by the plunger on the melt. It is reasonable to expect that the higher the plunger amplitude is, the higher the energy supplied to the melt exiting the orifice. Thus, the discontinuous stream emanating from an orifice would break up into droplets having a smaller average droplet size and a wider size distribution. This is seen in Figure 5-3 and will again be discussed in Sections 5.4.

**Table 5.1 Estimated Amplitude of the Impulse Applicator in Air**

<b>Frequency (Hz)</b>	<b>Relative Amplitude (%maximum)</b>	<b>Amplitude in Air (<math>10^{-3}</math> m)</b>
<b>100</b>	<b>19</b>	<b><math>\pm 0.5</math></b>
	<b>29</b>	<b><math>\pm 1.0</math></b>
	<b>57</b>	<b><math>\pm 1.5</math></b>
	<b>86</b>	<b><math>\pm 2</math></b>



#### **5.4 Effect of Acceleration**

The acceleration of the impulse applicator is determined by the characteristic of the pulsator and the voltage of the power supply. These in turn define the combination of frequency and amplitude that yield a corresponding acceleration. In each experiment, the voltage and the frequency were recorded, and the acceleration of each impulse calculated. Two vibrators were used: one for Pb-Sn alloy and another for all the other alloys. These two vibrators have the same model number, but their specification curves are slightly different. The relative amplitudes and frequencies used were converted into acceleration using the impulse generator characteristics shown in Appendix C.

As shown in Appendix C, if a frequency of 100 Hz is used from impulse generator A, an acceleration of  $313.6 \text{ m/s}^2$  is read from the graph. If 29% of maximum amplitude is used, then the actual acceleration would be  $90 \text{ m/s}^2$ . Figure 5-4 shows the effect of acceleration of the impulse applicator on the geometric mean size and geometric standard deviation for Sn-15wt%Pb alloy atomized at 640 K into nitrogen. Clearly, the geometric mean size decreases with increasing acceleration while the geometric standard deviation increases with acceleration.

The effect of plunger acceleration on size and size distribution was plotted in Figure 5-4. It is evident that the higher the plunger acceleration, the more energy is supplied to the melt, resulting in a decreased geometric mean size and a larger geometric deviation. It is also seen from this figure that both the average size and standard deviation of the powder produced can be varied over a large range. In this instance, the

geometric average size varies from  $7.5 \mu\text{m}$  to  $4.7 \times 10^{-4} \text{ m}$  and the geometric standard deviation changes from 1.39 to 1.71 by varying the plunger acceleration.

### **5.5 Effect of Orifice Size**

Orifice size is another important variable that can be used to affect the size and size distribution of droplets generated by IAP. Table 5-2 shows experimental conditions and results for Zn-0.05wt%Pb alloy atomized at 810-860 K in nitrogen at 200 Hz. The nozzle design is shown in Figure 4-3b. The nozzle-plunger distance was  $1.3 \times 10^{-3} \text{ m}$ . Pb-12wt%Sn alloy was atomized with an orifice configuration as shown in Figure 4-3c at 670 K in air with 160 Hz. In both runs, 60% of maximum amplitude was used. It can be clearly seen that the geometric mean size,  $d_{50}$ , increases with increasing orifice size, while the geometric standard deviation,  $\sigma_g$ , decreases with increasing orifice size (over this size range).

The results in Table 5-2 show that the particle size decreases with decreasing orifice size of the nozzle, but the decreasing trend is not linear. This trend occurs because for a smaller orifice size, the discontinuous stream generated by the plunger through an orifice is thinner. Under similar experimental conditions, the length of the ligaments are assumed to be the same. Thus the smaller hole sizes will yield ligaments of smaller volume which in turn will yield smaller-sized droplets. Note, however, that the powder mean size does not decrease monotonically with orifice size. This can be explained using the following analysis. According to the Hagen-Poiseuille law [Bird et al, 1971],

$$Q = \frac{\pi r^4}{8\mu L} (p_1 - p_2) \quad (95)$$

where  $Q$  is the volume flow rate,  $\mu$  is the dynamic viscosity,  $r$  and  $L$  are the radius and the length of the capillary respectively, and  $p_1$  and  $p_2$  are the values of the mean pressure at the two ends of the orifice. In terms of the average fluid velocity, the volume flow rate can be written as:

$$Q = \pi r^2 u_j \quad (96)$$

where  $u_j$  is the average jet velocity within the capillary. Equating Equations (95) and (96) and solving for  $p_1 - p_2$ , the pressure difference on either side of the orifice is given by:

$$p_1 - p_2 = \frac{8\mu L u_j}{r_j^2} \quad (97)$$

Clearly, the pressure difference is inversely proportional to  $r_j^2$ . Thus, a higher pressure, force or acceleration is required to achieve flow in a smaller orifice size having the same capillary length  $L$ . In other words, the force needed to push fluid through the capillary is inversely proportional to the square of the orifice size. However, the force applied for all three different orifice sizes (Table 5-2) is about the same. Hence the geometric mean size does not decrease linearly with a corresponding decrease in orifice size.

**Table 5-2. Effect of Orifice Size**

**a: Zn-0.05wt%Pb alloy, 200 Hz, 810-860 K, Nitrogen with 160-400 ppm  
Oxygen Content**

<b>Nominal Orifice Size (<math>10^{-6}</math> m)</b>	<b><math>d_{50}</math> (<math>10^{-6}</math> m)</b>	<b><math>\sigma_s</math></b>
130	439	1.68
250	569	1.52
500	679	1.44

**b: Pb-12wt%Sn alloy, 160 Hz, 60% maximum, 670 K, Air**

<b>Nominal Orifice Size (<math>10^{-6}</math> m)</b>	<b><math>d_{50}</math> (<math>10^{-6}</math> m)</b>	<b><math>\sigma_s</math></b>
250	775	1.60
500	1078	1.38

## **5.6 Effect of Nozzle-Impulse Applicator Distance**

Figure 5-5 shows the effect of nozzle-impulse applicator distance on the size and size distribution of spherical Al-10wt%Cu alloy atomized by IAP at 1060 K in nitrogen containing 80-100 ppm oxygen, using a frequency of 100 Hz and 32% of maximum amplitude. The nozzle design is as shown in Figure 4-3b. Increasing the nozzle-impulse applicator distance from  $1 \times 10^{-3}$  m to  $2.5 \times 10^{-3}$  m reduces the geometric mean size from  $4.62 \times 10^{-4}$  m to  $4.16 \times 10^{-4}$  m, but increases the geometric standard deviation from 1.26 to 1.31. However, when the crucible-piston distance increases further from  $2.5 \times 10^{-3}$  m to  $3.2 \times 10^{-3}$  m, the geometric mean size increases to  $4.64 \times 10^{-4}$  m and the geometric standard deviation decreases to 1.26 again. Conceptually, there is a limit to the maximum nozzle-impulse applicator distance, at which no atomization will occur. Increasing the plunger-nozzle distance will result in smaller energy transferred to the melt flowing through the orifice. This results in a larger geometric mean size and a smaller size distribution. This is consistent with the plunger acceleration results discussed earlier in Section 5.4.

## **5.7 Effect of Superheat**

The effect of superheat on the size and size distribution of Al-10wt%Cu alloy and Pb-12wt%Sn alloy are shown in Figure 5-6. The experiments of Al-10wt%Cu alloy were carried out using impulse generator A in a nitrogen atmosphere with the oxygen content

varying from 15 ppm to 110 ppm. The frequency used was 100 Hz and the relative amplitude was 32% of the maximum of the pulsator. From Figure 5-6 it is noticed that increasing superheat from 50 K to 200 K reduces the geometric mean size only slightly after the first 50 degree increase of superheat, while the geometric standard deviation is almost unchanged.

The experiments on Pb-12wt%Sn alloys were carried out using impulse generator B in air using the nozzle design shown in Figure 4-3c. The nominal diameter of the nozzle was  $5 \times 10^{-4}$  m. The frequency used was 160 Hz and the relative amplitude was set at medium (which is about 50% maximum). As the superheat increases from 50 K to 150 K, the geometric mean size decreases slightly from  $8.5 \times 10^{-6}$  m to  $7.5 \times 10^{-6}$  m. Similarly to Al-10wt%Cu alloy, the size reduction is more significant in the first 50 degree increase of superheat. The geometric standard deviation is again almost unchanged (from 1.25 to 1.29).

These results show that the average droplet size decreases slightly with increasing temperature or superheat. The slight reduction in mean size is probably due to the decrease in viscosity and surface tension with increasing temperature, which makes the molten metal ligaments break up more easily.

### **5.8 Effect of Oxygen Content on Size, Size Distribution and Powder Shape**

Figure 5-7 shows the effect of oxygen content of the gas atmosphere on the geometric mean size and geometric standard deviation of Zn-Pb alloy powder.

Atomization was carried out using 100 Hz impulse, 32-38% maximum relative amplitude (impulse generator A) with  $1.7 \times 10^{-3}$  m nozzle-plunger distance with seven holes in a row, except for the run in air, where a 1-hole nozzle design was used. The nominal size of the nozzle orifice is  $2.5 \times 10^{-4}$  m. From the figure, it is seen that both the geometric mean size and geometric standard deviation do not change very much with increasing oxygen content. The actual change might be larger than what is shown in the graph, since the larger the oxygen content, the more dripping was observed. The dripped droplets stuck together with atomized droplets, which could not pass through the sieves. The higher the oxygen content, the more significant was the dripping. When the experiments were carried out in inert gas such as nitrogen, spherical powders were obtained.

Another set of experiments was carried out on two Pb-Sn alloys. The frequency used was 160 Hz and relative amplitude was about 50% maximum. Figure 5-8a shows an example of Sn-15wt%Pb droplets produced at 640 K in nitrogen which contained 130 ppm oxygen. A single-hole  $5 \times 10^{-4}$  m nominal size nozzle was used. The frequency used was 100 Hz and the relative amplitude was 29% maximum. This is in contrast to the case when atomization of this alloy was carried out in air. In this case, the solidified powder had a tear drop shape as shown in Figure 5-8b. It is apparent that the oxide film formed on the surface of the ejected ligaments impeded further breaking up and spherodization. Thus, larger and tear shaped powder was obtained. Figure 5-8b is an example of Pb-12wt%Sn droplets produced at 670 K in air. In this picture, the spherodized end of the acicular particle was the first metal out of the orifice. It is seen

that it started to spherodize. A 37-hole nozzle as shown in Figure 4-3c was used with a nominal orifice size of  $2 \times 10^{-6}$  m. The length to diameter ratio of the droplets was up to 15, and 8 on average, which was larger than 4.4, the optimum length to diameter ratio given by Rayleigh's theory. This also shows that the elongated segments would break up further into smaller droplets had the experiment been performed under an inert gas atmosphere with the segments being allowed to break up before solidification of the oxidized shell. This will be further addressed in Section 5.13.

### **5.9 Effect of Number of Orifices**

Table 5-3 shows the effect of the number of orifices per nozzle plate of Al-10wt%Cu alloy atomized at 1060 K in nitrogen by using nozzles with a nominal size of 250  $\mu$ m. The frequency used was 100 Hz while the relative amplitude used was 30% maximum. The oxygen content of the atomization atmosphere was 60 ppm for the 1-hole nozzle plate and 80 ppm for the 7-hole nozzle plate.

It can be seen that both the geometric mean size and the geometric standard deviation increase with increasing number of holes. The overall change in both geometric mean size and geometric standard deviation is small.

Since the 7-hole nozzle was constructed in a line, the holes at the edge of the nozzle may see more damping than the hole in the centre, therefore slightly larger droplets may be produced from the orifices at the edge of the nozzle than those near the centre of the nozzle. This is why both the geometric mean size and the geometric standard



deviation are larger for 7 holes in a row than a single hole at the centre of the nozzle.

**Table 5-3 Effect of Number of Orifices per Nozzle Plate on Al-10wt%Cu Alloy**

	1 hole	7 holes
Temperature (K)	1060	1060
Frequency (Hz)	100	100
Relative Amplitude (%maximum)	30	30
Actual orifice size ( $10^{-6}$ m)	285	249
Oxygen Content in Atmosphere (ppm)	60	80
Geometric Mean Size ( $10^{-6}$ m)	396	445
Geometric Standard Deviation	1.19	1.27

### **5.10 Effect of Acceleration on Throughput**

Table 5-4 shows the melt throughput of Sn-15wt%Pb alloy under different accelerations. These experiments were performed at 640 K in a nitrogen atmosphere and in a crucible with a single  $10^{-4}$  m orifice. The frequency and relative amplitude used were 100 Hz and 29% maximum respectively. It can be seen that the alloy throughput of the IAP increases with increasing acceleration. The last column in Table 5-4 shows the melt throughput for multiple holes on the basis that the total area of holes is equivalent to a metal delivery tube of  $3 \times 10^{-3}$  m diameter.

The acceleration was determined using the data in Appendix C. From Table 5-4, it is evident that the alloy throughput increases with increasing acceleration provided by the impulse generator. The throughput per hole is small due to small orifice area of a hole. Had more orifice areas been available (e.g., using multiple holes), the production rate would have been increased. Converting the melt throughput per hole to that per a total orifice area equivalent to a melt delivery nozzle diameter of  $3 \times 10^{-3}$  m, a production rate of 0.028 kg/s can be achieved. This is comparable to some conventional gas atomization systems.

**Table 5-4 Throughput of Sn-15wt%Pb Alloy****( $5 \times 10^{-4}$  m orifice size, 640 K, nitrogen)**

Acceleration ( $\text{m/s}^2$ )	$d_{50}$ ( $10^{-6}$ m)	$\sigma_s$	Rate per Hole ( $10^{-3}$ kg/s)	Rate for Equivalent Metal Nozzle, for Diameter of $3 \times 10^{-3}$ m ( $10^{-3}$ kg/s)
58.8	751	1.39	0.32	11.7
107.8	676	1.48	0.48	16.7
127.4	629	1.49	0.58	21.7
176.4	589	1.58	0.78	28.3

### 5.11 Effect of Orifice Size on Throughput

Table 5-5 shows the throughput of a Zn-Pb alloy using different orifice sizes. The experiments were carried out at 810-860 K in an atomizing chamber filled with nitrogen, with a relative amplitude of 29-100% of the maximum of the pulsator at 200 Hz. Obviously the production rate per hole decreases with decreasing orifice size due to smaller cross-section area, higher capillary forces and higher friction forces in the orifices. Note that less force is needed to overcome the capillary forces in a larger-sized orifice than in one of smaller diameter.

**Table 5-5 Throughput of Zn-Pb Alloy (810-860 K, Nitrogen)**

Acceleration (m/s <sup>2</sup> )	Orifice Size (10 <sup>-6</sup> m)	d <sub>50</sub> (10 <sup>-6</sup> m)	σ <sub>g</sub>	Rate per Hole (10 <sup>-3</sup> kg/s)	Rate for Equivalent Metal Nozzle, for Diameter of 3 x 10 <sup>-3</sup> m (10 <sup>-3</sup> kg/s)
13	500	679	1.44	0.117	4.17
13	250	569	1.52	0.067	9.67
60	130	439	1.68	0.017	8.83

## **5.12 Effect of Melt Viscosity on the Process**

### **5.12.1 Background**

Experiments were made to investigate the feasibility of atomizing high viscosity melts such as Selenium using the Impulse Atomization Process. Molten metal was fed into the nozzle at the bottom of the crucible by an impulse applicator (plunger) which moved up and down in the crucible. It was believed that both the viscosity and plunger size must play a role in the atomization of high viscosity melts. Molasses, a highly viscous fluid at room temperature, with a viscosity of 40 Pa s, was chosen as a physical model of high viscosity melts. The experimental trials with molasses and Selenium will be described in this section.

### **5.12.2 Experiment**

An alumina crucible and nozzle plates with one hole and  $5 \times 10^{-4}$  m orifices were used for the physical modelling experiments with molasses. Different frequencies, relative amplitudes, plunger diameters, and nozzle-plunger distances were tested with this material. The results shown in Table 5-6 indicate that it is not possible to atomize highly viscous pure molasses with a  $3.7 \times 10^{-4}$  m plunger under the operating conditions shown in the Table 5-6.

**Table 5-6 Atomization of Pure Molasses with  $3.7 \times 10^{-2}$  m Diameter Plunger**

<b>Nozzle-Plunger Distance (<math>10^{-3}</math> m)</b>	<b>Frequency (Hz)</b>	<b>Relative Amplitude (%maximum)</b>	<b>Observation</b>
1.7	100	0-57*	not atomized
1.7	20-300	38	not atomized
1.7	2000	38	not atomized
1.7	20000	38	not atomized
0.6	100	0-57	not atomized
1.3	100	0-57	not atomized
2.5	100	0-100	not atomized

\*: Maximum relative amplitude to be used in this setting as the plunger will hit the nozzle.

Molasses was then mixed with different amounts of water to make fluids with varying viscosities to determine the maximum viscosity of the fluid that the current system can atomize. Table 5-7 shows it is possible to atomize viscous liquids with viscosities as high as 0.06 Pa s (which is 20 times higher than most of the metals) with a  $3.7 \times 10^{-4}$  m plunger. The viscosity of Selenium is 0.4 Pa s at 620 K and 2 Pa s at 570 K [Huôt, 1994]. As both of these are much higher than  $6 \times 10^{-2}$  Pa s, it is not possible to atomize selenium with a  $3.7 \times 10^{-3}$  m plunger with the impulse generator used for this thesis.

As shown in Equation (95), to obtain the same volume flow rate, higher pressure ( $p_1$ ) is required for a material with higher viscosity. The pressure of the plunger equals the force of the plunger divided by the cross section area of the plunger  $A_p$ . Since the maximum plunger force is the same for both viscous and non-viscous systems, the only way to achieve a higher pressure ( $p_1$ ) for a viscous system would be to reduce the plunger cross section area  $A_p$ .

Therefore, a smaller cross section plunger with a diameter of  $6.5 \times 10^{-3}$  m was used. Atomization of a mixture of molasses and water was carried out with a  $6.5 \times 10^{-3}$  m plunger using a  $4 \times 10^{-4}$  m single-hole crucible. Tables 5-8 to 5-11 show the physical model results of this experiment.

**Table 5-7 Atomization of Mixtures of Molasses and Water with  $3.7 \times 10^{-2}$  m Plunger**

Viscosity (p)	Water : Molasses (by volume)	Nozzle-Plunger Distance ( $10^{-3}$ m)	Frequency (Hz)	Relative Amplitude (%maximum)	Observation
0.009	1 : 0	1.3	100	10	began to atomize
	1 : 1	1.3	100	13	began to atomize
0.6	1 : 3	1.3	100	86-100	began to atomize

**Table 5-8 Effect of Frequency on the Atomization of Water with a  $6.5 \times 10^{-3}$  m Plunger**

Viscosity (p)	Water : Molasses (by volume)	Nozzle-Plunger Distance ( $10^{-3}$ m)	Frequency (Hz)	Relative Amplitude (%maximum)	Observation
0.009	1 : 0	1.7	25	35*	began to atomize
0.009	1 : 0	1.7	50	54	began to atomize
0.009	1 : 0	1.7	100	76	began to atomize
0.009	1 : 0	1.7	200	0-100	did not atomize
0.009	1 : 0	1.7	2000	0-100	did not atomize
0.009	1 : 0	1.7	20000	0-100	did not atomize



Since this was an experiment with the small diameter plunger, water was used to find the optimum operating conditions, as shown in Table 5-8. Different frequencies were used. It was found that at low frequencies, 25 Hz and 50 Hz, the absolute amplitudes of the plunger were too large. The plunger hit the bottom of the crucible at higher relative amplitudes. At higher frequencies of 200 Hz, 2000 Hz, and 20000 Hz, the absolute amplitudes were too small to initiate atomization. Therefore 100 Hz was still a reasonable frequency to use. With this frequency of 100 Hz, different nozzle-plunger distances were attempted, as shown in Table 5-9. From this table, it is clear that the smaller the nozzle-plunger distance, the smaller the relative amplitude needed to start atomization. A smaller nozzle-plunger distance was favoured for the runs. However, a nozzle-plunger distance close to zero is not a good choice, since it limits the absolute amplitude of the plunger. Therefore, a nozzle-plunger distance of around  $0.4 \times 10^{-3}$  m was proper.

A mixture of 25 vol% water and 75 vol% molasses (water:molasses = 1:3, viscosity = 0.6 p) was then tested, as shown in Table 5-10. This mixture atomized. The results for different nozzle-plunger distances show a similar trend as those with water. For a higher viscosity (0.2 Pa s) mixture of 1/6 of water and 5/6 of molasses, atomization was equally successful (Table 5-11). These results agree with the theory discussed in Section 5.12.2, confirming the feasibility of atomizing Selenium around 570-620 K. The results in Table 5-11 show that at 100 Hz and 38% maximum amplitude, atomization occurred for a fluid with viscosity of 0.2 Pa s, but no atomization occurred for pure molasses with a viscosity of 40 Pa s.

**Table 5-9 Effect of Nozzle-Plunger Distance on the Atomization of Water with a  $6.5 \times 10^{-3}$  m plunger**

Viscosity (Pa s)	Water : Molasses (by volume)	Nozzle- Plunger Distance ( $10^{-3}$ m)	Frequency (Hz)	Relative Amplitude (%maximum)	Observation
0.0009	1 : 0	1.3	100	57	began to atomize
0.0009	1 : 0	0.6	100	35	began to atomize
0.0009	1 : 0	0.4	100	25	began to atomize
0.0009	1 : 0	0.2	100	19	began to atomize
0.0009	1 : 0	-0	100	13	began to atomize

**Table 5-10 Effect of Nozzle-Plunger Distance on the Atomization of Mixtures of Molasses and Water with a  $6.5 \times 10^{-3}$  m Plunger**

Viscosity (Pa s)	Water : Molasses (by volume)	Nozzle- Plunger Distance ( $10^{-3}$ m)	Frequency (Hz)	Relative Amplitude (%maximum)	Observation
0.06	1 : 3	1.3	100	67	began to atomize
0.06	1 : 3	0.6	100	38	began to atomize
0.06	1 : 3	0.4	100	30	began to atomize
0.06	1 : 3	0.2	100	22	began to atomize

**Table 5-11 Effect of Water:Molasses Ratio on the Atomization of Mixtures of Molasses and water with a  $6.5 \times 10^{-3}$  m Plunger**

Viscosity (Pa s)	Water : Molasses (by volume)	Nozzle- Plunger Distance ( $10^{-3}$ m)	Frequency (Hz)	Relative Amplitude (%maximum)	Observation
0.2	1 : 6	0.4	100	38*	began to atomize
40	0 : 1	0.4	100	38	did not atomize

\*: sounds at higher amplitude.

It is known that the viscosity of Selenium at 620 K is 0.4 Pa s, and 2 Pa s at 570 K [Huôt, 1994]. This means that it is possible to atomize Selenium in the temperature range from 570 to 620 K. The experimental results shown in Section 5.12.2 and Figure 5-9 agree with the physical model prediction very well.

Based on the results of the physical model, an experimental trial was performed using selenium. A 1-hole nozzle of  $3.5 \times 10^{-4}$  m diameter was used together with a  $6.5 \times 10^{-3}$  m plunger. The crucible-plunger distance was  $0.4 \times 10^{-3}$  m. Selenium powder was collected with a one liter-sized beaker filled with  $8 \times 10^{-4}$  m<sup>3</sup> water at the bottom of the atomizer. The atomizer was filled with Argon with 320 ppm oxygen. Dripping was observed after the temperature reached 590 K. Atomization started at a frequency of 100 Hz and a relative amplitude of 22% of maximum at 610 K. A nice atomized stream was formed. No dripping and very little fuming were observed during atomization. After atomization at 610 K for 300 s and while still atomizing, the temperature was gradually reduced to 580 K when atomization stopped. Figure 5-9 shows the plot of temperature vs. time for this run. Thus by appropriate modification of the plunger, a highly viscous material such as Selenium can be atomized at a viscosity of nearly 2 p.

### **5.13 Proposed Atomization Mechanism of IAP**

The differences between the Impulse Atomization technique and other single fluid methods like the continuous jet and drop-on-demand methods will be described in this section. First, the formation of discontinuous streams will be described, then the number

of droplets produced per impulse will be determined and compared with those of the two methods above.

### **5.13.1 Formation of Discontinuous Streams by IAP**

Figure 5-10 is the schematic drawing of the formation mechanism of discontinuous streams in IAP. When the impulse applicator is immersed in the fluid and moves in the direction of the nozzle with sufficient acceleration as shown in Figure 5-10a, some fluid is pushed through the orifice in the nozzle, exits and detaches from the fluid in the crucible. An elongated segment of molten fluid stream is formed. This segment of stream is longer than  $\pi d$ . From Section 2.2.2.1, such a stream will be unstable and will break up into smaller fluid segments or ligaments. As shown in Figure 5-8, the length to diameter ratio of the segments is normally much larger than  $\pi$ , averaging 8. The ligaments then spherodize into droplets if they are still fluid. Figure 5-8b also shows the tendency toward break-up and spherodization. Had the droplet surface shown in Figure 5-8b not been oxidized, it would have broken up into smaller droplets as would occur under an inert gas. Meanwhile, the impulse applicator moves away from the nozzle, as shown in Figure 5-10b, and another cycle begins to form another elongated segment of molten fluid as shown in Figure 5-10c. If the segment was oxidized without breaking up, Figure 5-10d would be observed.

### 5.13.2 The Number of Drops per Second

The hypothesis is that discontinuous streams of fluid are produced by the applied impulses: one stream of discontinuous elongated segments per impulse per orifice. The purpose of the following analysis is to determine if the stream further breaks up and spherodizes into several droplets or simply spherodizes into a single droplet. This can be done by calculating the number of droplets produced per second and comparing this to the applied frequency. This will determine if multiple droplets were produced per impulse per orifice.

According to the sieving results, the mass fraction for each sieve corresponding to a mid-size  $d_i$  is  $f_i$ . If a total weight of powder  $W$  is atomized during a period of time,  $t$ , the number of particles corresponding to the size range per unit time can be obtained by the following formula:

$$n_i = \frac{f_i W}{\frac{\pi}{6} d_i^3 \rho t} \quad (98)$$

where  $\rho$  is the density of the material. Accordingly, the total number of droplets,  $n$ , can be calculated by summing the number of droplets in all the size ranges in a sieving test. Therefore,

$$n = \sum_{i=0}^k \frac{f_i W}{\frac{\pi}{6} d_i^3 \rho t} \quad (99)$$

A sample run using a single-hole nozzle was selected for this analysis. Al-

10wt%Cu was atomized at 1060 K in Nitrogen with 60 ppm Oxygen by impulse generator A. The frequency was 100 Hz. The relative amplitude was 32% maximum. A 49.6 g of sample was collected during a period of 1800 s. The orifice size of the nozzle was  $2.85 \times 10^{-4}$  m. The geometric mean size was  $4 \times 10^{-4}$  m and the geometric standard deviation was 1.19. The sieving results are shown in Table 5-12.

Hence, a total number of 319 droplets were produced per second using an impulse frequency of 100 Hz. In other words, about three droplets were produced per impulse per orifice.

As discussed in Chapter 2, the fundamental mechanism of the continuous jet method is the disintegration of continuous jets by applying a vibration with an optimum wavelength (Figure 2-2c). A sufficient amount of overpressure is necessary in order to supply the jet with enough velocity to make a continuous jet. On the other hand, as discussed in Chapter 2, only a small amplitude of vibration is necessary to disturb the jet. Therefore, not only is it important to use a sufficient amount of overpressure to ensure a sufficient amount of jet velocity, but also it is equally important to use the optimum frequency corresponding to an optimum wavelength to disturb the jet. However, with IAP the discontinuous streams are produced by an impulse applicator. The streams are discontinuous since they are produced during each half cycle of the wave, while during the other half cycle of the wave no fluid emanates from the orifice, as shown in Figure 5-10. The discontinuous streams or jets were formed by the impulses. It has been observed experimentally that the molten metal head used in the experiments presented in this thesis was not sufficient to push molten metal through holes. Therefore, it is

**important to ensure that sufficient amount of amplitude of impulses is used to generate the discontinuous streams.**

**As discussed in Chapter 2, with the drop-on-demand method, one drop is produced per impulse. However, with IAP, multiple droplets are produced per impulse as demonstrated in this section. Table 5-13 shows a few more examples chosen from various alloys calculated using Equation (98). It is clear that multiple droplets per impulse were produced. This shows that IAP is fundamentally different from the drop-on-demand method.**

**Furthermore, Figure 5-8b shows the segments of Pb-Sn alloy droplets produced in air which freeze the discontinuous segments before further breaking-up into smaller droplets. The segments would have broken further up in the necking places, had the experiments been performed in inert gas atmosphere.**



**Table 5-12 Calculation of Number of Droplets from Sieving Results**

<b>Sieve Ranges (10<sup>-6</sup> m)</b>	<b>Mid-Size (10<sup>-6</sup> m)</b>	<b>Mass Fraction</b>	<b>Number of Droplets (/s)</b>
125-150	137	0.0004	2.164
150-180	164	0.0003	0.939
180-212	195	0.0004	0.838
212-250	230	0.0013	1.651
250-300	274	0.0276	21.233
300-355	326	0.3514	160.018
355-425	388	0.3415	92.222
425-500	461	0.2040	32.965
500-600	548	0.0682	6.568
600-710	653	0.0041	0.235
710-850	777	0.0001	0.004
850-1000	922	0.0008	0.017
<b>Total</b>		<b>1</b>	<b>319</b>

**Table 5-13 Number of Droplets per Impulse Produced by IAP**

Run #	Alloy	Frequency (Hz)	Total Weight (kg)	Time (s)	Number of Droplets	Number of Droplets per Impulse per orifice
071492	Pure Zn	100	0.0856	20	1298	13
072092	Zn-0.05wt%Pb	200	0.0998	91	835	4
072892	Sn-15wt%Pb	100	0.0826	120	3255	33
080492	Sn-15wt%Pb	200	0.1168	120	2927	15
060993	Al-17wt%Cu	100	0.1001	1320	374	4
061493	Al-17wt%Cu	100	0.1345	1200	870	9
062193	Al-10wt%Cu	100	0.0950	1860	342	3
072393	Al-10wt%Cu	100	0.1157	1800	535	5

## **5.14 Advantages of Impulse Atomization Process**

In this section, the advantages of Impulse Atomization Process will be summarized and compared with those of other atomization techniques.

### **5.14.1 Advantages of IAP over Conventional Fluid Atomization**

Powders produced by IAP have narrower size distribution than those produced by conventional fluid atomization. As described in Section 2.1, the typical standard deviation of gas atomized powders is normally in the range of 1.8-2.4 [Dunkley and Palmer, 1986]. However, the typical standard deviation of IAP atomized powders achieved in this work is normally in the range of 1.2-1.5. This is significantly smaller than those achieved using conventional atomization techniques.

Since the particle size distribution of powders produced by IAP is narrower, the microstructure produced by IAP is also more uniform than gas-atomized droplets. Furthermore, the powder microstructure produced by IAP is more uniform than conventionally atomized powders since the heat transfer coefficient during IAP is much smaller. This results in a smaller droplet Biot number than in gas atomization.

IAP powder microstructure is finer than that from gas atomization due to the fact that the molten metal is stirred vigorously by the plunger, which may help reduce the number of potential nuclei in the melt. Therefore larger undercoolings and high cooling rates result, as will be described in Chapter 6. Another possible reason for larger

undercooling for IAP versus conventional gas atomization is the absence or minimization of turbulence. From SEM observations, no satellites were observed on large powder particles, while this kind of satellite is very common during the gas atomization process. This says that turbulence in the gas atomizer is a factor in microstructure.

Since IAP parameters can be controlled more accurately, reproducible atomization is easily achieved. No fluid is used to atomize the melt.

According to Yule and Dunkley [Yule and Dunkley, 1994], the efficiency, as defined in section 2.1, of gas atomized zinc in air with a closed nozzle at a molten metal flow rate of 0.33 kg/s is 0.009%. The average size (D50 ) was  $2.6 \times 10^{-5}$  m. The corresponding specific surface area is 50 m<sup>2</sup>/kg, specific powder input is  $440 \times 10^3$  J/kg, and the theoretical power requirement is 39 J/kg.

A similar calculation was done for a Sn-15wt%Pb run atomized at 690 K in nitrogen containing 150 ppm oxygen. The frequency used was 100 Hz. The relative amplitude was 29% maximum. The nozzle design was 1 hole in the centre of the nozzle plate. During 120 seconds,  $8.26 \times 10^{-2}$  kg of powder was collected. The geometric mean size produced from this run was  $4.8 \times 10^{-4}$  m with a standard deviation of 1.42. The power input was estimated at 30 W. The specific surface area,  $S_a$ , can be calculated according to the following equation for spherical particles:

$$S_a = \frac{\pi D^2 n}{W} = \frac{\pi D^2 \frac{W}{W_0}}{W} = \frac{\pi D^2}{\frac{1}{6} \pi D^3 \rho} = \frac{6}{D \rho} \quad (100)$$

where D is the diameter of droplets, W is the weight of droplets, n is the number of

droplets,  $W_0$  is the weight of a single droplet, and  $\rho$  is the density of the metal. Substituting  $D_{50}=4.8 \times 10^{-4}$  m and  $\rho=7880$  kg/m<sup>3</sup> yields  $S_d=1.5$  m<sup>2</sup>/kg.

The theoretical specific power,  $S_t$ , required to produce these droplets would be:

$$S_t = S_d \gamma \quad (101)$$

where  $\gamma$  is the surface energy of the droplets. Substituting  $\gamma=0.505$  J/m<sup>2</sup> yields  $S_t=0.76$  J/kg. The specific power input,  $S_p$ , can be calculated by multiplying the power input by the atomization duration time,  $t$ , divided by the total weight of powder collected during that period of time:

$$S_p = \frac{\text{power} \cdot t}{W} \quad (102)$$

Substituting power = 30 Watt,  $t=86$  s and  $W=0.194$  kg yields  $S_p=13 \times 10^3$  J/kg. Therefore the efficiency for this run is  $S_t/S_p=0.006\%$ , which is the same order of magnitude as that of gas atomization. With multiple orifice, the efficiency might be higher.

#### 5.14.2 Advantages of IAP over Continuous Jet and Drop-on-Demand Atomization

As discussed in Section 6.1.2.3, with the Impulse Atomization technique no gas overpressure is used over the melt; as a result, both the process and the apparatus are simpler. It is easier to control the starting and stopping of the process since it is not necessary to match the operation of overpressure with vibration. Commercially available materials such as ceramics, graphite, or metals are used to construct the crucible material and nozzle. Since discontinuous streams are generated by IAP instead of continuous jets,

droplets do not stick to each other, therefore, it is not necessary to use the high voltage sources as is the case in the continuous jet technique. Furthermore, since multiple droplets are produced per impulse, IAP is a more efficient technique than the drop-on-demand method. The simplicity and flexibility of IAP makes it possible to atomize high melting point materials such as copper, as shown in Figure 5-11.

## **CHAPTER 6: EXPERIMENTAL RESULTS AND DISCUSSION OF MICROSTRUCTURE ANALYSIS OF POWDERS PRODUCED BY IAP**

In Chapter 5, the effect of operating conditions on size, size distribution, powder shape, and throughput of droplets produced by IAP were illustrated and discussed. A mathematical model of the cooling rate for Al-Cu alloy droplets was presented in Chapter 3.

In this chapter, the microstructure of these atomized particles will be analyzed. Using predicted cooling rates obtained using the mathematical model developed in Chapter 3 and using the correlation between cooling rate and Secondary Dendrite Arm Spacing (SDAS) for the Al-Cu alloy system, Secondary Dendrite Arm Spacings were predicted for a few of the experimental conditions. These calculated SDAS results will be compared with the measured Secondary Dendrite Arm Spacings. In addition, the Secondary Dendrite Arm Spacing measurements of Al-Ni-Fe alloy droplets will be compared with those in the literature described in Chapter 2.

Three kinds of alloys were investigated in this study: Al-10wt%Cu, Al-17wt%Cu, and Al-3.7wt%Ni-1.5wt%Fe. These alloys were chosen because the cooling rate or particle size versus SDAS relationship is available in the literature and the alloys meet some of the production needs in the lab. For Al-17wt%Cu alloys, a master alloy was

prepared in a resistance furnace by using 99.85% pure Al ingots and 99.9% pure Cu strips (both purchased from Canada Metal Co. Limited, Calgary, AB, Canada) cast into cone-shaped ingots with sizes which fit into the crucible. For Al-10wt%Cu, 99.9% pure Al and 99.9% pure Cu shot (both were purchased from Alfa Aesar, Ward Hill, MA, USA) were used and melted directly in the crucible of the impulse atomizer. As for Al-3.7wt%Ni-1.5wt%Fe, the same aluminum shot was used, with the addition of 99.9% pure nickel and 99.9% pure iron wire, and melted directly in the crucible of the impulse atomizer.

### **6.1 Calibration of Image Analysis**

Before carrying out any image analysis measurements, a calibration of image magnification was performed to quantify the magnification associated with displaying SEM digitized images on the stand-alone image analysis system. This was necessitated, since the magnification marker (micron bar) generated by the SEM was not retained in the digital image saved by the SEM and since the area of digital image (0.254 m × 0.254 m) did not completely cover the area of the photo image (0.102 m × 0.152 m). The calibration was carried out as follows. An image of a known grid size ( $6.4 \times 10^{-5}$  m) was taken in the SEM at a known magnification of 200 times. Figure 6-1a shows the original image of the standard grids. This image was saved and transferred into a TIFF file format. The image processing steps on the image analysis system include adjusting the threshold to 128-255, filtering the image with a 5×5 filter, transferring the image into a black and white file, and inverting the black and white portions on the image. Then a



skeleton (centre lines of the grid) was obtained as shown in Figure 6-1b.

After the skeleton was obtained, horizontal lines were drawn across the image at different but regular vertical intervals. The luminance and the (x,y) coordinates of the intersection points between the vertical grid lines and the horizontal drawn lines were recorded. These luminance and coordinates were then converted into an ASCII file. A FORTRAN program (see Appendix D), IMAGE.FOR, was written to read both the (x,y) coordinates and luminance of the lines. The (x,y) coordinates of the highest luminance (the intersection between the drawn line and the grid line) were selected. The distance between the points with highest luminance was calculated in the program. This is the grid length measured by Optimas™ in centimetres. Similarly, calibration of the vertical distance was also carried out. The overall average in both directions is  $2.17 \times 10^{-2}$  m (with 144 measurements and a standard deviation of  $1 \times 10^{-4}$  m) for an original grid length of  $6.4 \times 10^{-6}$  m. This result shows that the image magnification with respect to the actual object on the PC-CRT was 338x, and with respect to the SEM image (200x) was 1.69x. The latter magnification factor was used on all microstructures to determine the magnification on the PC-CRT given the magnification from the SEM.

## 6.2 Uniformity of Microstructure of an Al-Cu Alloy Droplet

In the following example a description is given of image processing of the Al-Cu microstructure in order to measure the SDAS. Figure 6-2a shows the surface morphology of a 460  $\mu\text{m}$  Al-17wt%Cu alloy powder, Figure 6-2b shows the cross-section of the same

sized powder and Figure 6-2c shows typical micrographs of the particle taken at its centre. These particles were obtained by atomizing at 970 K with impulses of 100 Hz and 51% maximum relative amplitude, using a nozzle design as shown in Figure 4-3b. The average orifice size was  $1.6 \times 10^{-4}$  m. The powders were atomized in nitrogen with oxygen content of 45 ppm.

The characteristic dendritic structure of aluminum alloys is evident with Al-rich dendrites (dark phase) surrounded by an interdendritic eutectic ( $\text{CuAl}_2 + \text{Al}$ ) phase having a lamellar structure. Figure 6-3a is the original TIFF image corresponding to the micrograph shown Figure 6-2c, as saved in the SEM. Figure 6-3b is the same image after processing in the image analysis system to obtain a binary (black and white) image. This conversion was achieved in a manner similar to the grid described in the previous section. The threshold and image filtering were carried out to eliminate noise in the digital image. The image processing settings for threshold and filtering varied from image to image depending on conditions such as contrast. The purpose here was to obtain a clear binary image with minimum distortion and noise, which could be converted into a skeleton, Figure 6-3c. A skeleton set, which appears to be from the same primary dendrite, was chosen and a line was drawn across the skeleton set, as perpendicular as possible to it. The luminance and (x,y) coordinates along each line were recorded. The FORTRAN program IMAGE.FOR was again used to select those coordinates along a line with the maximum luminance. This data corresponds to the intersection points between the lines and the skeletons (i.e. co-ordinates of SDAS from a primary dendrite). The spacing between each skeleton (SDAS) was then calculated. Eighty-eight Secondary Dendrite

Arm Spacings were measured in this picture. The average SDAS was  $5.10 \times 10^{-6}$  m with a corresponding standard deviation of  $1.16 \times 10^{-6}$  m (see Table 6.1).

This procedure of analysis results in a measurement of SDAS at a given region in a particle. When particles of the same size are mounted and polished, different regions of a particle may be analyzed. The size of the polished area on a particle is a measure of the particle depth where the microstructure is being examined. Thus a small and a large cross-section would be indicative of a region close to the particle surface or close to the centre of the particle, respectively. This analysis is carried out to determine if there are significant microstructural variations in a given particle. The results are shown in Tables 6-1 and 6-2. Figures 6-2c and 6-3 were both taken from the centre of a large particle cross-section. Similarly, the images were taken at the edge of a large particle cross-section and a small particle cross-section of a  $4.6 \times 10^{-4}$  m particle as shown in Figure 6-4 a and b respectively. Ninety-eight SDAS measurements were taken at the edge of a large particle cross-section. The average SDAS was  $5.43 \times 10^{-6}$  m with a standard deviation of  $1.07 \times 10^{-6}$  m. Ninety-one SDAS measurements of the small particle section averaged  $5.42 \times 10^{-6}$  m with a standard deviation of 1.32. These SDAS results are listed in Table 6-1. It is evident that the microstructure variation is not significant throughout the powder particle. This indicates that there is little segregation and the amount of mass transfer is minimum. Therefore, Assumption (12) in Chapter 3 is valid.

**Table 6-1 SDAS Measurement of a  $4.6 \times 10^{-4}$  m Al-17wt%Cu Droplet at Different Regions of a Particle**

	SDAS ( $10^{-6}$ m)	Number of Measurements	Standard Deviation
Centre of a large particle cross-section	5.10	88	1.16
Edge of a large particle cross-section	5.43	98	1.07
Small particle cross-section	5.42	91	1.32

**Table 6-2 SDAS Measurement of a  $5.5 \times 10^{-6}$  m Al-10wt%Cu Droplet at Different Regions of a Particle**

	SDAS ( $10^{-6}$ m)	Number of Measurements	Standard Deviation
Centre of a large particle cross-section	6.38	66	1.61
Edge of a large particle cross-section	5.67	75	1.56
Small particle cross-section	5.74	87	1.48

For Al-10wt%Cu alloy, the microstructure are shown in Figure 6-5 and the SDAS data is listed in Table 6-12. From the above result it is clear that the microstructure of the Al-Cu alloys within one droplet is quite uniform. Therefore, it is suitable to apply the lumped capacitance model or Newtonian model presented in Chapter 3 for the cooling of a droplet.

### 6.3 Reproducibility of Microstructure

Figure 6-6 a and b show the microstructure of droplets from different runs for Al-17wt%Cu atomized under the same operating conditions. The droplets were atomized at 970 K with an impulse frequency of 100 Hz and a relative amplitude of 32% maximum by impulse generator A. The average nozzle orifice sizes were  $1.4 \times 10^{-6}$  m and  $1.5 \times 10^{-6}$  m, respectively for both runs, with the nozzle design of Figure 4-3b. The atomization atmospheres were nitrogen with 25 ppm and 40 ppm oxygen content respectively. The resultant geometric mean size and standard deviation were  $3.96 \times 10^{-4}$  m and 1.29 respectively for both runs.

The average SDAS was  $5.09 \times 10^{-6}$  m with standard deviation of 1.27 from 126 measurements for Figure 6-6a, and  $5.29 \times 10^{-6}$  m with standard deviation of 1.01 from 87 measurements for Figure 6-6b, respectively.

During the experiment, inert gas was continuously purged into the atomizing chamber and bled out of it. The bottom cone was always at room temperature, therefore the ambient temperature in the tower away from the furnace did not change very much

from the beginning to the end of the run. Therefore, it is expected that within a single run the powder microstructure of the same sized particle will be the same at the start and end of a run when atomized under the same operating conditions.

#### **6.4 Effect of Particle Size on Microstructure of Al-Cu Alloys**

Al-17wt%Cu alloy powder was atomized at 970 K in a nitrogen atmosphere containing 45 ppm oxygen. A 7-hole nozzle design of  $1.6 \times 10^{-6}$  m in diameter was used. The average particle size and standard deviation of Al-17wt%Cu alloy were  $4.12 \times 10^{-4}$  m and 1.25 respectively. The particle size was taken as the mid-size of the sieve size range. The measured SDAS at the edge of particle for each size range of particles is shown in Figure 6-7 and listed in Table 6-3:

Similar results were obtained for Al-10wt%Cu alloy atomized at 1060 K with 100 Hz frequency and 32% maximum relative amplitude. The average nozzle size was  $2.5 \times 10^{-6}$  m with a nozzle design as shown in Figure 4-3b. The droplets were produced in nitrogen with 80 ppm oxygen. The nozzle to impulse applicator distance was  $1.7 \times 10^{-3}$  m. The effect of particle size on the Secondary Dendrite Arm Spacing measured at the edge of the droplets is shown in Figure 6-8 and in Table 6-4. Clearly, the SDAS increases with increasing particle size. These results are consistent with the trend in the literature as shown in Equation (27).

**Table 6-3 Effect of Particle Size on SDAS of Al-17wt%Cu Alloys**

Particle Size ( $10^{-6}$ m)	Measurement			
	SDAS ( $10^{-6}$ m)	Geometric Standard Deviation	Total Number of Measurement	Under Cooling Temperature (K)
230	3.26	0.74	120	64
330	4.74	1.22	151	53
460	5.43	1.07	98	44
660	6.45	1.50	53	38

**Table 6-4 Effect of Particle Size on SDAS of Al-10wt% Cu Alloys**

Particle Size ( $10^{-6}$ m)	Measurement			
	SDAS ( $10^{-6}$ m)	Geometric Standard Deviation	Total Number of Measurements	Under Cooling Temperature (K)
140	3.00	0.94	264	73
200	3.48	0.90	178	58
280	4.81	1.26	95	47
390	5.14	1.29	125	38
550	5.67	1.56	75	30
760	6.72	1.37	52	24

## **6.5 Effect of Superheat on Microstructure of Al-10wt%Cu Alloys**

Four atomization experiments were carried out with Al-10wt%Cu at four different melt temperatures. The nozzle design used in all the runs is shown in Figure 4-3b with a nominal orifice size of  $2.5 \times 10^{-4}$  m. The nozzle to impulse applicator distance was  $1.7 \times 10^{-3}$  m. The frequency used was 100 Hz and the relative amplitude was 32% maximum. The first was atomized at 960 K in nitrogen (100 ppm oxygen) which corresponds to 50 K superheat; the second at 1010 K in nitrogen with 110 ppm oxygen (i.e. 100 K superheat); the third at 1060 K corresponding to 150 K superheat (nitrogen with 80 ppm oxygen); and the fourth at 1110 K corresponding to 200 K superheat (nitrogen with 15 ppm oxygen). Figure 6-9 and Table 6-5 show the effect of superheat on SDAS of Al-10wt%Cu alloys in the size range of  $5 \times 10^{-4}$  m to  $6 \times 10^{-4}$  m. The trend shows that the higher the superheat, the finer the microstructure. This is true even though the error involved in the SDAS measurement was large because of the varied orientations of dendrite arms. This result is in agreement with the literature result for an aluminium alloy described in Section 2.3.2.



**Table 6-5 Effect of Superheat on SDAS of Al-10wt% Cu Alloys**

Superheat (K)	Measurement		
	SDAS ( $10^{-6}$ m)	Standard Deviation	Total Number of Measurement
50	8.25	2.25	131
100	6.83	1.41	53
150	6.43	1.64	193
200	5.55	1.33	89

## 6.6 Microstructural Analysis of Al-Cu Powders

### 6.6.1 Cooling Rate versus SDAS Relationship Based on Literature

Table 2-2 shows the effect of cooling rate on the SDAS of Al-10wt%Cu, Al-15wt%Cu, and Al-20wt%Cu alloys respectively [Horwath and Mondolfo, 1962]. Regressions were performed on these results to obtain the relationship between cooling rate and SDAS for each of the three alloys. Interpolation was performed for Al-17wt%Cu alloy by using the data of Al-15wt%Cu and Al-20wt%Cu alloys. The regression results on  $\log \lambda_2$  are:

$$\lambda_2 = 124 T_c^{-0.32} \quad (103)$$

for Al-10wt%Cu alloy with a regression coefficient of 0.99 and

$$\lambda_2 = 86 T_c^{-0.28} \quad (104)$$

for Al-17wt%Cu alloy with a regression coefficient of 0.99. After the cooling rates,  $T_c$ , have been calculated using the model described in Chapter 3, the Secondary Dendrite Arm Spacings can be predicted using Equations (103) and (104) for Al-10wt%Cu and Al-17wt%Cu alloys respectively. This calculated SDAS is essentially a predicted SDAS which will be compared with SDAS measured from the atomized powder. These predicted and measured SDAS results will be shown in the next section and Tables 6-6 and 6-7.

### **6.6.2 Calculated Cooling Rates from the Model and Estimated SDAS According to the Literature**

A Newtonian cooling model was developed for Al-Cu binary alloys based on the following assumptions which were described in Chapter 3. A spherical droplet solidifies with a given amount of undercooling, crystal growth occurs from a single nucleus, the thermophysical properties can be evaluated using a weighted average of each element in the alloy, and radiation losses are neglected.

It was shown in Section 6.2 that the microstructure within a droplet is nearly uniform. Therefore, the lump capacitance model is valid for treating the solidification of Al-Cu droplets produced by IAP.

Droplet velocity at a fixed position in the atomizing chamber was measured using a high-speed shutter video camera as described in Chapters 3 and 4. The initial velocity of the droplet was back calculated given the position of the camera below the nozzle plate. Using the cooling model, the cooling curve of a  $3.3 \times 10^{-4}$  m Al-17wt%Cu droplet was then calculated as shown in Figure 3-9. The droplet loses its superheat and undercools until a given assumed nucleation temperature,  $T_n$  (53 K), is reached, then solidification begins. Recalescence takes place since the amount of latent heat released at the beginning of solidification is too large to be completely released to the environment by convection. Part of this latent heat is used to reheat the droplet until the temperature reaches the recalescence temperature,  $T_r$ , at which point the rate of heat convected to the

environment is equal to the rate of latent heat generated during solidification. After this more pro-eutectic phase will be formed followed by the eutectic phase transformation at  $T_e$ . Finally the temperature of the solidified particle is reduced by convection.

From this calculated cooling curve, the average solidification cooling rate of the Al-17wt%Cu droplet can be estimated to be 499 K/s. Substituting this cooling rate into Equation (104) yields a Secondary Dendrite Arm Spacing of  $4.80 \times 10^{-6}$  m. Equation (104) was obtained based on the literature information as shown in Section 6.6.1 [Horwath and Mondolfo, 1962]. This is called predicted SDAS. SDAS can also be measured using image analysis described in Section 6.2. Table 6-6 shows two examples of these results. From this table it is seen that the predicted SDAS is in good agreement with measured SDAS, considering many assumptions made in the model.

Similarly, two examples of Al-10wt%Cu alloy droplets of different superheat are shown in Table 6-7. The predicted SDAS are calculated using Equation (103) from cooling rates, which were calculated by running the model presented in Chapter 3. The amount of undercooling was adjusted by particle size but not by superheat, since the information of how much undercooling is increased with increasing superheat is not available. As shown before, Figure 3-6 shows that the predicted SDAS decreased  $6 \times 10^{-7}$  m from 0 to the maximum undercooling.

These results also show a good agreement between predicted SDAS and measured SDAS and are also in agreement with the results of Marcantonio and Mondolfo [Marcantonio and Mondolfo, 1974] and Mondolfo and Barlock [Mondolfo and Barlock, 1975]. This means at higher superheat, the chances of removing nucleants are higher,

thereby giving a higher possibility of homogeneous nucleation. The system will freeze at higher undercoolings and therefore at a faster rate.

Comparing the calculated cooling rates and the assumed undercooling (53 K) with Figure 2-12b, the results are also in reasonably good agreement.

**Table 6-6 Comparison between Measured and Predicted SDAS as a Function of Particle Diameter for an Al-17wt% Cu Alloy**

Particle Diameter ( x 10 <sup>-6</sup> m)	SDAS ( x 10 <sup>-6</sup> m)	
	Measured	Predicted
460	5.43±1.07	5.52
330	4.74±1.22	4.85

**Table 6-7 Comparison between Measured and Predicted SDAS as a Function of Superheat for an Al-10wt% Cu Alloy**

(Particle Diameter = 5.5 x 10<sup>-4</sup> m)

Superheat (K)	SDAS ( x 10 <sup>-6</sup> m)	
	Measured	Predicted
100	6.83±1.41	6.66
150	6.43±1.64	5.90

## **6.7 Effect of Particle Size on the Microstructure of Al-Ni-Fe Powder**

**Al-3.7wt%Ni-1.5wt%Fe alloy was atomized by impulse generator A at 1040 K in nitrogen with 10 ppm oxygen content. A single  $2.5 \times 10^{-4}$  m hole nozzle (Figure 4-3a) was used. The nozzle-impulse applicator distance was  $1.7 \times 10^{-3}$  m. The droplets were atomized using 100 Hz frequency and 48% maximum relative amplitude impulse into nitrogen with 10 ppm oxygen. In order to ensure complete dissolution of the solute in aluminum, the alloys were held for 9000 s and vibrated for 2700 s with low amplitude above their melting temperature before atomization.**

**The apparent density of the Al-3.7wt%Ni-1.5wt%Fe powder, was  $1.7 \times 10^3$  kg/m<sup>3</sup> and the flow rate was  $55 \text{ s}/50 \times 10^{-3}$  kg determined by the Standard Test Methods for Metal Powders and Powder Metallurgy Products [MPIF Standard 04 and 05, 1985]. Powders atomized under the above conditions were spherical. Powders atomized by IAP were sieved and the size distribution plotted using log-normal plots. Figure 6-10 shows that the average particle size of Al-3.7wt%Ni-1.5wt%Fe is  $4.2 \times 10^{-4}$  m with a small standard deviation of 1.14.**

**Figure 6-11a shows the surface morphology of a  $2.5 \times 10^{-4}$  m Al-3.7wt%Ni-1.5wt%Fe droplet produced in nitrogen. Al-3.7wt%Ni-1.5wt%Fe droplets typically solidified into a duplex microstructure as shown in Figure 6-11b. This duplex microstructure indicates that the lumped capacitance model is not valid for this alloy. The modelling of a ternary alloy would be very complicated and was not attempted in this thesis. Solidification appears to have initiated in an internal part of the droplet and began**

to grow in a cellular eutectic structure as shown in Figure 6-11b. As the solidification progresses, the dendritic microstructure begins to develop and covers the rest of the particle (Figures 6-11b and 6-12) [Hildeman, 1982]. SDAS was measured in the dendritic region of each particle as shown in Figure 6-12 in a similar way to that carried out with the aluminum-copper alloys. About three hundred measurements were performed on three to four different micrographs for each data point. The measured results together with standard deviation are plotted in Figure 6-13.

#### **6.8 Effect of Atomization Atmosphere on Microstructure of Al-Ni-Fe System**

Similar microstructural analysis was performed for an atomization run of Al-3.7wt%Ni-1.5wt%Fe system in helium. A 7-hole nozzle as shown in Figure 4-3b was used with a nominal hole size of  $5 \times 10^{-4}$  m. The atomization temperature was 1040 K, the frequency was 100 Hz, the relative amplitude was 29% maximum.

The particle size distribution is shown in Figure 6-14 which corresponds to a geometric mean size of  $4.12 \times 10^{-4}$  m and geometric standard deviation of 1.25. The powder flow rate was  $10.97 \text{ s}/50 \times 10^{-3} \text{ kg}$  and the apparent density was  $1.7 \times 10^{-3} \text{ kg/m}^3$  by using the Carney funnel (it did not flow through the Hall funnel).

Figure 6-15 shows the microstructure of the alloy atomized in helium for different particle-size ranges. Helium has larger thermal conductivity than nitrogen, hence finer microstructure was obtained for the same particle size. The measurement results are shown in Figure 6-13. Similarly about three hundred measurements were performed on



three to four different micrographs on each data point. Figure 6-16 shows very fine lamellar eutectic microstructure (about  $1 \times 10^{-7}$  m spacing) of a  $3.3 \times 10^{-4}$  m Al-3.7wt%Ni-1.5wt%Fe droplet produced by IAP in helium.

#### **6.9 Microstructural Analysis of Al-Ni-Fe Powders**

The relationship between SDAS and powder size shown in Figure 6-13 for Al-3.7wt%Ni-1.5wt%Fe alloy powders follows the general relationship of Equation (27) described in Section 2.3.5. That is, the SDAS increases with increasing particle size following a power law relationship.

Experimental results of gas atomized powders processed by Alcoa and centrifugally atomized powders were also plotted [Hildeman et al, 1983]. The straight lines are the curve fit for these two sets of data. Table 6-8 shows the regression results using best fit for three of these atomization techniques by assuming a power relationship between SDAS and the particle size as shown in Equation (27). It is clearly seen that the slopes for IAP in Figure 6-13 are smaller than that for centrifugal atomization and gas atomization, which means that for the same particle size produced, especially in the large particle size range, the microstructure obtained by IAP is finer than that by centrifugal and gas atomization. The difference was caused by the difference in process conditions. Had the conditions been the same, same microstructure would have been obtained for the same particle size.

The SDAS for a few size ranges of Al-3.7wt%Ni-1.5wt%Fe alloy powders produced by IAP were also measured and compared with published results obtained by gas and centrifugal atomization processes. The measured SDAS for three different particle sizes atomized in nitrogen using IAP were plotted as shown in Figure 6-13. Because of the difference the dendrite arm orientation, the error bar in SDAS measurements are fairly large. It is not possible to distinguish the orientation of the dendrite arms and take the orientation difference into account in the SDAS measurement. The error bar would be shorter if the number of images taken from each particle size were statistically large enough and the standard deviation of the measurements were calculated from the average SDAS of each image. The SDAS of powders made by IAP are finer than the corresponding ones made by air atomized and centrifugally atomized powders. For example, for a  $3.3 \times 10^{-4}$  m particle size, the SDAS is about  $6.5 \times 10^{-6}$  m by gas and centrifugal atomization,  $4.5 \times 10^{-6}$  m by IAP in nitrogen, and  $2.8 \times 10^{-6}$  m by IAP in helium. This may be due to intense stirring of the melt, thus reducing the number of nucleants and involving larger undercooling in IAP atomized powders. Alternatively, the stagnant gas into which droplets are atomized may enhance the amount of undercooling. In gas and centrifugal atomization there is a great deal of turbulence in the atomizer, resulting in many droplet-particle collisions, with large droplets starting to solidify at lower undercooling than might otherwise be the case in the absence of collisions. In either case, a finer microstructure results for IAP powders than would occur with similar-sized powders of gas and centrifugal atomization processes.

**Table 6-8 Linear Regression Results for  $\lambda_2 = a_2 D^{b_2}$  for Al-3.7wt%Ni-1.5wt%Cu from Various Atomization Techniques**

Atomization Method	$a_2$	$b_2$
Gas and Centrifugal Atomized	0.02	1.04
IAP He atomized	0.13	0.53
IAP N <sub>2</sub> atomized	0.26	0.49

## **CHAPTER 7: SUMMARY**

**A novel technique, Impulse Atomization Process (IAP), was developed and patented [Yuan et. al, 1997]. In IAP, an impulse force is applied at a given frequency to a melt in a crucible. This force is sufficient to push the fluid through an orifice at the bottom of the crucible, thereby forming an elongated jet of finite length. The frequency of generation of these jets corresponds to the frequency of the applied impulse. This same impulse source also applied a disturbance in the discontinuous jet.**

**IAP can provide tailored droplet sizes and size distribution and shows good reproducibility. Both the average size and the standard deviation of the powders produced by IAP can be controlled over a wide range by changing the atomizing conditions. It differs fundamentally from both the continuous jet method and the drop-on-demand method. Unique features of IAP can be summarized as follows:**

- 1. IAP produces droplets with a narrow size distribution. The typical geometric standard deviation values in this work are between 1.2 and 1.5.**
- 2. IAP produces droplets that are reproducible. The typical geometric mean size is within  $2 \times 10^{-5}$  m for  $5 \times 10^{-4}$  m powder and the typical standard deviation is within 5%.**

3. **The geometric droplet mean size atomized using IAP decreases and the geometric standard deviation increases with increasing vibration frequency.**
4. **The geometric droplet mean size atomized using IAP decreases and the geometric standard deviation increases with increasing relative amplitude.**
5. **The geometric droplet mean size atomized using IAP decreases and the geometric standard deviation increases with increasing acceleration.**
6. **The geometric droplet mean size atomized using IAP increases and the geometric standard deviation decreases with increasing orifice size.**
7. **Different nozzle-impulse applicator distances also change both geometric mean size and geometric standard deviation.**
8. **Increasing superheat slightly reduces the size of droplets produced by IAP, while the geometric standard deviation is almost unchanged.**
9. **The particle shape can also be controlled.**
10. **A narrower size distribution and smaller droplets are produced with a single orifice at the centre of the nozzle, compared with a nozzle with seven orifices in a row.**
11. **Higher throughput is obtained with higher acceleration of the plunger. The nominal flow rate of molten metal is comparable to that for gas atomization.**
12. **Higher throughput is achieved with a larger orifice size.**
13. **IAP is very flexible. It also works for highly viscous materials such as Selenium. The mathematical model showed that a smaller diameter plunger was required for highly viscous material. The physical model predicted under conditions the molten Selenium can be atomized.**

14. **The microstructure of powders produced by IAP is generally uniform within a droplet and from one experiment to another under the same atomization conditions.**
15. **The SDAS of a droplet is finer as the melt superheat is increased from 50 K to 200 K.**
16. **The SDAS of Al-3.7wt%Ni-1.5wt%Fe alloy powders atomized using IAP is smaller than that achieved using gas and atomization. This suggests that for the same size droplets, larger undercoolings result when using IAP rather than gas atomization.**
17. **Finer SDAS of Al-3.7wt%Ni-1.5wt%Fe droplets are obtained by atomizing them into helium instead of nitrogen.**
18. **Conventional materials are used to construct the crucible and nozzle.**
19. **Molten fluids at temperatures to 1900 K can be atomized with the current apparatus.**
20. **IAP produces multiple droplets per impulse.**
21. **The efficiency of IAP is comparable with that of gas atomization.**

#### **Future Work**

**The development of IAP is far from complete. More research is required in order to better understand the technique. Some future work is suggested for this Impulse Atomization Process.**

**The nozzle plates and the precess should be modified to produce finer droplets.**

**In addition to the experimental parameters studied in this thesis, other parameters such as orifice shape, the interfacial tension of the nozzle, and the melt head should be investigated.**

**A non-Newtonian model should be developed, especially for Al-Ni-Fe system where the microstructure within a droplet is not uniform. The assumption for the amount of droplet undercooling needs to be further verified and adjusted.**

**Conditions to produce finer droplets should be also developed.**

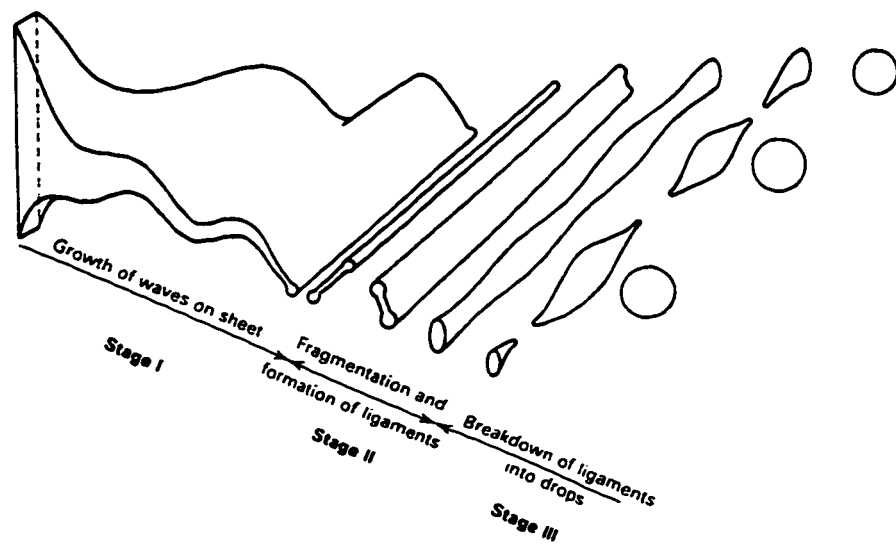


Figure 2-1. Schematic representation of the disintegration of a liquid sheet by a high velocity gas jet. Stage I: Growth of waves on a sheet; stage II: Fragmentation and formation of ligaments; stage III: Breakdown of ligaments into drops. [Dombrowski and Johns, 1963]



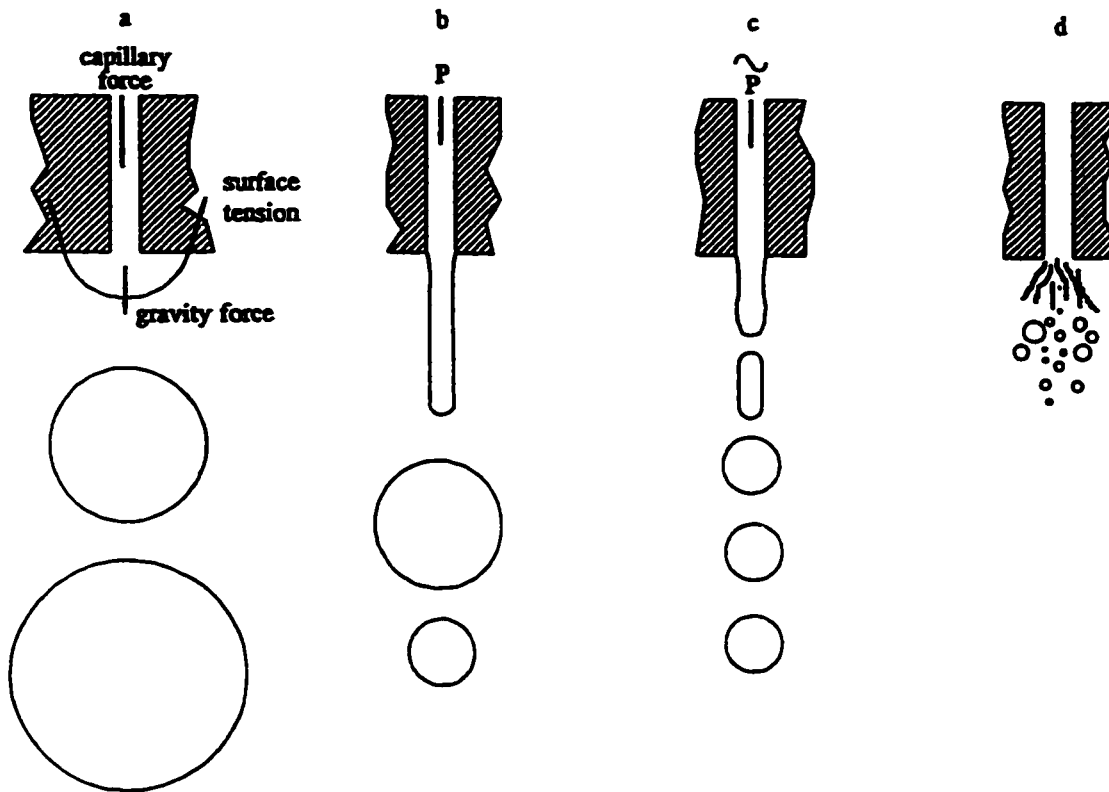


Figure 2-2. Mechanisms of droplet disintegration. [Schmidt, 1967]

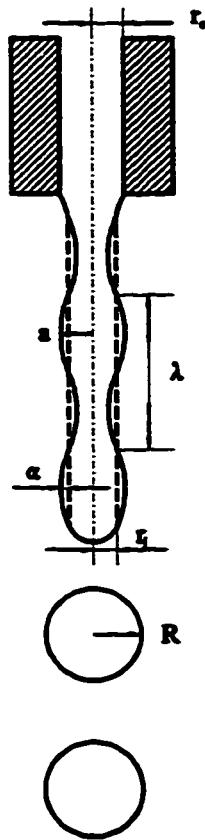


Figure 2-3. Disintegration of a liquid jet under the action of vibration.

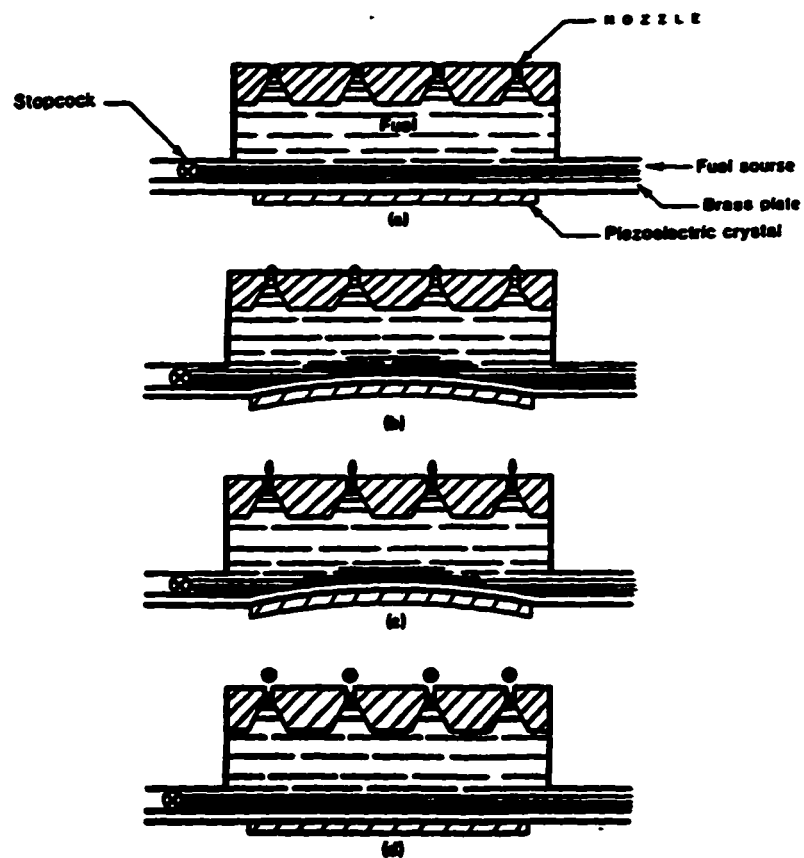


Figure 2-4. Drop-on-demand mode operating sequences: a. rest position; b. early injecting position; c. later injecting position; d. refilling position. [Ashgriz and Yao, 1987].

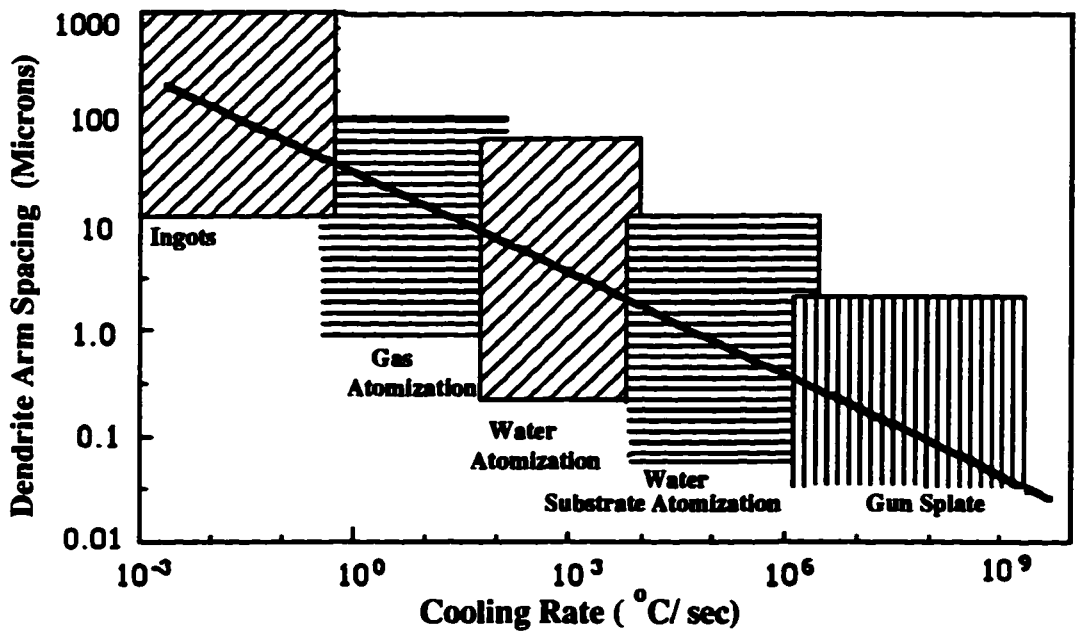


Figure 2-5. Dendrite arm spacing as a function of cooling rate for aluminum & aluminum alloys. [Grant and Perlloux, 1983]

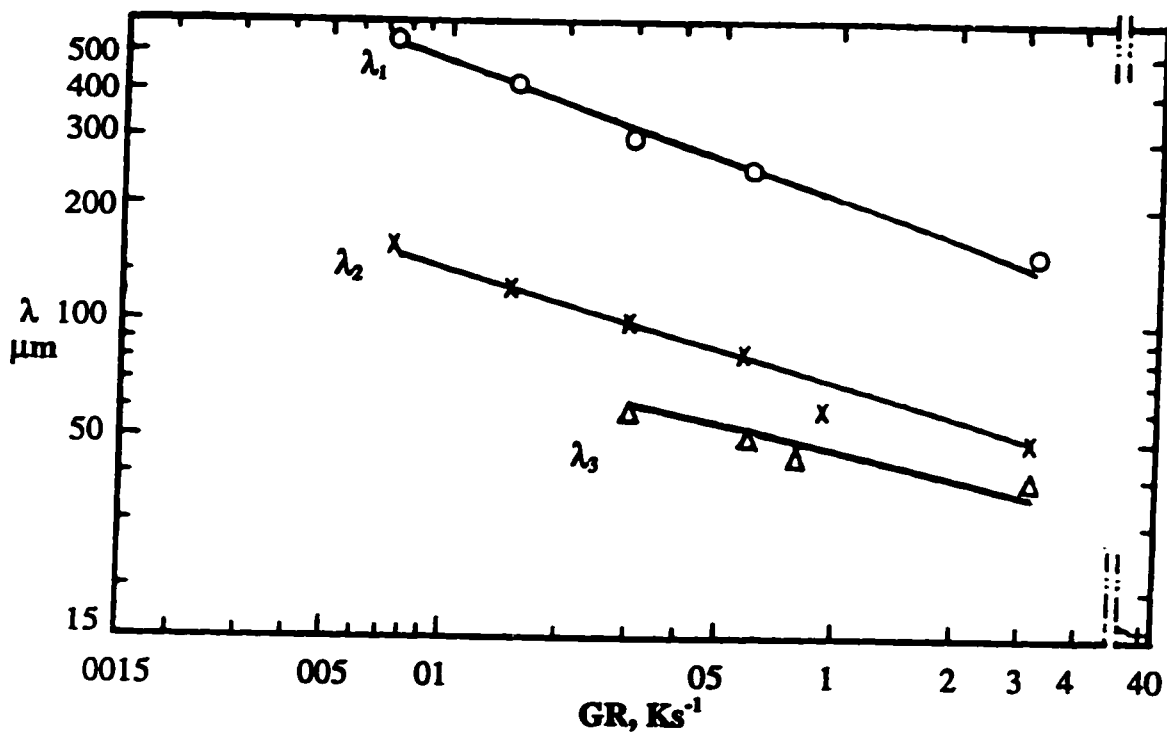


Figure 2-6. Effect of cooling rate on primary dendrite arm spacing  $\lambda_1$ , secondary dendrite arm spacing  $\lambda_2$  and tertiary dendrite arm spacing  $\lambda_3$  of Al-5.7wt%Cu alloy. [Taha, 1979]

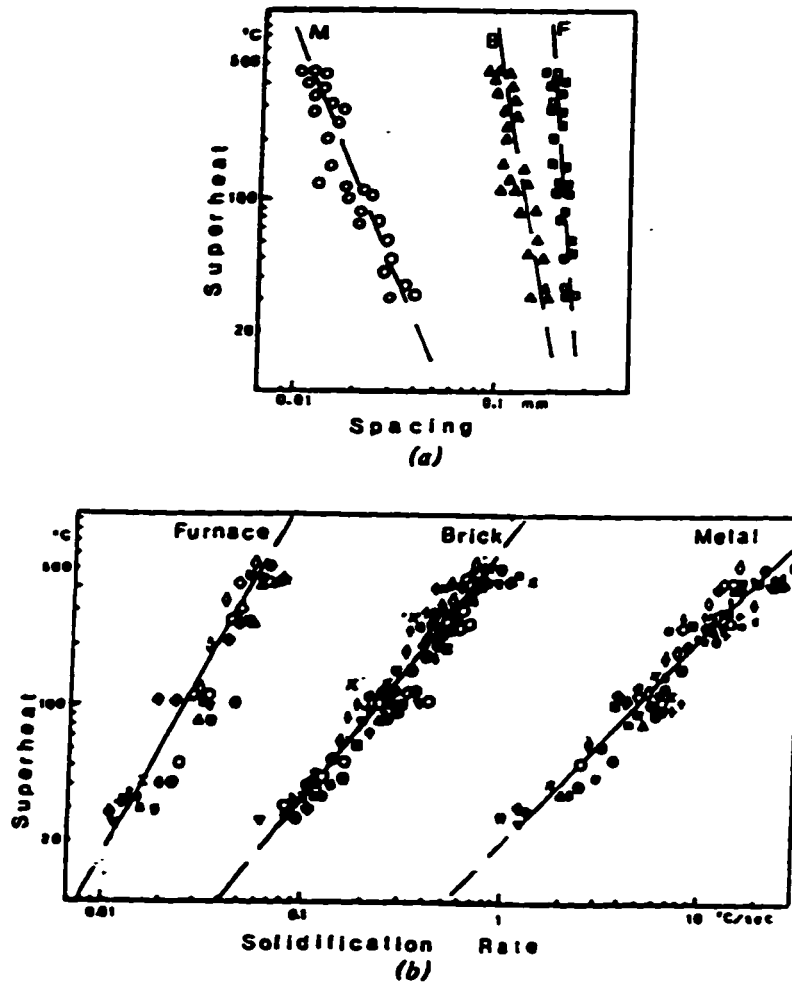


Figure 2-7. (a) Dendrite spacing of 3003 aluminum alloy as function of superheat, M=metal mold, B=brick mold, F=furnace cooled; (b) solidification rate as function of superheat for various aluminum alloys cast in the metal and insulating brick mold and furnace cooled. [Mondolfo and Barlock, 1975]

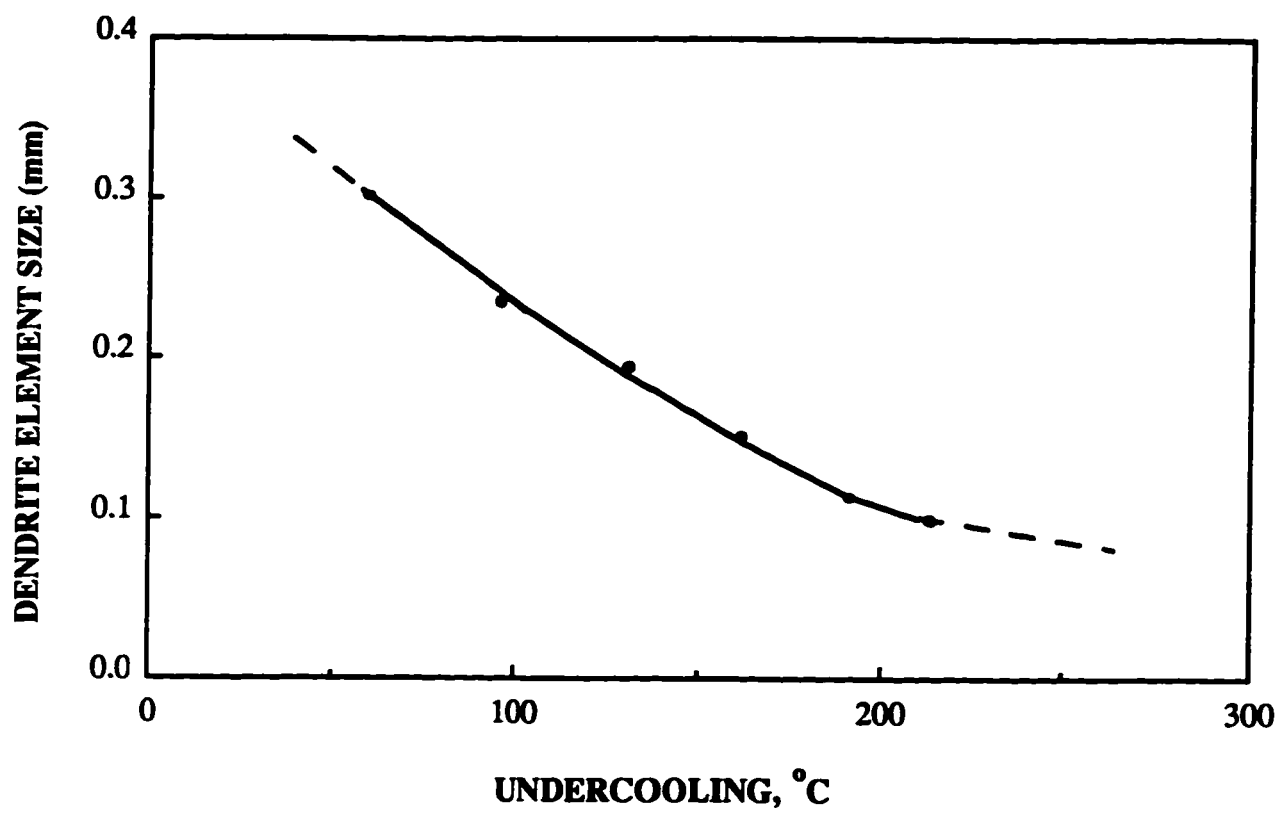


Figure 2-8. Relationship between undercooling and dendrite-element size in pure copper ingots. [Jones, 1972]

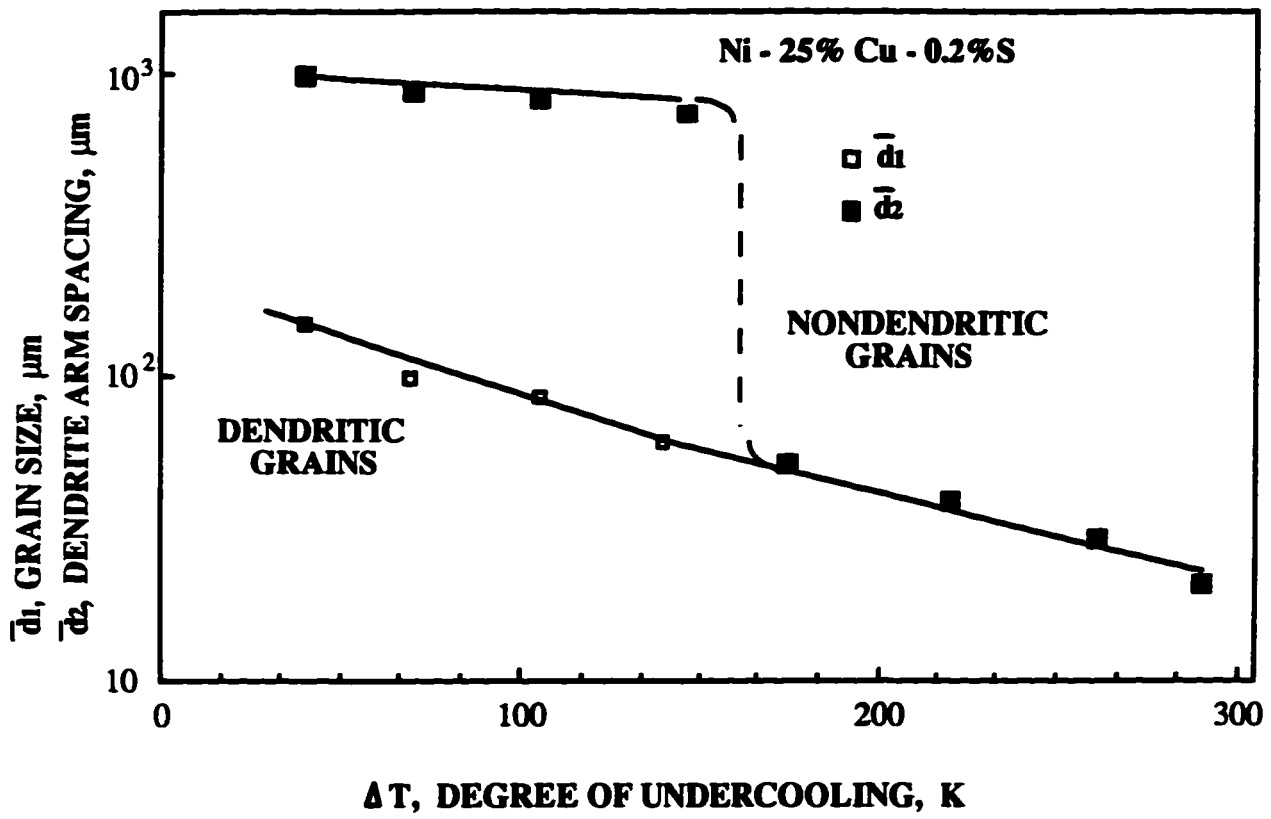


Figure 2-9. Dendrite arm spacing for dendritic specimens and grain size for both dendritic and nondendritic specimens versus degree of undercooling. Ni-25%Cu-0.2%S alloy. [Skolianos et al, 1982]



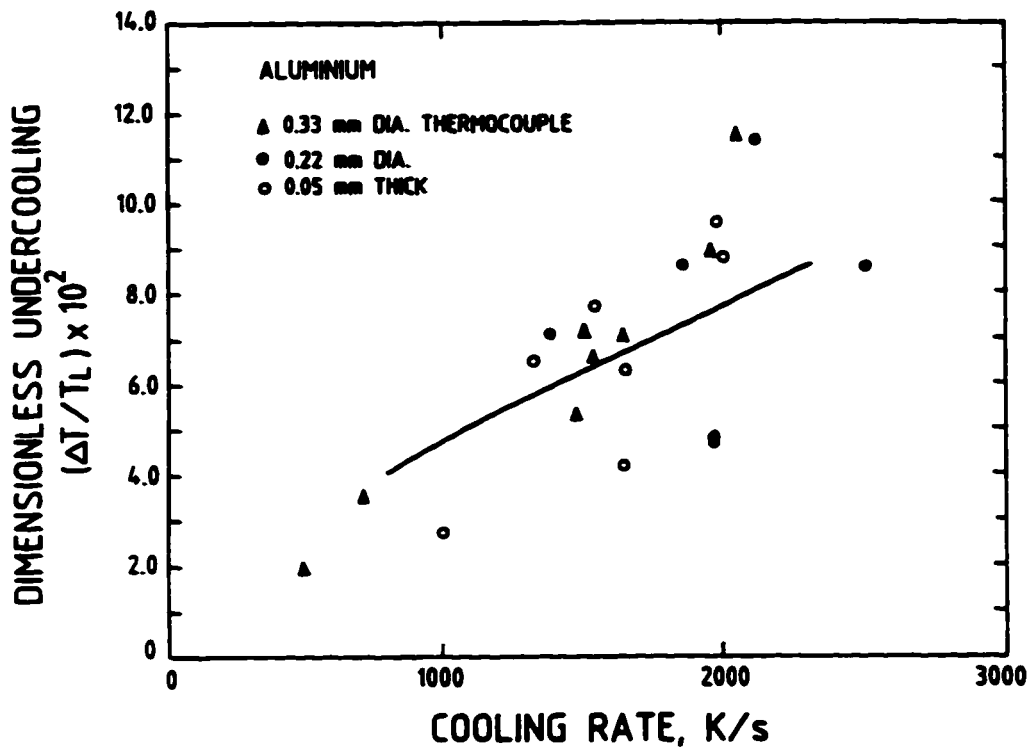


Figure 2-10. Dimensionless undercooling  $(\Delta T/T_L \times 10^2)$  versus cooling rate for aluminium.  $\Delta T$  and  $T_L$  represent undercooling and equilibrium melting temperature respectively. [Reddy and Sekhar, 1989]

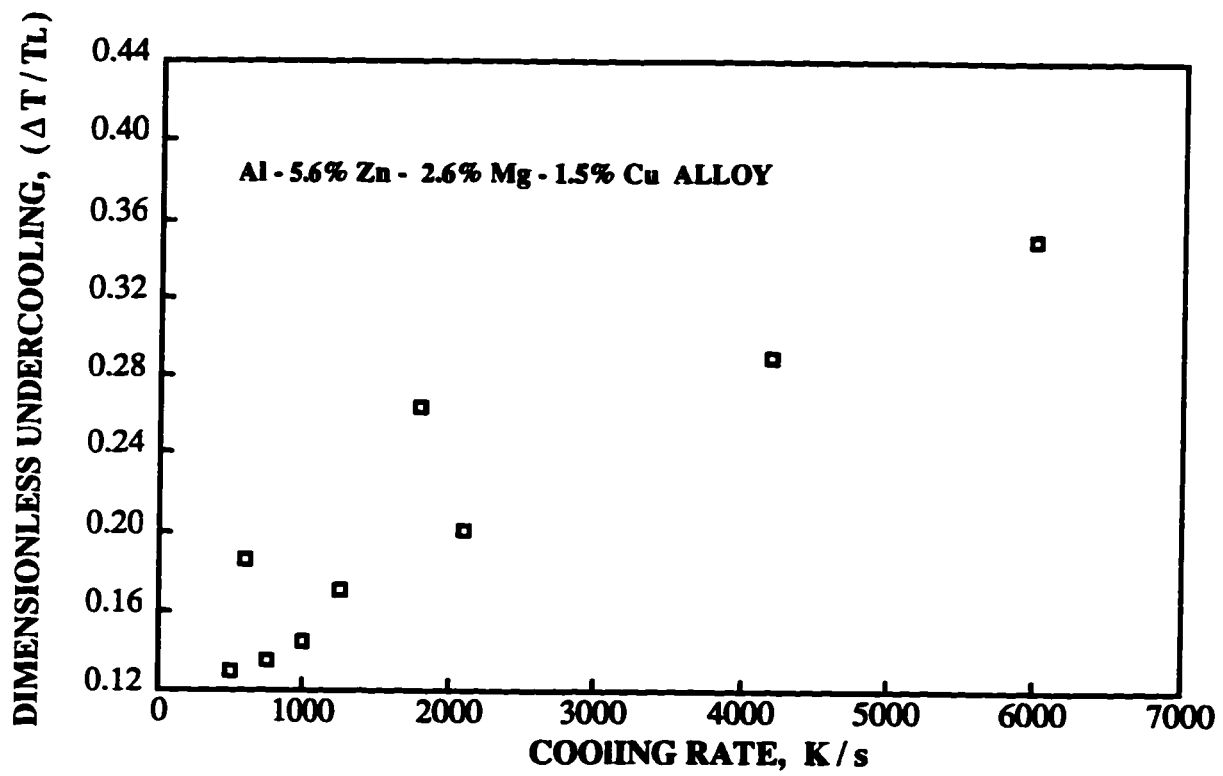


Figure 2-11. Dimensionless undercooling versus cooling rate for Al-5.6%Zn-2.6%Mg-1.5%Cu alloy. [Reddy and Sekhar, 1989]

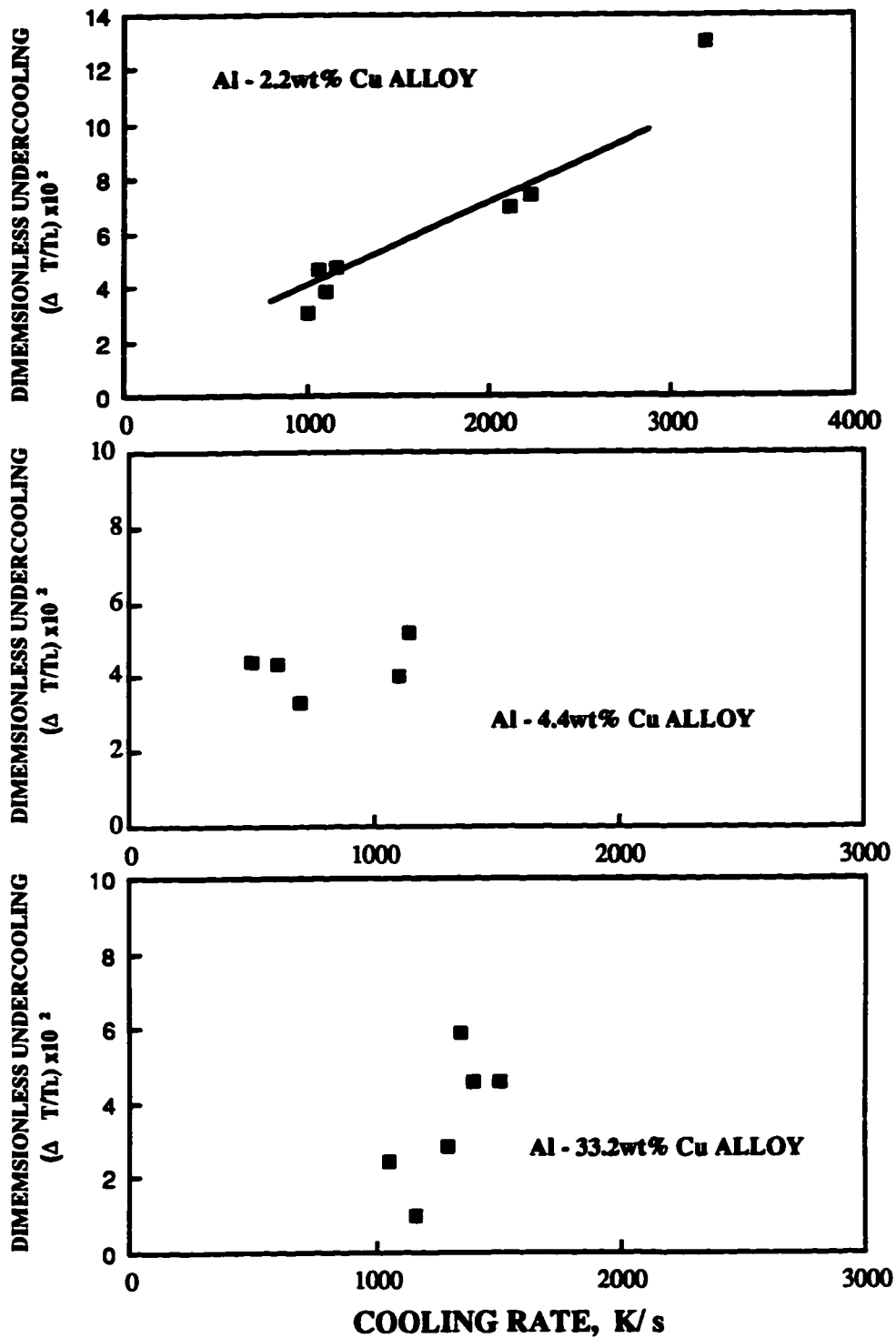


Figure 2-12. Dimensionless undercooling versus cooling rate for the aluminum copper alloys solidified under an applied pressure of 277.3 MPa; (a) Al-2.2wt%Cu (b) Al-4.4wt%Cu (c) Al-33.2wtCu. [Reddy and Sekhar, 1989]

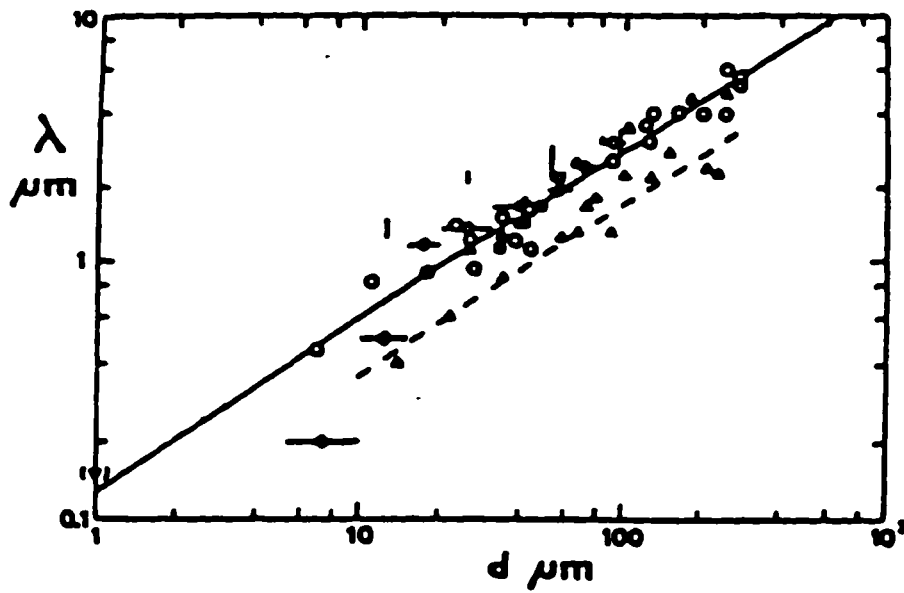


Figure 2-13. Dendrite arm spacing (secondary) as a function of powder particle diameter for high strength aluminum alloys. [Jones, 1986]

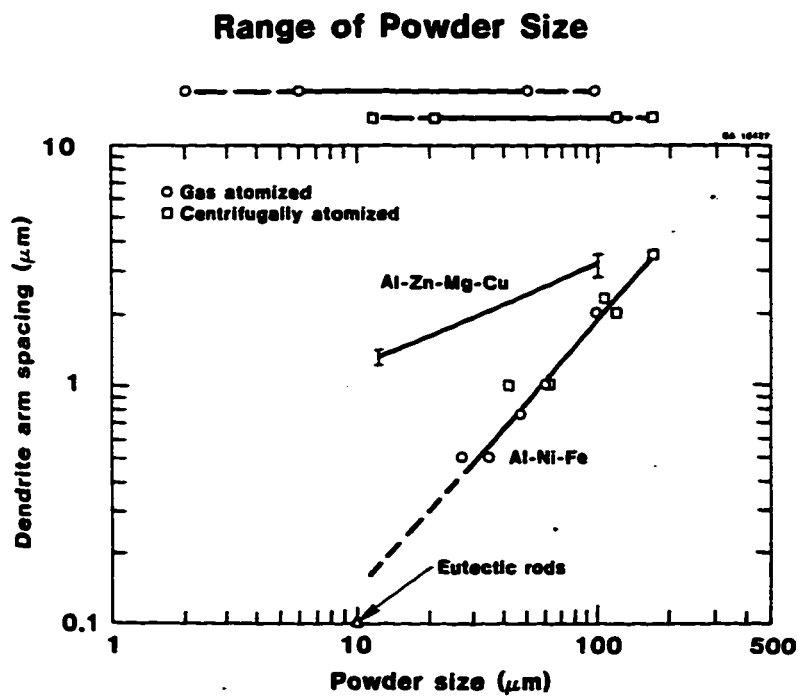


Figure 2-14. Dendrite arm spacing as a function of powder particle diameter for Al-3.7wt%Ni-1.5wt%Fe alloy. [Hildeman et al, 1983]

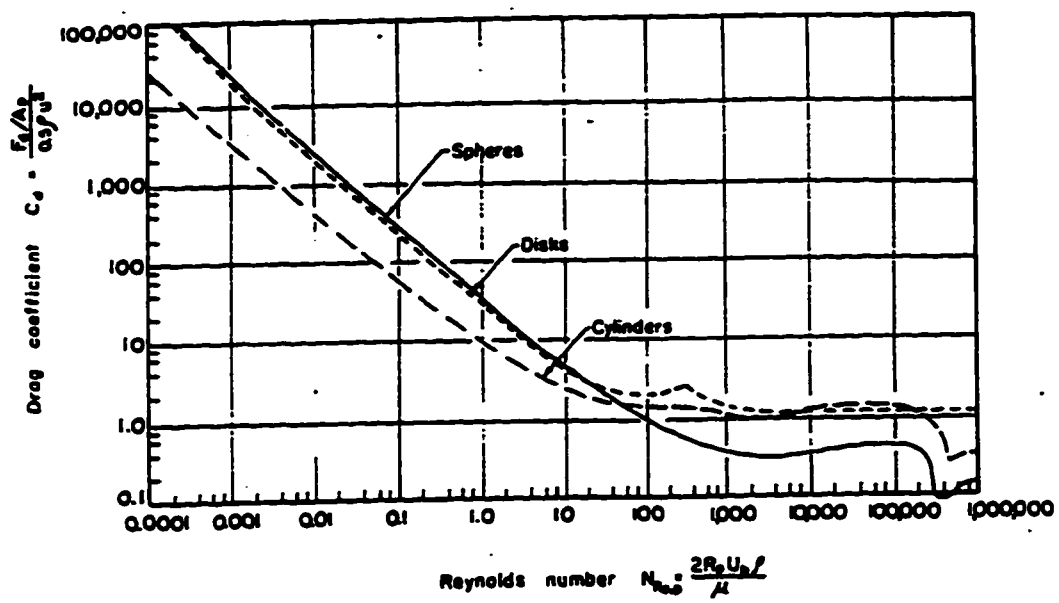


Figure 2-15. Plot of the drag coefficient against the particle Reynolds number. [Szekely, 1979]

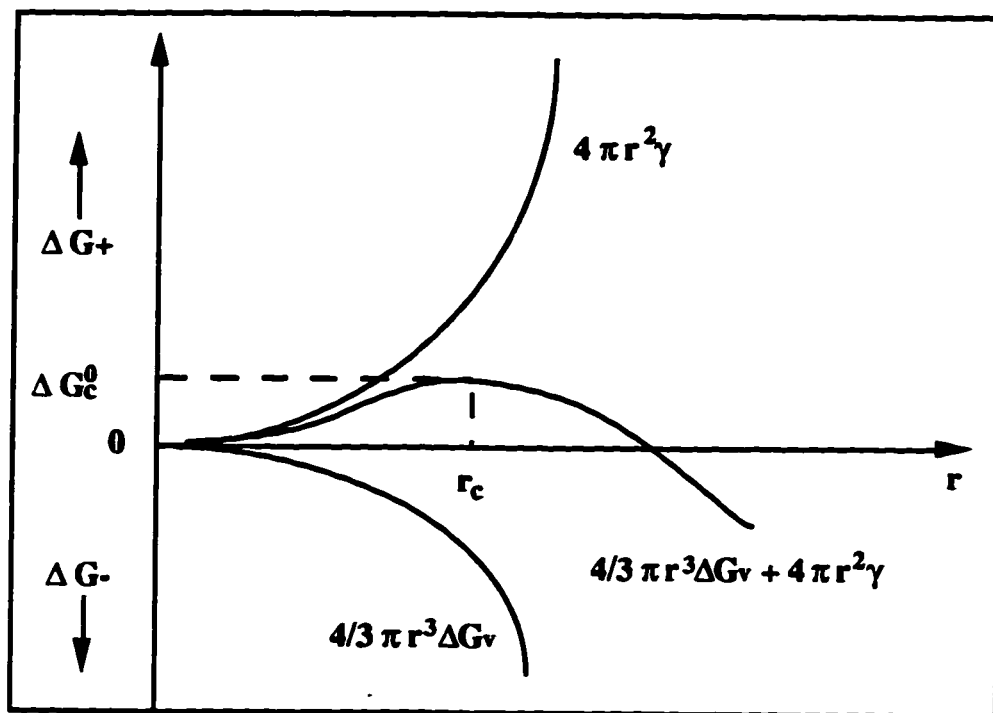


Figure 2-16. Free energy change during nucleation. [Minkoff, 1986]

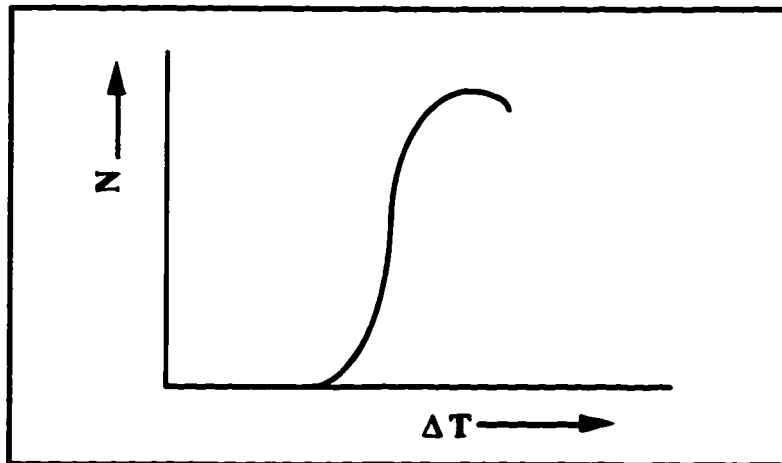


Figure 2-17. Relationship between nucleation rate and undercooling. [Liu, 1980]



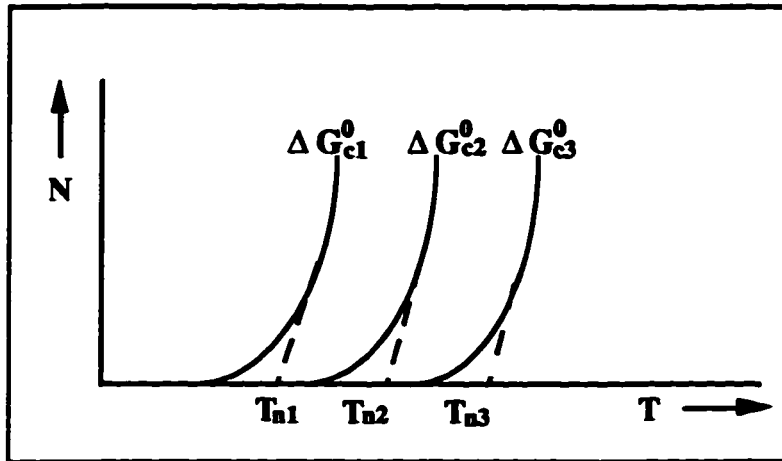


Figure 2-18. The dependence of nucleation temperature  $T^*$  on critical energy barrier  $\Delta G^*$ . For large values of  $\Delta G^*$ , as for example in homogeneous nucleation ( $\Delta G_3^*$ ),  $T^*$  will give a maximum value to undercooling. [Minkoff, 1986]

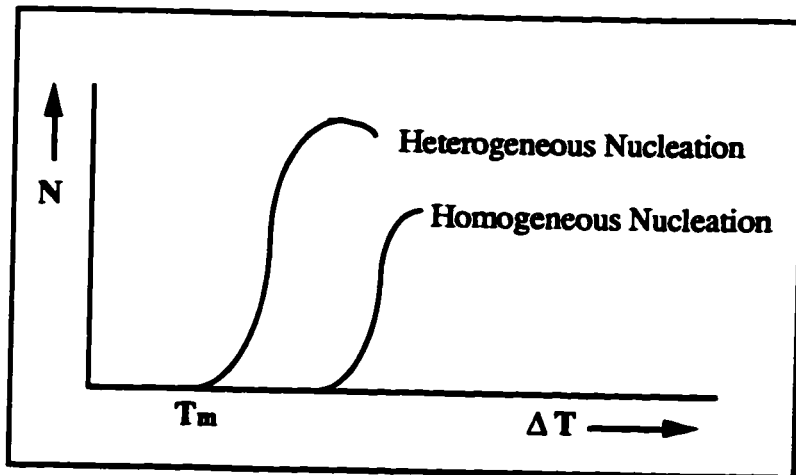


Figure 2-19. Schematic of dependence of nucleation rate on undercooling. [Liu, 1980]

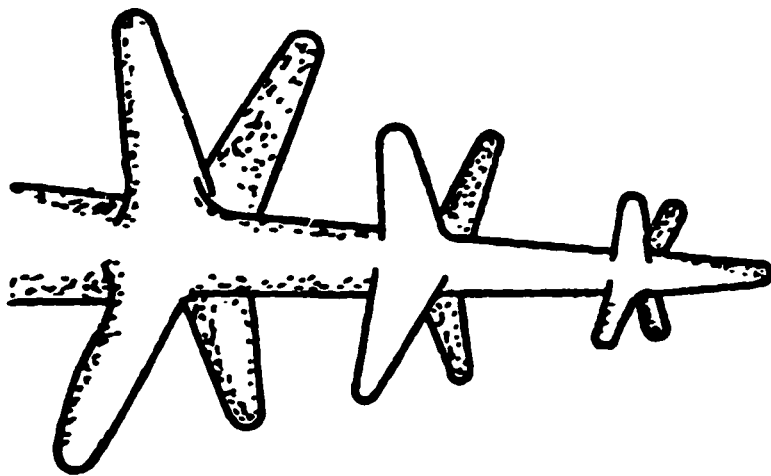


Figure 2-20. Schematic of a dendrite. [Liu, 1980]

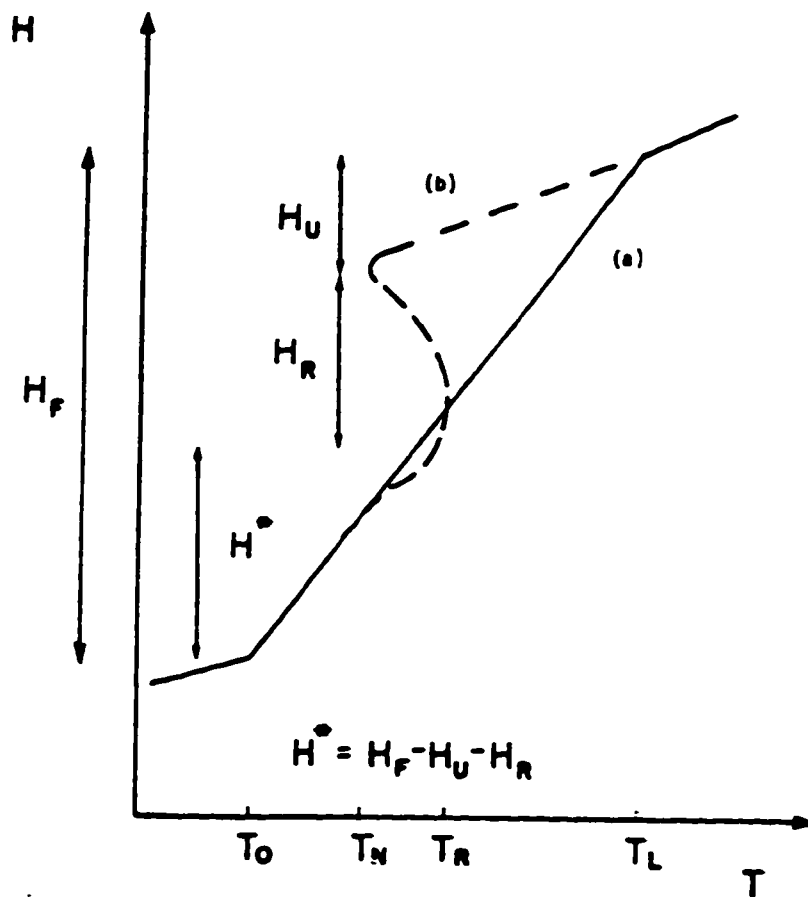


Figure 2-21. Schematic enthalpy versus temperature diagram for cooling and solidification of small alloy droplet for (a) equilibrium freezing and (b) freezing from an undercooled melt. [Lavernia et al, 1988]

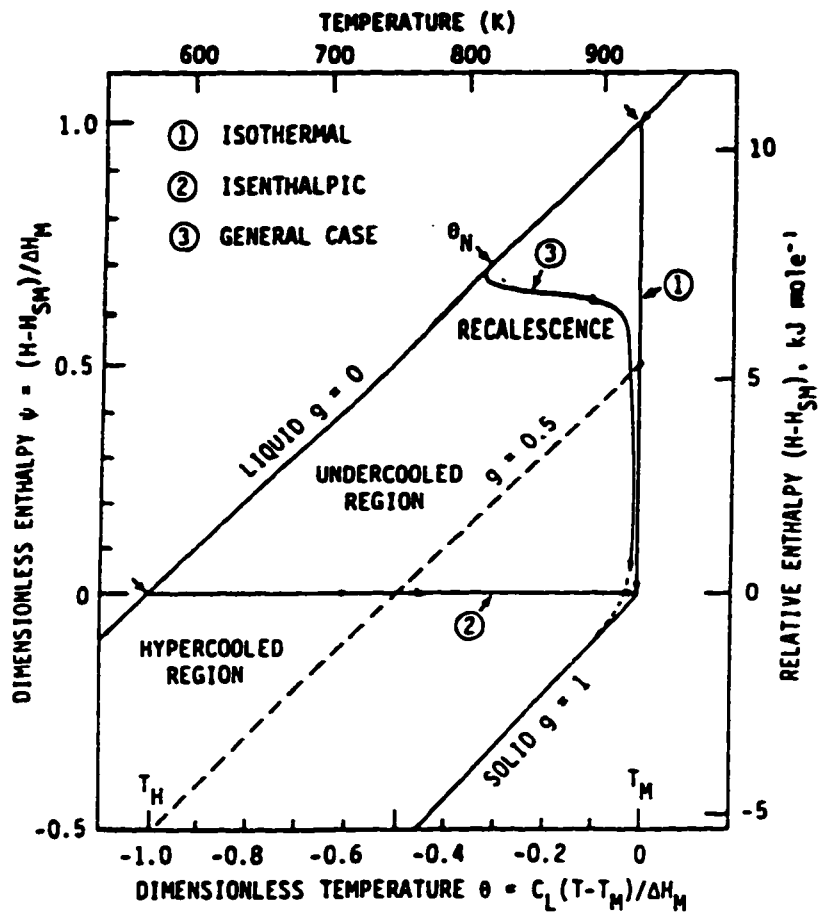


Figure 2-22. Enthalpy-temperature diagram showing possible solidification "paths". [Levi and Mehrabian, 1982]

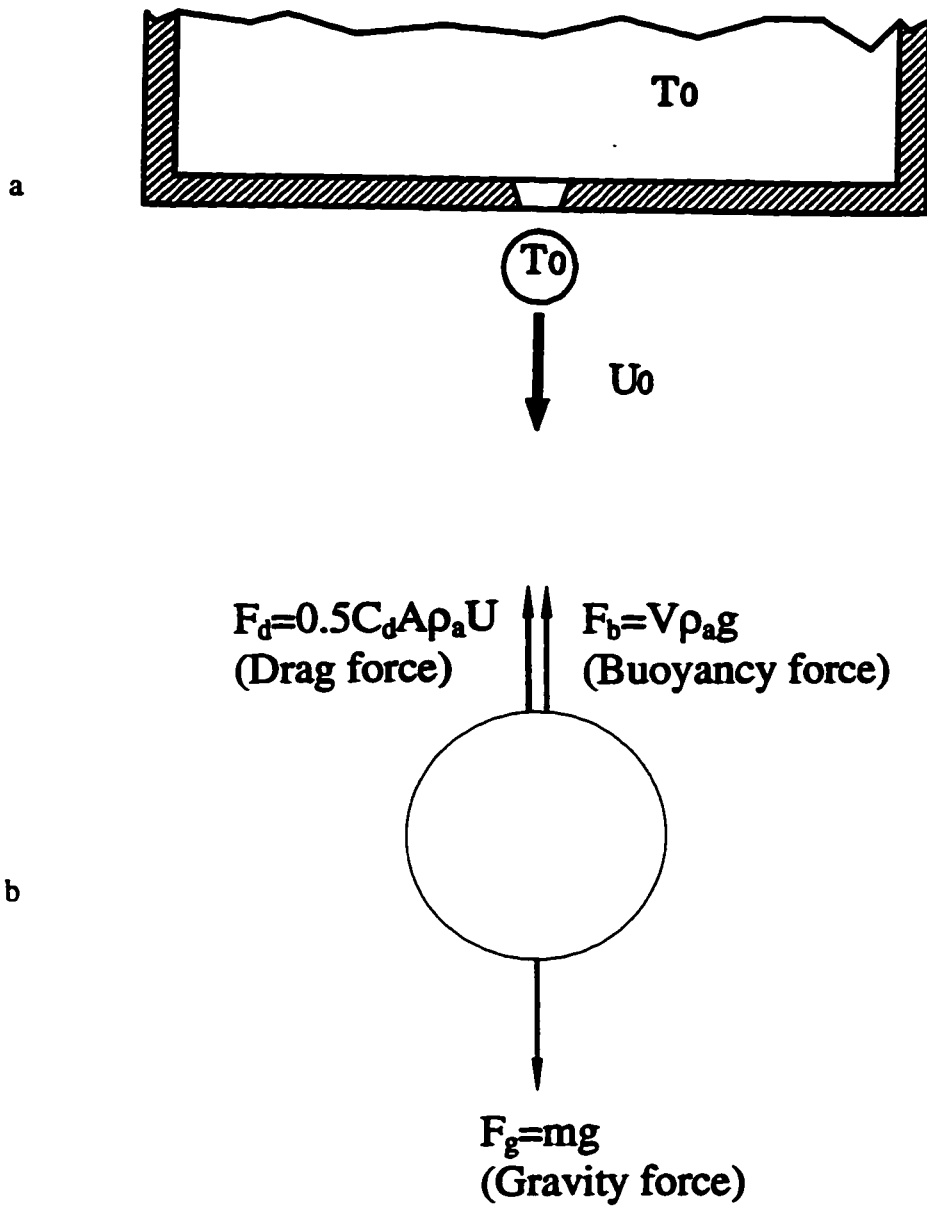


Figure 3-1. Schematic of a: an atomized droplet by IAP; and b: the forces acting on a droplet during free fall.

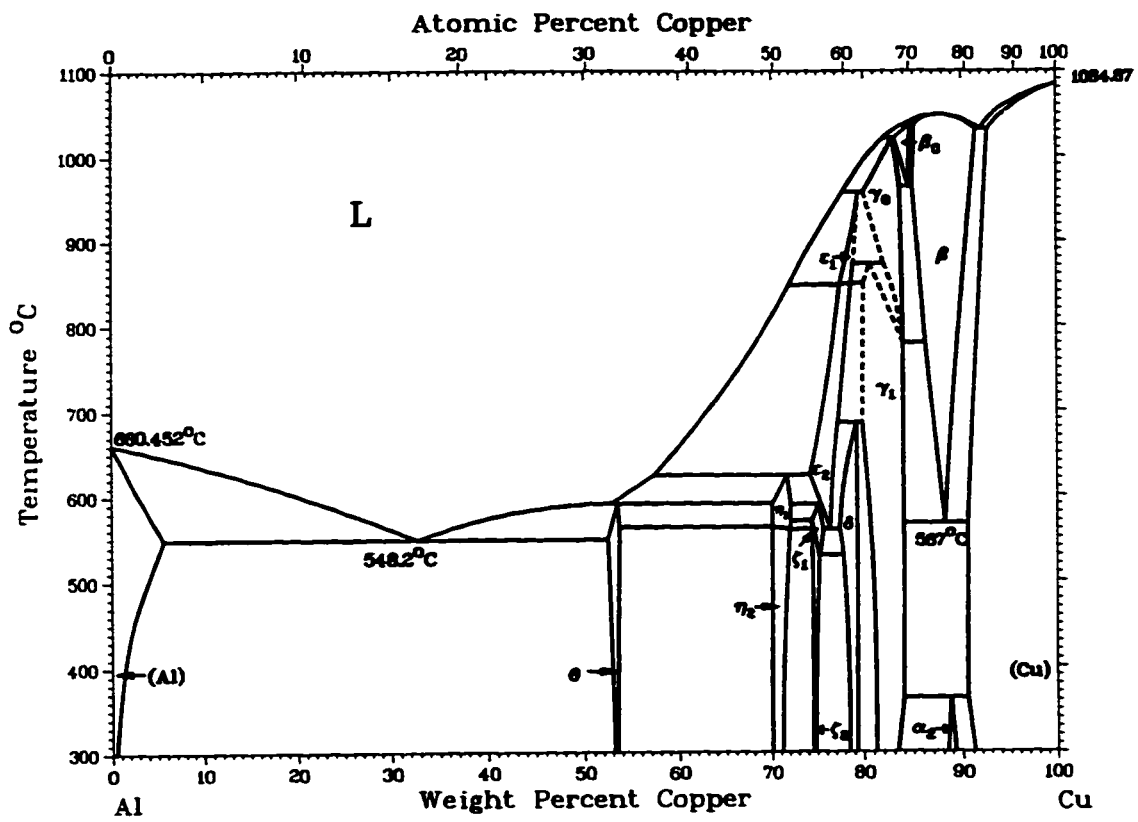


Figure 3-2. Phase diagram of Al-Cu alloy. [Massalski et al, 1990]

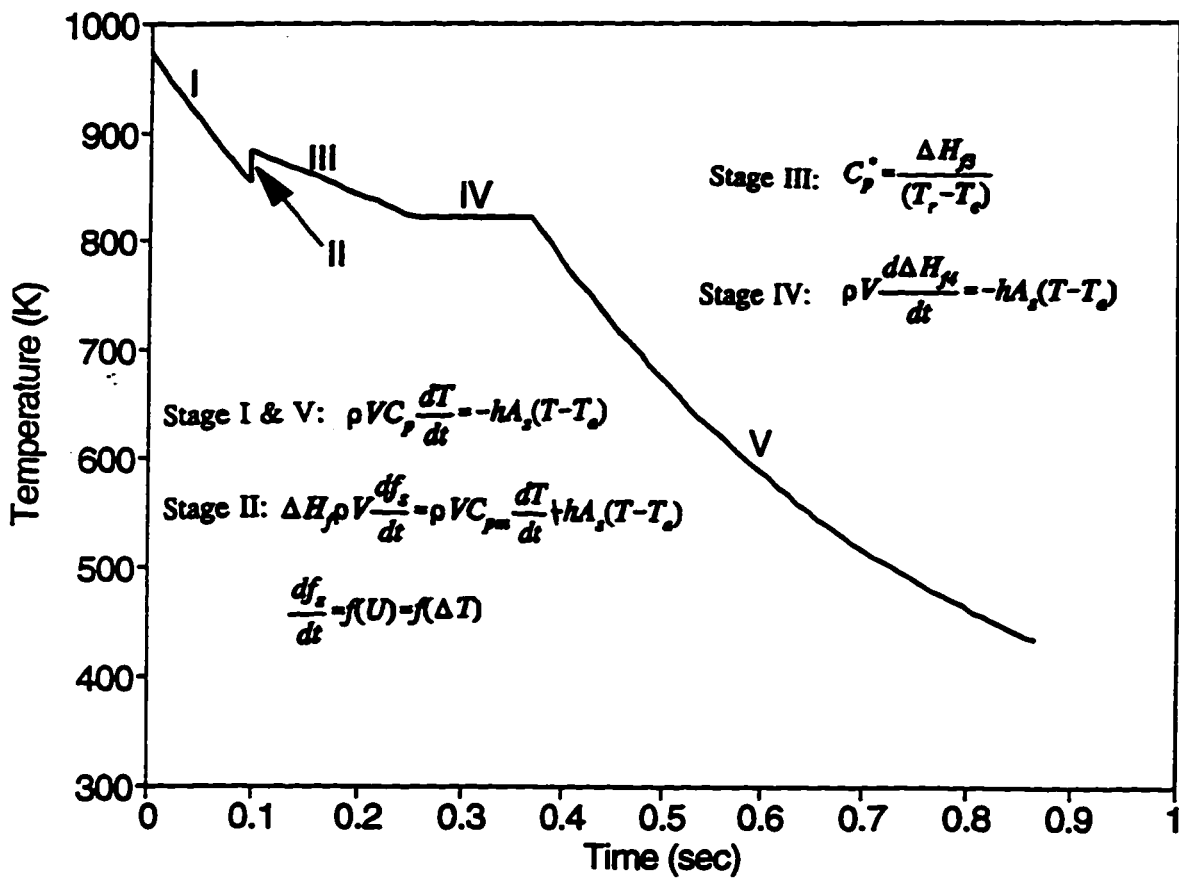


Figure 3-3. Schematic of cooling curve of a Al-Cu droplet in the composition range between 5.65wt%Cu to 33.2wt%Cu.



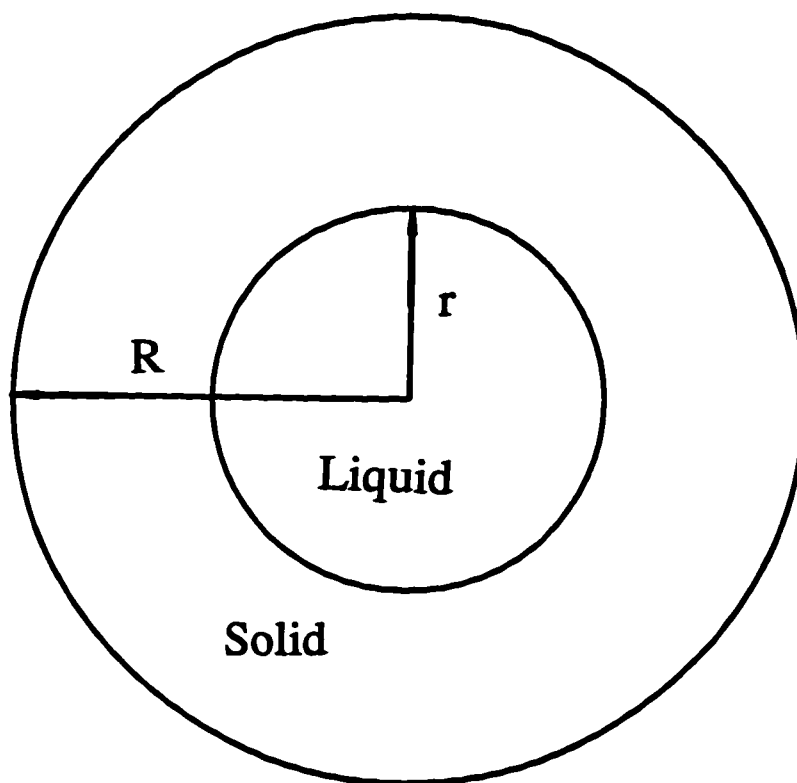
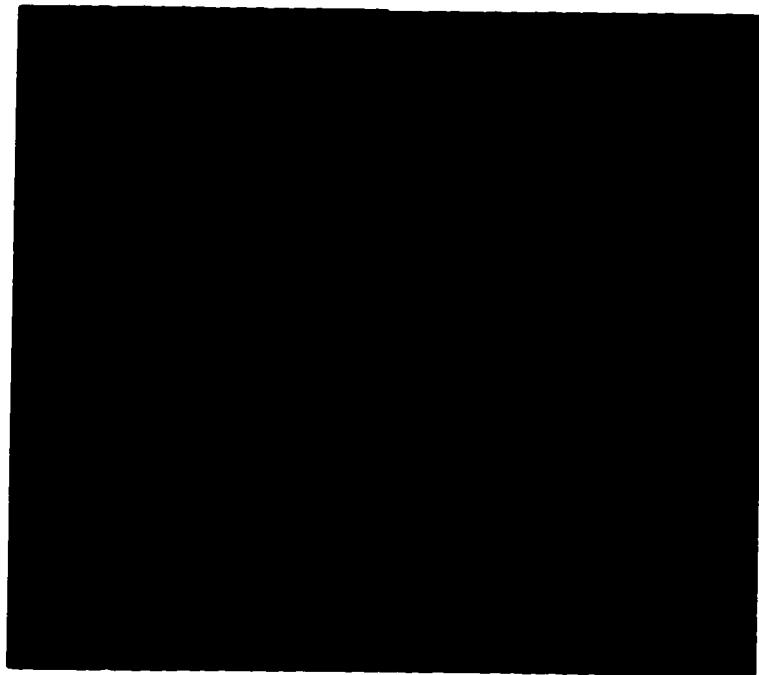


Figure 3-4 Schematic of solidification of a droplet with a radius  $R$  and its solidified fraction with a radius  $r$ .



**Figure 3-5. Droplet streaks for velocity measurement taken by video camera with shutter speed=1/250 sec.**

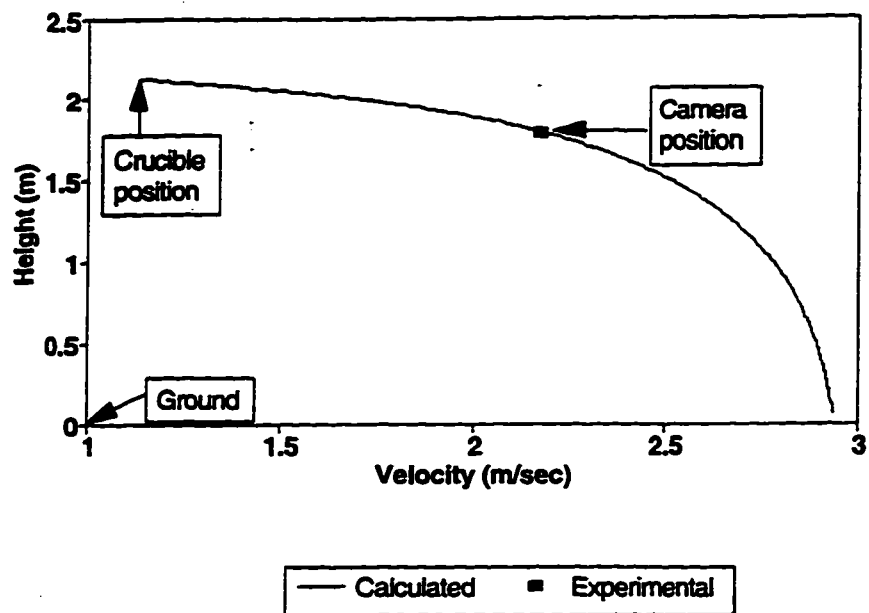


Figure 3-6. Velocity profile of a  $3.3 \times 10^{-4}$  m Al-17wt%Cu droplet with an initial velocity of 1.13 m/sec.

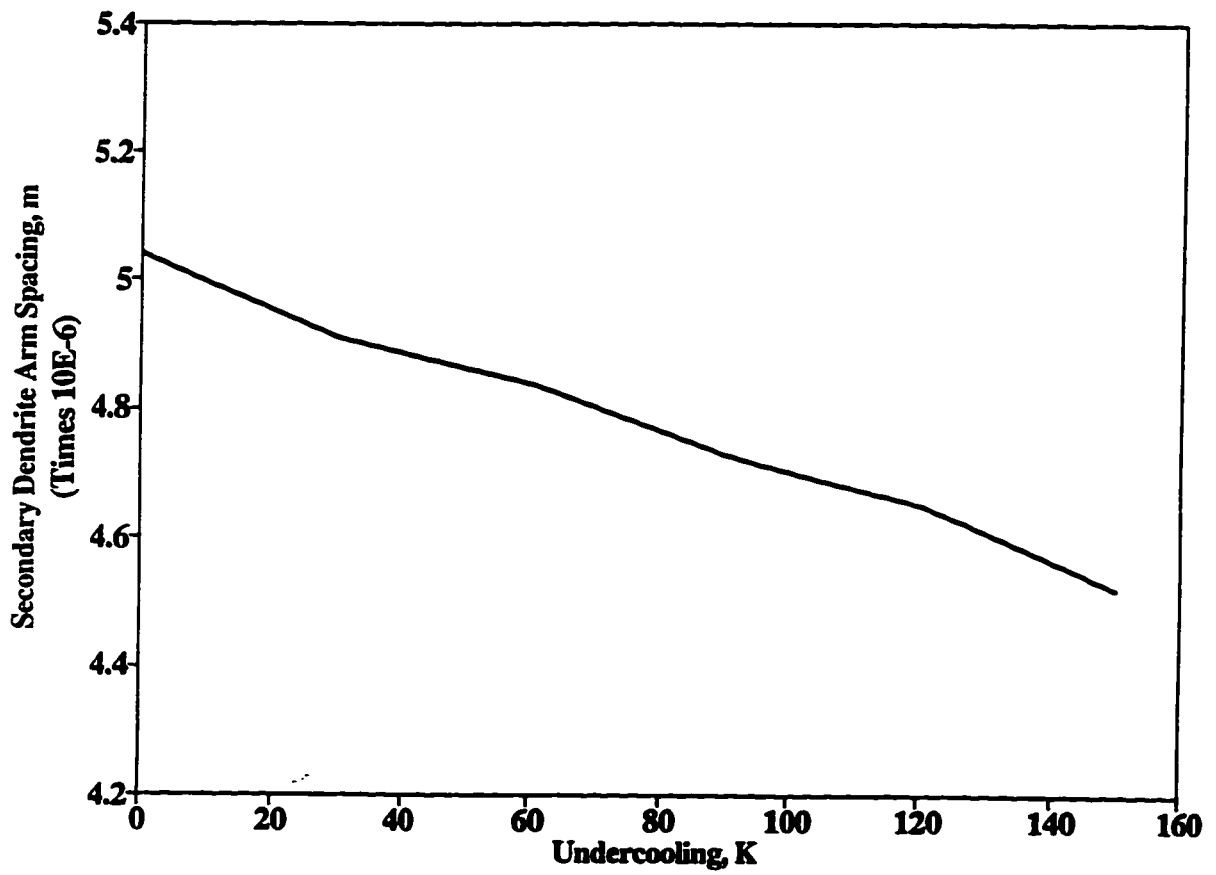


Figure 3-7. Effect of undercooling on SDAS of a  $3.3 \times 10^{-4}$  m Al-17wt%Cu droplet.

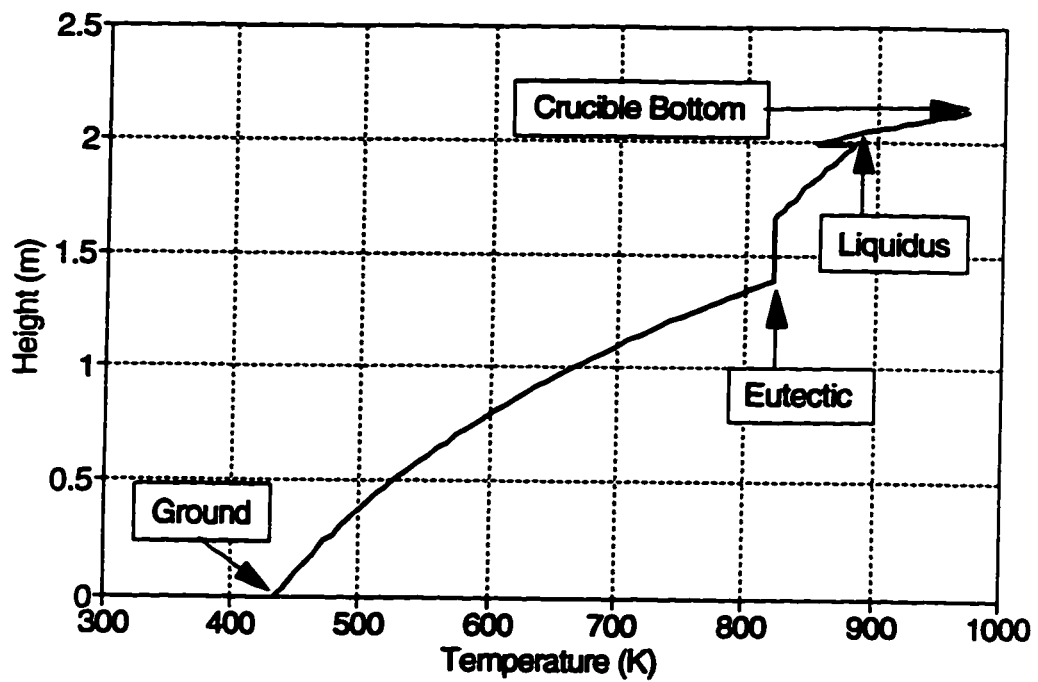


Figure 3-8. Temperature profile of a  $3.3 \times 10^{-4}$  m Al-17wt%Cu droplet with an initial velocity of 1.13 m/sec. The amount of superheat was 100 K. The amount of undercooling assumed was 53 K, the time step size was 0.01 sec except in stage II where  $2 \times 10^{-5}$  sec was used.

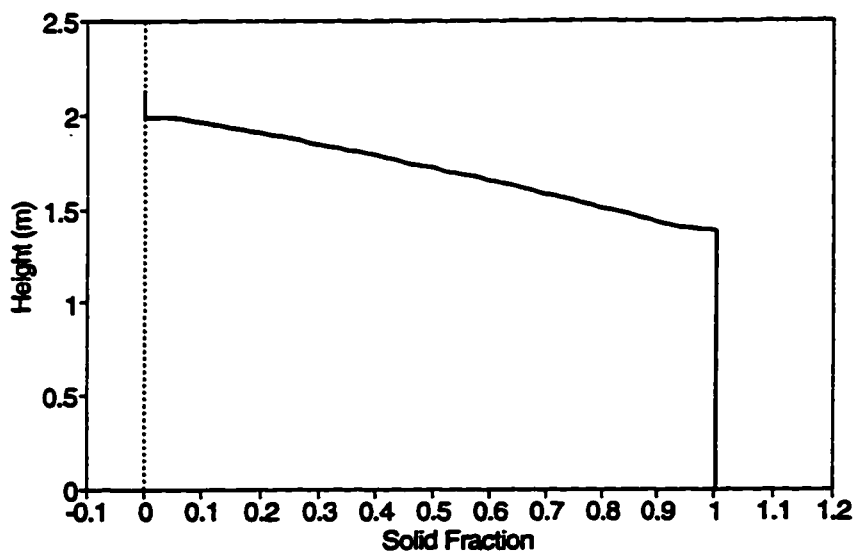


Figure 3-9. Solid fraction profile of a  $3.3 \times 10^{-4}$  m Al-17wt%Cu droplet with an initial velocity of 1.13 m/sec. The amount of superheat was 100 K. The amount of undercooling assumed was 53 K, the time step size was 0.01 sec except in stage II where  $2 \times 10^{-5}$  sec was used.

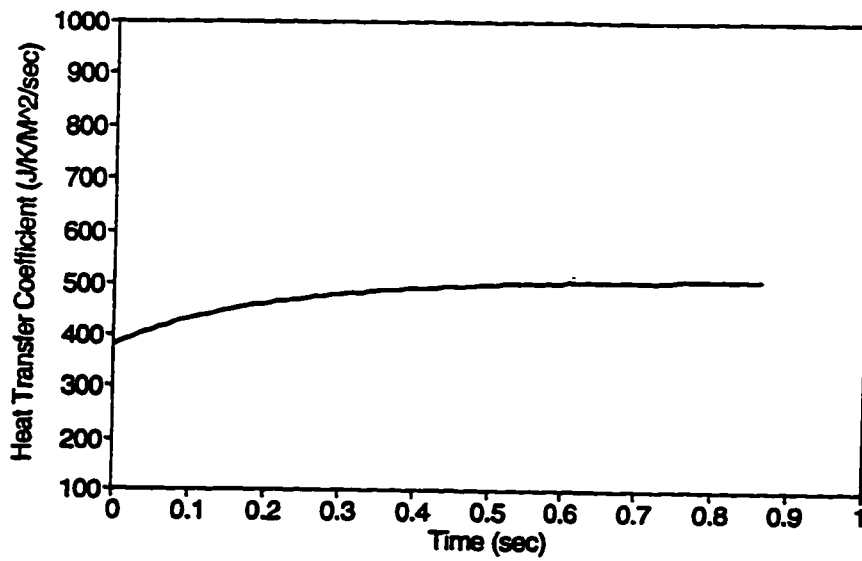


Figure 3-10. Heat transfer coefficient of a  $3.3 \times 10^{-4}$  m Al-17wt%Cu droplet with an initial velocity of 1.13 m/sec.

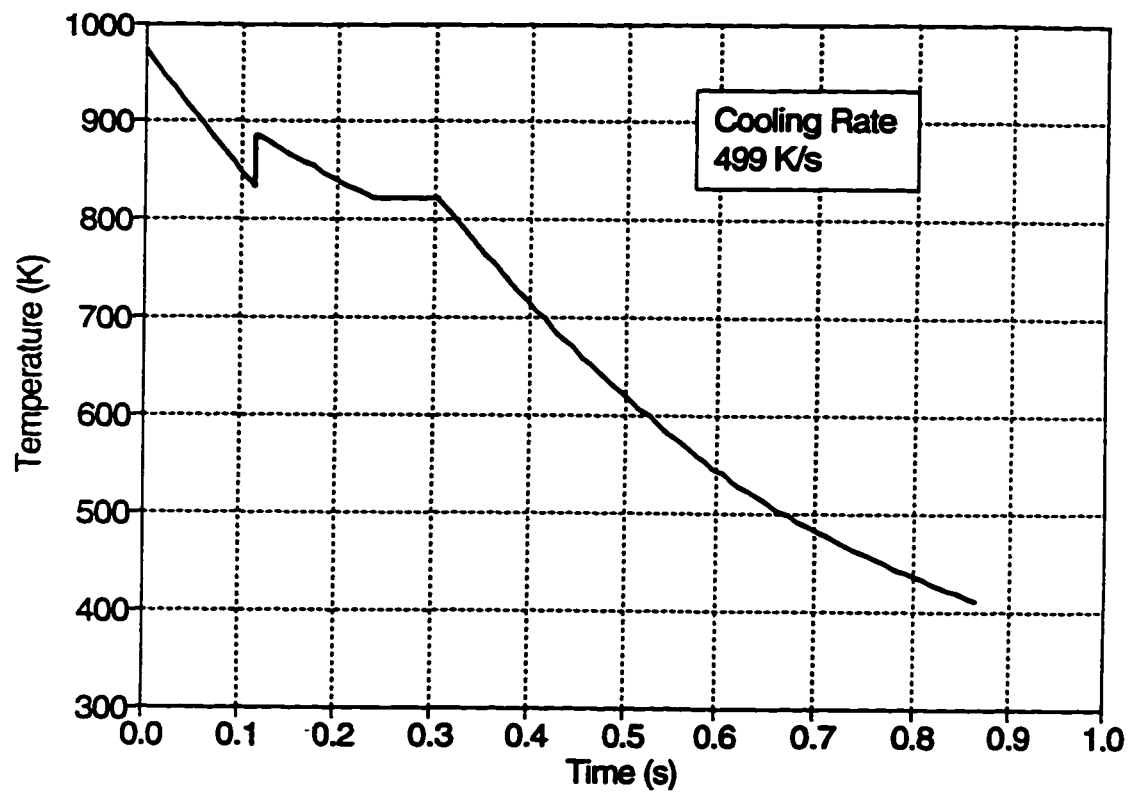


Figure 3-11. Cooling curve of a  $3.3 \times 10^{-4}$  m Al-17wt%Cu droplet with an initial velocity of 1.13 m/sec. The amount of superheat was 100 K. The amount of undercooling assumed was 53 K, the time step size was 0.01s except in stage II where  $2 \times 10^{-5}$  sec was used.



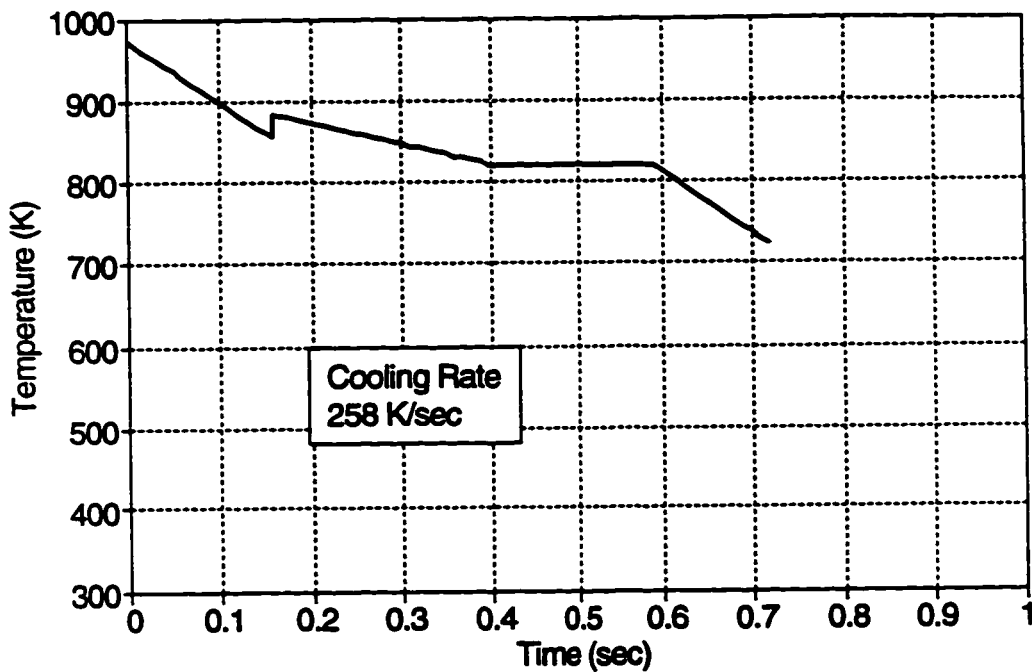


Figure 3-12. Cooling curve of a  $4.6 \times 10^{-4}$  m Al-17wt%Cu droplet with an initial velocity of 1.13 m/sec. The amount of superheat was 100 K. The amount of undercooling assumed was 44 K, the time step size was 0.01s except in stage II where  $2 \times 10^{-5}$  sec was used.

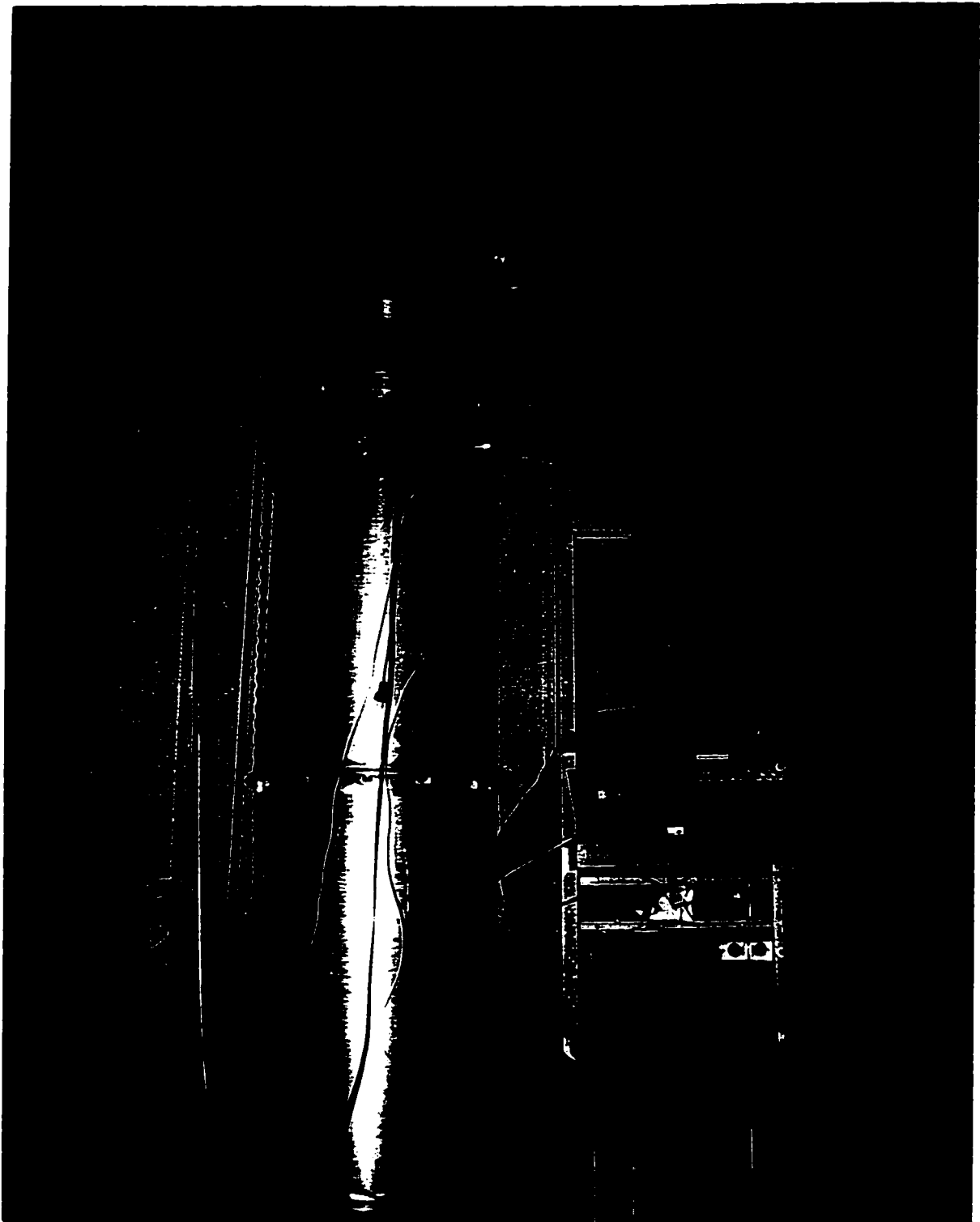


Figure 4-1 Photograph of the impulse atomization apparatus.

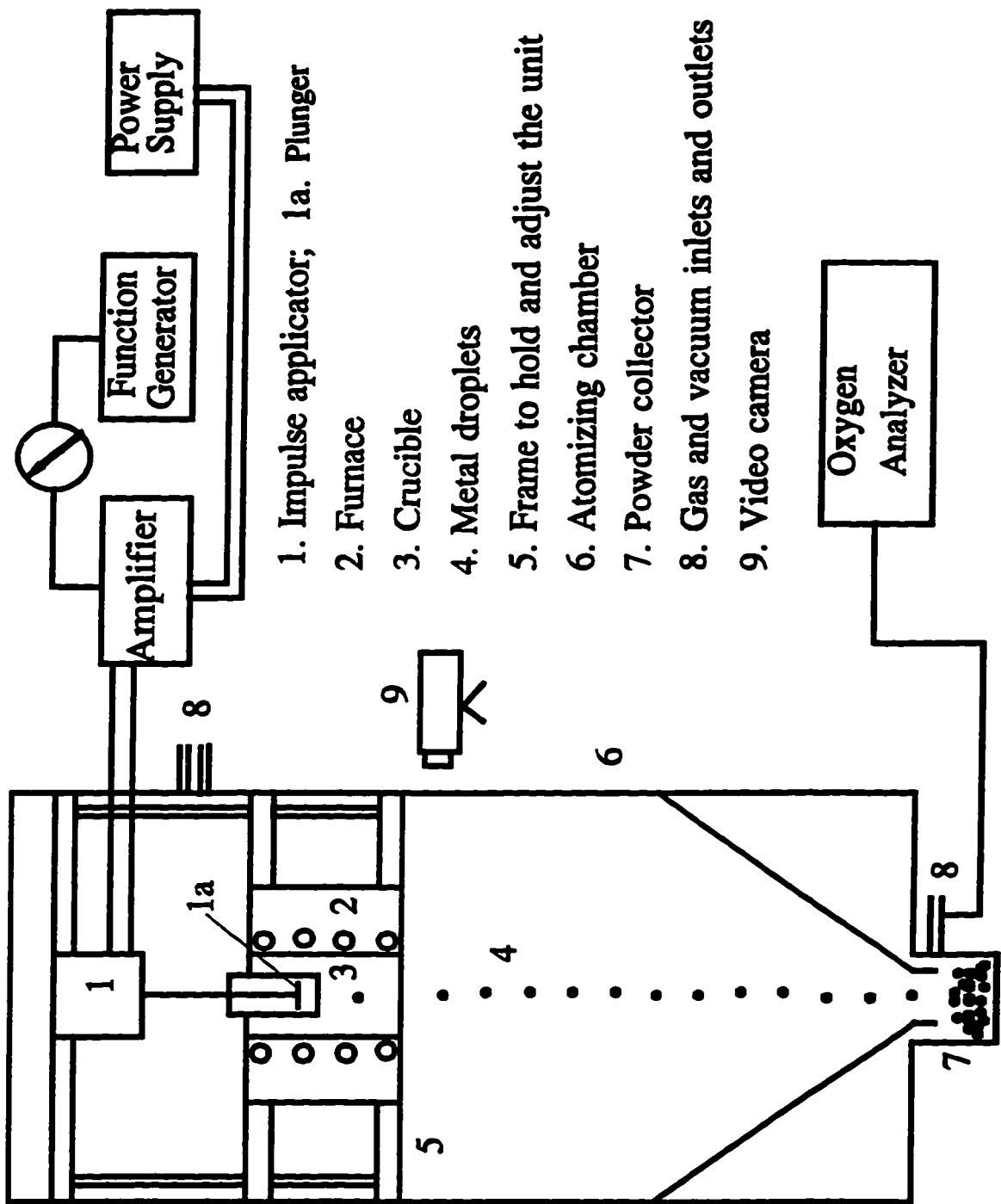


Figure 4-2. A schematic of experimental apparatus.

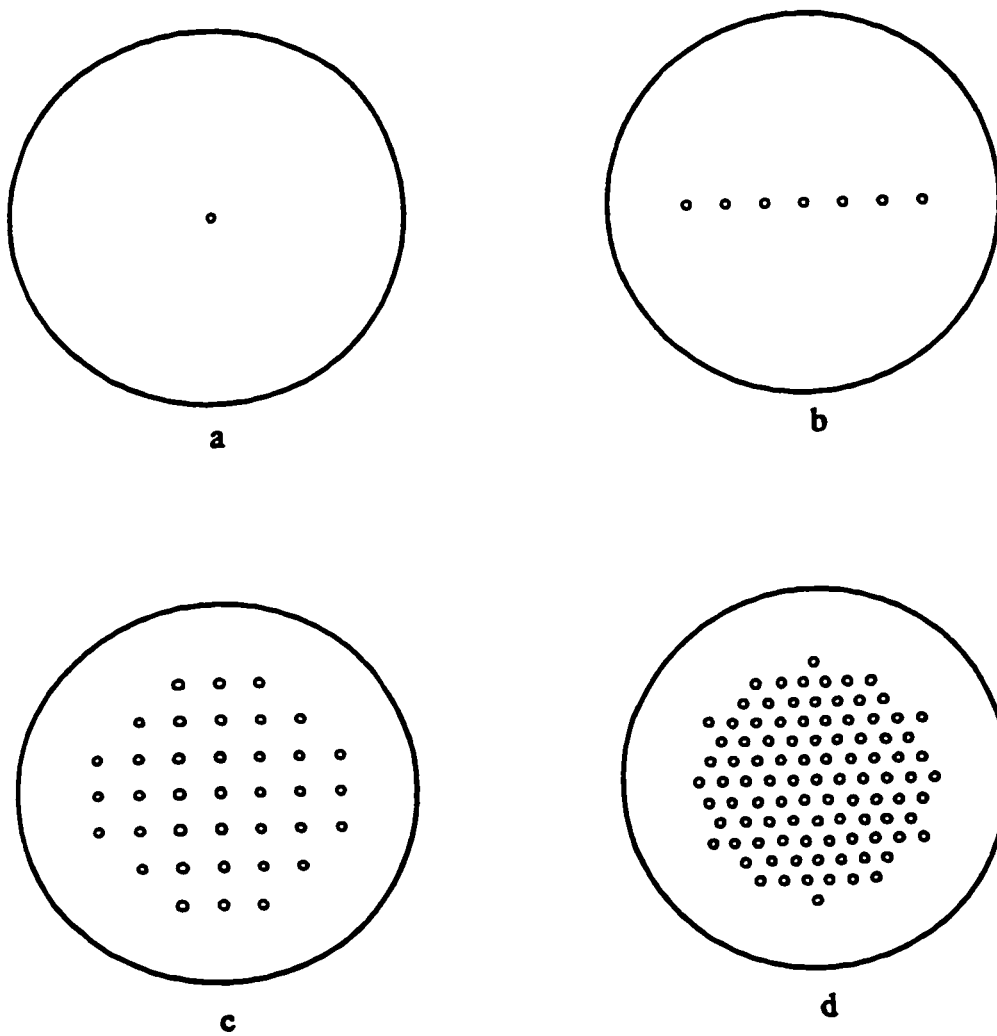
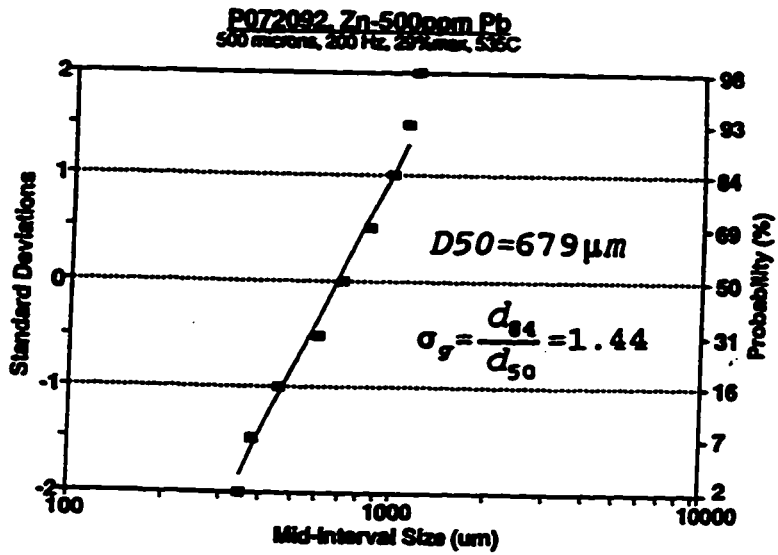
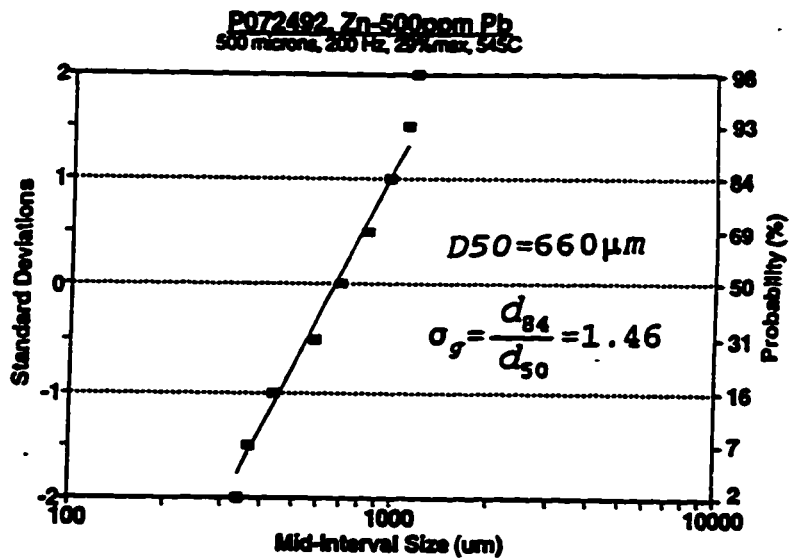


Figure 4-3. Nozzle pattern used in various atomization experiments.



(a)



(b)

Figure 5-1. Reproducibility of Impulse Atomization Process.

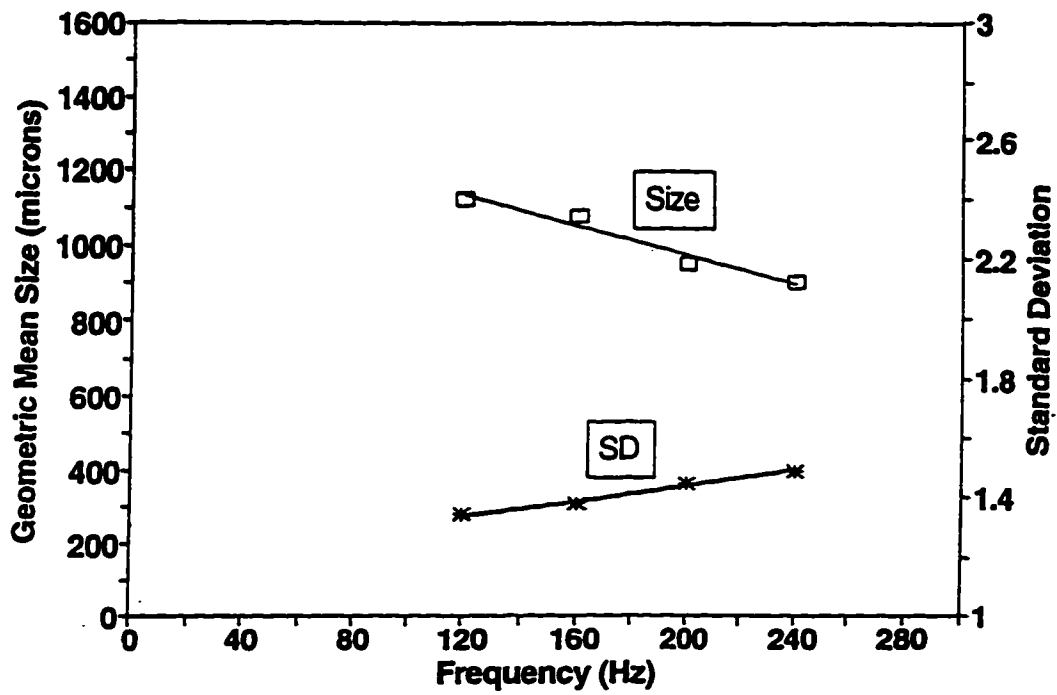


Figure 5-2. Effect of frequency on geometric mean size and geometric standard deviations.

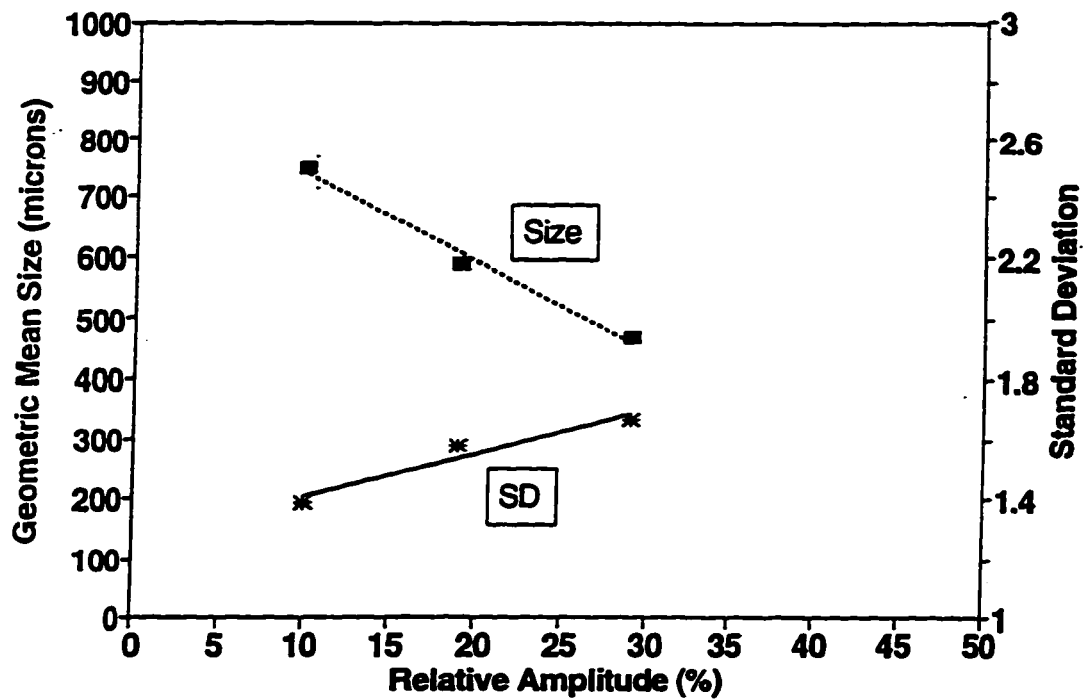


Figure 5-3. Effect of relative amplitude on geometric mean size and geometric standard deviations.

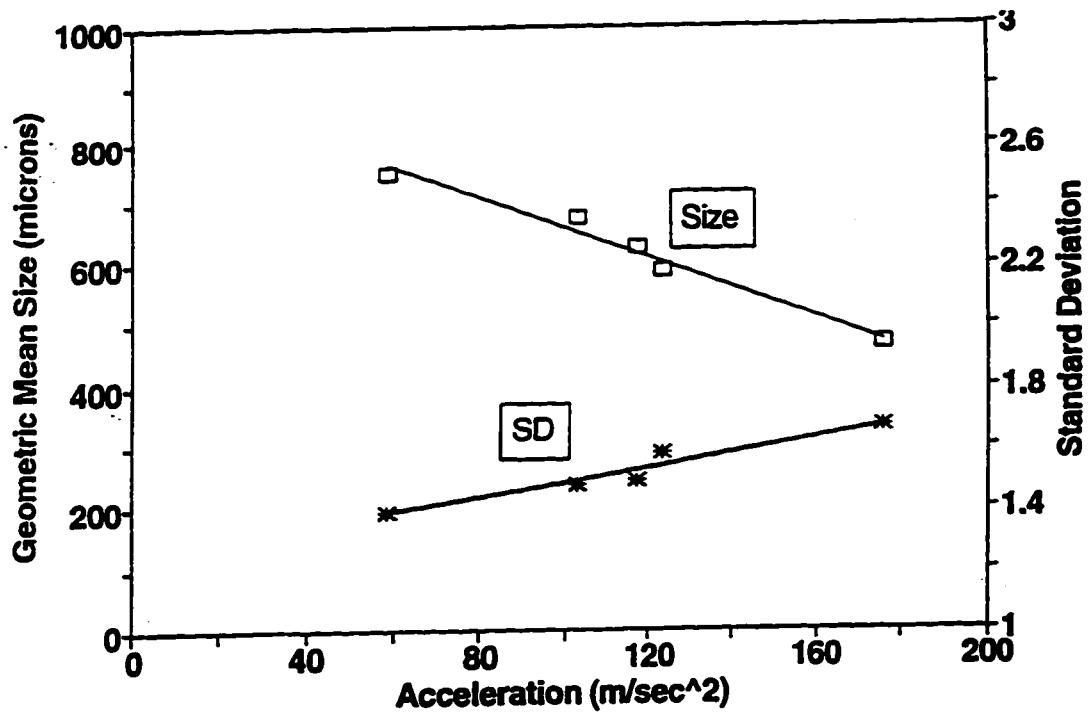


Figure 5-4. Effect of acceleration on geometric mean size and geometric standard deviations.



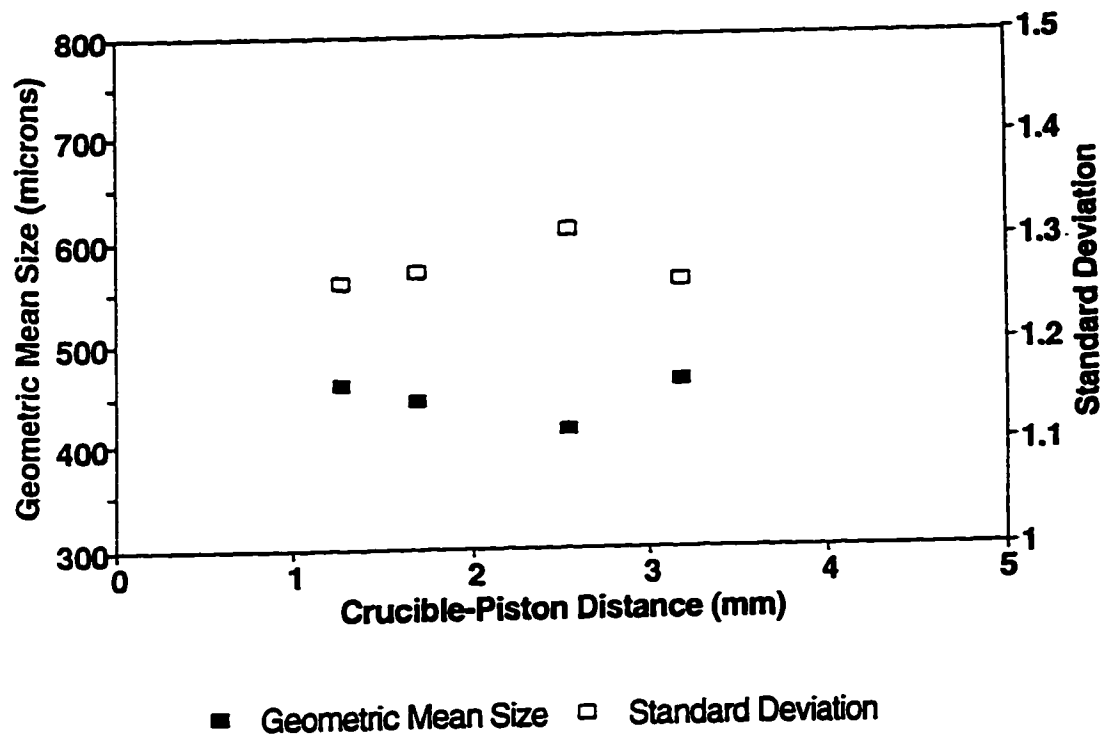


Figure 5-5. Effect of nozzle-impulse applicator distance on geometric mean size and geometric standard deviations.

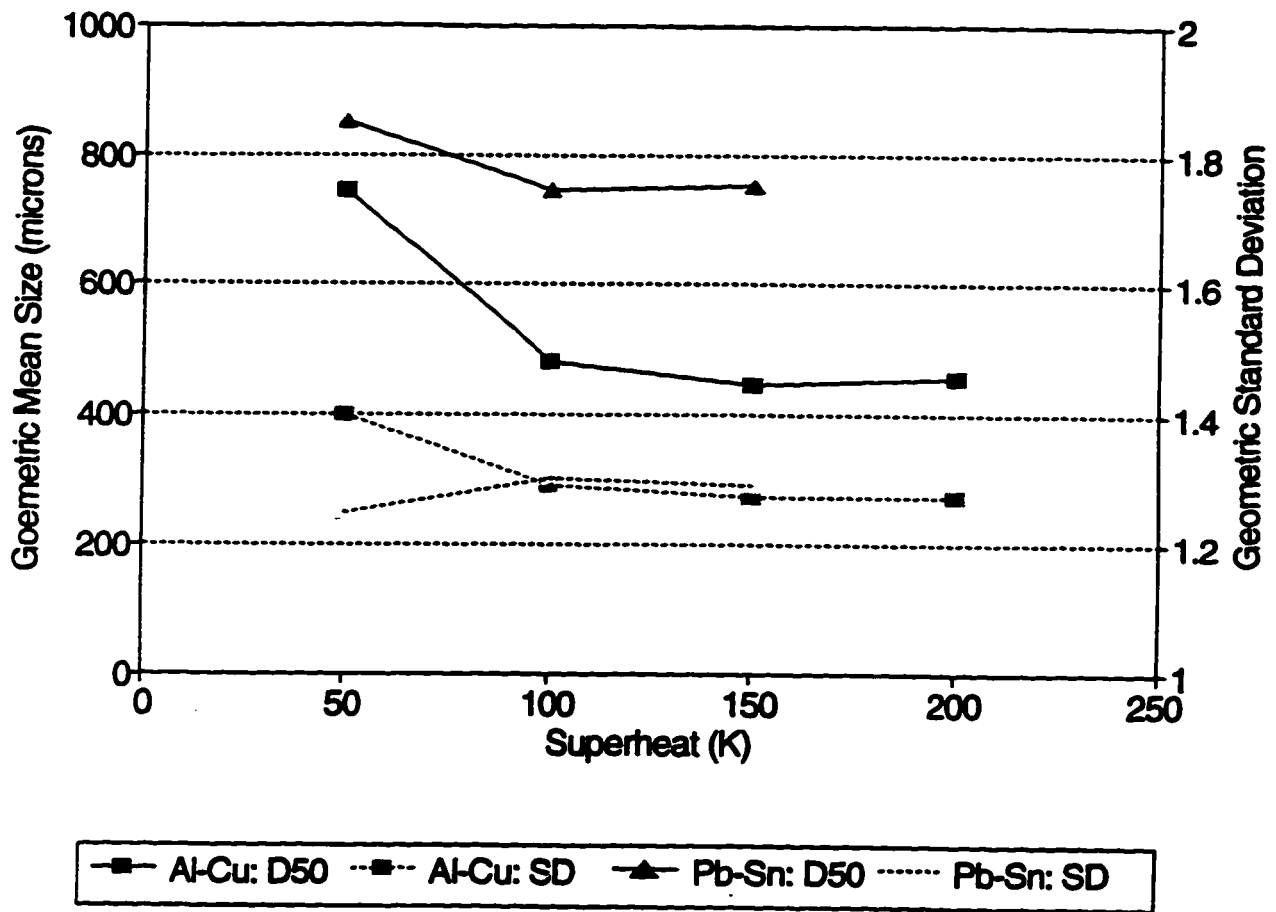


Figure 5-6. Effect of superheat on geometric mean size and geometric standard deviations.

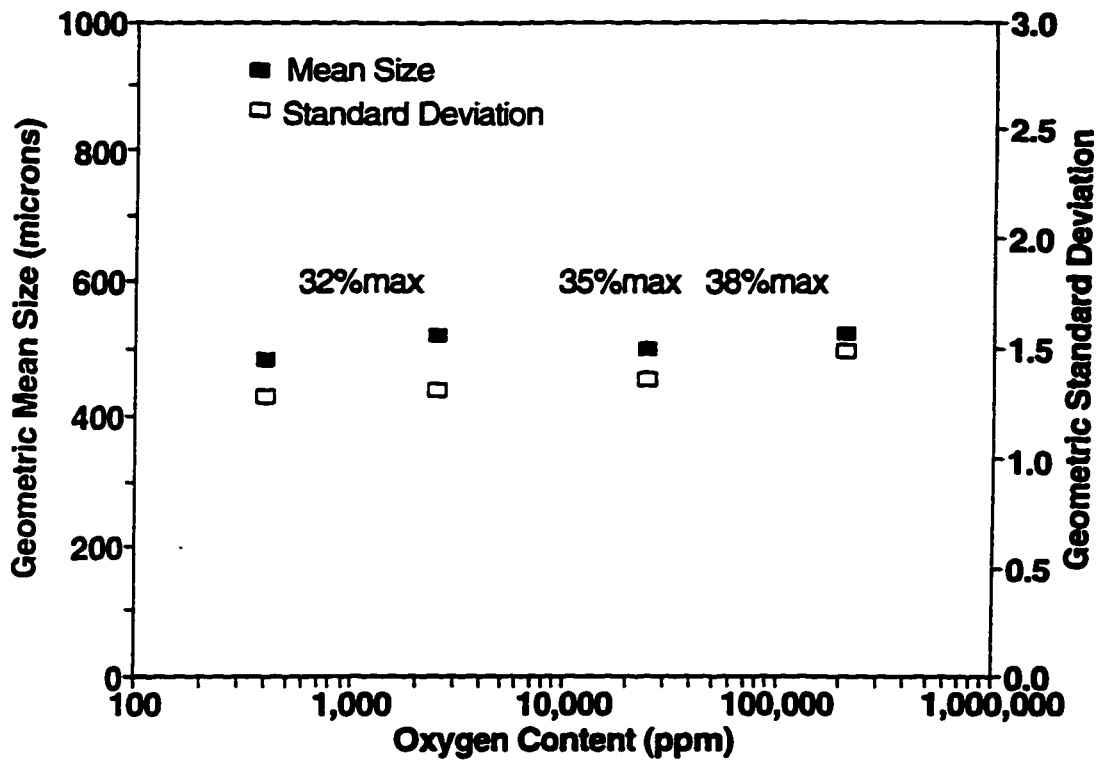
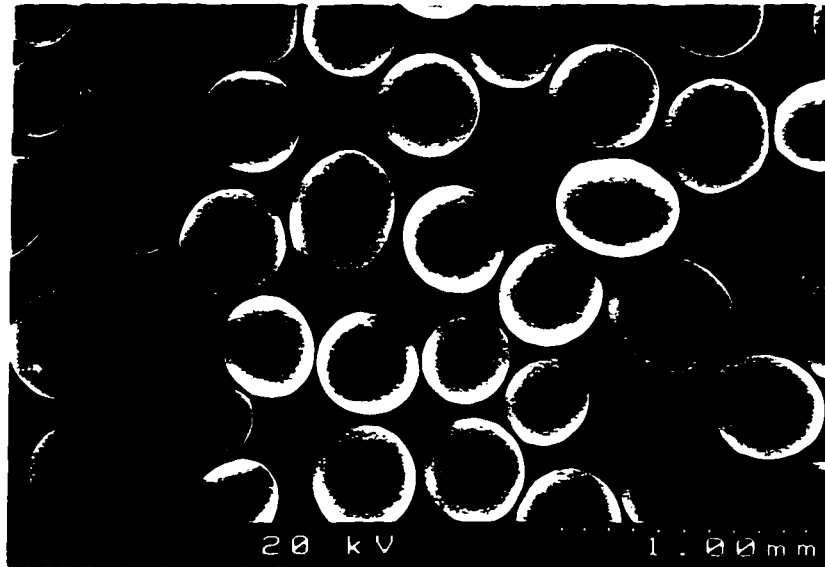


Figure 5-7. Effect of oxygen content on geometric mean size and geometric standard deviations.

a



b



Figure 5-8. Effect of oxygen content on powder shape. a). Sn-15wt%Pb atomized in nitrogen; b). Pb-12wt%Sn atomized in air.

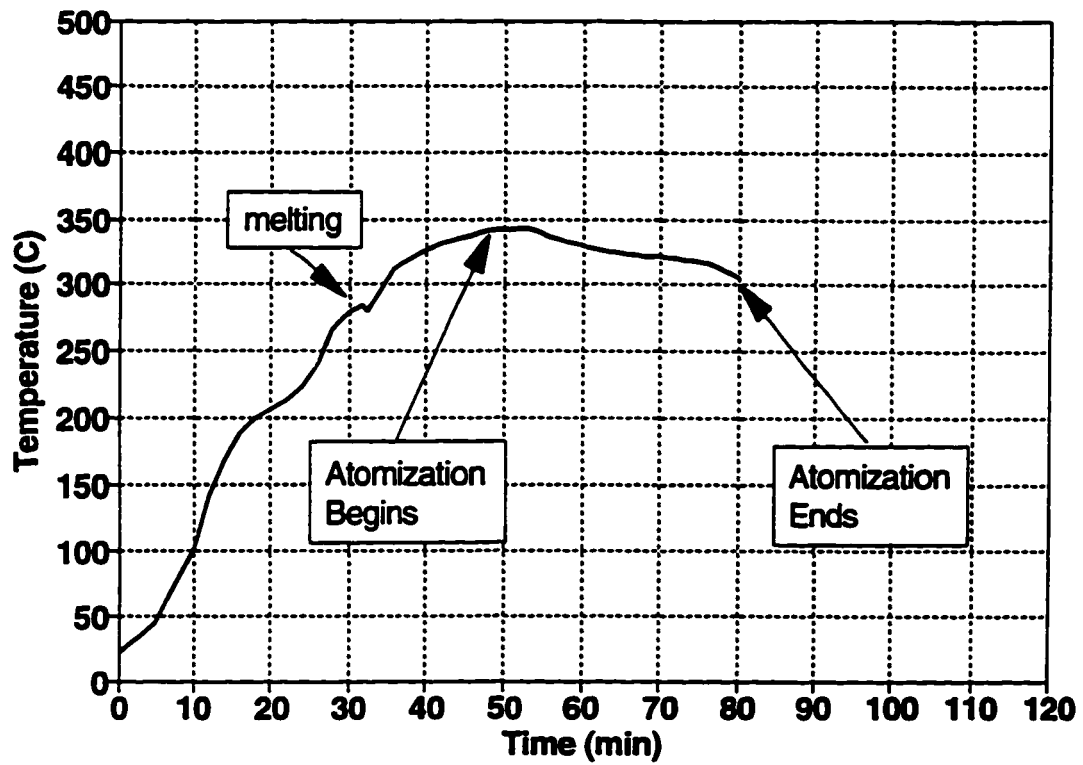


Figure 5-9. Temperature vs. time for the atomization of Se.

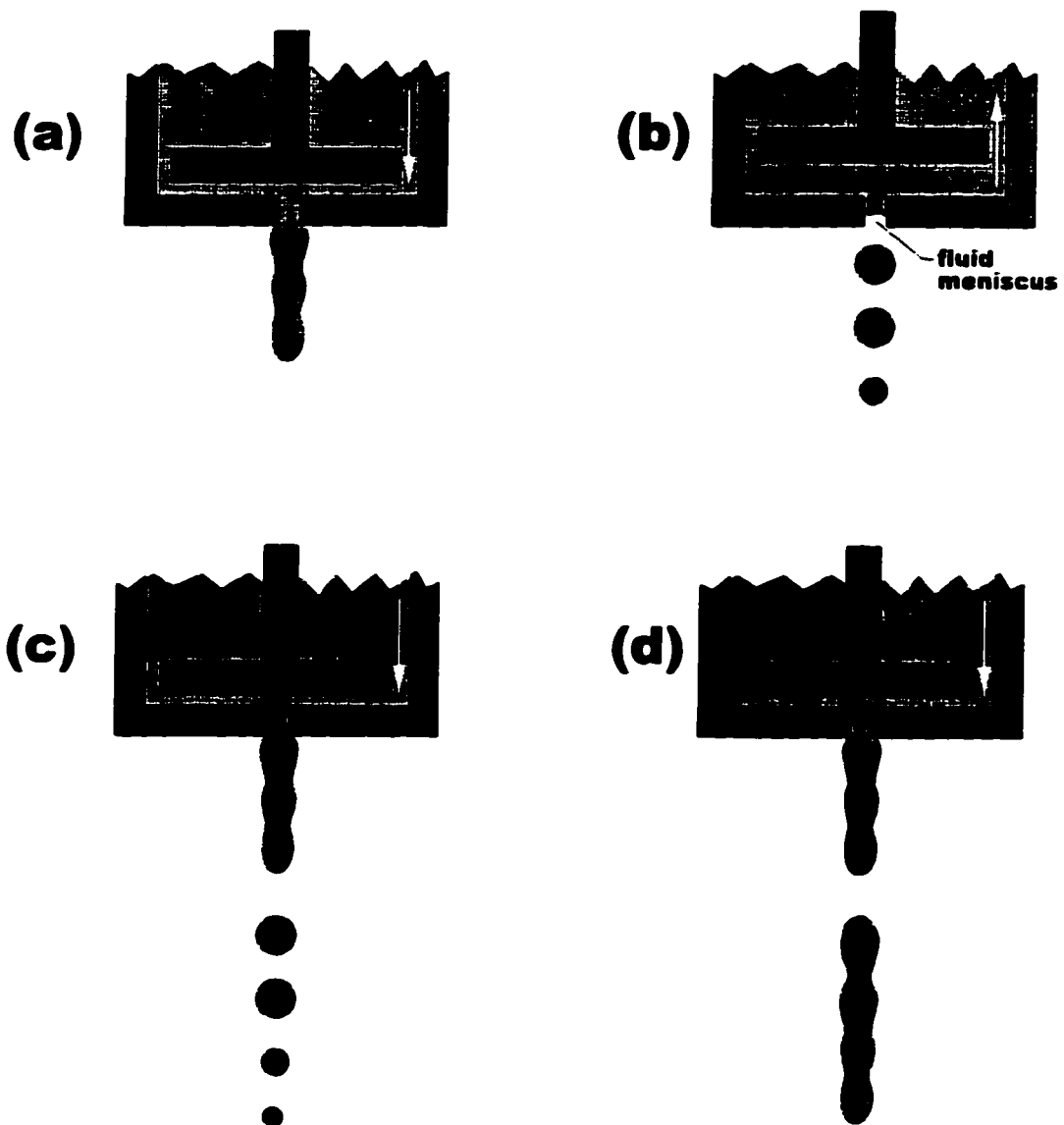


Figure 5-10. Schematic drawing of the formation procedure of discontinuous streams by IAP. (a) formation of a discontinuous stream with application plunger; (b) break up of the discontinuous stream and retrieve of the plunger; (c) second cycle of (a); (d) oxidized condition without breaking up of the discontinuous stream.

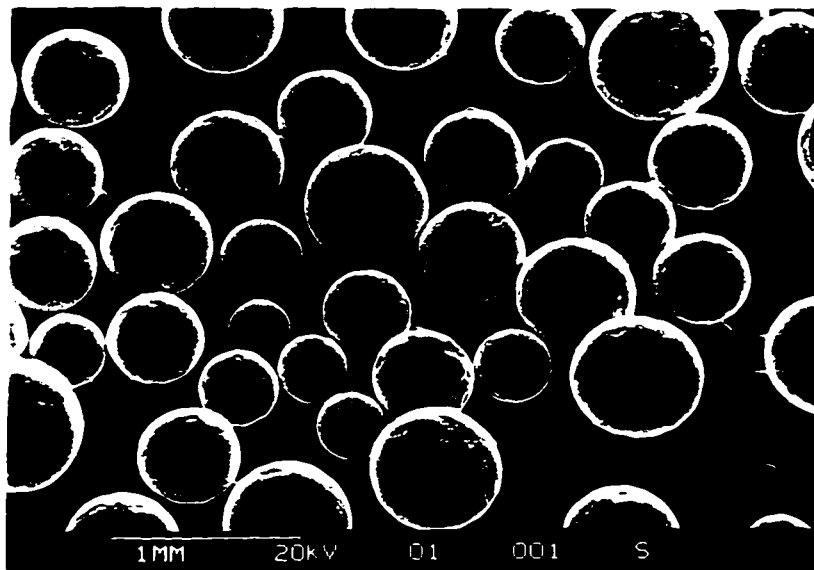


Figure 5-11. SEM photograph of Copper droplets produced by IAP.

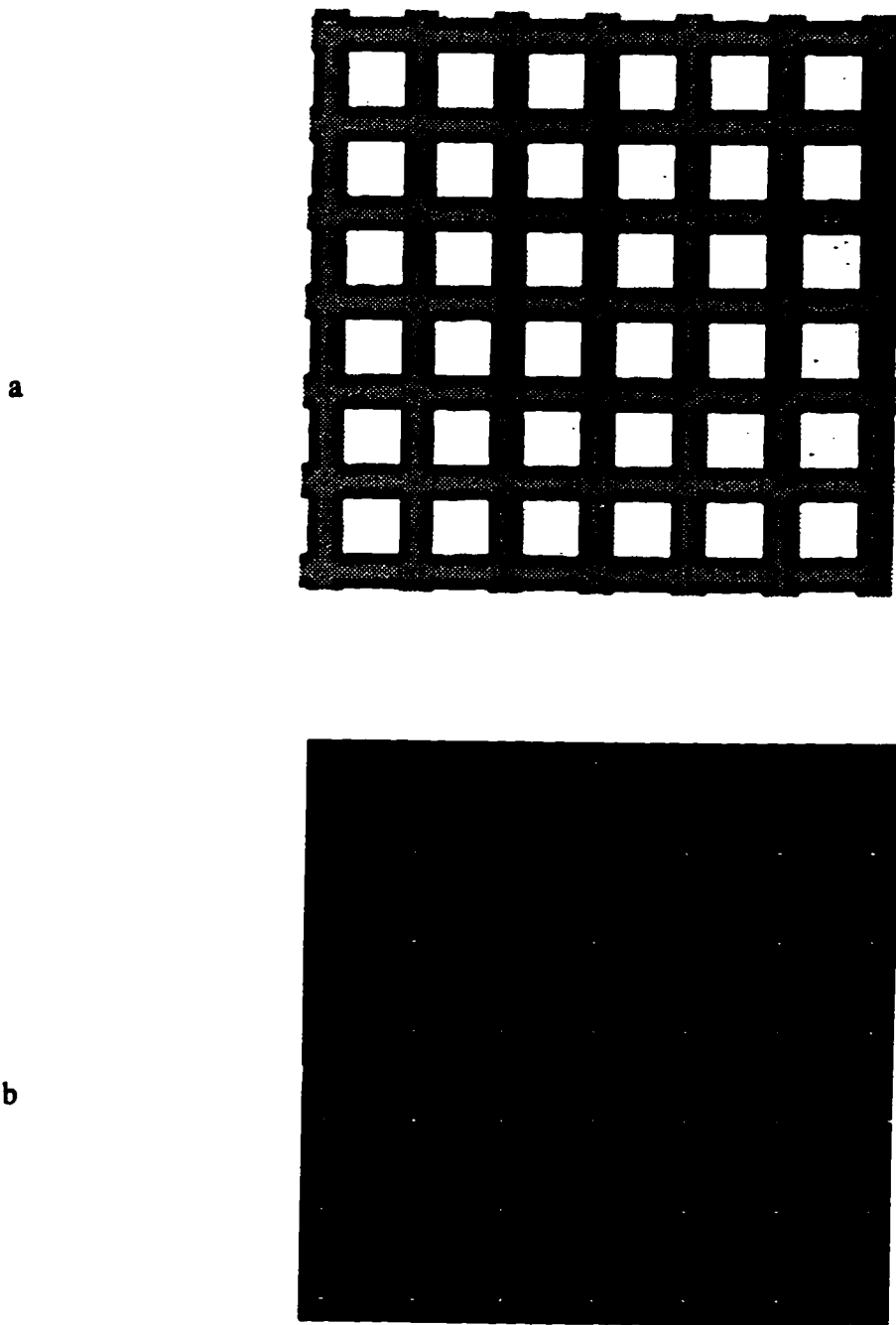
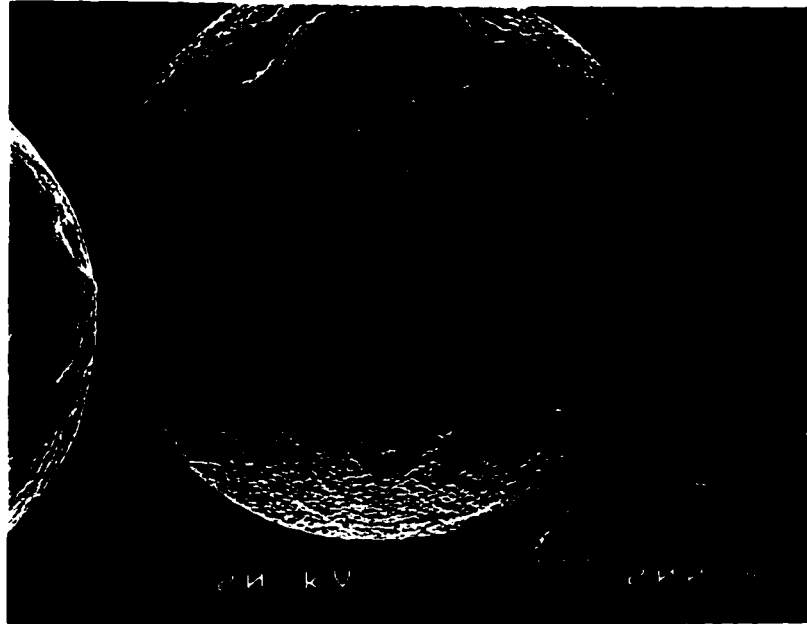


Figure 6-1. Standard grid taken under SEM. One grid =  $6.4 \times 10^{-5}$  m. a). original picture of the grid; b). skeleton of the grid.



a



b

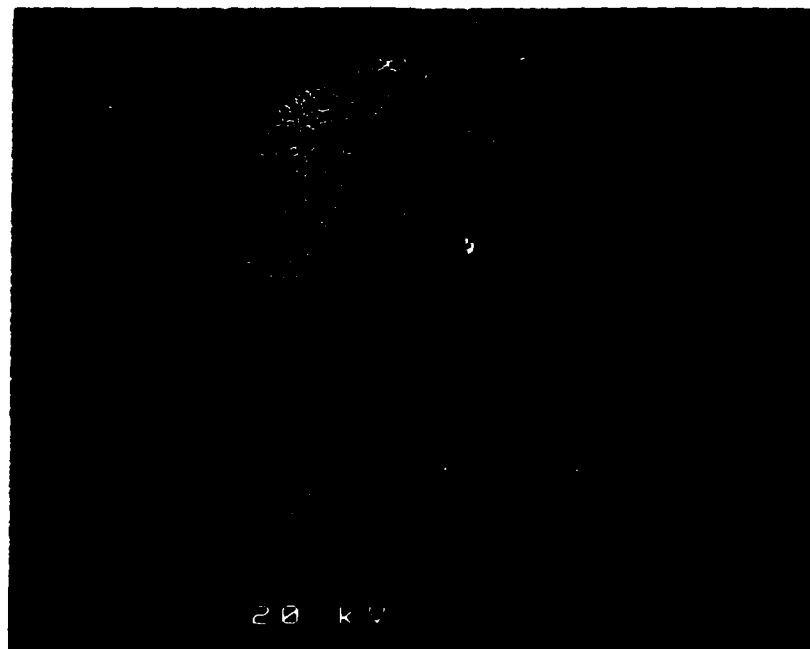


Figure 6-2. SEM micrographs of Al-17wt%Cu droplet. a). surface morphology of the droplet; b). microstructure at the centre part of a  $4.6 \times 10^{-4}$  m droplet; c). microstructure at the centre part of the  $4.6 \times 10^{-4}$  m droplet.

c

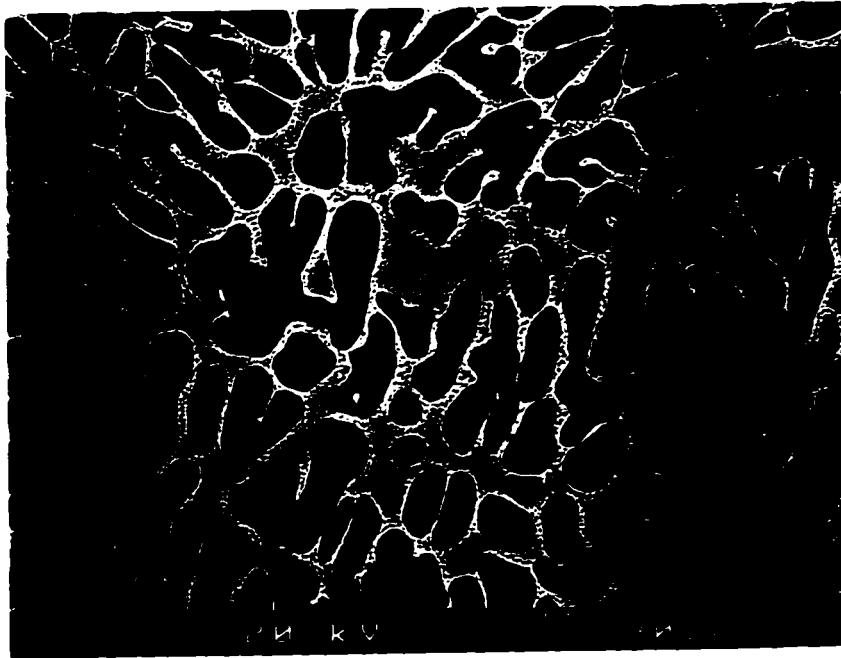
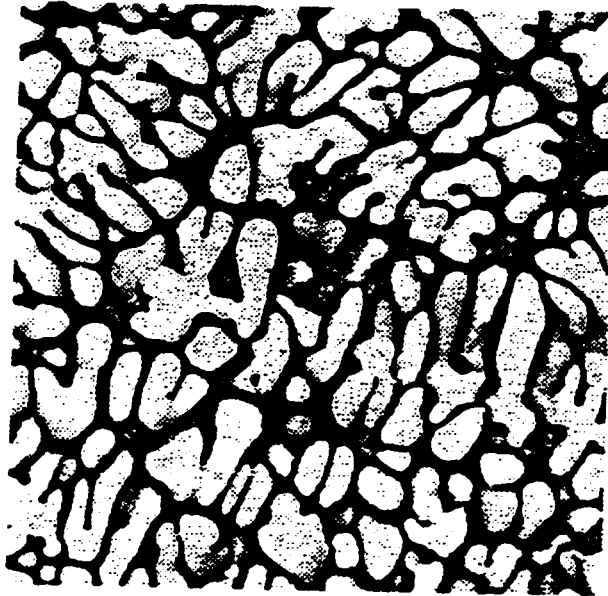


Figure 6-2. Continued.

a



b

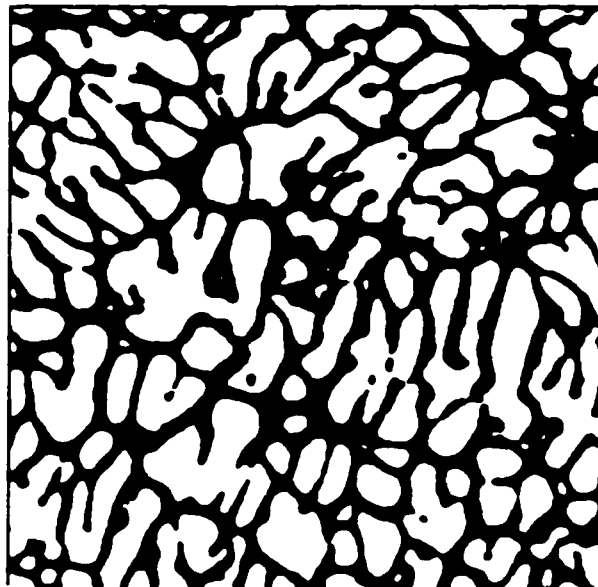


Figure 6-3. Transferred images of a  $4.6 \times 10^{-4}$  m Al-17wt%Cu droplet. a). original image; b). processed binary image; c). processed skeleton image.

c

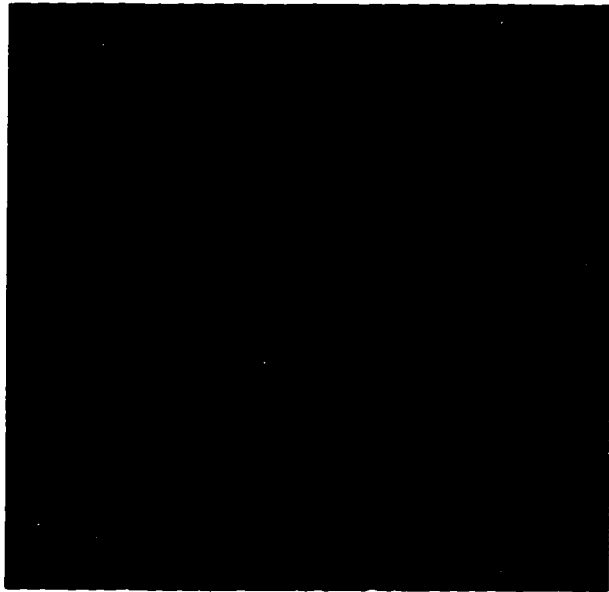


Figure 6-3. Continued.

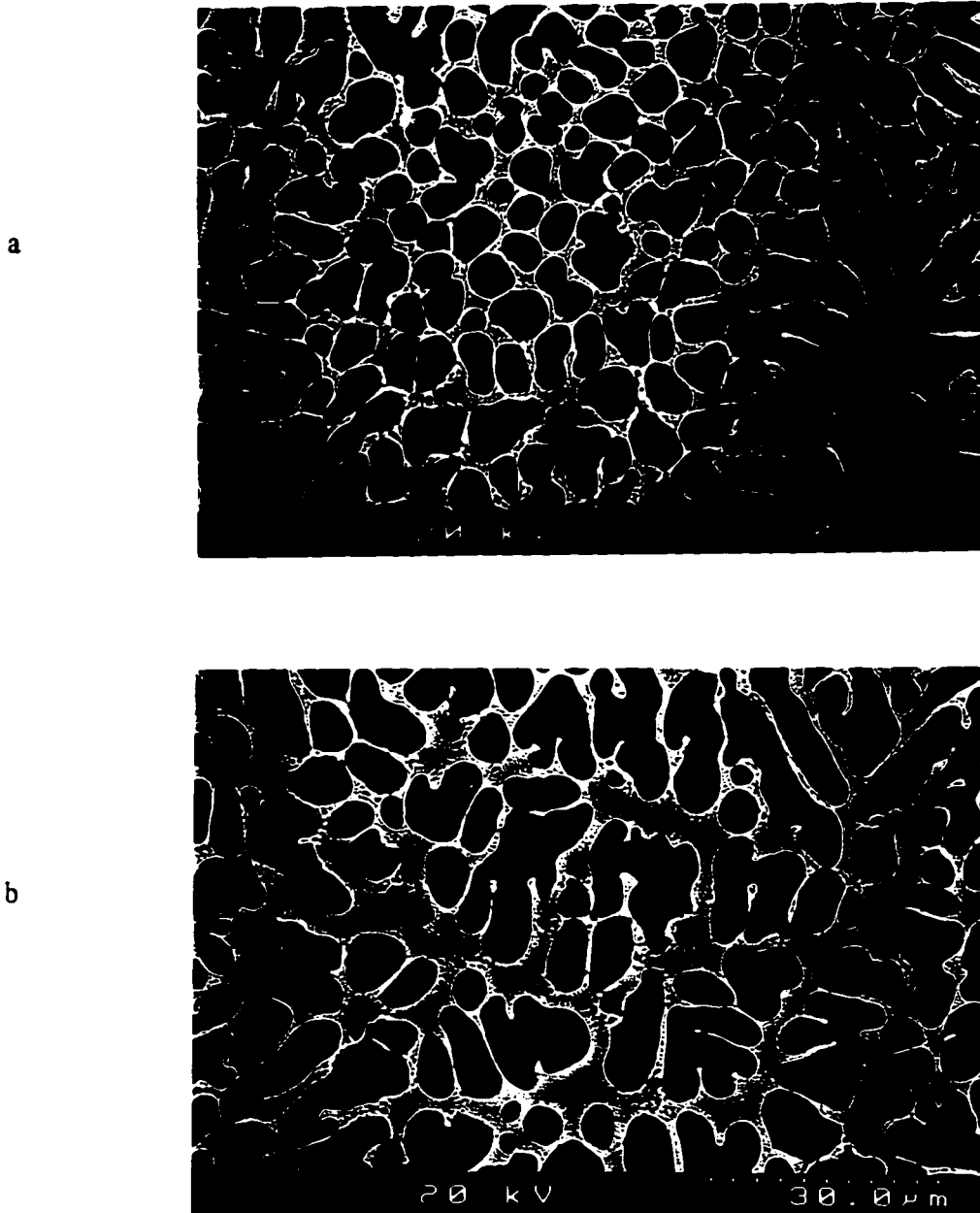
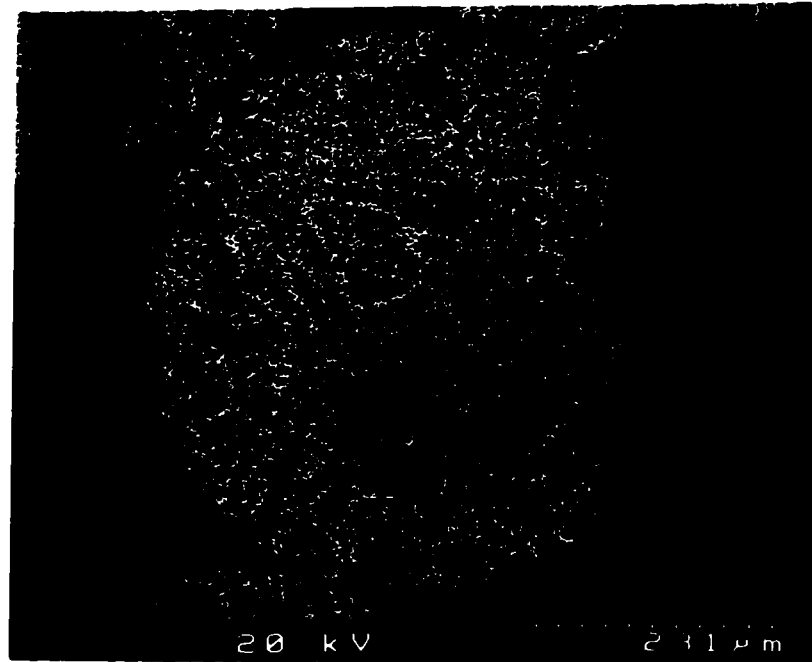


Figure 6-4. SEM micrographs of a  $4.6 \times 10^{-4}$  m Al-17wt%Cu droplet. a). microstructure at the edge of image shown in Fig.6-2b; b) a microstructure of a small cross section of another droplet.

a



b

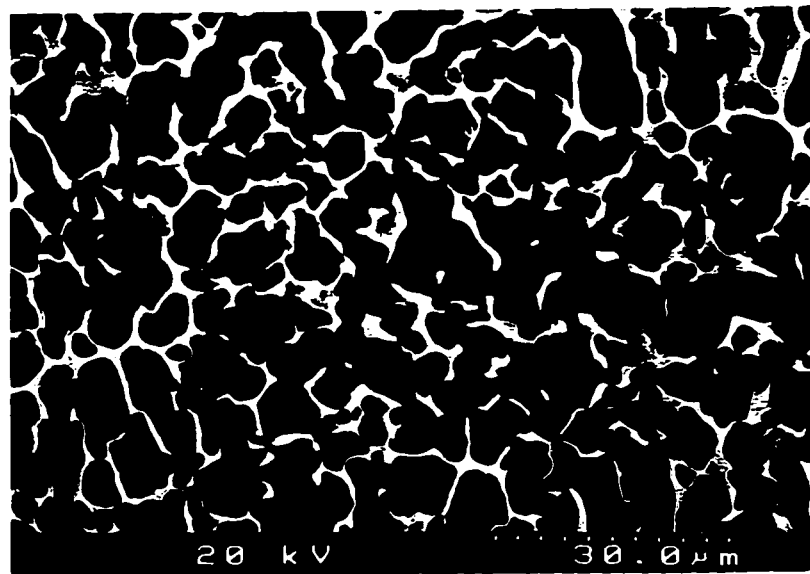
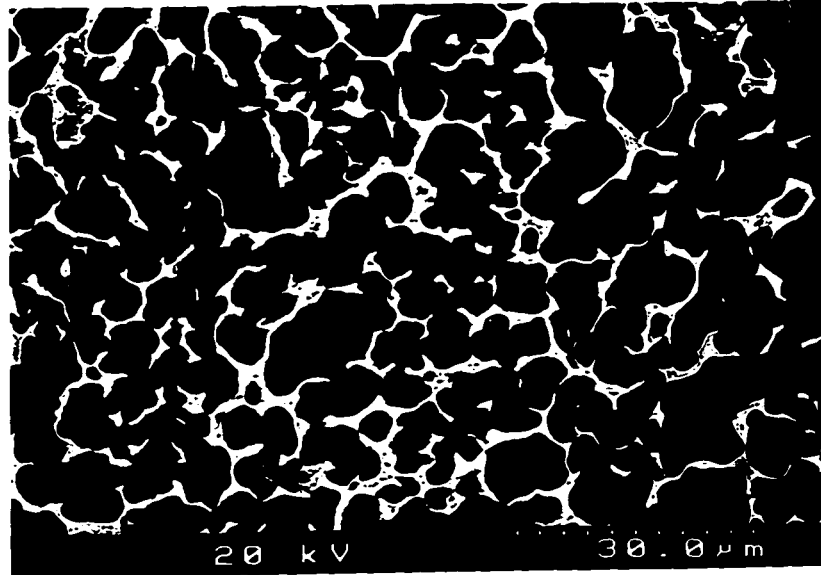


Figure 6-5. SEM micrographs of a  $5.5 \times 10^{-4}$  m Al-10wt%Cu droplet. a). overall microstructure of the droplet; b). microstructure at the centre part of the droplet; c). microstructure at the edge part; d). microstructure at the small section of another droplet.

c



d

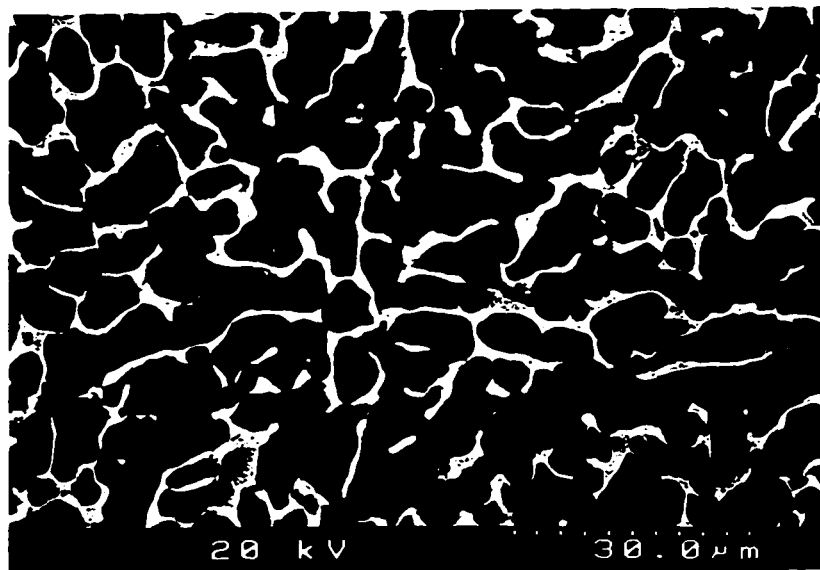
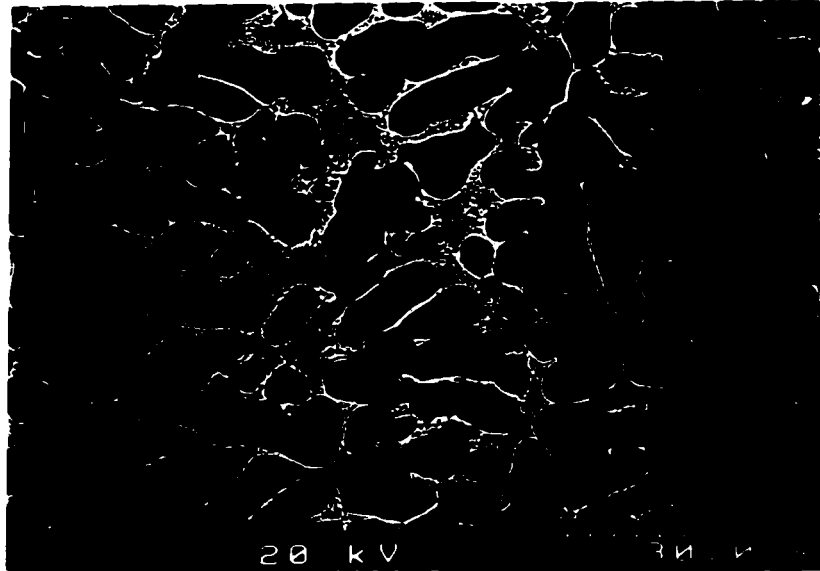


Figure 6-5. Continued.

a



b

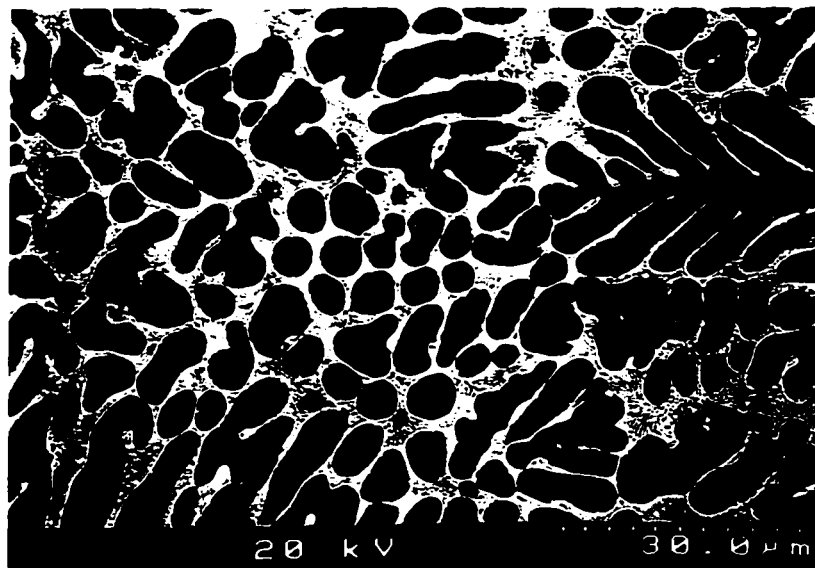
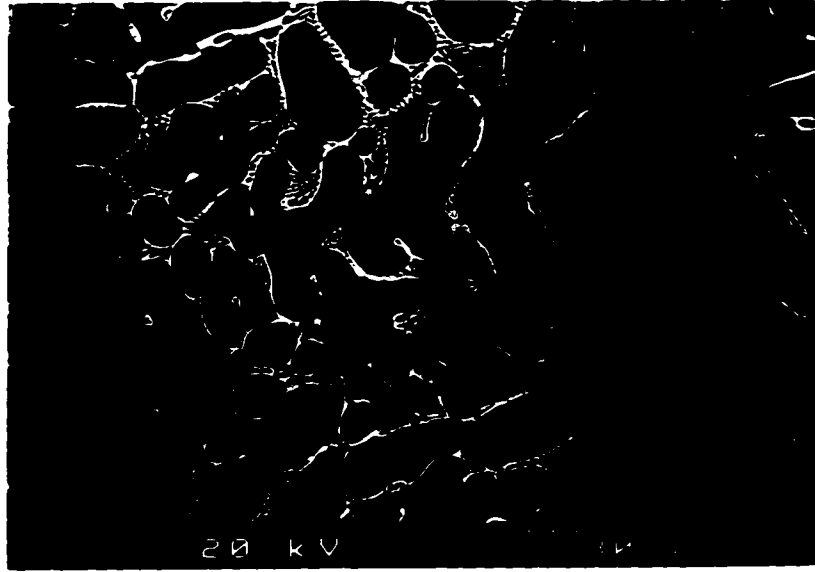


Figure 6-6. SEM micrographs of a  $4.6 \times 10^{-4}$  m Al-17wt%Cu droplet from two similar runs.



a



b

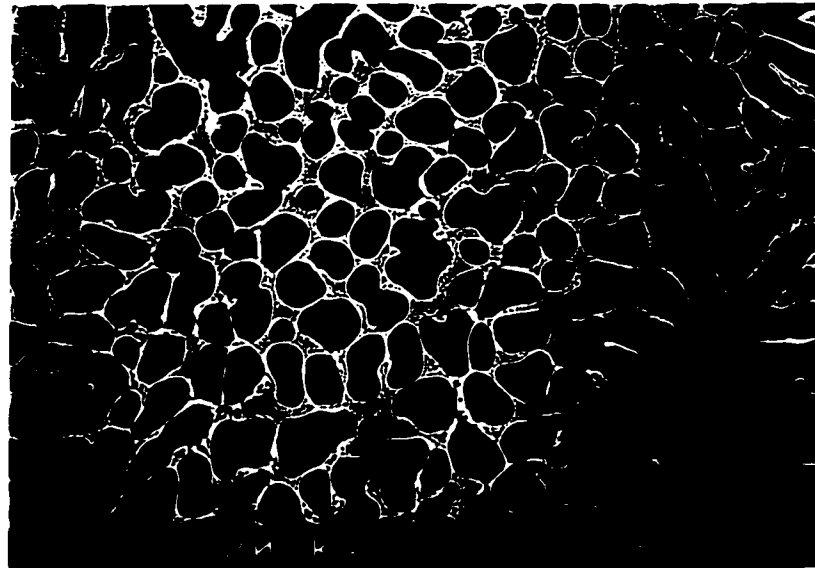
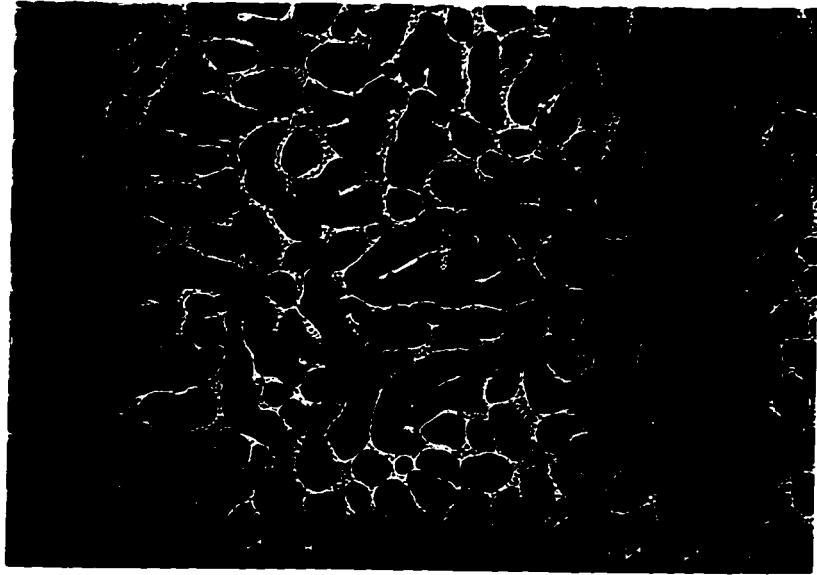


Figure 6-7. SEM micrographs of Al-17wt%Cu droplets in different size ranges. a). mid size =  $660\ \mu\text{m}$ ; b). mid size =  $4.6 \times 10^{-4}\ \text{m}$ ; c). mid size =  $3.3 \times 10^{-4}\ \text{m}$ ; d). mid size =  $2.3 \times 10^{-4}\ \text{m}$ .

c



d

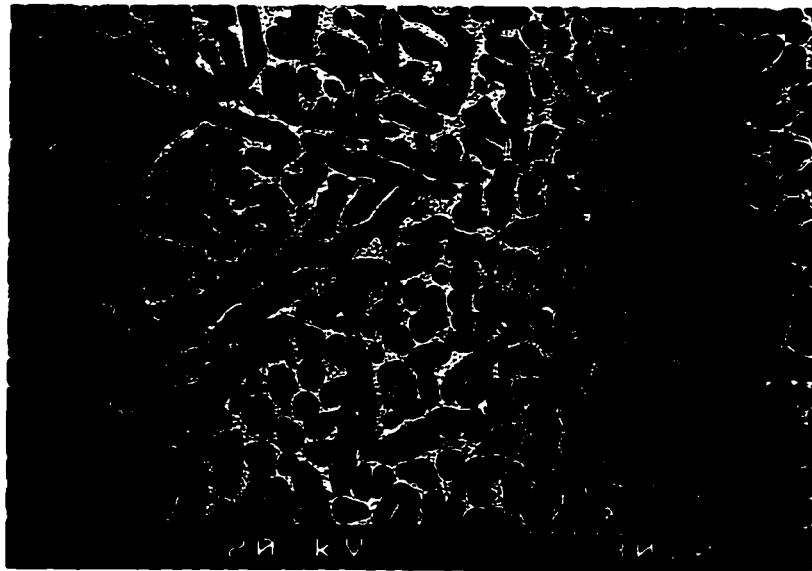


Figure 6-7. Continued.

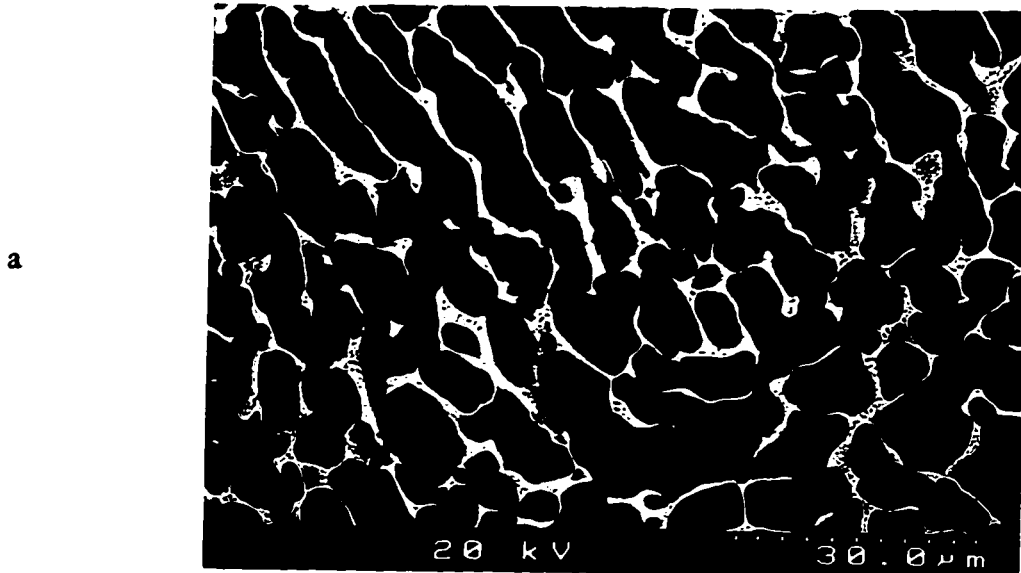
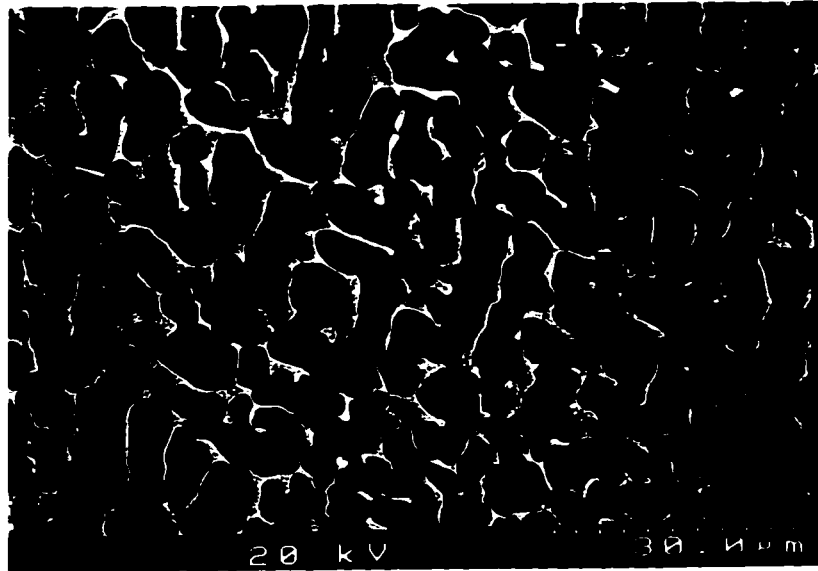


Figure 6-8. SEM micrographs of Al-10wt%Cu droplets in different size ranges.  
a). mid size =  $7.8 \times 10^{-4}$  m; b). mid size =  $5.5 \times 10^{-4}$  m;  
c). mid size =  $3.9 \times 10^{-4}$  m; d). mid size =  $2.8 \times 10^{-4}$  m;  
e). mid size =  $2.0 \times 10^{-4}$  m; f). mid size =  $1.4 \times 10^{-4}$  m.

c



d

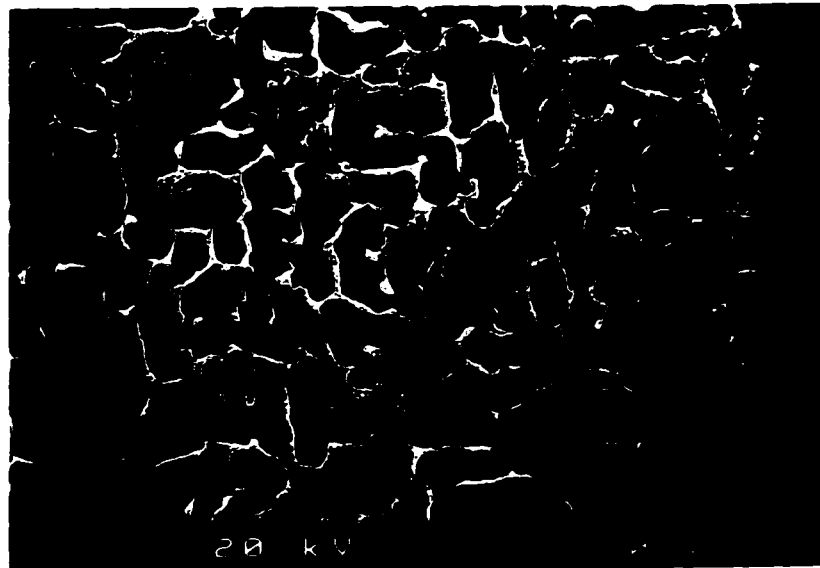
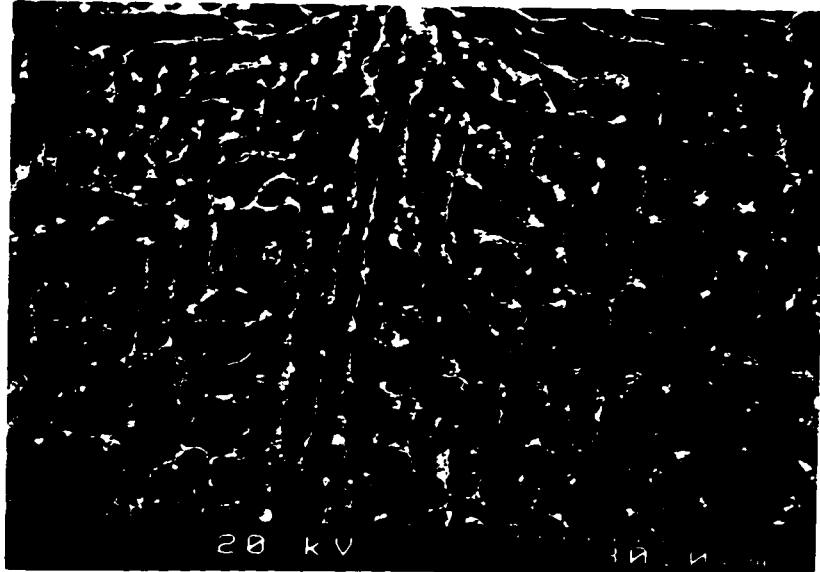


Figure 6-8. Continued.

e



f

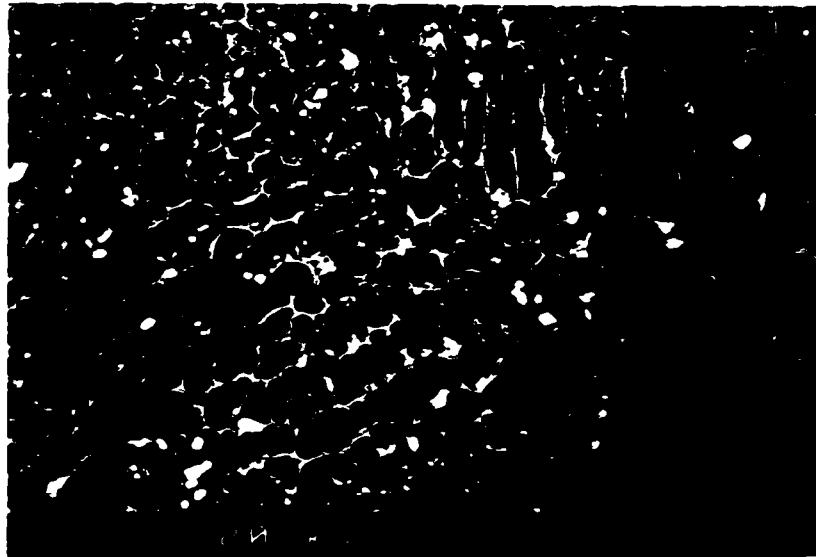
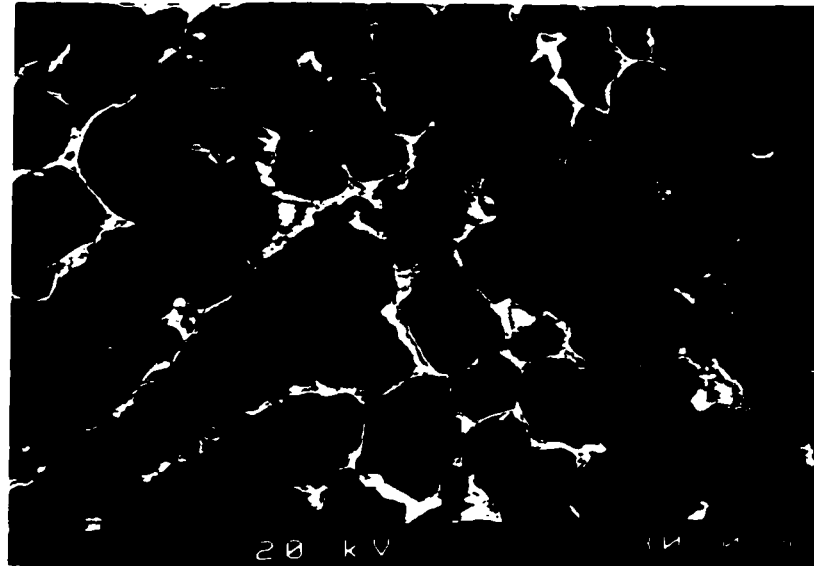


Figure 6-8. Continued.

a



b

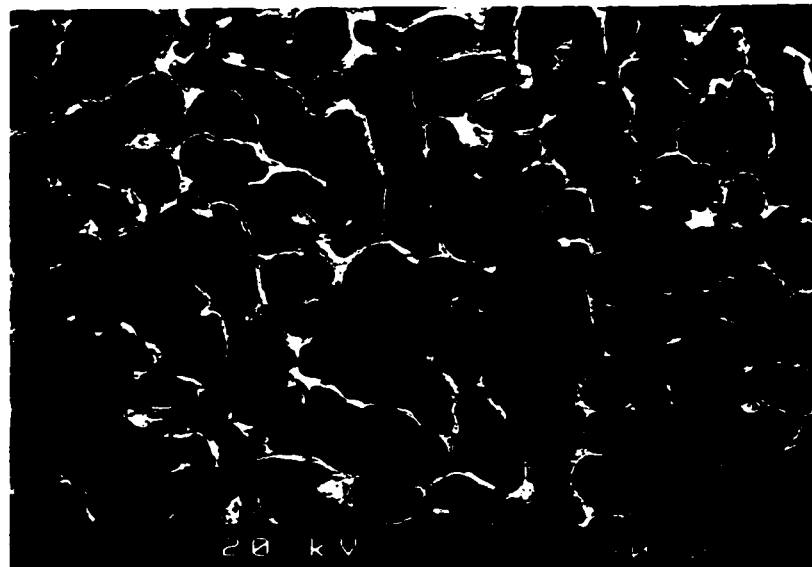
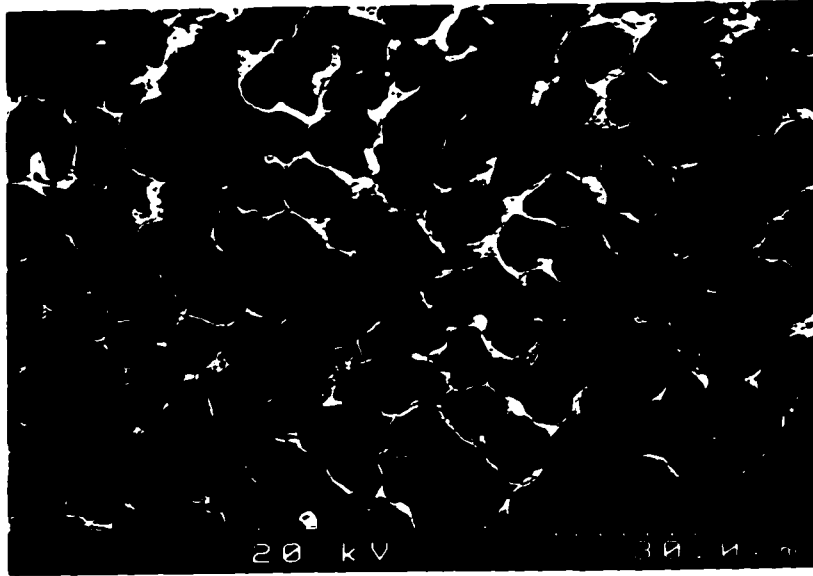


Figure 6-9. SEM micrographs of a  $5.5 \times 10^{-4}$  m Al-10wt%Cu droplets with different superheat. a). 50 K; b). 100 K; c). 150 K; d). 200 K.

c



d

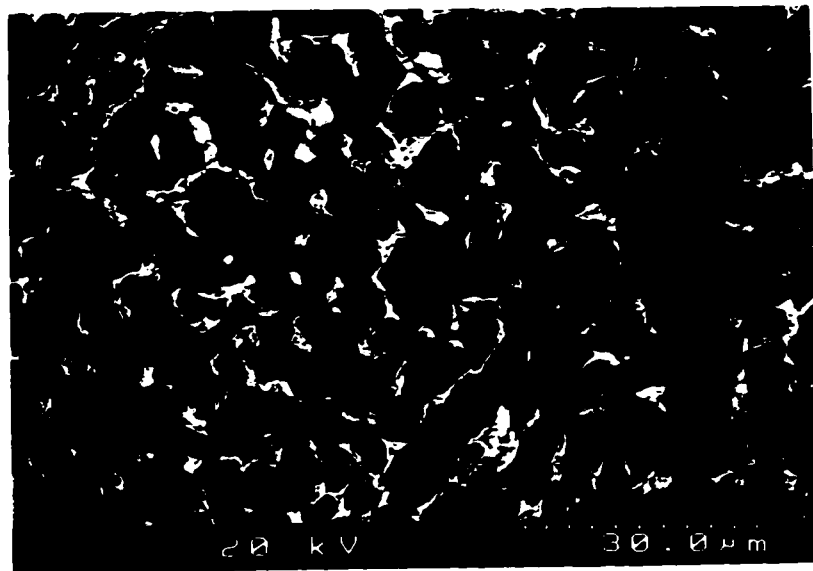


Figure 6-9. Continued.

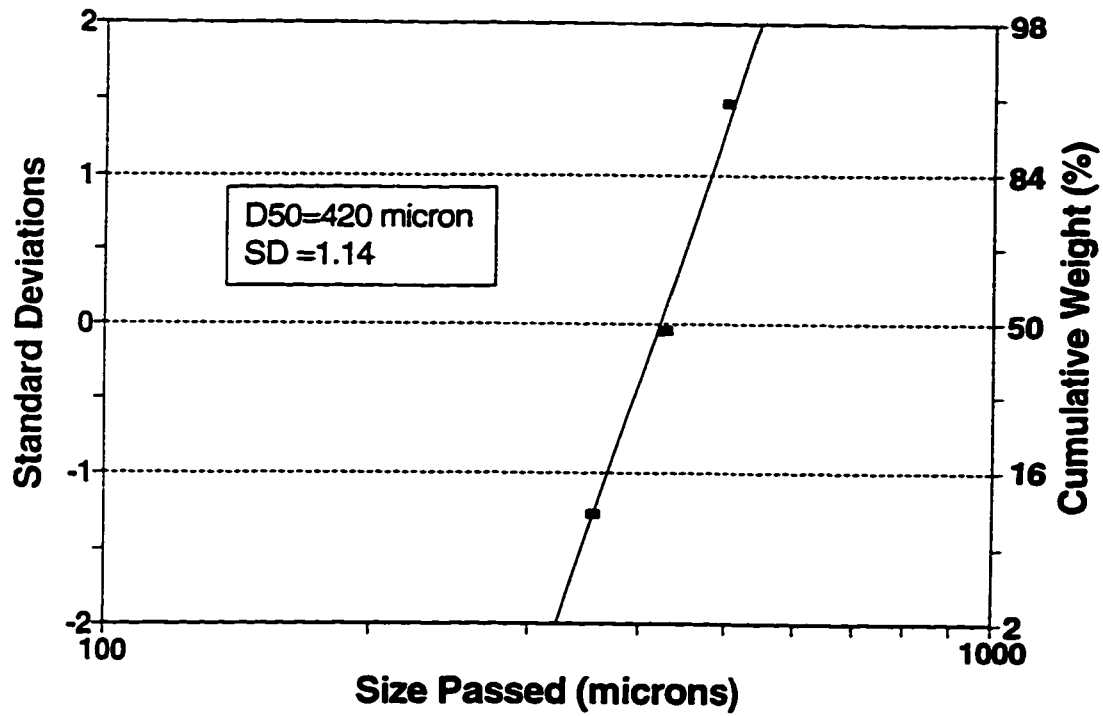
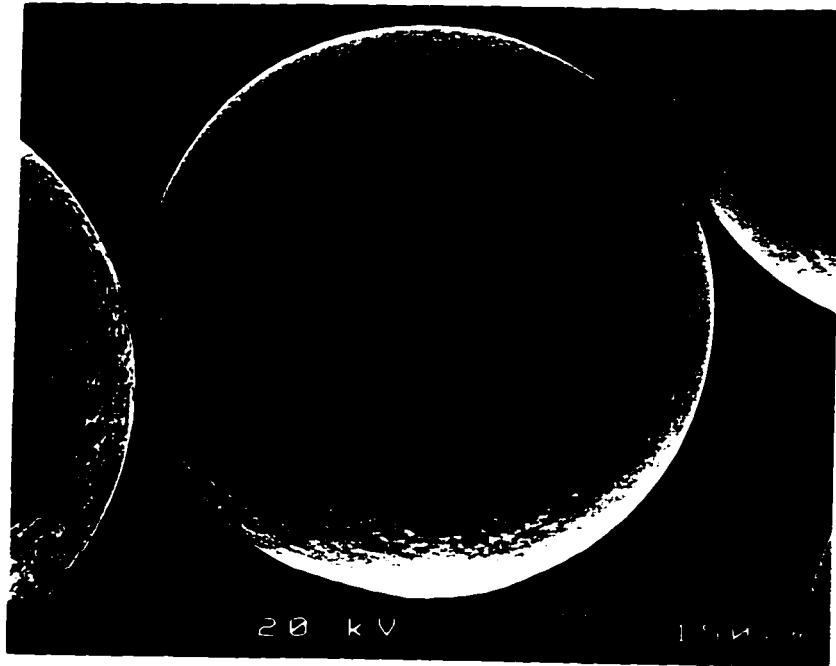


Figure 6-10. Log-normal plot of Al-3.7wt%Ni-1.5wt%Fe produced by IAP in nitrogen.



a



b



Figure 6-11. SEM micrograph of an Al-3.7wt%Ni-1.5wt%Fe droplet produced by IAP in nitrogen. a). surface morphology of the powder; b). cross section of a powder; c). micrograph showing the cellular region of the powder.

c

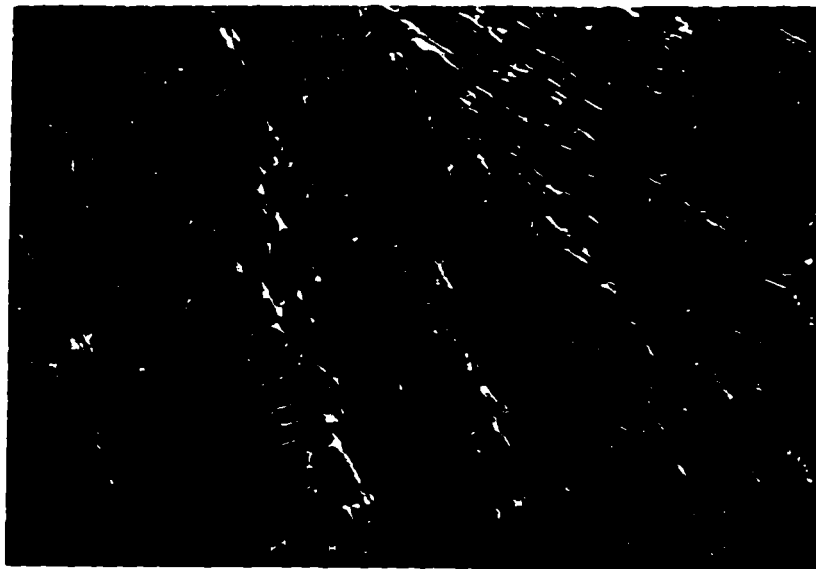
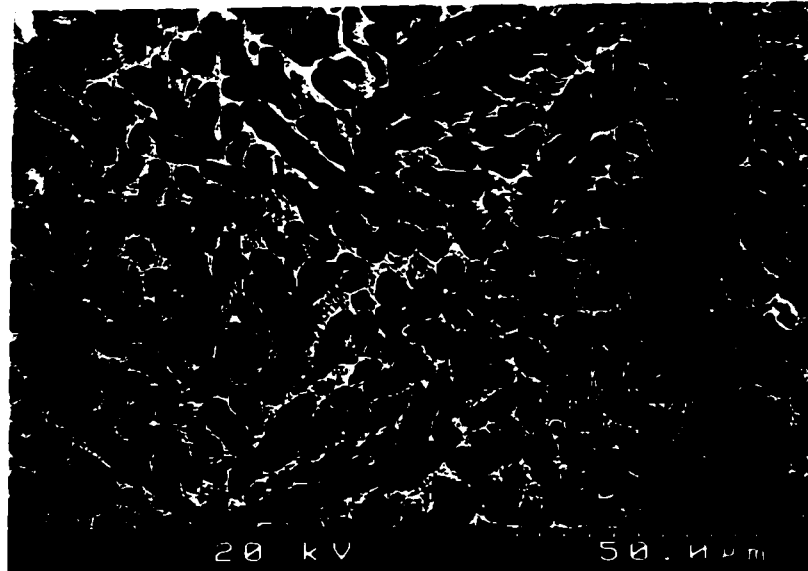


Figure 6-11. Continued.

a



b

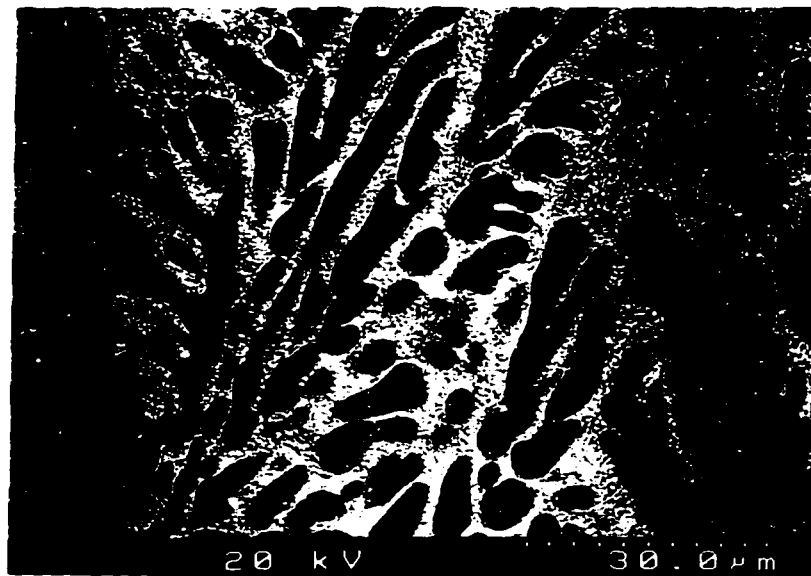


Figure 6-12. SEM micrographs showing dendrite regions of Al-3.7wt%Ni-1.5wt%Fe droplets in different size ranges produced by IAP in nitrogen. a). mid size =  $5.5 \times 10^{-4}$  m; b). mid size =  $3.9 \times 10^{-4}$  m; c). mid size =  $2.8 \times 10^{-4}$  m.

c

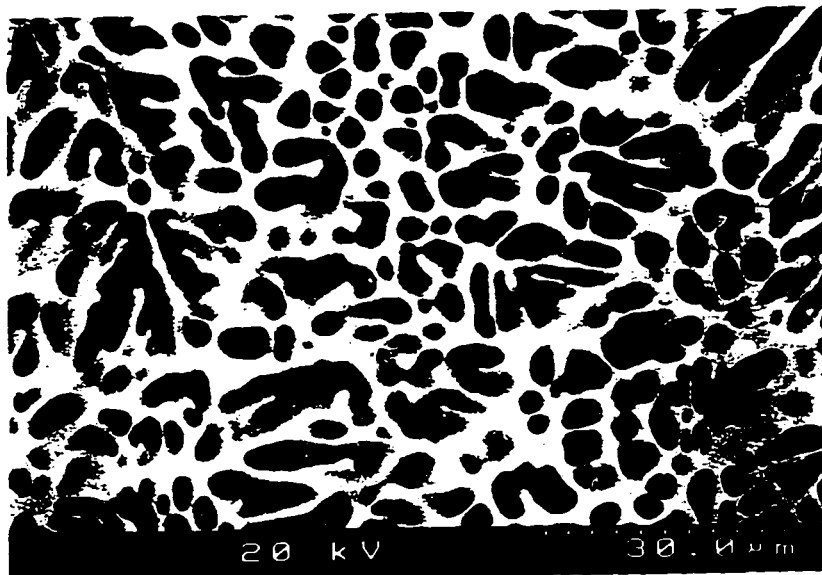


Figure 6-12. Continued.

IAP Particle Size Range: 165-925 microns

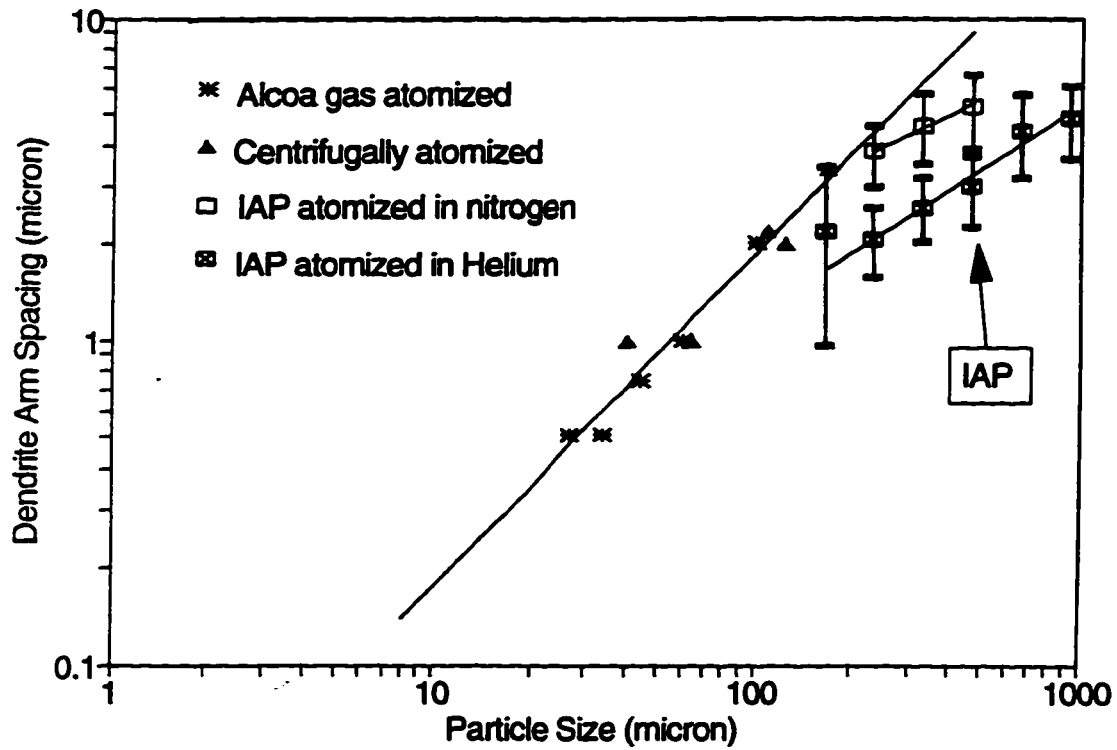


Figure 6-13. Effect of particle size on the secondary dendrite arm spacing of Al-3.7wt%Ni-1.5wt%Fe droplets produced by IAP in nitrogen and helium.

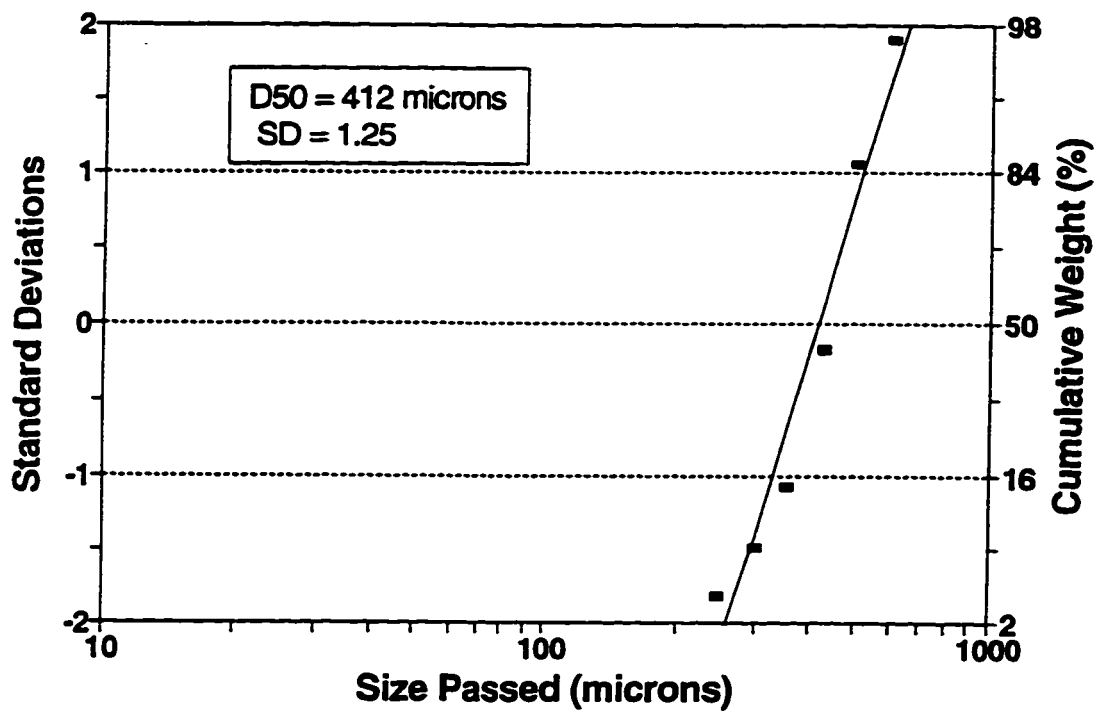


Figure 6-14. Log-normal plot of Al-3.7wt%Ni-1.5wt%Fe produced by IAP in helium.

a



b

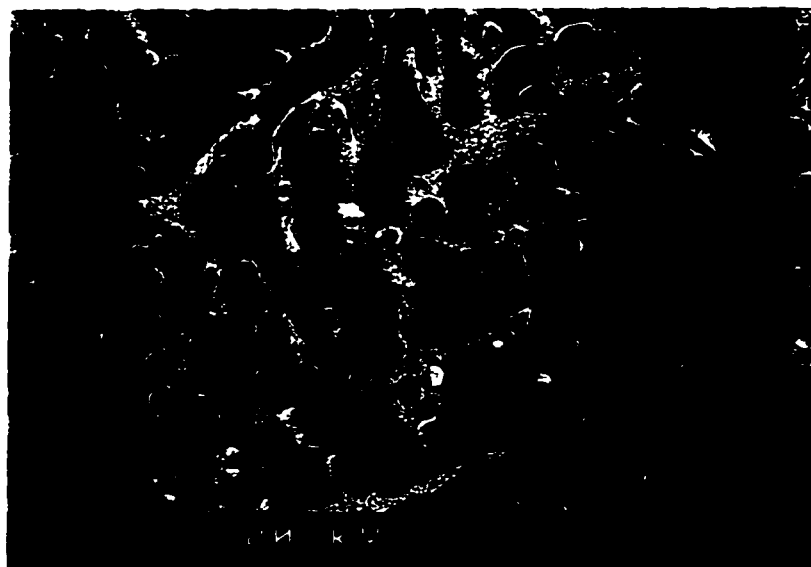


Figure 6-15. SEM micrographs of Al-3.7wt%Ni-1.5wt%Fe droplets in different size ranges produced by IAP in helium. a). mid size =  $1.09 \times 10^{-3}$  m; b). mid size =  $7.8 \times 10^{-4}$  m; c). mid size =  $5.5 \times 10^{-4}$  m; d). mid size =  $3.9 \times 10^{-4}$  m; e). mid size =  $2.8 \times 10^{-4}$  m; f). mid size =  $2.0 \times 10^{-4}$  m.

c



d

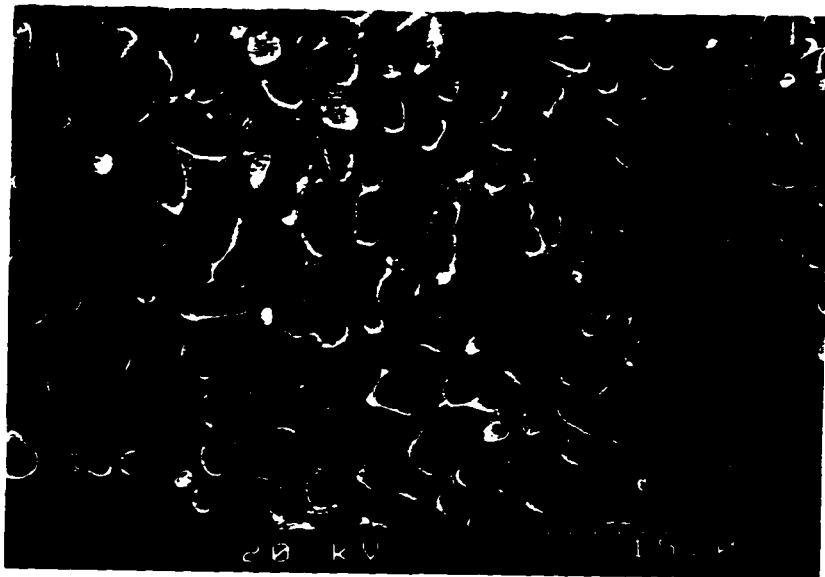


Figure 6-15. Continued.



e



f

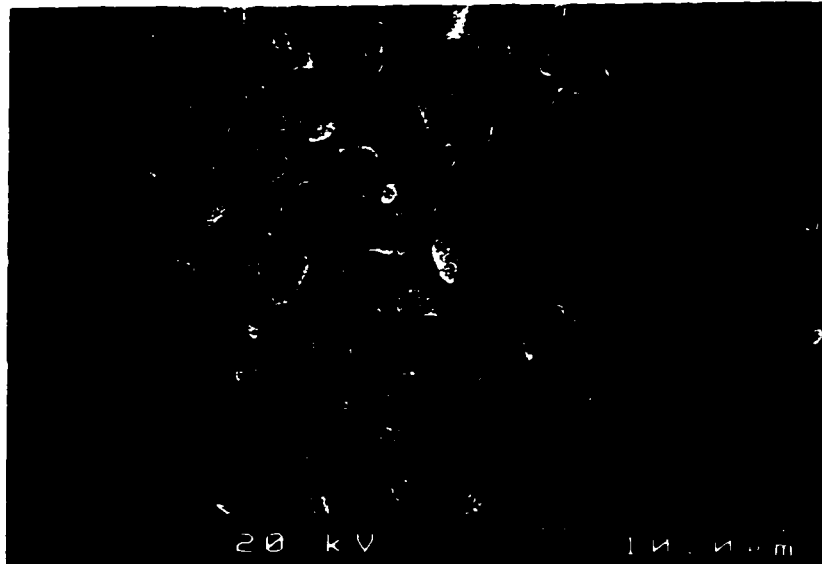


Figure 6-15. Continued.

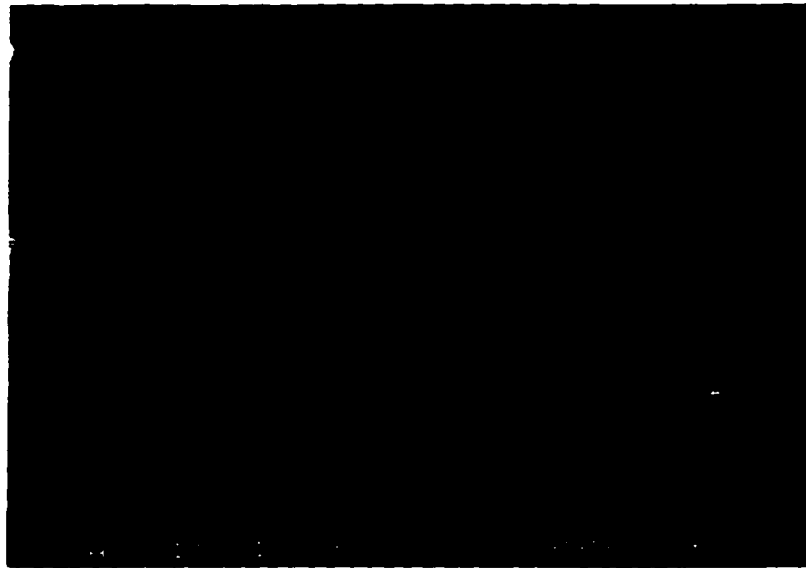


Figure 6-16. SEM micrograph of Al-3.7wt%Ni-1.5wt%Fe showing very fine lamellar eutectic microstructure.

## REFERENCES

- Acrivos, C.: "A relationship between Dendrite Arm Spacing and Atomized Powder Diameter", *J. Mater. Sci.*, 1976, vol.11, pp.1159-1160.
- Aldinger, F., Linck, E. and Claussen, N.: "A Melt-drop Technique for the Production of High-purity Metal Powder" in *Modern Developments in Powder Metallurgy*, vol. 9, P/M Principles and Production Processes, Hausner, H. H. and Taubenblat, P.V., Metal Powder Industries Federation, Princeton, 1977, pp. 141-151.
- Apelian, D.: "Solidification Mechanics and Mechanisms" in *Encyclopedia of Materials Science and Engineering*, Vol. 6, Bever, M. B., editor, Pergamon Press, The MIT Press, Cambridge, Massachusetts, 1986, pp. 4525-4529.
- Araki, N. and Masuda, A.: "Production of Droplets of Uniform Size by Vibration" in *Proc. of the 1st International Conference on Liquid Atomization and Spray Systems*, Tokyo, Aug. 27-31, 1978, The Fuel Society of Japan, 1979, pp. 173-180.
- Ashgriz, N. and Yao, S. C.: "Development of a Controlled Spray Generator", *Rev. Sci. Instrum.*, 1987, vol. 58, pp. 1291-1296.
- Beasley, J. D.: "Model for Fluid Ejection and Refill in an Impulse Drive Jet", *Photographic Science and Engineering*, 1977, vol. 21, pp. 78-82
- Berglund, R. N. and Liu, B. Y. H.: "Generation of Monodisperse Aerosol Standards", *Environmental Science and Technology*, 1973, vol. 7, pp. 147-153.
- Biennu, G.: "Method of Production of Metallic Granules, Products Obtained and a Device for the Application of the Said Method", US patent #4,428,894, Jan. 31, 1984.
- BioScan, Optimas, User Guide, BioScan, Incorporated, Edmonds, 1990.
- Bird, R. B., Stewart, W. E. and Lightfoot, E. N.: *Transport Phenomena*, John Wiley & Sons, Inc., New York, 1971, p.46.
- Bouse, L. F., Haile, D. G. and Kunze, O. R.: "Cyclic Disturbance of Jets to Control Spray Drop Size", *Transactions of the ASAE*, 1974, vol. 17, pp.235-239.

- Boyko, C. M. and Henein, H.: "Log-normal Particle Size Distribution Using a Spreadsheet Procedure" in *"Computer Software in Chemical and Extractive Metallurgy"*, Bale, C.W. and Irons, G. A., Editors, Metallurgical Society of CIM, Montreal, 1993, pp. 289-301.
- Brandau, E., Huschka, H., Kadner, M. and Schröder, W.: "Method for Manufacturing Spherical Particles out of Liquid Phase", U. S. Patent No. 5,183,493, Feb. 2, 1993.
- Broderick, T. F., Jackson, A. G., Jones, H. and Froes, F. H.: "The Effect of Cooling Conditions on the Microstructure of Rapidly Solidified Ti-6Al-4V", *Metall. Trans. A*, 1985, vol.16A(11), pp. 1951-1959.
- Brower, Jr. W. E., Strachan, R. and Flemings, M. C.: "Effect of Cooling Rate on Structure of Ferrous Alloys", *AFS Cast Metals Research Journal*, December, 1974, pp. 176-180.
- Burgoyne, H. and Cohen, L.: "The Production of Monodisperse Aerosols of Large Drop Size", *J. Colloid Sci.*, 1953, vol. 8, pp. 364-366.
- Cahn, J. W., W. B. Hillig, and G. W. Sears: "The Molecular Mechanism of Solidification", *Acta Metall.*, 1964, vol. 12, pp. 1421-1439.
- Caretti, J. C. and Bertorello, H. R.: "Nucleation in Massive Transformation: An Interpretation of the Correlation between Transformation Temperature and Cooling Rate", *Acta Metall.*, 1983, vol. 31, pp. 325-333.
- Chapra, S. C. and Canale, R. P.: *"Numerical Methods for Engineers with Personal Computer Applications"*, McGraw-Hill Book Company, New York, Toronto, 1985, P. 603.
- <sup>a</sup>Chaudhary, K. C. and Redekopp, L. G.: "The Nonlinear Capillary Instability of a Liquid Jet, Part 1: Theory", *J. Fluid. Mech.*, 1980, vol. 96, part 2, pp. 257-274.
- <sup>b</sup>Chaudhary, K. C. and Redekopp, L. G.: "The Nonlinear Capillary Instability of a Liquid Jet, Part 2: Experiments on Jet Behaviour before Droplet Formation", *J. Fluid. Mech.*, 1980, vol. 96, part 2, pp. 275-286.
- <sup>c</sup>Chaudhary, K. C. and Redekopp, L. G.: "The Nonlinear Capillary Instability of a Liquid Jet, Part 3: Experiments on Satellite Drop Formation and Control", *J. Fluid. Mech.*, 1980, vol. 96, part 2, pp. 287-297.
- Chun, J-H and Passow, C. H.: "A Study of Spray Forming Using Uniform Droplet Sprays" in *"Powder Production and Spray Forming: Advances in Powder Metallurgy and Particulate Materials"*, Metal Powder Industries Federation, Princeton, 1992, vol. 1, pp. 377-391.

Chun, J-H, and Passow, C. H.: "Production of Charged Uniformly Sized Metal Droplets", U.S. Patent No. 5,266,098, Nov. 30, 1993.

Cleary, H. J.: "The Microstructure and Corrosion Resistance of 55% Al-Zn Coating on Sheet Steel" in *"Microstructure Science, vol. 12, Corrosion, Microstructure and Metallography"*, Northwood, D. O., White, W. E. and Vander Voort, G. F., Editors, ASM International, Materials Park, OH, 1985, pp. 102-112.

Clyne, T. W.: "Numerical Treatment of Rapid Solidification", *Metall. Trans. B*, 1984, vol.15B, pp. 369-381.

Coriell, S. R. and Turnbull, D.: "Relative Roles of Heat Transport and Interface Rearrangement Rates in the Rapid Growth of Crystals in Undercooled Metals", *Acta Metall.*, 1982, vol.30, pp. 2135-2139.

Cosandey, F., Kissinger, R. D. and Tien, J. K.: "Cooling Rates and Fine Microstructures of RSR and Argon Atomized Superalloy Powders" in *"Rapidly Solidified Amorphous and Crystalline Alloys"*, Kear, B. H., Giessen, B. C. and Cohe, M., Editors, Elsevier Science Publishing Co., New York, 1982, pp. 173-178.

Crane, L., Birch, S. and McCormack, P. D.: "The Effect of Mechanical Vibration on the Break-up of a Cylindrical Water Jet in Air", *Brit. J. Appl. Phys.*, 1964, vol. 15, pp. 743-750.

Curry, S. A. and Portig, H.: "Scale Model of an Ink Jet". *IBM J. Res. Dev.*, 1977, vol. 21, pp.10-20.

Dabora, E. K.: "Production of Monodisperse Sprays", *The Review of Scientific Instruments*, 1967, vol. 38, pp. 502-506.

Dixon, C. F.: "Atomizing Molten Metals - a Review", *Canadian Metallurgical Quarterly*, 1973, vol. 12, No.3, pp. 309-322.

Dombrowski, N. and Johns, W. R.: "The Aerodynamic Instability and Disintegration of Viscous Liquid Sheets", *Chem. Eng. Sci.*, 1963, vol. 18, pp. 203-214.

Duflos, F.: "Cooling Rate Measurement on Pure Iron Rapidly Solidified by Piston Quenching", *J. Mater. Sci.*, 1987, vol.22, pp. 3765-3770.

Dunkley, J. J. and Palmer, J. D.: "Factors Affecting Particle Size of Atomized Metal Powders", *Powder Metallurgy*, 1986, vol. 29, No. 4, pp. 287-290.

Flemings, M. C.: *"Rapid Solidification Processing"*, McGraw-Hill, New York, 1974, pp. 58-92.

Frommeyer, G.: "Microstructures of Melt-Atomized and Rapidly Solidified Eutectic Fe-C and Ni-Cr Martensitic White Cast Iron Alloys", *Z. Metallkde*, 1985, vol. 76(10), pp. 662-668.

Frommeyer, G. and Vogt, E.: "Solidification Parameter, Microstructures, and Mechanical Properties of Rapidly Solidified Iron-Based Alloys", *Steel Research*, 1987, vol.58, pp. 491-497.

German, R. M.: "*Powder Metallurgy Science*", 2nd Edition, Metal Powder Industries Federation, Princeton, 1994, pp. 27-165.

Gill, W. N., Jang, J. Y., Mollendorf, J. C. and Adam, C. M.: "Rapid Solidification of Subcooled Small Metallic Drops: Internal Nucleation", *J. of Crystal Growth*, 1984, vol. 66, pp. 351-368.

Goedde, E. F. and Yuen, M. C.: "Experiments on Liquid Jet Instability", *J. Fluid Mech.*, 1970, vol. 40, part 3, pp. 495-511.

Grant, N. J. and Perlloux, R. M.: "Liquid-Metal Atomization for Hot Working Preforms", "*Rapid Solidification Technology*", Source Book, a Collection of Outstanding Articles from the Technical Literature, Ashbrook, R. L., Editor, ASM, Materials Park, Ohio, 1983, pp. 361-380.

Gummesson, P. U.: "Modern Atomizing Techniques", *Powder Metallurgy*, 1972, vol. 15, No. 29.

Guthrie, R. I. L., Clift, R. and Henein, H.: "Contacting Problems Associated with Aluminium and Ferro-Alloy Additions in Steelmaking-Hydrodynamic Aspects", *Metall. Trans. B*, 1975, vol. 6B, pp. 321-329.

Gutierrez-Miravete, E., Lavernia, E. J., Trapaga, G. M., Szekely, J. and Grant, N. J.: "A Mathematical Model of the Spray Deposition Process", *Metall. Trans. A*, 1989, vol. 20A, pp. 71-85.

Heinzl, L. and Hertz, C. H.: "Ink-Jet Printing", *Advances in Electronics and Electron Physics*, 1985, vol. 65, pp. 91-171.

Hildeman, G. J., Lege, D. J. and Vasudevan, A. K.: "Influence of Powder Morphology on the Mechanical Properties of Rapidly Solidified Aluminum Alloys" in "*High-Strength Powder Metallurgy Aluminum Alloys*", Koczak, M. J. and Hildeman, G. J., Editors, The Metallurgical Society of AIME, Texas, 1982. pp. 249-276.

Hildeman, G. J., Paris, H. G. and Billman, F. R.: "Powder Size, Solidification and Microstructure Relationships in Gas Atomized Aluminum Alloy Powders", Private Communication and Oral Presentation, Powder Symposium, TMS, Atlanta, 1983.

Hirth, J. P.: "Nucleation, Undercooling and Homogeneous Structures in Rapidly Solidified Powders", *Metall. Trans. A*, 1978, vol. 9A, pp. 401-404.

Holliday, D. and Resnick, R.: "*Fundamentals of Physics*", 3rd Edition, John Wiley & Sons, New York, 1988, p. 446.

Holloman, J. H.: "Heterogeneous nucleation" in "*Thermodynamics in Physical Metallurgy*", Am. Soc. Met., Cleveland, Ohio, 1950.

Horwath, J. A. and Mondolfo, L. F.: "Dendritic Growth", *Acta Metall.*, 1962, vol. 10, pp. 1037-1042.

Huang, Peiyun: "*Fundamental of Powder Metallurgy*", Metallurgical Industry Press, (in Chinese), Beijing, 1982, pp. 95-110.

Huôt, J-Y.: Private Communication, Fax on Nov. 26, 1994 from Noranda Technology Centre, Pointe Claire, Quebec, Canada.

Incropera, F. P. and Dewitt, D. P.: "*Fundamentals of Heat Transfer*", John Wiley & Sons, New York, 1981, pp. 283-293.

Jackson, K. A., Hunt, J. D., Uhlmann, D. R. and Seward, T. P.: III, "On the Origin of the Equiaxed Zone in Castings", *Transactions of the Metallurgical Society of AIME*, 1966, vol. 236, pp.149-158.

Joly, P. A. and Mehrabian, R.: "Complex Alloy Powders Produced by Different Atomization Techniques: Relationship between Heat Flow and Structure", *J. Mater. Sci.*, 1974, vol. 9, pp. 1446-1455.

Jones, B. J.: "Structure Effect of Solidification at Large Undercooling", "*Solidification Technology*", Burke, J. J., Flemings, M. C., and Gorum, A. E., Editors, Brook Hill Publishing Co., Columbus, Ohio, 1972, pp. 407-425.

Jones, H.: "Production and Characterization of Rapidly-Solidified Particulates" in "*Science and Technology of the Undercooled Melt*", Sahm, P. R., Jones, H. and Adam, C. M., Editors, Nartinus Nijhoff Publishers, Boston, 1986, pp. 156-184.

Josson, B.: "Modeling of Crystal Growth during Rapid Solidification", *Metall. Trans. A.*, 1991, vol. 22A, pp. 2475-2485.

- Kawasaki, A., Kuroki U. and Wantanabe, R.: "Preparation of Monosized Metal Powders by Pulsated Orifice Injection" in *Proceedings of 1993 Powder Metallurgy World Congress*, Bando, Y. and Kosuge, K., Kyoto, Editors, Japan, 1993, pp. 27-30.
- Keur, R. I. and Stone, J. J.: "Some effects of fluid jet dynamics on ink jet printing", *IEEE Trans. Ind. Appl.*, 1976, vol. IA-12, pp. 86-90.
- Khedkar, P. and Nash, P.: "Relationship of DAS to Cooling Rate in Solidified U-700 Alloy", *J. Mater. Sci. Letters*, 1986, vol. 5, pp. 1273-1274.
- Kolesnichenko, A. F.: "Electromagnetic Processes in Liquid Materials in the USSR and East European Countries", *ISIJ International*, 1990, vol. 30, No. 1, pp. 8-26.
- Kim, W. T., Zhang, D. L. and Cantor, B.: "Nucleation of Solidification in Liquid Droplets", *Metall. Trans. A*, 1991, vol. 22A, pp. 2487-2501.
- Kolesnichenko, A. F.: "New Methods of Materials Granulation from Conductive and Non-conductive Liquids", 1994, Unpublished work.
- Lavernia, E. J., Gutierrez, E. M., Szekely, J. and Grant, N. J.: "Heat Flow Behaviour During Spray Deposition of a Nickel Base Superalloy by Liquid Dynamic Compaction" in *Progress in Powder Metallurgy*, Cynthia, L. F., Hjort, H., Editors, Metal Powder Industries Federation, Princeton, 1987, vol. 43, pp. 683-709.
- Lavernia, E. J., Gutierrez, E. M., Szekely, J. and Grant, N. J.: *International J. of Rapid Solidification*, 1988, vol. 4, pp. 89-124.
- Levanoni, M.: "Study of Fluid Flow through Scaled-up Ink Jet Nozzles", *IBM J. Res. Dev.*, 1977, vol. 21, pp. 56-68.
- Levi, C. G.: "The Evolution of Microstalline Structures in Supercooled Metal Powders", *Metall. Trans. A*, 1988, vol. 19A, pp. 699-708.
- Levi, C. G. and Mehrabian, R.: "Heat Flow during Rapid Solidification of Undercooled Metal Droplets", *Metall. Trans. A*, 1982, vol. 13A, pp. 221-234.
- Lindblad, N. R. and Schneider, J. M.: "Production of uniform-sized liquid droplets", *J. Sci. Instrum.*, 1965, vol. 42, pp. 635-638.
- Liu G. X.: *Fundamental of Metallurgy*, Metallurgical Industry Press, (in Chinese), Beijing, 1980.
- Lubanska, H.: "Correlation of Spray Ring Data for Gas Atomization of Liquid Metals", *Jurnal of Metals*, February, 1970, vol. 22, pp. 45-49.



- Lyman, T., Boyer, H. E., Carnes, W. J., Chevalier, M. W., Durand, E. A., Unterweiser, P. M., Baker, H., Darvey, P. D., Waldorf, H. L., Bukovics, H. V., Kirkpatrick, C. W. and Kothera, J. W.: "*Metallography, Structures and Phase Diagrams, Metals Handbook*", 8th Edition, vol. 8, , American Society for Metals, Metals Park, Ohio, 1973, p. 124, p. 259.
- Marcantonio, J. A. and Mondolfo, L. F.: "Denucleation", *Metall. Trans.*, 1974, vol. 5, pp. 1325-1329.
- Markworth, A. J.: "A Kinematical Model of Liquid-Drop Solidification due to Multiple Surface-Nucleation Events", *Materials Science and Engineering*, 1988, vol.100, pp. 169-176.
- Mason, B. J., Jayaratine, O. W. and Woods, J. D.: "An Improved Vibrating Capillary Device for Producing Uniform Water Droplets of 15 to 500  $\mu\text{m}$  Radius", *J. Sci. Instrum.*, 1963, vol. 40, pp. 247-249.
- Mason, B. J. and Brownscombe, J. L.: "Production of Uniform-size Drops at Controllable Frequency and Spacing from a Vibrating Capillary", *J. Sci. Instrum.*, 1964, vol. 41, p. 258.
- Massalski, T. B., Okamoto, H., Subramanian, P. R. and Kacprzak, L.: "*Binary Alloy Phase Diagrams*", 2nd Edition, vol. 1, ASM International, Materials Park, 1990, p. 142.
- Mater, G., Bicsak, E., Huppmann, W. J. and Claussen, N.: in "*Modern Developments in Powder Metallurgy*", Hausce, H. H. and Taubenblat, P. W., Editors, MPIF, Princeton, N. J., 1977, pp. 153-159.
- Mills, K., Davis, J. R., Destefani, J. D., Dieterich, D. A., Crankovic, G. M. and Frissell, H. J.: "*Metallography and Microstructure, ASM Handbook*", vol. 9, American Society for Metals, Metals Park, 1985, p. 4.
- Mills, K., Davis, J. R., Refsnes, S. K., Sanders, B. R. and Frissell, H. J.: "*Powder Metallurgy, Metals Handbook*", vol. 7, American Society for Metals, Metals Park, 1984, pp. 21-208.
- Minkoff, I.: "*Solidification and Cast Structure*", John Wiley & Sons, New York, 1986.
- Miyazawa, Y. and Pound, G. M.: "Homogeneous Nucleation of Crystalline Gallium from Liquid Gallium", *J. of Crystal Growth*, 1973, vol.23, pp. 45-57.
- Mondolfo, L. F. and Barlock, J. G.: "Effect of Superheating on Structure of Some Aluminum Alloys", *Metall. Trans. B*, 1975, vol. 6B, pp. 565-572.

**MPIF Standard 03: "Determination of Flow Rate of Free-Flowing Metal Powders Using the Hall Apparatus", *Standard Test Methods for Metal Powders and Powder Metallurgy Products*, Metal Powder Industries Federation Standard 03, Metal Powder Industries Federation, Princeton, 1991.**

**MPIF Standard 04: "Determination of Apparent Density of Free-Flowing Metal Powders Using the Hall Apparatus", *Standard Test Methods for Metal Powders and Powder Metallurgy Products*, Metal Powder Industries Federation Standard 04, Metal Powder Industries Federation, Princeton, 1991.**

**MPIF Standard 05: "Determination of Sieve Analysis of Metal Powders", *Standard Test Methods for Metal Powders and Powder Metallurgy Products*, Metal Powder Industries Federation Standard 05, Metal Powder Industries Federation, Princeton, 1991.**

**MPIF Standard 28: "Determination of Apparent Density of Non-Free-Flowing Metal Powders Using the Carney Apparatus", *Standard Test Methods for Metal Powders and Powder Metallurgy Products*, Metal Powder Industries Federation Standard 28, Metal Powder Industries Federation, Princeton, 1991**

**Nichiporenko, O. S.: "Shaping of Powder Particles During the Atomization of a Melt with Water", *Sov. Powd. Metall. Met. Ceram.*, 1976, vol.165, pp. 665-669.**

**Perepezko, J. H., Galaup, C. and Rasmussen, D. H.: "Solidification of Highly Undercooled Liquid Metals and Alloys" in "*Proc. of 3rd European Sump. on Material Sciences in Space*", Grenoble 24-27 April 1979 - ESA SP-142, European Space Agency, Paris, 1979, pp. 375-383.**

**Pound, G. M. and La Mer, V. K.: "Kinetics of Crystalline Nucleus Formation in Supercooled Liquid Tin", *J. Amer. Chem. Soc.*, 1952, vol. 74, pp. 2323-2332.**

**Rai, G., Lavernia, E. and Grant., N. J.: "Powder Size and Distribution in Ultrasonic Gas Atomization", *J. of Metals.*, Aug., 1985, vol. 37, pp. 22-26.**

**Ranz, W. and Marshall, W. R. Jr.: "Evaporation from Drop: Part 1", *Chem. Eng. Prog.*, 1952, vol. 48, pp. 141-148.**

**Rayleigh, J. W. S.: "*The Theory of Sound*", Vol. 2, Dover Publications, New York, 1945, pp.360-365.**

**Rayleigh, L.: "On the Instability of Jets", *Proceedings of the London Mathematical Society*, 1878, vol. 10, pp.4-13.**

**Reddy, G. S. and Sekhar, J. A.: "Moderate Pressure Solidification: Undercooling at Moderate Cooling Rates", *Acta Metall.*, 1989, vol.37, pp. 1509-1519.**

Roth, Lawrence O. and Jay G. Porterfield: "Spray Drop Size Control", *Transactions of the ASAE*, 1970, vol. 13, pp. 779-781, and 784.

Sassa, K., Agata, A., Koxuka, T. and Asai, S.: "Atomization of Molten Metal by Use of Electromagnetic Force", *ISIJ*, 1989, vol.75, pp. 1294-1299.

Schmidt, P.: "Zerteilen von Flüssigkeiten in Gleich Grobe Tropfen", *Chemie-Ingenieur-Technik (Chem.-Ing.-Techn.)*, 1967, vol. 39, pp. 375-379.

Schneider, J. M.: "*The Stability of Electrified Liquid Surfaces*", PhD thesis, University of Illinois, Urbana, 1964.

Schneider, J. M. and Hendricks, C. D.: "Source of Uniform-sized Liquid Droplets", *The Review of Scientific Instruments*, 1964, vol. 35, pp. 1349-1350.

Schummer, P. and Tebel, K. H.: "Production of Monodisperesed Drops by Forced Disturbance of a Free Jet", *German Chemical Engineering*, 1982, vol. 5, pp. 209-220.

See, J. B., Runkle, J. and King, T. B.: "The Disintegration of Liquid Lead Streams by Nitrogen Jets", *Metall. Trans.*, 1973, vol. 4, pp. 2669-2673.

Singer, A. R. E. and Roche, A. D.: "Roller Atomization of Molten Metals for the Production of Powders" in "*Modern Developments in Powder Metallurgy*", Hausce, H. H. and Taubenblat, P. W., Editors, MPIF, Princeton, N. J., 1977, pp. 127-140.

Skolianos, S., Liu, P. S. and Kattamis, T. Z.: "Effect of Coarsening During Solidification on Grain Size" in "*Grain Refinement in Casting and Welds*", Abbaschian, G. J. and David, S. A., Editors, The Metallurgical Society of AIME, Warrendale, 1982, pp. 97-116.

Skolianos, S., Chen, M. and Kattamis, T. Z.: "Contribution of Coarsening to the Establishment of Grain Size in Bulk-undercooling Ni-Ag Alloys" in "*Undercooled Alloy Phases*", Collings, E. W. and Koch, C. C., Editors, The Metallurgical Society of AIME, Warrendale, 1987, pp. 123-144.

Stone, I. C. and Tsakiroopoulos, P.: "Cooling rates in gas atomized Al-4wt%Cu alloy powders", *International Journal of Rapid Solidification*, 1992, Vol. 7, pp. 177-190.

Strom, L.: "The Generation of Monodisperse Aerosols by Means of a Disintegrated Jet of Liquid". *The Review of Scientific Instruments*, 1969, vol. 40, pp. 778-782.

Szekely, J.: "*Fluid Flow Phenomena in Metals Processing*", Academic Press, New York, 1979, p. 256.

- Taha, M. A.: "Some Observation on Dendrite Morphology and Dendrite Arm Spacings", *Metal Science*, 1979, vol.13, pp. 9-12.
- Tallmadge, J. A.: "Chapter 1, Powder Production by Gas and Water Atomization of Liquid Metals" in *"Powder Metallurgy Processing"*, Kuhn, H. A. and Lawley, A., Editors, Academic Press, New York, 1978, pp. 1-32.
- Trivedi, R.: "Dendritic Solidification" in *"Encyclopedia of Materials Science and Engineering"*, Bever, M. B., Editor, The MIT Press, Oxford, Syden, Frankfurt, Cambridge, Massachusetts, 1989, Vol. 6, pp. 1044-1047.
- Turnbull, D.: "The Subcooling of Liquid Metal", *J. Appl. Phys.*, 1949, vol. 20, p. 817
- Turnbull, D.: "Formation of Crystal Nuclei in Liquid Metals", *J. Appl. Phys.*, 1950, vol. 21, pp. 1022-1028.
- Turnbull, D.: "Kinetics of Solidification of Supercooled Liquid Mercury Droplet", *J. of Chemical Physics*, 1952, vol. 20 (3), pp. 411-424.
- Turnbull, D. and Cech, R. E.: "Microscopic Observation of the Solidification of Small Metal Droplets", *J. Appl. Phys.*, 1950, vol 21, pp. 804-810.
- Weast, R. C.: "*CRC Handbook of Chemistry and Physics*", 49th Edition, The Chemical Rubber Co., Cleveland, Ohio, 1968, p. F-19.
- Weast, R. C., Astle, M. J. and Beyer, W. H.: "*CRC Handbook of Chemistry and Physics*", 69th Edition, CRC Press, Boca Rotan, 1988, p. B-68, p. B-88, p. B-111, p. D-44, p. E-3, p. E-12, p. E-13, p. F-47.
- Wedding, J. B.: "Operational Characteristics of the Vibrating Orifice Aerosol Generator", *Environmental Science and Technology*, 1975, vol. 7, pp. 673-674.
- Wentzell, J. M.: "Metal Powder Production by Vacuum Atomization", *J. Vac. Sci. Technology*, 1974, vol.11 (6), pp. 1035-1037.
- Wicks, C. E. and Block, F. E.: "*Thermodynamic Properties of 65 Elements-Their Oxides, Halides, Carbides, and Nitrides*", U. S. Govt. Print. Off., Washington DC, 1963, p. 10, p. 41.
- Yates, W. E. and Akesson, N. B.: "Monodisperse Atomization Systems for Pesticide Sprays", "*Proc. of the 1st International Conference on Liquid Atomization and Spray Systems*", The Fuel Society of Japan, Tokyo, 1979, pp. 181-185.

**Yuan, D., Henein, H. and Fallavollita, J.: "Method and Apparatus for Producing Droplets", U.S. Patent No.5,609,919, Mar. 11, 1997.**

**Yuen, M.-C.: "Non-linear Capillary Instability of a Liquid Jet", *J. Fluid Mech.*, 1968, vol. 33, part 1, pp. 151-163.**

**Yule, A. J. and Dunkley, J. J.: "*Atomization of Melts for Powder Production and Spray Deposition*", Clarendon Press, Oxford, 1994, pp. 143-218.**

**APPENDIX A**

**FORTRAN PROGRAM TO CALCULATE  
THE TEMPERATURE PROFILE OF AN Al-17wt%Cu DROPLET**

\*\*\*\*\*

\* This program will calculate the thermal profile of a 83%wtAl-17%wtCu \*  
 \* alloy droplet during free falling by using 4th-order Runge-Kutta method. \*  
 \* The units used in calculation are in SI units as shown in the \*  
 \* and are also shown as follows, except for particle size where m is used in \*  
 \* calculation, but  $10^{-6}$  m is used in keyboard entry for convenience. \*

*	Variables	Definitions	Units	*
*	beta:	Cahn's parameter in the kinetic equation		*
*	B:	kinetic coefficient	m/s/K	*
*	D:	droplet diameter	m	*
*	R0:	droplet radius	m	*
*	density:	density of droplet	kg/m <sup>3</sup>	*
*	densitya:	density of nitrogen	kg/m <sup>3</sup>	*
*	viscosa:	viscosity of nitrogen	P.s	*
*	ka:	thermal conductivity of nitrogen	W/m/K	*
*	km:	thermal conductivity of metal	W/m/K	*
*	Pr:	Prandtle numble		*
*	Ta:	temperature of nitrogen	K	*
*	Tl:	liquidius temperature of alloy	K	*
*	Te:	eutectic temperature of alloy	K	*
*	Tu:	undercooling	K	*
*	Tn:	nucleation temperature	K	*
*	Tr:	recalescence temperature	K	*

* fsr:	solid fraction at end of recalescence		*
* fsp:	solid fraction of pre-eutectic phase		*
* Hft:	total latent heat of fusion	J/kg	*
* Hfp:	heat of fusion for pre-eutectic phase	J/kg	*
* Hfe:	heat of fusion for eutectic phase	J/kg	*
* Cpsource:	effective specific heat for pro-eutectic	J/kg/K	*
* Cpold:	effective specific heat for equilibrium	J/kg/K	*
* Cpm:	specific heat of mushy metal	J/kg/K	*
* deltat:	step size of time	s	*
* x:	dummy variable for temperature	K	*
* ReD:	dummy variable for Reynolds number		*
* term:	dummy variable	s/m	*
* time:	array variable for time	s	*
* U:	array variable for velocity	m/s	*
* height:	array variable for position of droplet	m	*
* Re:	array variable for Reynolds number		*
* Nu:	array variable for Nusselt number		*
* h:	array variable for heat transfer coefficient	W/K/m <sup>2</sup>	*
* T:	array variable for temperature of droplet	K	*
* fs:	array variable for solid fraction of droplet		*
* Hf:	array variable for heat of formation	J/kg	*
* r:	array variable for radius	m	*
* q1:	array variable for rate of heat evolved	J/s	*
* q2:	array variable for rate of heat extracted	J/s	*
* Um:	velocity at half step size	m/s	*
* Rem:	Reynolds number at half step size		*
* hm:	heat transfer coefficient at half step size	W/K/m <sup>2</sup>	*
* kn:	n=1,2,3,4, variables used in RK method		*
* deltam:	n=1,2,3, variables for partial step sizes	s	*
* Un:	n=1,2,3, velocities at partial step sizes	m/s	*



* heightn:	n=1,2,3, heights at partial step sizes (pss)	m	*
* Ren:	n=1,2,3, Reynolds number at pss		*
* Nun:	n=1,2,3, Nusselt number at pss		*
* hn:	n=1,2,3, heat transfer coefficient at pss	W/K/m <sup>2</sup>	*
* Tn:	n=1,2,3, temperature at partial step sizes	K	*
* fsn:	n=1,2,3, solid fraction at pss		*
* Hfn:	n=1,2,3, heat of formation at pss	J/kg	*
* rn:	n=1, radius at partial step sizes	m	*

\*\*\*\*\*

**PROGRAM MAIN**

REAL D, density, densitya, viscosa, ka, km, Pr, B, beta,  
 \$ Ta, Tl, Te, Tu, Tn, Tr, R0, fsr, factor, deltaH,  
 \$ fsp, Hft, Hfp, Hfe, Cpsource, Cpm, deltat, x, ReD, term,  
 \$ time(10000), U(10000), height(10000), Re(10000),  
 \$ Nu(10000), h(10000), T(10000), fs(10000), Hf(10000),  
 \$ r(10000), q1(10000), q2(10000),  
 \$ Um,Rem,Num,hm, k1, k2, k3, k4,  
 \$ deltat1, deltat2, deltat3, time1, time2, time3,  
 \$ U1, U2, U3, height1, height2, height3, Re1, Re2, Re3,  
 \$ Nu1, Nu2, Nu3, h1, h2, h3, T1, T2, T3, fs1, fs2, fs3,  
 \$ Hf1, Hf2, Hf3, r1

**INTEGER I**

- \* Define functions to calculate: 1). specific heat of alloy at
- \* different temperature ranges, funcCpl for liquid range, funcCpls
- \* for liquid + solid solution range, and solid solution range;
- \* 2). drag coefficient from Reynolds number:

funcCpl(x)=984.013

funcCpls(x)=(227.314-0.257143\*x)/(197.248-0.206697\*x)

\$ \*(695.738+0.397412\*x)+(1-(227.314-0.257143\*x))

\$ /(197.248-0.206697\*x))\*984.013

funcCps(x)=695.738+0.397412\*x

Cd(ReD)=18.5/ReD\*\*0.6

OPEN(UNIT=8, FILE='THERMAL.OUT', STATUS='OLD')

- \* Assign values for constants:

density=3759

densitya=1.2506

viscosa=1.781e-5

ka=0.0261

km=111.0

B=0.0426

Pr=0.71

beta=1

Ta=293.0

Tl=884.0

Te=821.0

fsp=0.588

Hft=276177.0

**WRITE(6,\*) 'ENTER UNDERCOOLING:'**

**READ(5,\*) Tu**

**\* WRITE(6,\*) 'PLEASE ENTER DIAMETER OF DROPLET IN MICRONS:'**

**\* READ(5,\*) D**

**D=326**

**WRITE(6,\*) 'PLEASE ENTER TIME STEP IN SECONDS ( > 0.0001 sec ):'**

**READ(5,\*) deltat**

**\* deltat=0.01**

**WRITE(6,\*) 'ENTER TIME STEP FACTOR:'**

**READ(5,\*) factor**

**\* WRITE(6,\*) 'ENTER T(1):'**

**\* READ(5,\*) T(1)**

**T(1)=973**

**\* WRITE(6,\*) 'ENTER U(1):'**

**\* READ(5,\*) U(1)**

**U(1)=1.13**

**Tn=Tl-Tu**

**deltaH=984.013\*Tu**

**Hft=Hft-deltaH**

**Hfp=Hft\*fsp**

**Hfe=Hft-Hfp**

**D=D\*0.000001**

**R0=D/2.0**

**\* Assign initial values to the variables:**

**I=1**

**time(1)=0.0**

**height(1)=2.13**

**fs(1)=0.0**

**Hf(1)=0.0**

**r(1)=0.0**

**q1(1)=0.0**

**q2(1)=0.0**

**term=D\*densitya/viscosa**

**Re(1)=U(1)\*term**

**Nu(1)=2+0.6\*SQRT(Re(1))\*Pr\*\*(1.0/3.0)**

**h(1)=Nu(1)\*ka/D**

**\* Output title and the initial conditions:**

**WRITE(8,\*) ' RESULTS USING 4TH-ORDER RUNGE-KUTTA**

**\* METHOD'**

**WRITE(8,\*) ' '**

**WRITE(8,\*) ' I t(I)(sec) T(I)(K)',**

**\$ ' height(I)(m) U(I)(m/sec) fs Hf(I)(J/kg) h(I)'**

**WRITE(8,100) I, time(I), T(I), height(I), U(I), fs(I),Hf(I),**

**\$ h(I), r(I), q1(I), q2(I)**

**100 FORMAT(' ', I4, ' ', F7.4,3X,F9.3,4X,F7.4,4X,F8.4,4X,F7.4,**

**\$ 4X, F8.0, 4x, F10.2, 4X, F16.14, 4X, F16.8, 4X, F16.8)**

\* Loop to calculate variables in liquid range:

```
10  IF(T(I).GT.Tn.AND.height(I).GT.0.0) THEN

      time(I+1)=time(I)+deltat
      U(I+1)=U(I)+(9.8*(density-densitya)/density
$     -3.0/4.0*densitya/density*Cd(Re(I))/D*U(I)*U(I))*deltat
      height(I+1)=height(I)-U(I+1)*deltat
      Re(I+1)=U(I+1)*term
      Nu(I+1)=2+0.6*SQRT(Re(I+1))*Pr**(1.0/3.0)
      h(I+1)=Nu(I+1)*ka/D

      Um=U(I)+(9.8*(density-densitya)/density-3.0/4.0
$     *densitya/density*Cd(Re(I))/D*U(I)*U(I))*deltat/2.0
      Rem=Um*term
      Num=2+0.6*SQRT(Rem)*Pr**(1.0/3.0)
      hm=Num*ka/D

      k1=-6.0*h(I)*(T(I)-Ta)/(D*density*funcCpl(T(I)))
      k2=-6.0*hm*(T(I)+k1*deltat/2.0-Ta)/(D*density
$     *funcCpl(T(I)+k1*deltat/2.0))
      k3=-6.0*hm*(T(I)+k2*deltat/2.0-Ta)/(D*density
$     *funcCpl(T(I)+k2*deltat/2.0))
      k4=-6.0*h(I+1)*(T(I)+k3*deltat-Ta)/(D*density
$     *funcCpl(T(I)+k3*deltat))

      T(I+1)=T(I)+(k1+2.0*k2+2.0*k3+k4)/6.0*deltat

      fs(I+1)=0.0
      Hf(I+1)=0.0
```

**r(I+1) =0.0**

**q1(I+1)=0.0**

**q2(I+1)=0.0**

**WRITE(8,100) I+1,time(I+1),T(I+1),height(I+1),U(I+1),  
\$ fs(I+1), Hf(I+1), h(I+1), r(I+1), q1(I+1), q2(I+1)**

**I=I+1**

**GOTO 10**

**ENDIF**

- \* To calculate parameters at nucleation temperature with a partial**
- \* time step:**

**deltat1=(T(I-1)-Tn)/(T(I-1)-T(I))\*deltat**

**time1=time(I-1)+deltat1**

**U1=U(I-1)+(9.8\*(density-densitya)/density-3.0/4.0**

**\$ \*densitya/density\*Cd(Re(I-1))/D\*U(I-1)\*U(I-1))\*deltat1**

**height1=height(I-1)-U1\*deltat1**

**Re1=U1\*term**

**Nu1=2+0.6\*SQRT(Re1)\*Pr\*\*(1.0/3.0)**

**h1=Nu1\*ka/D**

**T1=Tn**

**fs1=0.0**

**Hf1=0.0**

**r1 =0.0**

```
WRITE(8,200) time1, Tn, height1, U1, fs1, Hf1, h1, r1
write(6,*) 'NUCLEATION TIME=', time1
```

```
200  FORMAT(' ', 6X, F7.4,3X,F9.3,4X,F7.4,4X,F8.4,4X,F7.4,4X,F8.0,
$      4X, F10.2, 4X, F16.14)
```

\* Reassign step size and calculate 1st step:

```
deltat=deltat/factor
```

```
time(I)=time1+deltat
```

```
U(I)=U1+(9.8*(density-densitya)/density
```

```
$ -3.0/4.0*densitya/density*Cd(Re1)/D*U1*U1)*deltat
```

```
height(I)=height1-U(I)*deltat
```

```
Re(I)=U(I)*term
```

```
Nu(I)=2+0.6*SQRT(Re(I))*Pr**(1.0/3.0)
```

```
h(I)=Nu(I)*ka/D
```

```
Cpm=funcCps(T1)*fs1+funcCpl(T1)*(1-fs1)
```

```
r(I) =r1+B*(T1-T1)*deltat
```

```
k1=3.0*B*Hft*r(I)**2.0/(R0**3.0*Cpm)*(T1-T1)
```

```
$ -3.0*h(I)/(R0*density*Cpm)*(T1-Ta)
```

```
k2=3.0*B*Hft*r(I)**2.0/(R0**3.0*Cpm)*(T1-T1-k1*deltat/2.0)
```

```
$ -3.0*h(I)/(R0*density*Cpm)*(T1+k1*deltat/2.0-Ta)
```

```
k3=3.0*B*Hft*r(I)**2.0/(R0**3.0*Cpm)*(T1-T1-k2*deltat/2.0)
```

```
$ -3.0*h(I)/(R0*density*Cpm)*(T1+k2*deltat/2.0-Ta)
```

```
k4=3.0*B*Hft*r(I)**2.0/(R0**3.0*Cpm)*(T1-T1-k3*deltat)
```

```
$ -3.0*h(I)/(R0*density*Cpm)*(T1+k3*deltat-Ta)
```

$$T(I)=T1+(k1+2.0*k2+2.0*k3+k4)/6.0*deltat$$

$$fs(I)=(r(I)/R0)**3.0$$

$$Hf(I)=Hft*fs(I)$$

$$q1(I)=4.0*3.1415926*r(I)*r(I)*B*density*Hft*(T1-T(I))$$

$$q2(I)=4.0*3.1415926*R0*R0*h(I)*(T(I)-Ta)$$

```
WRITE(8,100) I,time(I),T(I),height(I),U(I),
$          fs(I), Hf(I), h(I), r(I), q1(I), q2(I)
```

\* Calculate parameters at recalescence range:

```
20 IF(q1(I).GT.q2(I).AND.height(I).GT.0.0) THEN
```

$$time(I+1)=time(I)+deltat$$

$$U(I+1)=U(I)+(9.8*(density-densitya)/density$$

```
$ -3.0/4.0*densitya/density*Cd(Re(I))/D*U(I)*U(I))*deltat
```

$$height(I+1)=height(I)-U(I+1)*deltat$$

$$Re(I+1)=U(I+1)*term$$

$$Nu(I+1)=2+0.6*SQRT(Re(I+1))*Pr**(1.0/3.0)$$

$$h(I+1)=Nu(I+1)*ka/D$$

$$Cpm=funcCps(T(I))*fs(I)+funcCpl(T(I))*(1-fs(I))$$

$$k1=3.0*B*Hft*r(I)*r(I)/(R0**3.0*Cpm)*(T1-T(I))$$

```
$ -3.0*h(I+1)/(R0*density*Cpm)*(T(I)-Ta)
```

$$k2=3.0*B*Hft*r(I)*r(I)/(R0**3.0*Cpm)$$

```
$ *(T1-T(I)-k1*deltat/2.0)
```

```
$ -3.0*h(I+1)/(R0*density*Cpm)*(T(I)+k1*deltat/2.0-Ta)
```



```

k3=3.0*B*Hft*r(I)*r(I)/(R0**3.0*Cpm)
$      *(T1-T(I)-k2*deltat/2.0)
$      -3.0*h(I+1)/(R0*density*Cpm)*(T(I)+k2*deltat/2.0-Ta)
k4=3.0*B*Hft*r(I)*r(I)/(R0**3.0*Cpm)*(T1-T(I)
$      -k3*deltat)
$      -3.0*h(I+1)/(R0*density*Cpm)*(T(I)+k3*deltat-Ta)

```

```

T(I+1)=T(I)+(k1+2.0*k2+2.0*k3+k4)/6.0*deltat

```

```

r(I+1)=r(I)+B*(T1-T(I+1))*deltat
fs(I+1)=(r(I+1)/R0)**3.0
Hf(I+1)=Hft*fs(I+1)
q1(I+1)=4.0*3.1415926*r(I+1)*r(I+1)*B*density*Hft
$      *(T1-T(I+1))
q2(I+1)=4.0*3.1415926*R0*R0*h(I+1)*(T(I+1)-Ta)

```

```

WRITE(8,100) I+1,time(I+1),T(I+1),height(I+1),U(I+1),
$      fs(I+1), Hf(I+1), h(I+1), r(I+1), q1(I+1), q2(I+1)

```

```

I=I+1
GOTO 20

```

```

ENDIF

```

```

write(6,*) ' I tr(sec)    fsr    Hfsr    rsr '

```

```

write(6,500) I,time(I),fs(I), Hf(I), r(I)*1000000

```

```

500  format(' ', I4, ' ', F6.4,2X,F6.4,
$      2X,F8.0,2X,F4.0)

```

deltat=deltat\*factor

Tr=T(I)

fsr=fs(I)

IF(fs(I).LT.fsp) THEN

GOTO 30

ELSEIF(fs(I).LT.1.0) THEN

Hfp=Hf(I)

fsp=fs(I)

GOTO 40

ELSE

GOTO 50

ENDIF

\* Calculate parameters at liquid + solid solution range:

30 Cpsource=(Hft-Hf(I)-Hfe)/(Tr-Te)

\* write(6,\*) 'cpsource=',cpsource

31 IF((T(I)-1.0).GT.Te.AND.height(I).GT.0.0) THEN

time(I+1)=time(I)+deltat

U(I+1)=U(I)+(9.8\*(density-densitya)/density-3.0/4.0

\$ \*densitya/density\*Cd(Re(I))/D\*U(I)\*U(I))\*deltat

height(I+1)=height(I)-U(I+1)\*deltat

Re(I+1)=U(I+1)\*term

Nu(I+1)=2+0.6\*SQRT(Re(I+1))\*Pr\*\*(1.0/3.0)

h(I+1)=Nu(I+1)\*ka/D

```

Um=U(I)+(9.8*(density-densitya)/density-3.0/4.0
$   *densitya/density*Cd(Re(I))/D*U(I)*U(I)*deltat/2.0
Rem=Um*term
Num=2+0.6*SQRT(Rem)*Pr**(1.0/3.0)
hm=Num*ka/D

k1=-6.0*h(I)*(T(I)-Ta)/(D*density
$   *(Cpsource+funcCpls(T(I))))
k2=-6.0*hm*(T(I)+k1*deltat/2.0-Ta)/(D*density
$   *(Cpsource+funcCpls(T(I)+k1*deltat/2.0)))
k3=-6.0*hm*(T(I)+k2*deltat/2.0-Ta)/(D*density
$   *(Cpsource+funcCpls(T(I)+k2*deltat/2.0)))
k4=-6.0*h(I+1)*(T(I)+k3*deltat-Ta)/(D*density
$   *(Cpsource+funcCpls(T(I)+k3*deltat)))

T(I+1)=T(I)+(k1+2.0*k2+2.0*k3+k4)/6.0*deltat

fs(I+1)=fsr+(Tr-T(I+1))/(Tr-Te)*(fsp-fsr)
Hf(I+1)=Hft*fs(I+1)

WRITE(8,100) I+1,time(I+1),T(I+1),height(I+1),U(I+1),
$           fs(I+1), Hf(I+1), h(I+1)

I=I+1

GOTO 31

ENDIF

```

\* Calculate parameters at the beginning of eutectic transformation:

$$\text{deltat2}=(T(I-1)-T_e)/(T(I-1)-T(I))*\text{deltat}$$

$$\text{time2}=\text{time}(I-1)+\text{deltat2}$$

$$U2=U(I-1)+(9.8*(\text{density}-\text{density}_a)/\text{density}-3.0/4.0$$

$$\$ \quad * \text{density}_a/\text{density} * C_d(\text{Re}(I-1))/D * U(I-1) * U(I-1)) * \text{deltat2}$$

$$\text{height2}=\text{height}(I-1)-U2 * \text{deltat2}$$

$$\text{Re2}=U2 * \text{term}$$

$$\text{Nu2}=2+0.6 * \text{SQRT}(\text{Re2}) * \text{Pr}^{1.0/3.0}$$

$$h2=\text{Nu2} * k_a/D$$

$$T2=T_e$$

$$Hf2=H_{fp}$$

$$fs2=f_{sp}$$

$$\text{WRITE}(8,200) \text{ time2}, T2, \text{height2}, U2, fs2, Hf2, h2$$

\* Recalculate parameters for the first partial time step during  
\* eutectic transformation:

$$U_m=U2+(9.8*(\text{density}-\text{density}_a)/\text{density}-3.0/4.0$$

$$\$ \quad * \text{density}_a/\text{density} * C_d(\text{Re2})/D * U2 * U2) * (\text{deltat}-\text{deltat2})/2.0$$

$$\text{Re}_m=U_m * \text{term}$$

$$\text{Nu}_m=2+0.6 * \text{SQRT}(\text{Re}_m) * \text{Pr}^{1.0/3.0}$$

$$h_m=\text{Nu}_m * k_a/D$$

$$k1=6.0 * h2 * (T_e - T_a) / (D * \text{density})$$

$$k2=6.0 * h_m * (T_e - T_a) / (D * \text{density})$$

$$k3=6.0 * h_m * (T_e - T_a) / (D * \text{density})$$

$$k4=6.0*h(I)*(Te-Ta)/(D*density)$$

$$Hf(I)=Hf2+(k1+2.0*k2+2.0*k3+k4)/6.0*(deltat-deltat2)$$

$$T(I)=Te$$

$$fs(I)=fsp+(Hf(I)-Hfp)/Hfe*(1.0-fsp)$$

WRITE(8,100) I,time(I),T(I),height(I),U(I),fs(I), Hf(I), h(I)

GOTO 41

\* Calculate parameters during eutectic transformation:

40 Hf(I)=Hfp

fs(I)=fsp

41 IF((Hf(I)-100).LT.(Hft).AND.height(I).GT.0.0) THEN

time(I+1)=time(I)+deltat

U(I+1)=U(I)+(9.8\*(density-densitya)/density-3.0/4.0

\$ \*densitya/density\*Cd(Re(I))/D\*U(I)\*U(I))\*deltat

height(I+1)=height(I)-U(I+1)\*deltat

Re(I+1)=U(I+1)\*term

Nu(I+1)=2+0.6\*SQRT(Re(I+1))\*Pr\*\*(1.0/3.0)

h(I+1)=Nu(I+1)\*ka/D

Um=U(I)+(9.8\*(density-densitya)/density-3.0/4.0

\$ \*densitya/density\*Cd(Re(I))/D\*U(I)\*U(I))\*deltat/2.0

Rem=Um\*term

$$\text{Num}=2+0.6*\text{SQRT}(\text{Rem})*\text{Pr}^{**}(1.0/3.0)$$

$$\text{hm}=\text{Num}*k_a/D$$

$$k_1=6.0*h(I)*(T_e-T_a)/(D*\text{density})$$

$$k_2=6.0*hm*(T_e-T_a)/(D*\text{density})$$

$$k_3=6.0*hm*(T_e-T_a)/(D*\text{density})$$

$$k_4=6.0*h(I+1)*(T_e-T_a)/(D*\text{density})$$

$$\text{Hf}(I+1)=\text{Hf}(I)+(k_1+2.0*k_2+2.0*k_3+k_4)/6.0*\text{deltat}$$

$$\text{fs}(I+1)=\text{fsp}+(\text{Hf}(I+1)-\text{Hfp})/\text{Hfe}*(1.0-\text{fsp})$$

$$T(I+1)=T_e$$

WRITE(8,100) I+1,time(I+1),T(I+1),height(I+1),U(I+1),

\$ fs(I+1), Hf(I+1), h(I+1)

I=I+1

GOTO 41

ENDIF

\* Calculate parameters at the end of eutectic transformation:

$$\text{deltat}_3=(\text{Hf}(I-1)-\text{Hft})/\text{Hft}*\text{deltat}$$

$$\text{time}_3=\text{time}(I-1)+\text{deltat}_3$$

$$U_3=U(I-1)+(9.8*(\text{density}-\text{density}_a)/\text{density}-3.0/4.0$$

$$\$ \quad * \text{density}_a/\text{density}*\text{Cd}(\text{Re}(I-1))/D*U(I-1)*U(I-1))*\text{deltat}_3$$

$$\text{height}_3=\text{height}(I-1)-U_3*\text{deltat}_3$$

$$\text{Re}_3=U_3*\text{term}$$

$$\text{Nu}_3=2+0.6*\text{SQRT}(\text{Re}_3)*\text{Pr}^{**}(1.0/3.0)$$

$$h3 = Nu3 * ka / D$$

$$T3 = Te$$

$$Hf3 = Hft$$

$$fs3 = 1.0$$

WRITE(8,200) time3, T3, height3, U3, fs3, Hf3, h3

write(6,\*) 'SOLIDIFICATION TIME=', time3

write(6,\*) 'COOLING RATE=', (T(1)-Te)/time3

- \* Recalculate parameters for the first partial time step in solid
- \* solution range:

$$Um = U3 + (9.8 * (density - densitya) / density - 3.0 / 4.0$$

$$\$ \quad * densitya / density * Cd(Re3) / D * U1 * U1 * (deltat - deltat3) / 2.0$$

$$Rem = Um * term$$

$$Num = 2 + 0.6 * SQRT(Rem) * Pr ** (1.0 / 3.0)$$

$$hm = Num * ka / D$$

$$k1 = -6.0 * h3 * (T3 - Ta) / (D * density$$

$$\$ \quad * funcCps(T3))$$

$$k2 = -6.0 * hm * (T3 + k1 * (deltat - deltat3) / 2.0 - Ta) / (D * density$$

$$\$ \quad * funcCps(T3 + k1 * (deltat - deltat3) / 2.0))$$

$$k3 = -6.0 * hm * (T3 + k2 * (deltat - deltat3) / 2.0 - Ta) / (D * density$$

$$\$ \quad * funcCps(T3 + k2 * (deltat - deltat3) / 2.0))$$

$$k4 = -6.0 * h(I) * (T3 + k3 * (deltat - deltat3) - Ta) / (D * density$$

$$\$ \quad * funcCps(T3 + k3 * (deltat - deltat3)))$$

$$T(I)=T3+(k1+2.0*k2+2.0*k3+k4)/6.0*(deltat-deltat3)$$

$$fs(I)=1.0$$

$$Hf(I)=Hft$$

WRITE(8,100) I,time(I),T(I),height(I),U(I),fs(I),Hf(I), h(I)

\* Calculate parameters at the solid solution range:

50 IF(T(I).GT.Ta.AND.height(I).GT.0.0) THEN

$$time(I+1)=time(I)+deltat$$

$$U(I+1)=U(I)+(9.8*(density-densitya)/density-3.0/4.0$$

$$\$ \quad *densitya/density*Cd(Re(I))/D*U(I)*U(I))*deltat$$

$$height(I+1)=height(I)-U(I+1)*deltat$$

$$Re(I+1)=U(I+1)*term$$

$$Nu(I+1)=2+0.6*SQRT(Re(I+1))*Pr**(1.0/3.0)$$

$$h(I+1)=Nu(I+1)*ka/D$$

$$Um=U(I)+(9.8*(density-densitya)/density-3.0/4.0$$

$$\$ \quad *densitya/density*Cd(Re(I))/D*U(I)*U(I))*deltat/2.0$$

$$Rem=Um*term$$

$$Num=2+0.6*SQRT(Rem)*Pr**(1.0/3.0)$$

$$hm=Num*ka/D$$

$$k1=-6.0*h(I)*(T(I)-Ta)/(D*density*funcCps(T(I)))$$

$$k2=-6.0*hm*(T(I)+k1*deltat/2.0-Ta)/(D*density$$

$$\$ \quad *funcCps(T(I)+k1*deltat/2.0))$$

$$k3=-6.0*hm*(T(I)+k2*deltat/2.0-Ta)/(D*density$$

$$\$ \quad *funcCps(T(I)+k2*deltat/2.0))$$



```

          k4=-6.0*h(I+1)*(T(I)+k3*deltat-Ta)/(D*density
$          *funcCps(T(I)+k3*deltat))

          T(I+1)=T(I)+(k1+2.0*k2+2.0*k3+k4)/6.0*deltat

          fs(I+1)=1.0
          Hf(I+1)=Hft

          WRITE(8,100) I+1,time(I+1),T(I+1),height(I+1),U(I+1),
$          fs(I+1), Hf(I+1), h(I+1)

          I=I+1
          GOTO 50

      ENDIF

      WRITE(8,*) ' '
      WRITE(8,300) D*1000000.0, deltat
300  FORMAT(' ', 'Diameter =', F5.0, ' microns', 10x, 'Deltat =',
$      F8.6, ' seconds')

      STOP

      END

```

**APPENDIX B**

**FORTRAN PROGRAM TO CALCULATE  
THE TEMPERATURE PROFILE OF AN Al-10wt%Cu DROPLET**

\*\*\*\*\*

\* This program will calculate the thermal profile of a 90%wtAl-10%wtCu \*  
 \* alloy droplet during free falling by using 4th-order Runge-Kutta method. \*  
 \* The units used in calculation are in SI units as shown in the \*  
 \* and are also shown as follows, except for particle size where m is used in \*  
 \* calculation, but  $10^{-6}$  m is used in keyboard entry for convenience. \*

* Variables	* Definitions	* Units
* beta:	* Cahn's parameter in the kinetic equation	
* B:	* kinetic coefficient	* m/s/K
* D:	* droplet diameter	* m
* R0:	* droplet radius	* m
* density:	* density of droplet	* kg/m <sup>3</sup>
* densitya:	* density of nitrogen	* kg/m <sup>3</sup>
* viscosa:	* viscosity of nitrogen	* P <sub>a</sub> s
* ka:	* thermal conductivity of nitrogen	* W/m/K
* km:	* thermal conductivity of metal	* W/m/K
* Pr:	* Prandtle numble	
* Ta:	* temperature of nitrogen	* K
* Tl:	* liquidius temperature of alloy	* K
* Te:	* eutectic temperature of alloy	* K
* Tu:	* undercooling	* K
* Tn:	* nucleation temperature	* K
* Tr:	* recalescence temperature	* K

* fsr:	solid fraction at end of recalescence		*
* fsp:	solid fraction of pre-eutectic phase		*
* Hft:	total latent heat of fusion	J/kg	*
* Hfp:	heat of fusion for pre-eutectic phase	J/kg	*
* Hfe:	heat of fusion for eutectic phase	J/kg	*
* Cpsource:	effective specific heat for pro-eutectic	J/kg/K	*
* Cpload:	effective specific heat for equilibrium	J/kg/K	*
* Cpm:	specific heat of mushy metal	J/kg/K	*
* deltat:	step size of time	s	*
* x:	dummy variable for temperature	K	*
* ReD:	dummy variable for Reynolds number		*
* term:	dummy variable	s/m	*
* time:	array variable for time	s	*
* U:	array variable for velocity	m/s	*
* height:	array variable for position of droplet	m	*
* Re:	array variable for Reynolds number		*
* Nu:	array variable for Nusselt number		*
* h:	array variable for heat transfer coefficient	W/K/m <sup>2</sup>	*
* T:	array variable for temperature of droplet	K	*
* fs:	array variable for solid fraction of droplet		*
* Hf:	array variable for heat of formation	J/kg	*
* r:	array variable for radius	m	*
* q1:	array variable for rate of heat evolved	J/s	*
* q2:	array variable for rate of heat extracted	J/s	*
* Um:	velocity at half step size	m/s	*
* Rem:	Reynolds number at half step size		*
* hm:	heat transfer coefficient at half step size	W/K/m <sup>2</sup>	*
* kn:	n=1,2,3,4, variables used in RK method		*
* deltatn:	n=1,2,3, variables for partial step sizes	s	*
* Un:	n=1,2,3, velocities at partial step sizes	m/s	*

* heightn:	n=1,2,3, heights at partial step sizes (pss)	m	*
* Ren:	n=1,2,3, Reynolds number at pss		*
* Nun:	n=1,2,3, Nusselt number at pss		*
* hn:	n=1,2,3, heat transfer coefficient at pss	W/K/m <sup>2</sup>	*
* Tn:	n=1,2,3, temperature at partial step sizes	K	*
* fsn:	n=1,2,3, solid fraction at pss		*
* Hfn:	n=1,2,3, heat of formation at pss	J/kg	*
* rn:	n=1, radius at partial step sizes	m	*

\*\*\*\*\*

#### PROGRAM MAIN

REAL D, density, densitya, viscosa, ka, km, Pr, B, beta,  
 \$ Ta, Tl, Te, Tu, Tn, Tr, R0, fsr, factor,  
 \$ fsp, Hft, Hfp, Hfe, Cpsource, Cpm, deltat, x, ReD, term,  
 \$ time(10000), U(10000), height(10000), Re(10000),  
 \$ Nu(10000), h(10000), T(10000), fs(10000), Hf(10000),  
 \$ r(10000), q1(10000), q2(10000),  
 \$ Um,Rem,Num,hm, k1, k2, k3, k4,  
 \$ deltat1, deltat2, deltat3, time1, time2, time3,  
 \$ U1, U2, U3, height1, height2, height3, Re1, Re2, Re3,  
 \$ Nu1, Nu2, Nu3, h1, h2, h3, T1, T2, T3, fs1, fs2, fs3,  
 \$ Hf1, Hf2, Hf3, r1

#### INTEGER I

- \* Define functions to calculate: 1). specific heat of alloy at
- \* different temperature ranges, funcCpl for liquid range, funcCpls
- \* for liquid + solid solution range, and solid solution range;
- \* 2). drag coefficient from Reynolds number:

funcCpl(x)=1025.4

funcCpls(x)=(185.643-0.296432\*x)/(162.348-0.245982\*x)

\$ \*(724.4+0.4226\*x)+(-23.2946+0.05045\*x)

\$ /(162.348-0.245982\*x)\*1025.4

funcCps(x)=724.4+0.4226\*x

Cd(ReD)=18.5/ReD\*\*0.6

OPEN(UNIT=8, FILE='THERMAL.OUT', STATUS='OLD')

- \* Assign values for constants:

density=3324

densitya=1.2506

viscosa=1.781e-5

ka=0.0261

km=155.45

B=0.0426

Pr=0.71

beta=1

Ta=293.0

Tl=908.0

Te=821.0

fsp=0.8421

Hft=274902.0

**WRITE(6,\*) 'ENTER UNDERCOOLING:'**

**READ(5,\*) Tu**

**WRITE(6,\*) 'PLEASE ENTER DIAMETER OF DROPLET IN MICRONS:'**

**READ(5,\*) D**

**WRITE(6,\*) 'PLEASE ENTER TIME STEP IN SECONDS ( > 0.0001 sec ):'**

**READ(5,\*) deltat**

**WRITE(6,\*) 'ENTER TIME STEP FACTOR:'**

**READ(5,\*) factor**

**WRITE(6,\*) 'ENTER T(1):'**

**READ(5,\*) T(1)**

**Tn=Tl-Tu**

**deltaH=1025.4\*Tu**

**Hft=Hft-deltaH**

**Hfp=Hft\*fsp**

**Hfe=Hft-Hfp**

**D=D\*0.000001**

**R0=D/2.0**

**\* Assign initial values to the variables:**

**I=1**

**U(1)=0.55**

**time(1)=0.0**

height(1)=2.13

fs(1)=0.0

Hf(1)=0.0

r(1)=0.0

q1(1)=0.0

q2(1)=0.0

term=D\*densitya/viscosa

Re(1)=U(1)\*term

Nu(1)=2+0.6\*SQRT(Re(1))\*Pr\*\*(1.0/3.0)

h(1)=Nu(1)\*ka/D

\* Output title and the initial conditions:

```
WRITE(8,*) '      RESULTS USING 4TH-ORDER RUNGE-KUTTA  
METHOD'
```

```
WRITE(8,*) ' '
```

```
WRITE(8,*) ' I t(I)(sec) T(I)(K)'
```

```
$ ' height(I)(m) U(I)(m/sec) fs Hf(I)(J/kg) h(I)'
```

```
WRITE(8,100) I, time(I), T(I), height(I), U(I), fs(I),Hf(I),
```

```
$ h(I), r(I), q1(I), q2(I)
```

```
100 FORMAT(' ', I4, ' ', F7.4,3X,F9.3,4X,F7.4,4X,F8.4,4X,F7.4,
```

```
$ 4X, F8.0, 4x, F10.2, 4X, F16.14, 4X, F16.8, 4X, F16.8)
```

\* Loop to calculate variables in liquid range:

```
10 IF(T(I).GT.Tn.AND.height(I).GT.0.0) THEN
```



```

time(I+1)=time(I)+deltat
U(I+1)=U(I)+(9.8*(density-densitya)/density
$ -3.0/4.0*densitya/density*Cd(Re(I))/D*U(I)*U(I))*deltat
height(I+1)=height(I)-U(I+1)*deltat
Re(I+1)=U(I+1)*term
Nu(I+1)=2+0.6*SQRT(Re(I+1))*Pr**(1.0/3.0)
h(I+1)=Nu(I+1)*ka/D

Um=U(I)+(9.8*(density-densitya)/density-3.0/4.0
$ *densitya/density*Cd(Re(I))/D*U(I)*U(I))*deltat/2.0
Rem=Um*term
Num=2+0.6*SQRT(Rem)*Pr**(1.0/3.0)
hm=Num*ka/D

k1=-6.0*h(I)*(T(I)-Ta)/(D*density*funcCpl(T(I)))
k2=-6.0*hm*(T(I)+k1*deltat/2.0-Ta)/(D*density
$ *funcCpl(T(I)+k1*deltat/2.0))
k3=-6.0*hm*(T(I)+k2*deltat/2.0-Ta)/(D*density
$ *funcCpl(T(I)+k2*deltat/2.0))
k4=-6.0*h(I+1)*(T(I)+k3*deltat-Ta)/(D*density
$ *funcCpl(T(I)+k3*deltat))

T(I+1)=T(I)+(k1+2.0*k2+2.0*k3+k4)/6.0*deltat

fs(I+1)=0.0
Hf(I+1)=0.0
r(I+1) =0.0
q1(I+1)=0.0
q2(I+1)=0.0

```

```

WRITE(8,100) I+1,time(I+1),T(I+1),height(I+1),U(I+1),
$      fs(I+1), Hf(I+1), h(I+1), r(I+1), q1(I+1), q2(I+1)

I=I+1
GOTO 10

```

ENDIF

- \* To calculate parameters at nucleation temperature with a partial
- \* time step:

```

deltat1=(T(I-1)-Tn)/(T(I-1)-T(I))*deltat
time1=time(I-1)+deltat1
U1=U(I-1)+(9.8*(density-densitya)/density-3.0/4.0
$ *densitya/density*Cd(Re(I-1))/D*U(I-1)*U(I-1))*deltat1
height1=height(I-1)-U1*deltat1
Re1=U1*term
Nu1=2+0.6*SQRT(Re1)*Pr**(1.0/3.0)
h1=Nu1*ka/D

T1=Tn

fs1=0.0
Hf1=0.0
r1 =0.0

WRITE(8,200) time1, Tn, height1, U1, fs1, Hf1, h1, r1

200  FORMAT(' ', 6X, F7.4,3X,F9.3,4X,F7.4,4X,F8.4,4X,F7.4,4X,F8.0,
$      4X, F10.2, 4X, F16.14)

```

\* Reassign step size and calculate 1st step:

$$\text{deltat}=\text{deltat}/\text{factor}$$

$$\text{time}(I)=\text{time}1+\text{deltat}$$

$$U(I)=U1+(9.8*(\text{density}-\text{density}a)/\text{density}$$

$$\$ \quad -3.0/4.0*\text{density}a/\text{density}*Cd(\text{Re}1)/D*U1*U1)*\text{deltat}$$

$$\text{height}(I)=\text{height}1-U(I)*\text{deltat}$$

$$\text{Re}(I)=U(I)*\text{term}$$

$$\text{Nu}(I)=2+0.6*\text{SQRT}(\text{Re}(I))*Pr^{**}(1.0/3.0)$$

$$h(I)=\text{Nu}(I)*ka/D$$

$$\text{Cpm}=\text{funcCps}(T1)*fs1+\text{funcCpl}(T1)*(1-fs1)$$

$$r(I) =r1+B*(T1-T1)*\text{deltat}$$

$$k1=3.0*B*Hft*r(I)**2.0/(R0**3.0*Cpm)*(T1-T1)$$

$$\$ \quad -3.0*h(I)/(R0*\text{density}*Cpm)*(T1-Ta)$$

$$k2=3.0*B*Hft*r(I)**2/(R0**3*Cpm)*(T1-T1-k1*\text{deltat}/2.0)$$

$$\$ \quad -3.0*h(I)/(R0*\text{density}*Cpm)*(T1+k1*\text{deltat}/2.0-Ta)$$

$$k3=3.0*B*Hft*r(I)**2/(R0**3*Cpm)*(T1-T1-k2*\text{deltat}/2.0)$$

$$\$ \quad -3.0*h(I)/(R0*\text{density}*Cpm)*(T1+k2*\text{deltat}/2.0-Ta)$$

$$k4=3.0*B*Hft*r(I)**2.0/(R0**3.0*Cpm)*(T1-T1-k3*\text{deltat})$$

$$\$ \quad -3.0*h(I)/(R0*\text{density}*Cpm)*(T1+k3*\text{deltat}-Ta)$$

$$T(I)=T1+(k1+2.0*k2+2.0*k3+k4)/6.0*\text{deltat}$$

$$fs(I)=(r(I)/R0)**3.0$$

$$Hf(I)=Hft*fs(I)$$

```

q1(I)=4.0*3.1415926*r(I)*r(I)*B*density*Hft*(Tl-T(I))
q2(I)=4.0*3.1415926*R0*R0*h(I)*(T(I)-Ta)

```

```

WRITE(8,100) I,time(I),T(I),height(I),U(I),
$          fs(I), Hf(I), h(I), r(I), q1(I), q2(I)

```

\* Calculate parameters at recalescence range:

```

20  IF(q1(I).GT.q2(I).AND.height(I).GT.0.0) THEN

```

```

    time(I+1)=time(I)+deltat
    U(I+1)=U(I)+(9.8*(density-densitya)/density
$   -3.0/4.0*densitya/density*Cd(Re(I))/D*U(I)*U(I))*deltat
    height(I+1)=height(I)-U(I+1)*deltat
    Re(I+1)=U(I+1)*term
    Nu(I+1)=2+0.6*SQRT(Re(I+1))*Pr**(1.0/3.0)
    h(I+1)=Nu(I+1)*ka/D

    Cpm=funcCps(T(I))*fs(I)+funcCpl(T(I))*(1-fs(I))

    k1=3.0*B*Hft*r(I)*r(I)/(R0**3.0*Cpm)*(Tl-T(I))
$   -3.0*h(I+1)/(R0*density*Cpm)*(T(I)-Ta)
    k2=3.0*B*Hft*r(I)*r(I)/(R0**3.0*Cpm)
$   *(Tl-T(I)-k1*deltat/2.0)
$   -3.0*h(I+1)/(R0*density*Cpm)*(T(I)+k1*deltat/2.0-Ta)
    k3=3.0*B*Hft*r(I)*r(I)/(R0**3.0*Cpm)
$   *(Tl-T(I)-k2*deltat/2.0)
$   -3.0*h(I+1)/(R0*density*Cpm)*(T(I)+k2*deltat/2.0-Ta)
    k4=3.0*B*Hft*r(I)*r(I)/(R0**3.0*Cpm)*(Tl-T(I))
$   -k3*deltat)

```

\$  $-3.0 \cdot h(I+1) / (R0 \cdot \text{density} \cdot Cpm) \cdot (T(I) + k3 \cdot \text{deltat} - Ta)$

$T(I+1) = T(I) + (k1 + 2.0 \cdot k2 + 2.0 \cdot k3 + k4) / 6.0 \cdot \text{deltat}$

$r(I+1) = r(I) + B \cdot (T1 - T(I+1)) \cdot \text{deltat}$

$fs(I+1) = (r(I+1) / R0) ** 3.0$

$Hf(I+1) = Hft \cdot fs(I+1)$

$q1(I+1) = 4.0 \cdot 3.1415926 \cdot r(I+1) \cdot r(I+1) \cdot B \cdot \text{density} \cdot Hft$

\$  $\cdot (T1 - T(I+1))$

$q2(I+1) = 4.0 \cdot 3.1415926 \cdot R0 \cdot R0 \cdot h(I+1) \cdot (T(I+1) - Ta)$

WRITE(8,100) I+1,time(I+1),T(I+1),height(I+1),U(I+1),

\$ fs(I+1), Hf(I+1), h(I+1), r(I+1), q1(I+1), q2(I+1)

I=I+1

GOTO 20

ENDIF

write(6,\*) ' I tr(sec) fsr Hfsr rsr '

write(6,500) I, time(I), fs(I), Hf(I), r(I)\*1000000

500 format(' ', I4, ' ', F6.4, 2x, F6.4, 2x, F8.0, 2x, F4.0)

deltat=deltat\*factor

Tr=T(I)

fsr=fs(I)

```

IF(fs(I).LT.fsp) THEN
    GOTO 30
ELSEIF(fs(I).LT.1.0) THEN
    Hfp=Hf(I)
    fsp=fs(I)
    GOTO 40
ELSE
    GOTO 50
ENDIF

```

\* Calculate parameters at liquid + solid solution range:

```

30  Cpsource=(Hft-Hf(I)-Hfe)/(Tr-Te)
    write(6,*) 'cpsource=',cpsource

31  IF((T(I)-1.0).GT.Te.AND.height(I).GT.0.0) THEN

        time(I+1)=time(I)+deltat
        U(I+1)=U(I)+(9.8*(density-densitya)/density-3.0/4.0
$      *densitya/density*Cd(Re(I))/D*U(I)*U(I))*deltat
        height(I+1)=height(I)-U(I+1)*deltat
        Re(I+1)=U(I+1)*term
        Nu(I+1)=2+0.6*SQRT(Re(I+1))*Pr**(1.0/3.0)
        h(I+1)=Nu(I+1)*ka/D

        Um=U(I)+(9.8*(density-densitya)/density-3.0/4.0
$      *densitya/density*Cd(Re(I))/D*U(I)*U(I))*deltat/2.0
        Rem=Um*term
        Num=2+0.6*SQRT(Rem)*Pr**(1.0/3.0)
        hm=Num*ka/D

```

```

      k1=-6.0*h(I)*(T(I)-Ta)/(D*density
$      *(Cpsource+funcCpls(T(I))))
      k2=-6.0*hm*(T(I)+k1*deltat/2.0-Ta)/(D*density
$      *(Cpsource+funcCpls(T(I)+k1*deltat/2.0)))
      k3=-6.0*hm*(T(I)+k2*deltat/2.0-Ta)/(D*density
$      *(Cpsource+funcCpls(T(I)+k2*deltat/2.0)))
      k4=-6.0*h(I+1)*(T(I)+k3*deltat-Ta)/(D*density
$      *(Cpsource+funcCpls(T(I)+k3*deltat)))

      T(I+1)=T(I)+(k1+2.0*k2+2.0*k3+k4)/6.0*deltat

      fs(I+1)=fsr+(Tr-T(I+1))/(Tr-Te)*(fsp-fsr)
      Hf(I+1)=Hft*fs(I+1)

      WRITE(8,100) I+1,time(I+1),T(I+1),height(I+1),U(I+1),
$      fs(I+1), Hf(I+1), h(I+1)

      I=I+1
      GOTO 31

ENDIF

```

\* Calculate parameters at the beginning of eutectic transformation:

```

      deltat2=(T(I-1)-Te)/(T(I-1)-T(I))*deltat
      time2=time(I-1)+deltat2
      U2=U(I-1)+(9.8*(density-densitya)/density-3.0/4.0
$      *densitya/density*Cd(Re(I-1))/D*U(I-1)*U(I-1))*deltat2
      height2=height(I-1)-U2*deltat2
      Re2=U2*term

```

$$Nu2=2+0.6*\text{SQRT}(Re2)*Pr^{(1.0/3.0)}$$

$$h2=Nu2*ka/D$$

$$T2=Te$$

$$Hf2=Hfp$$

$$fs2=fsp$$

WRITE(8,200) time2, T2, height2, U2, fs2, Hf2, h2

- \* Recalculate parameters for the first partial time step during
- \* eutectic transformation:

$$Um=U2+(9.8*(\text{density}-\text{densitya})/\text{density}-3.0/4.0$$

$$\$ \quad * \text{densitya}/\text{density} * Cd(Re2)/D * U2 * U2) * (\text{deltat}-\text{deltat2})/2.0$$

$$Rem=Um*term$$

$$Num=2+0.6*\text{SQRT}(Rem)*Pr^{(1.0/3.0)}$$

$$hm=Num*ka/D$$

$$k1=6.0*h2*(Te-Ta)/(D*\text{density})$$

$$k2=6.0*hm*(Te-Ta)/(D*\text{density})$$

$$k3=6.0*hm*(Te-Ta)/(D*\text{density})$$

$$k4=6.0*h(I)*(Te-Ta)/(D*\text{density})$$

$$Hf(I)=Hf2+(k1+2.0*k2+2.0*k3+k4)/6.0*(\text{deltat}-\text{deltat2})$$

$$T(I)=Te$$

$$fs(I)=fsp+(Hf(I)-Hfp)/Hfe*(1.0-fsp)$$



**WRITE(8,100) I,time(I),T(I),height(I),U(I),fs(I), Hf(I), h(I)**

**GOTO 41**

**\* Calculate parameters during eutectic transformation:**

**40 Hf(I)=Hfp**

**fs(I)=fsp**

**41 IF((Hf(I)-100)LT.(Hft).AND.height(I).GT.0.0) THEN**

**time(I+1)=time(I)+deltat**

**U(I+1)=U(I)+(9.8\*(density-densitya)/density-3.0/4.0**

**\$ \*densitya/density\*Cd(Re(I))/D\*U(I)\*U(I)\*deltat**

**height(I+1)=height(I)-U(I+1)\*deltat**

**Re(I+1)=U(I+1)\*term**

**Nu(I+1)=2+0.6\*SQRT(Re(I+1))\*Pr\*\*(1.0/3.0)**

**h(I+1)=Nu(I+1)\*ka/D**

**Um=U(I)+(9.8\*(density-densitya)/density-3.0/4.0**

**\$ \*densitya/density\*Cd(Re(I))/D\*U(I)\*U(I)\*deltat/2.0**

**Rem=Um\*term**

**Num=2+0.6\*SQRT(Rem)\*Pr\*\*(1.0/3.0)**

**hm=Num\*ka/D**

**k1=6.0\*h(I)\*(Te-Ta)/(D\*density)**

**k2=6.0\*hm\*(Te-Ta)/(D\*density)**

**k3=6.0\*hm\*(Te-Ta)/(D\*density)**

**k4=6.0\*h(I+1)\*(Te-Ta)/(D\*density)**

$$Hf(I+1)=Hf(I)+(k1+2.0*k2+2.0*k3+k4)/6.0*deltat$$

$$fs(I+1)=fsp+(Hf(I+1)-Hfp)/Hfe*(1.0-fsp)$$

$$T(I+1)=Te$$

**WRITE(8,100) I+1,time(I+1),T(I+1),height(I+1),U(I+1),**  
**\$ fs(I+1), Hf(I+1), h(I+1)**

$$I=I+1$$

**GOTO 41**

**ENDIF**

**\* Calculate parameters at the end of eutectic transformation:**

$$deltat3=(Hf(I-1)-Hft)/Hft*deltat$$

$$time3=time(I-1)+deltat3$$

$$U3=U(I-1)+(9.8*(density-densitya)/density-3.0/4.0$$

$$\$ *densitya/density*Cd(Re(I-1))/D*U(I-1)*U(I-1))*deltat3$$

$$height3=height(I-1)-U3*deltat3$$

$$Re3=U3*term$$

$$Nu3=2+0.6*SQRT(Re3)*Pr**(1.0/3.0)$$

$$h3=Nu3*ka/D$$

$$T3=Te$$

$$Hf3=Hft$$

$$fs3=1.0$$

```
WRITE(8,200) time3, T3, height3, U3, fs3, Hf3, h3
```

```
write(6,*) 'SOLIDIFICATION TIME=', time3
```

```
write(6,*) 'COOLING RATE=', (T(1)-Te)/time3
```

- \* Recalculate parameters for the first partial time step in solid
- \* solution range:

```
Um=U3+(9.8*(density-densitya)/density-3.0/4.0
```

```
$ *densitya/density*Cd(Re3)/D*U1*U1)*(deltat-deltat3)/2.0
```

```
Rem=Um*term
```

```
Num=2+0.6*SQRT(Rem)*Pr**(1.0/3.0)
```

```
hm=Num*ka/D
```

```
k1=-6.0*h3*(T3-Ta)/(D*density
```

```
$ *funcCps(T3))
```

```
k2=-6.0*hm*(T3+k1*(deltat-deltat3)/2.0-Ta)/(D*density
```

```
$ *funcCps(T3+k1*(deltat-deltat3)/2.0))
```

```
k3=-6.0*hm*(T3+k2*(deltat-deltat3)/2.0-Ta)/(D*density
```

```
$ *funcCps(T3+k2*(deltat-deltat3)/2.0))
```

```
k4=-6.0*h(I)*(T3+k3*(deltat-deltat3)-Ta)/(D*density
```

```
$ *funcCps(T3+k3*(deltat-deltat3)))
```

```
T(I)=T3+(k1+2.0*k2+2.0*k3+k4)/6.0*(deltat-deltat3)
```

```
fs(I)=1.0
```

```
Hf(I)=Hft
```

```
WRITE(8,100) I,time(I),T(I),height(I),U(I),fs(I),Hf(I), h(I)
```

\* Calculate parameters at the solid solution range:

```

50  IF(T(I).GT.Ta.AND.height(I).GT.0.0) THEN

      time(I+1)=time(I)+deltat
      U(I+1)=U(I)+(9.8*(density-densitya)/density-3.0/4.0
$      *densitya/density*Cd(Re(I))/D*U(I)*U(I))*deltat
      height(I+1)=height(I)-U(I+1)*deltat
      Re(I+1)=U(I+1)*term
      Nu(I+1)=2+0.6*SQRT(Re(I+1))*Pr**(1.0/3.0)
      h(I+1)=Nu(I+1)*ka/D

      Um=U(I)+(9.8*(density-densitya)/density-3.0/4.0
$      *densitya/density*Cd(Re(I))/D*U(I)*U(I))*deltat/2.0
      Rem=Um*term
      Num=2+0.6*SQRT(Rem)*Pr**(1.0/3.0)
      hm=Num*ka/D

      k1=-6.0*h(I)*(T(I)-Ta)/(D*density*funcCps(T(I)))
      k2=-6.0*hm*(T(I)+k1*deltat/2.0-Ta)/(D*density
$      *funcCps(T(I)+k1*deltat/2.0))
      k3=-6.0*hm*(T(I)+k2*deltat/2.0-Ta)/(D*density
$      *funcCps(T(I)+k2*deltat/2.0))
      k4=-6.0*h(I+1)*(T(I)+k3*deltat-Ta)/(D*density
$      *funcCps(T(I)+k3*deltat))

      T(I+1)=T(I)+(k1+2.0*k2+2.0*k3+k4)/6.0*deltat

      fs(I+1)=1.0
      Hf(I+1)=Hft

```

```

WRITE(8,100) I+1,time(I+1),T(I+1),height(I+1),U(I+1),
$           fs(I+1), Hf(I+1), h(I+1)

I=I+1
GOTO 50

ENDIF

WRITE(8,*) ''
WRITE(8,300) D*1000000.0, deltat
300  FORMAT(' ', 'Diameter =', F5.0, ' microns', 10x, 'Deltat =',
$       F8.6, ' seconds')

STOP

END

```

**APPENDIX C**

**ACCELERATION CHARACTERISTICS  
OF IMPULSE GENERATORS**

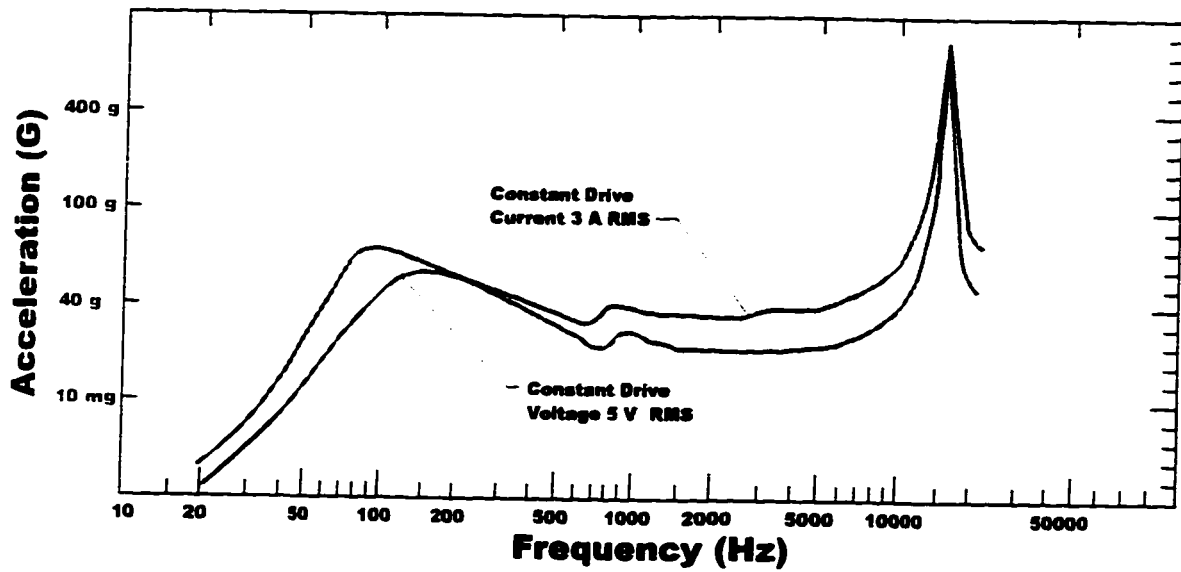


Figure C-1. Acceleration vs frequency of impulse generator A used in Pb-Sn alloy runs.

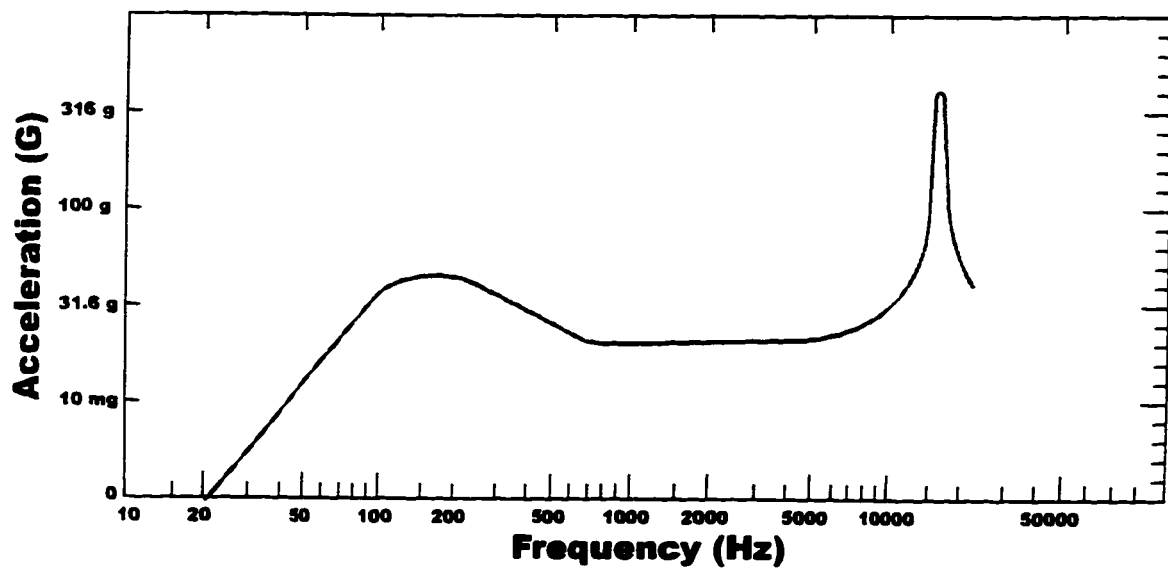


Figure C-2. Acceleration vs frequency of impulse generator B used in most of runs.



**APPENDIX D**

**FORTRAN PROGRAM TO CALCULATE  
SECONDARY DENDRITE ARM SPACING**

## PROGRAM IMAGE

```
*****  
* This program calculate dendrite arm spacing from the data measured by Optimas.  
*****  
* Before this program is used, [LnSampledPoints]' were replaced by integers of  
* 1000s between intensity and coordinate data, a character line (e.g. END) and a  
* number of 2000 had to be added to the end of the data file.  
*****  
* I: counter of intensity (luminance)  
* J: counter of x, y coordinates  
* K: counter of intensity peaks  
* L: counter for calculating dendrite arm spacing  
* M: counter for calculating average dendrite arm spacing  
* INT: array variable for intensity (luminance)  
* IMAX: array variable for intensity (luminance) peak  
* SUM: sum of dendrite arm spacing  
* AVG: average of dendrite arm spacing  
* SMAG: magnification of dendrite arm spacing  
* X: array variable for x coordinates  
* Y: array variable for y coordinates  
* SPACING: array variable for measured dendrite arm spacing  
* RSPACING: array variable for real dendrite arm spacing  
*****
```

INTEGER I, J, K, L, M, INT(1000), IMAX(100)

REAL SUM, AVG, SMAG, X(1000), Y(1000), SPACING(100),  
\$ RSPACING(100)

OPEN (UNIT=7, FILE='IMAGE.ASC', STATUS='OLD')  
OPEN (UNIT=8, FILE='IMAGE.OUT', STATUS='UNKNOWN')

SUM=0.0

M=0

I=1

J=1

K=1

\* for magnification=508, micron bar=60 micron

SMAG=33.84306/60\*150/1000

\* dummy read statement to jump the character line [Lnluminance]

READ(7, \*)

READ(7, \*) INT(I)

WRITE(8,\*) 'DENDRITE ARM SPACING (micron)'

1 IF (INT(I).NE.2000) THEN

I=I+1

READ(7,\*) INT(I)

10 IF (INT(I).NE. 1000) THEN

I=I+1

READ(7,\*) INT(I)

IF (INT(I-2).LT.INT(I-1).AND.INT(I-1).GE.INT(I)) THEN

IMAX(K)=I-1

```

        K=K+1
    ENDIF
    GOTO 10
ENDIF

DO 20 J=1, I-1
    READ(7,*) X(J), Y(J)
20 CONTINUE

*   dummy read statement to jump the character line [Lnluminance]
    READ(7,*)

DO 30 L=1,K-2
    SPACING(L)=SQRT((X(IMAX(L+1))-X(IMAX(L)))**2
$      +(Y(IMAX(L+1))-Y(IMAX(L)))**2)
    RSPACING(L)=SPACING(L)/SMAG
    SUM=SUM+RSPACING(L)
    WRITE(8,*) RSPACING(L)
30 CONTINUE

M=M+K-2

I=1
J=1
K=1

READ(7,*) INT(I)

GOTO 1

```

**ENDIF**

**AVG=SUM/M**

**WRITE(8,\*) 'AVERAGE=', AVG**

**STOP**

**END**